Cold dwell fatigue of Titanium

Yi Xiong

St Anne's College
University of Oxford

A thesis submitted for the degree of
Doctor of Philosophy

Trinity 2021

Abstract

- **Title:** Cold dwell fatigue of Titanium
- **Candidate:** Yi Xiong
- **College:** St Anne's college
- **Degree:** Doctor of Philosophy in Materials
- **Supervisors:** Prof. Angus J. Wilkinson and Prof. Edmund Tarleton

There is a long-standing technological problem in which a stress dwell during cyclic loading at room temperature in Ti causes a drastic fatigue life reduction. It is thought that localised time dependent plasticity in 'soft' grains oriented for easy plastic slip leads to load shedding and an increase in stress within a neighbouring 'hard' grain that is poorly oriented for easy slip. Quantifying this time dependent plasticity process is key to successfully predicting the complex cold dwell fatigue problem. Incorporating the influence of operating temperatures and common alloying elements on cold dwell fatigue will be beneficial for future alloy design to address this problem.

Firstly, stress relaxation tests were performed at four different temperatures on three major alloy systems: commercially pure titanium (two alloys with different oxygen content), Ti-6Al-4V (two microstructures with differing β phase fractions) and Ti-6Al-2Sn-4Zr-xMo (two alloys with different Mo content x=2 or 6 and portion of β phase). Key parameters controlling the time dependent plasticity were determined as a function of temperature from the macroscopic stress relaxation results. It was found that the dwell fatigue effect is more significant by oxygen alloying but is suppressed by the addition of Mo. The presence of the β phase did not strongly affect the dwell fatigue, however, it was suppressed at high temperature due to the low strain rate and strain rate sensitivity.

To understand the mechanism in greater detail, synchrotron X-ray diffraction technique during stress relaxation experiments was utilised to characterise the time dependent plastic behaviour of two commercially pure titanium samples (grade 1 and grade 4) with different oxygen content at 4 different temperatures (room temperature, 75 °C, 145 °C and 250 °C). Such experiments enable direct assessment of lattice strains from grain families with common grain orientations from polycrystal sample. By monitoring the lattice strain response, it is possible to infer the behaviour of different slip systems. Lattice strains were measured by tracking the diffraction rings radii changes from multiple plane families (21 diffraction rings) as a function of their orientation with respect to the loading direction. The critical resolved shear stress, activation energy and activation volume were established for both prismatic and basal slip modes by fitting a crystal plasticity finite element model to the lattice strain relaxation responses measured along the loading axis for five strong reflections.

It was found that cold dwell fatigue highly depends on crystallographic orientation, where accumulation of plastic strain during a stress relaxation period was found to be higher in 'soft' grains over 'hard' grains, which results from the higher strain rate sensitivity of these 'soft' grains. The prism slip parameters correspond to a stronger strain rate sensitivity compared to basal slip. This slip system dependence on strain rate has a significant effect on stress redistribution to 'hard' grain orientations during cold dwell fatigue.

Oxygen was found to enhance the cold dwell effect, as plastic accumulation and strain rate sensitivity were both found to be higher in the higher oxygen content CP-Ti grade 4 samples. Among the four temperature assessed, 75 °C was found to be the worse-case scenario, where the macroscopic plastic strain accumulation was significant during a relaxation cycle due to the greatest activity of both prism and basal slip systems.

Digital image correlation (DIC) and crystal plasticity simulation were utilised to study cold dwell behaviour in a coarse grain Ti-6Al alloy at 3 different temperatures up to 230 °C. Strains extracted from large volume grains were measured during creep by DIC and were used to calibrate the crystal plasticity model. Stress along paths across the boundaries of two grain pairs, (1) a 'rogue' grain pair and (2) a 'non-rogue' grain pair, were determined at different temperatures. Load shedding was observed in the 'rogue' grain pair, where a stress increment during the creep period was found in the 'hard' grain. At elevated temperatures, 120 °C was found to be the worst case scenario as the

stress difference at the grain boundaries of these two grain pairs were found to be the largest among the three temperatures. Local stress state plays a more important role in the activation of slip systems compared to grain orientations with respect to macroscopic load direction in large polycrystals. As a result, the 'soft' and the 'hard' grain would dynamically vary depending on the applied stress and operating temperature.

Cold dwell fatigue of Titanium



Yi Xiong

St Anne's College

University of Oxford

A thesis submitted for the degree of

Doctor of Philosophy

Trinity 2021

Acknowledgements

This thesis would not have been possible without the invaluable help and assistance from many people and I would like to take this opportunity to thank them.

First and foremost, I would like to express my gratitude to my main supervisor, Prof. Angus J. Wilkinson and co-supervisor, Prof. Edmund Tarleton. I am grateful to my supervisors for providing me the opportunity to be engaged in such an interesting project. Throughout this project, they have always made time to help me with experiments, data analysis, modelling and academic writing. The meetings with them were always positive and inspiring, I learnt a lot from the way they design experiments, trouble shooting and their ideas when processing the results. I appreciate that they let me be involved in many international conferences, which were very valuable experience for my career. Thanks for their patient guidance and support over the years, which help me growing into a professional researcher.

I would also like to give special thanks to Dr. Phani S. Karamched and Dr. David M. Collins who taught me a lot of on experiments (such as EBSD, synchrotron diffraction and mechanical testing), data analysis, coding and academic writing.

A big thanks to Dr. Chi-Toan Nguyen and my colleague Christopher M. Magazzeni who kindly offered help in the most important experiments during my whole DPhil. The experiments at Diamond Light Source were performed extremely successful, and the results contribute a lot to my publications and this thesis. I would like to thank Dr.Thomas Connolley, Dr.Robert Atwood and Dr.Stefan Michalik for their friendly and patient help at the beamline I12 at Diamond Light Source.

Thanks also to my colleague, Dr. Nicolò Grilli who contributed a lot in managing the CPFE code for the group and helping me to apply this code on my project.

I would also like to acknowledge my colleagues Dr. Jicheng Gong and Dr. Bo-Shiuan Li whose advice on experimental setup has been very constructive and inspiring.

I would like to thank the all the colleagues in the OMG group especially Prof. David Armstrong, Dr. Junliang Liu, Dr. Yuanbo Tang, Dr. Arutyun Arutyunyan and Dr. Robin De Meyere for their questions and comments on the group meetings, which are always helpful.

I also want to thank all the support staff in the David Cockayne Centre for Electron Microscopy especially Dr. Neil Young, Dr. Gareth Hughes, Dr. Ian

Griffiths and Mr. Greg Cook, Mr. Graham Wyatt, Mrs. Jennifer Holter for keeping the equipments in good working conditions, and always willing to give me a helping hand. I want to thank the support staff in the department, Mrs. Marion L. Beckett, Mr Anthony D. Wheeler, Mrs. Rebecca L. Bradford, Mr. Ashley J. Brown and Dr. Paul J. Warren for their kindly help. My warmest thanks to my friend Dr. Xiao Pan from Imperial College London for his encouragement in both work and life. Thanking him for tutoring me in LaTeX.

I acknowledge funding from the EPSRC through the HexMat programme grant (EP/K034332/1) and the Diamond Light Source for beam time under experiment EE17222. In the meantime, I sincerely express gratitude to the financial support of China Scholarship Council (CSC).

Finally, I wish to express my gratitude to my family. Thank my parents for providing me opportunity to chase my dreams. I always knew that you believed in me and supported me during my ups and downs. And to Yi Yi, thank you for your love, encouragement and accompany especially during the COVID-19 pandemic.

Preface

The research described in this thesis was carried out by the author in the Department of Materials at the University of Oxford between October 2017 and August 2021, under the supervision of Prof. Angus J. Wilkinson and Prof. Edmund Tarleton. All of the work is original, and where the work of others is included it has been referenced. Neither the entire nor any part of thesis has been submitted for any other degree at this university or elsewhere.

Parts of the work in this thesis have been or will be published in peer-reviewed journals:

1. Y. Xiong, P.S. Karamched, C.-T Nguyen, D.M. Collins, N. Grilli, C.M. Magazzeni, E. Tarleton, A.J. Wilkinson, An in-situ synchrotron diffraction study of stress relaxation in titanium: Effect of temperature and oxygen on cold dwell fatigue, **Acta Materialia** 213 (2021) 116937. `https://doi.org/10.1016/j.actamat.2021.116937`

2. Y. Xiong, P.S. Karamched, C.-T Nguyen, D.M. Collins, C.M. Magazzeni, E. Tarleton, A.J. Wilkinson, Cold creep of titanium: Analysis of stress relaxation using synchrotron diffraction and crystal plasticity simulations, **Acta Materialia** 199 (2020) 561-577. `https://doi.org/10.1016/j.actamat.2020.08.010`

3. Y. Xiong, N. Grilli, P.S. Karamched, B.-S. Li, E. Tarleton, A.J. Wilkinson, Cold dwell behaviour of Ti6Al alloy: Understanding load shedding using digital image correlation and crystal plasticity simulations, **Journal of the Mechanics and Physics of Solids** (under review)

4. P.S. Karamched, Y. Xiong, C.-T Nguyen, D.M. Collins, C.M. Magazzeni, A.J. Wilkinson, Weighted ellipse fitting routine for spotty/incomplete Debye-Scherrer rings on a 2D detector, **Journal of Applied Crystallography** (under review)

5. Y. Xiong, P.S. Karamched, C.-T Nguyen, D.M. Collins, C.M. Magazzeni, E. Tarleton, A.J. Wilkinson, Key parameters for time dependent plasticity in Ti alloys, **Journal of Materials Science & Technology** (under review)

Oral presentations have also been given at the following conferences:

1. Cold Creep of Ti Alloys: in-situ synchrotron diffraction and crystal plasticity finite element analysis, TMS 2019, San Antonio, 10^{th}-14^{th} March 2019.

2. An In-situ Synchrotron Diffraction Study of Stress Relaxation in Ti Alloys, Hexmat 2nd International Workshop on Mechanistic Behaviour of HCP Alloys, Pembroke College, University of Oxford, 17^{th}-19^{th} September 2018.

3. In-situ synchrotron X-ray diffraction studies of cold dwell effects in Ti alloys, Hexmat HCP Alloys Workshop, Imperial College London, 5^{th} April 2018.

Abstract

- **Title:** Cold dwell fatigue of Titanium
- **Candidate:** Yi Xiong
- **College:** St Anne's college
- **Degree:** Doctor of Philosophy in Materials
- **Supervisors:** Prof. Angus J. Wilkinson and Prof. Edmund Tarleton

There is a long-standing technological problem in which a stress dwell during cyclic loading at room temperature in Ti causes a drastic fatigue life reduction. It is thought that localised time dependent plasticity in 'soft' grains oriented for easy plastic slip leads to load shedding and an increase in stress within a neighbouring 'hard' grain that is poorly oriented for easy slip. Quantifying this time dependent plasticity process is key to successfully predicting the complex cold dwell fatigue problem. Incorporating the influence of operating temperatures and common alloying elements on cold dwell fatigue will be beneficial for future alloy design to address this problem.

Firstly, stress relaxation tests were performed at four different temperatures on three major alloy systems: commercially pure titanium (two alloys with different oxygen content), Ti-6Al-4V (two microstructures with differing β phase fractions) and Ti-6Al-2Sn-4Zr-xMo (two alloys with different Mo content x=2 or 6 and portion of β phase). Key parameters controlling the time dependent plasticity were determined as a function of temperature from the macroscopic stress relaxation results. It was found that the dwell fatigue effect is more significant by oxygen alloying but is suppressed by the addition of Mo. The presence of the β phase did not strongly affect the dwell fatigue, however, it was suppressed at high temperature due to the low strain rate and strain rate sensitivity.

To understand the mechanism in greater detail, synchrotron X-ray diffraction technique during stress relaxation experiments was utilised to characterise the time dependent plastic behaviour of two commercially pure titanium samples (grade 1 and grade 4) with different oxygen content at 4 different temperatures (room temperature, 75 °C, 145 °C and 250 °C). Such experiments enable direct assessment

of lattice strains from grain families with common grain orientations from polycrystal sample. By monitoring the lattice strain response, it is possible to infer the behaviour of different slip systems. Lattice strains were measured by tracking the diffraction rings radii changes from multiple plane families (21 diffraction rings) as a function of their orientation with respect to the loading direction. The critical resolved shear stress, activation energy and activation volume were established for both prismatic and basal slip modes by fitting a crystal plasticity finite element model to the lattice strain relaxation responses measured along the loading axis for five strong reflections.

It was found that cold dwell fatigue highly depends on crystallographic orientation, where accumulation of plastic strain during a stress relaxation period was found to be higher in 'soft' grains over 'hard' grains, which results from the higher strain rate sensitivity of these 'soft' grains. The prism slip parameters correspond to a stronger strain rate sensitivity compared to basal slip. This slip system dependence on strain rate has a significant effect on stress redistribution to 'hard' grain orientations during cold dwell fatigue.

Oxygen was found to enhance the cold dwell effect, as plastic accumulation and strain rate sensitivity were both found to be higher in the higher oxygen content CP-Ti grade 4 samples. Among the four temperature assessed, 75 °C was found to be the worse-case scenario, where the macroscopic plastic strain accumulation was significant during a relaxation cycle due to the greatest activity of both prism and basal slip systems.

Digital image correlation (DIC) and crystal plasticity simulation were utilised to study cold dwell behaviour in a coarse grain Ti-6Al alloy at 3 different temperatures up to 230 °C. Strains extracted from large volume grains were measured during creep by DIC and were used to calibrate the crystal plasticity model. Stress along paths across the boundaries of two grain pairs, (1) a 'rogue' grain pair and (2) a 'non-rogue' grain pair, were determined at different temperatures. Load shedding was observed in the 'rogue' grain pair, where a stress increment during the creep period was found in the 'hard' grain. At elevated temperatures, 120 °C was found to be the worst case scenario as the stress difference at the grain boundaries of these two grain pairs were found to be the largest among the three temperatures. Local stress state plays a more important role in the activation of slip systems compared to grain orientations with respect to macroscopic load direction in large polycrystals. As a result, the 'soft' and the 'hard' grain would dynamically vary depending on the applied stress and operating temperature.

Contents

List of Abbreviations **xiii**

1 Introduction **1**

2 Literature review **5**

2.1 Metallurgy of Ti and its alloys 5

2.1.1 Physical properties of Ti 5

2.1.2 Crystal structure 7

2.1.3 Deformation in Titanium 7

2.1.4 Effect of alloying elements 13

2.2 Cold dwell fatigue 16

2.2.1 Overview 16

2.2.2 Stress redistribution 20

2.2.3 Strain rate sensitivity 24

2.3 Techniques and Instruments 25

2.3.1 Electron Back Scatter Diffraction 25

2.3.2 Crystal plasticity finite element modelling 28

2.3.3 Synchrotron X-ray diffraction 30

2.4 Summary 31

3 Techniques and methods **35**

3.1 Electron back scattered diffraction 35

3.2 Synchrotron X-ray diffraction 36

3.3 Crystal plasticity finite element model 40

3.4 Digital image correlation 43

4 Macroscopic analysis of time dependent plasticity in some selected Ti alloys **47**

4.1 Introduction 47

4.2 Materials 49

4.3 Stress relaxation tests 52

4.4 Relaxation curves analysis 53

4.5 Key parameters 56

4.6 Strain rate sensitivity . . . 58
4.7 Summary . . . 60

5 Effect of crystallographic orientation on cold dwell fatigue 61
5.1 Introduction . . . 61
5.2 Material and experiment procedures . . . 62
5.2.1 Material . . . 62
5.2.2 Stress relaxation tests . . . 63
5.2.3 Diffraction pattern analysis . . . 65
5.2.4 Crystal plasticity finite element model . . . 67
5.3 Results and discussion . . . 69
5.3.1 Macroscopic stress relaxation . . . 69
5.3.2 Development of lattice strain during loading phase . . . 70
5.3.3 Modelling results . . . 74
5.3.4 Strain rate sensitivity . . . 78
5.3.5 GND densities . . . 83
5.4 Summary . . . 84

6 Effect of oxygen content and temperature on cold dwell fatigue 87
6.1 Introduction . . . 87
6.2 Materials and experiment procedures . . . 88
6.2.1 Materials . . . 88
6.2.2 Stress relaxation tests . . . 91
6.2.3 Crystal plasticity model . . . 93
6.3 Results and discussion . . . 94
6.3.1 Thermal expansion and elastic deformation . . . 94
6.3.2 Macroscopic stress relaxation . . . 97
6.3.3 Lattice strain simulation results . . . 99
6.3.4 Strain rate sensitivity . . . 106
6.4 Summary . . . 111

7 A digital image correlation study of cold dwell fatigue:Load shedding in rogue and non-rogue grain pairs 113
7.1 Introduction . . . 113
7.2 Materials and experiment procedures . . . 114
7.2.1 Materials . . . 114
7.2.2 Creep tests . . . 115
7.2.3 Crystal plasticity model and simulations . . . 116
7.3 Results . . . 119
7.3.1 Critical resolved shear stress . . . 119

7.3.2 Macroscopic stress 122
7.3.3 Slip activity and trace analysis 124
7.3.4 Load shedding 125
7.4 Discussion 129
7.5 Summary 134

8 Conclusions and future works **135**
8.1 Conclusions 135
8.2 Future works 138

Appendices

A Appendices **143**
A.1 Evaluation of the effect of residual strain 143
A.2 Justification of element size using lattice strain evolution 145
A.3 Sensitivity of lattice strain with changing parameters 147
A.4 Sensitivity of lattice strain to the initial orientation assignment . . . 149
A.5 Variation of the dislocation density 151
A.6 Validation of the cubic grain morphology 154
A.7 Justification of the depth of the model 155
A.8 Fitting errors and optimisation efficiency 156
A.9 DIC error analysis 156
A.10 Peak width study 158

Bibliography **161**

List of Abbreviations

HCP . . . . . Hexagonal close packed.

EBSD . . . . . Electron backscatter diffraction.

CPFE . . . . . Crystal plasticity finite element.

CPFEM . . . . Crystal plasticity finite element model.

DIC . . . . . Digital image correlation.

CP-Ti . . . . . Commercially pure titanium.

CRSS . . . . . Critical resolved shear stress.

BCC . . . . . Body centered cubic.

STEM . . . . . Scanning transmission electron microscopy.

DFT . . . . . Density functional theory.

SRO . . . . . Short range order.

SRS . . . . . Strain rate sensitivity.

SEM . . . . . Scanning electron microscope.

GND . . . . . Geometrically necessary dislocations.

FCC . . . . . Face centered cubic.

RSS . . . . . Resolved shear stress.

XRD . . . . . X-ray diffraction.

DC . . . . . Direct current.

ETMT . . . . . Electro-Thermal-Mechanical Tester.

FE . . . . . Finite element.

UMAT . . . . User material.

LED . . . . . Light-emitting diode.

DAWN . . . . Data Analysis WorkbeNch.

CRSM . . . . . Constant strain rate method.

SRM . . . . . Stress relaxation methos.

RMSD . . . . . Root-mean-squared deviation.

wt% . . . . . Weight percent.

at% . . . . . Atom percent.

1 Introduction

Titanium alloys are light-weight high-strength materials which have been widely applied in aerospace. They are used in aeroengines, often under extremes of load in components such as compressor discs and fan blades [1]. In many applications the service life of titanium alloy components are highly dependent on their fatigue properties. One important aspect of fatigue behaviour of Ti alloys is called "cold dwell fatigue" [2, 3]. At ambient temperature fatigue of Ti alloys held at peak loads can have a profound and detrimental effect on the fatigue life, resulting in drastic fatigue life reduction. This phenomenon was first recognised in late 1972/early 1973 through the uncontained failure of two titanium alloy fan discs in Rolls-Royce RB211 engines [2], which at that time, were manufactured from near α alloy IMI 685 [4]. Although it has been recognised and has been studied for over 40 years, it still continues to be a significant industrial concern because its non-destructive evaluation management is hugely costly, and it remains a critical safety issue [5]. Therefore to understand deeply those factors influencing the fatigue properties of Ti alloys will be undoubtedly useful for finding the ways to prolong the fatigue life so that we can decrease the cost of Ti alloys and improve the safety of aviation.

Prior modelling studies of dwell fatigue in titanium alloys indicate that the cold dwell effect is controlled by load shedding between 'soft' and 'hard' grain pairs [3, 6]. The 'soft' grain has its crystallographic c-axis approximately perpendicular to the

loading direction while a 'hard' grain has its c-axis approximately parallel to the loading direction. Characteristic of the HCP α-titanium crystal structure, plastic slip systems in the 'soft' grain will be activated but within the 'hard' grain no easy slip systems exist and the elastic stiffness is at its highest [7, 8]. During a dwell period, localised time dependent plasticity in the 'soft' grain leads to load shedding as dislocations accumulate and glide. Due to grain compatibility, the 'soft' grain may impose an increased stress in a neighbouring 'hard' grain [9, 10]. With multiple loading cycles, the stress in the 'hard' grain incrementally increases until it fractures. Fractography has revealed facet formation associated with these 'hard' grains, where the facets themselves were typically parallel to the basal plane [2, 11]. Such a mechanism, however, has not been satisfactorily confirmed with experimental observations. To make progress beyond present understanding of dwell fatigue behaviour, it is necessary to understand the different deformation behaviour in grains with different crystal orientations (i.e. 'hard' and 'soft' grain orientations) and especially the plastic deformation during the stress dwell period. To achieve this, it is important to quantify the plasticity processes as a function of time. Specifically, this must describe the dislocation processes on prismatic and basal slip systems with respect to their critical resolved shear stresses.

Oxygen is known to be interstitial in alpha Ti and has a profound strengthening effect which is more pronounced on the softer $\overrightarrow{a}$ prism slip system than $\overrightarrow{a}$ basal slip, due to the stronger interaction between oxygen and the core of dislocations that mainly glide on prismatic planes over that on basal planes [12, 13]. Typically, in high strength grade Ti alloys, oxygen is intentionally added in order to improve the strength, corrosion and wear resistance of the alloys [14, 15]. However, in most of Ti alloys, oxygen is unintentionally introduced during its raw metal processing or due to service conditions [12]. Although oxygen is present in almost all Ti alloys, the role of oxygen on time dependent plasticity and cold dwell fatigue is not clear; a better understanding may guide future alloy design strategies and impurity control to suppress the cold dwell effect.

The majority of studies that have investigated cold dwell fatigue have been performed at ambient temperature. However, there is clear evidence showing that the cold dwell effect is also sensitive to temperature, noting that the effect is not observed at high temperature [16]. Zhang *et al.* [17] utilised a crystal plasticity model to show that the worst-case scenario temperature in Ti6Al alloy is around 120 °C (where load shedding is the strongest at this temperature) and is diminished when the temperature exceeds 230 °C (where load shedding effect is suppressed). To understand this effect in greater detail, the effect of temperature on dislocation activity of different slip systems needs to be understood and quantified in the context of cold dwell fatigue.

Chapter 2 will contain literature covering areas of metallurgy, cold dwell fatigue of titanium alloys and a review of the techniques used in the literature.

In Chapter 3, an overview is given of the techniques as specifically used in this study: Electron back scattered diffraction (EBSD); Synchrotron X-ray diffraction; Crystal plasticity finite element (CPFE) model and Digital image correlation (DIC).

In Chapter 4, results of a set of stress relaxation experiments will be introduced. These experiments covered a range of commercially used titanium alloys: Commercially pure Ti (CP-Ti), Ti-6Al-4V system and Ti-6Al-2Sn-4Zr-xMo, a range of temperatures, from room temperature to 250°C, and different microstructures: near α and $\alpha + \beta$ bimodal. A numerical method for analysing the macroscopic stress relaxation curves will be introduced to determine the materials key parameters for time dependent plasticity in these Ti alloys. The results allow us to compare the effects of common alloying elements: Oxygen and Molybdenum, different microstructures and temperatures on cold dwell fatigue.

In Chapter 5, synchrotron X-ray diffraction during stress relaxation experiments was performed to characterise the time dependent plastic behaviour of CP-Ti (grade 4) at room temperature. Lattice strains were measured by tracking the changes of diffraction rings radii from multiple plane families (21 diffraction rings) as a function of their orientation with respect to the loading direction. The behaviours of grains with similar crystallographic orientations were grouped and

compared and the effect of crystal orientation on cold dwell fatigue was revealed. The critical resolved shear stress, activation energy and activation volume were established for both prismatic and basal slip modes by fitting a crystal plasticity finite element model to the lattice strain relaxation responses measured along the loading axis for three strong reflections.

In Chapter 6, characterisation of the time dependent plastic behaviour of two commercially pure titanium samples (grade 1 and grade 4) with different oxygen content at 4 different temperatures (room temperature, 75 °C, 145 °C and 250 °C) was performed during stress relaxation using synchrotron X-ray diffraction. Key parameters that govern the dislocation motion were determined for the major prismatic and basal slip systems as a function of temperature and oxygen content by calibrating a crystal plasticity finite element model with the measured lattice strain relaxation responses. The influence of operating temperatures and common alloying element, Oxygen, on plasticity and dwell fatigue was studied.

In Chapter 7, digital image correlation (DIC) and crystal plasticity simulation were utilised to study cold dwell behaviour in a coarse grain Ti-6Al alloy at 3 different temperatures up to 230 °C. Stress along paths across the boundaries of two grain pairs, (1) a 'rogue' grain pair and (2) a 'non-rogue' grain pair, were determined at different temperatures. The load shedding behaviour in rogue and non-rogue grain pairs was compared and the worst-case scenario temperature was evidenced and explained.

Chapter 8 summarises the achievements and major conclusions of the work reported, and makes some suggestions for future works that could improve the understanding of this long-standing cold dwell fatigue problem in Ti alloys.

2 Literature review

Contents

2.1 Metallurgy of Ti and its alloys 5
2.1.1 Physical properties of Ti 5
2.1.2 Crystal structure 7
2.1.3 Deformation in Titanium 7
2.1.4 Effect of alloying elements 13
2.2 Cold dwell fatigue 16
2.2.1 Overview 16
2.2.2 Stress redistribution 20
2.2.3 Strain rate sensitivity 24
2.3 Techniques and Instruments 25
2.3.1 Electron Back Scatter Diffraction 25
2.3.2 Crystal plasticity finite element modelling 28
2.3.3 Synchrotron X-ray diffraction 30
2.4 Summary 31

2.1 Metallurgy of Ti and its alloys

2.1.1 Physical properties of Ti

Table 2.1 lists the basic physical properties of four commonly used metals in industry. Compared to other structural metallic materials based on Fe, Ni, and Al, Ti has the highest strength to density ratio as well as the best corrosion resistance. Due to these excellent properties, titanium alloys have been applied in the aerospace sector,

especially in aero-engines components such as fan blades and compressor disks, often subjected to extreme mechanical loading but at relatively low temperatures [1]. However, it is still not widely used in other areas mainly due to its high price. This high price is mainly a result of the high reactivity of titanium with oxygen. The use of inert atmosphere or vacuum is required during the production process of titanium sponge from titanium tetrachloride as well as during the melting process. The cost of energy during processing and the initial high cost of titanium tetrachloride make Ti alloys very expensive. On the other hand, the high reactivity with oxygen leads to the immediate formation of a stable and adherent oxide surface layer when exposed to air, resulting in the superior corrosion resistance of titanium in various kinds of aggressive environments, especially in aqueous acid environments. The much higher melting temperature of titanium as compared to aluminium, the main competitor in light weight structural applications, gives titanium a definite advantage above application temperatures of about 150 °C. The high reactivity of titanium with oxygen limits the maximum use temperature of titanium alloys to about 600 °C [16]. Above this temperature the diffusion of oxygen through the oxide surface layer becomes too fast resulting in excessive growth of the oxide layer and embrittlement of the adjacent oxygen rich layer of the titanium alloy [18].

Table 2.1: Some important characteristics of titanium and titanium based alloys as compared to other structural metallic materials based on Fe, Ni, and Al [16].

	Ti	Fe	Ni	Al
Melting temperature (°C)	1670	1538	1455	660
Allotropic transformation (°C)	882	912	-	-
Crystal structure	HCP → BCC	BCC → FCC	FCC	FCC
Room temperature E (GPa)	115	215	200	72
Yield stress (MPa)	1000	1000	1000	500
Density (g/cm^3)	4.5	7.9	8.9	2.7
Corrosion resistance	Very high	Low	Medium	High
Reactivity with Oxygen	Very high	Low	Low	High
Price	Very high	Low	High	Medium

2.1.2 Crystal structure

Pure titanium has a hexagonal close-packed (HCP) crystal structure at low temperature which is known as the α phase. The lattice parameters of α-titanium was reported to be a=0.295 nm, c=0.468 nm and c/a=1.588 [19], as shown in Figure 2.1(a). The c/a ratio is slightly lower than ideal close packing ratio (c/a=1.63), which then means the prismatic $\{01\bar{1}0\}$ planes are more widely separated apart than in an ideal HCP crystal and $\overrightarrow{a}$ prismatic slip is the preferred slip system in α-Ti [20]. Slip can also occur on the $\{0002\}$ (basal) and $\{01\bar{1}1\}$ (pyramidal) planes, for certain orientations; in all three planes, the slip direction is usually the <1120> the $\overrightarrow{a}$ directions, which is the close-packed direction. Slip is also possible in the <1123> $\overrightarrow{c}+\overrightarrow{a}$ directions on the pyramidal systems. However, $\overrightarrow{c}+\overrightarrow{a}$ slip is significantly harder to activate [3, 8, 21]. Once the temperature is above 882 °C in pure titanium, the hexagonal α phase transforms to a body-centred cubic phase known as β phase. As shown in Figure 2.1(b), the lattice parameter for β titanium is reported to be 0.332 nm [16]. The four <111> directions are the close-packed directions. The transformation takes place in such a way that a $\{110\}$ plane of the β phase is parallel to the $\{0002\}$ planes of the α phase and the <1120> directions in the α phase are parallel to a <111> directions in the β phase [19].

2.1.3 Deformation in Titanium

The elastic deformation properties of Ti and its alloys are strongly affected by the intrinsically anisotropic character of the hexagonal crystal structure of the α phase. The variation of the modulus of elasticity E of pure α-titanium single crystals at room temperature as a function of the angle γ between the c-axis of the unit cell and the stress axis is shown in Figure 2.2 [16, 22]. It is found that the modulus of elasticity E varies between 145 GPa (stress axis parallel to the c-axis) and 100 GPa (stress axis perpendicular to the c-axis). Similarly, a variation of shear modulus G is also observed in titanium. The shear modulus G varies between 46 GPa (shear stresses applied in $< 11\bar{2}0 >$ direction in $\{0002\}$ planes) and 34 GPa (shear stresses applied in $< 11\bar{2}0 >$ direction in $\{10\bar{1}0\}$ planes) [23].

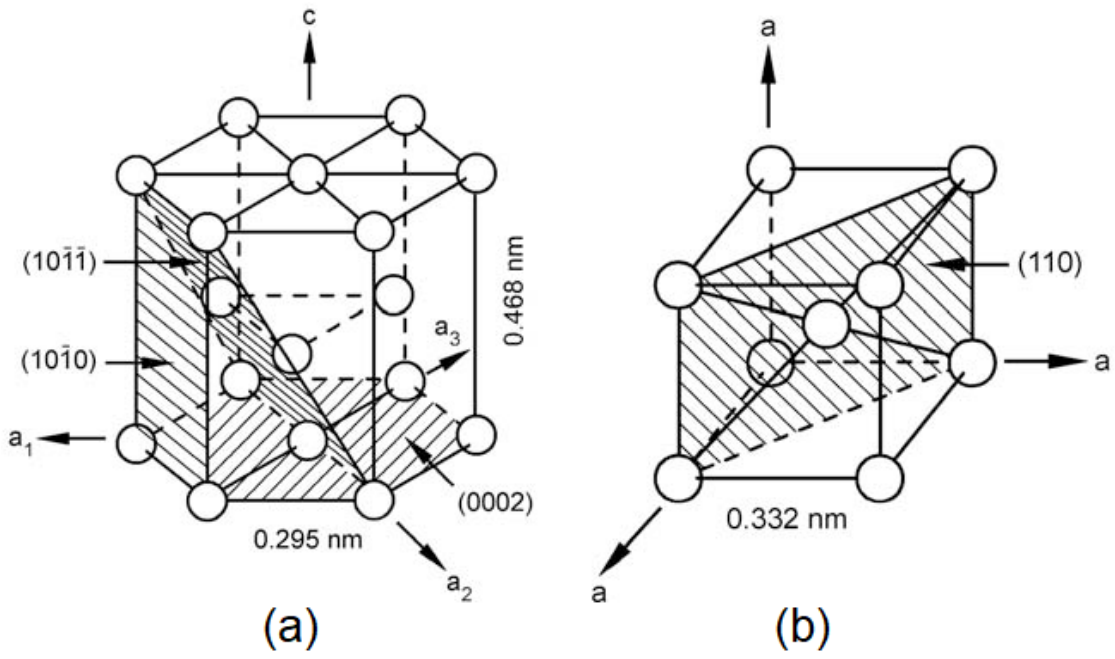


Figure 2.1: Unit cell of Ti: (a)α and (b)β phases [16].

Another reason to cause the variations in elastic properties is crystallographic texture in polycrystalline α titanium. The actual variations in modulus depend on the nature and intensity of the texture [16].

As temperature increases, both the modulus of elasticity (E) and the shear modulus (G) decrease for polycrystalline texture-free α-titanium. The relationship between modulus and temperature is almost linear as shown in Figure 2.3. It can be seen that E drops from about 115 GPa at room temperature to about 58 GPa at the β transus temperature, while G is decreasing from about 42 to 20 GPa over the same temperature range.

Figure 2.4 shows the temperature dependence elastic constants measured by Ogi [24] and Fisher and Renken [25]. B denotes the bulk modulus, and E_a and E_c denote Young's moduli along the a and c axes, respectively. It was found that both E_a and E_c decreased linearly with increased temperature up to β transus temperature, E_c was found higher than E_a, resulting the bulk modulus B lie in between them.

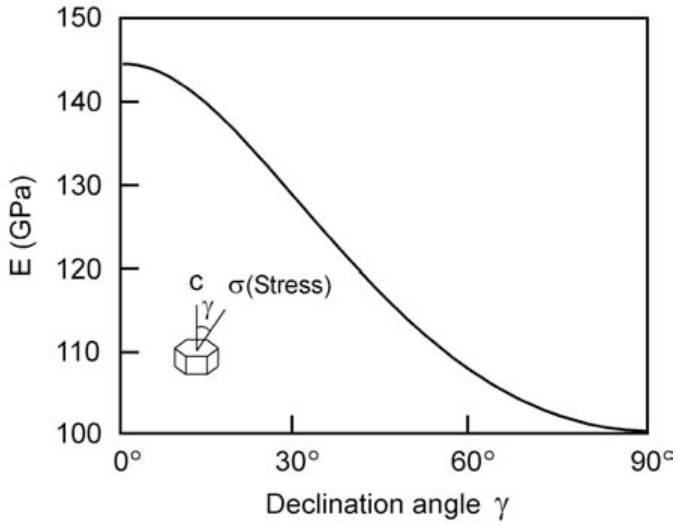


Figure 2.2: Modulus of elasticity E of α titanium single crystals versus declination angle γ [22].

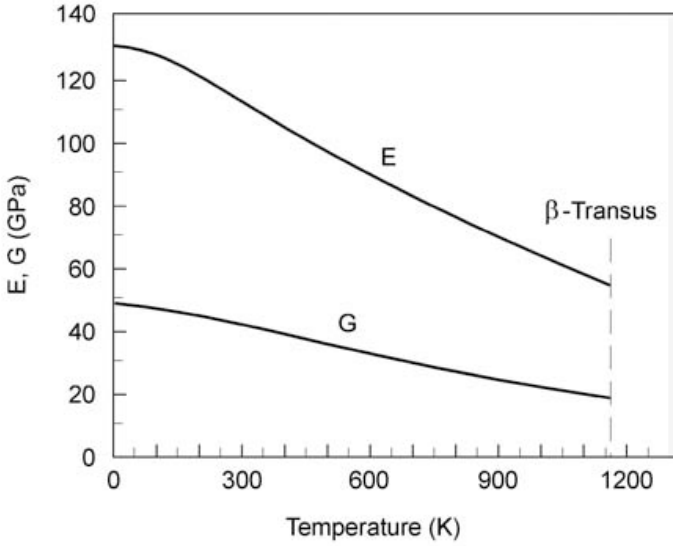


Figure 2.3: Modulus of elasticity E and shear modulus G as a function of temperature of α-titanium polycrystals [23].

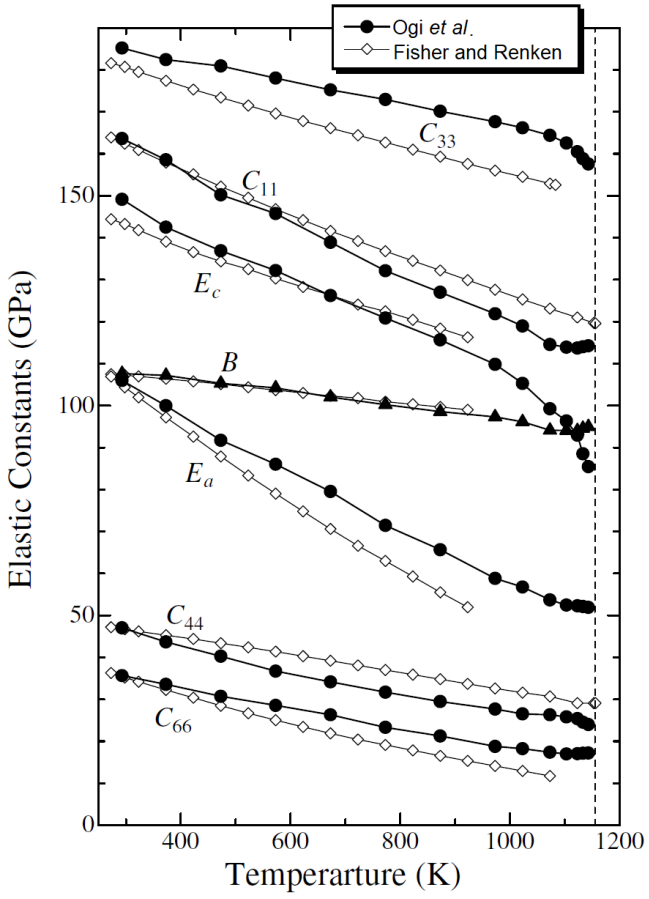


Figure 2.4: Temperature dependence of single crystal hcp-Ti elastic constants (measured by Ogi *et al.* [24] and Fisher and Renken [25]).

In the case of plastic deformation, slip of dislocations is very important to consider. Figure 2.5 summaries the slip planes as well as the slip directions for α-titanium. Mainly the slip directions are along the close-packed directions which is $< 11\bar{2}0 >$ for HCP. Slip planes containing these $\overrightarrow{a}$ type Burgers vector are $\{0002\}$ plane, the three $\{10\bar{1}0\}$ planes and six $\{10\bar{1}1\}$ planes. These three different slip plane types together with the possible slip directions give rise to total 12 slip systems, which are shown in Table 2.2. Nominally these 12 systems can be reduced to 8 independent slip systems.

Furthermore, because the deformation that is produced by type 3 can be reached by combining action of slip system types 1 and 2 (see Table 2.2), which $\overrightarrow{a}$ basal modes (type 1) are independent of $\overrightarrow{a}$ prism modes (type 2), but $\overrightarrow{a}$ pyramidal modes (type 3) are not independent of either basal and prism modes. Therefore, the number can be further reduced to 4 independent slip systems. According to von Mises criterion, which states at least five independent slip systems are required to accommodate a homogeneous plastic deformation of polycrystals, the operation of one of the slip systems with a so-called non-basal Burgers vector needs to be activated, either the $\overrightarrow{c}$ type with the slip direction $< 0001 >$ or the $\overrightarrow{c} + \overrightarrow{a}$ type with the slip direction $< 11\bar{2}3 >$ (see Figure 2.5 and Table 2.2). Several researchers have confirmed the presence of $\overrightarrow{c} + \overrightarrow{a}$ type dislocations in different titanium alloys by TEM observations [23, 26].

Table 2.2: Slip systems in the hexagonal α phase [27, 28].

Slip system type	Burgers vector type	Slip direction	Slip plane	No. of slip systems	
				Total	Independent
1	$\overrightarrow{a}$	$< 11\bar{2}0 >$	(0002)	3	2
2	$\overrightarrow{a}$	$< 11\bar{2}0 >$	$\{10\bar{1}0\}$	3	2
3	$\overrightarrow{a}$	$< 11\bar{2}0 >$	$\{10\bar{1}1\}$	6	4
4	$\overrightarrow{c} + \overrightarrow{a}$	$< 11\bar{2}3 >$	$\{10\bar{1}1\}$	6	5

There is a large difference in CRSS between $\overrightarrow{c} + \overrightarrow{a}$ slip and $\overrightarrow{a}$ slip, which was measured by Paton *et al.* [8] using Ti-6.6Al single crystals. The percentage of grains deforming by $\overrightarrow{c} + \overrightarrow{a}$ slip will be very low in α-titanium polycrystals without crystallographic texture, because the activation of $\overrightarrow{a}$ slip is easier even

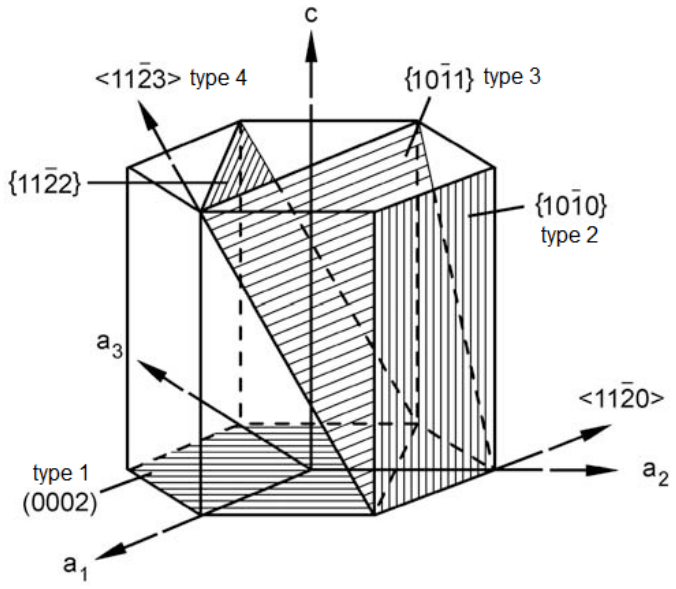


Figure 2.5: Slip planes and slip directions in the hexagonal α phase [16].

for an angle of about 10° between the stress axis and the c-axis. Even more extreme similar results are observed in intermetallic/ceramic compounds such as MAX phases [29, 30]. As shown in Figure 2.6, CRSS of $\overrightarrow{c} + \overrightarrow{a}$ type slip is more than two times larger than both basal and prismatic slip [8]. The CRSS value is highly dependent on the temperature. As the temperature increases the CRSS value for all slip systems decreases and the small differences in CRSS at room temperature between the three types of slip systems with a basal ($\overrightarrow{a}$ type) Burgers vector,$\{10\bar{1}0\} < \{10\bar{1}1\} < \{0002\}$, become even smaller [8]. As reported for binary Ti-V alloys [31], the slip systems in BCC β titanium alloys are $\{110\}$, $\{112\}$ and $\{123\}$, all with the same Burgers vector of the type $< 111 >$, in agreement with the generally observed slip modes in BCC metals.

Twinning deformation could also occur in CP-Ti and some α-titanium alloys, especially at low temperature. Twinning is frequently observed in extreme high strain conditions, as noted by Laine [32]. However, twinning is suppressed nearly completely in α/β alloys by the presence of small fraction of β phase, high solute content and Ti_3Al precipitates [16]. Therefore, twinning deformation mode is less important to be considered in low strain condition such as cold dwell fatigue.

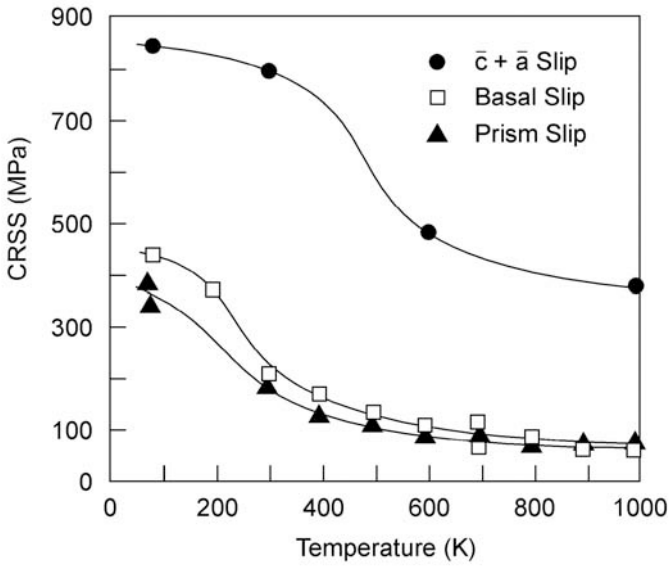


Figure 2.6: Temperature dependence of CRSS for slip with $\overrightarrow{a}$ and $\overrightarrow{c}+\overrightarrow{a}$ Burgers vectors in single crystals of Ti-6.6Al [8].

2.1.4 Effect of alloying elements

There are generally two types of alloying in Ti alloys: alloying atoms exist in the interstitial sites in the HCP unit cell (interstitial alloying) and atoms occupied the Ti atoms sites (substitutional alloying). Elements with small atomic radii such as oxygen, nitrogen and carbon are the most common interstitial alloying addition to Ti. Their small atomic size allow them to adopt octahedral sites of the HCP Ti unit cell, which have a very pronounced effect on CRSS values even at low concentrations [13, 33, 34, 35]. The oxygen-equivalent content is used to sum up the strengthening contributions of oxygen, nitrogen and carbon depending on their potency [16]:

$$[O_{eq}] = [O] + 2.0[N] + 0.75[C] \tag{2.1}$$

where $[X]$ is the atomic percentage of the element X.

Many authors have reported CRSS values for basal and prism slip at room temperature in Ti over a range of different oxygen equivalent concentrations (see Figure 2.7). It is found that with increasing oxygen concentration the strength of both prism and basal slip increase but the effect is much more pronounced for the easier prism slip. As a result, it can be expected that basal slip would

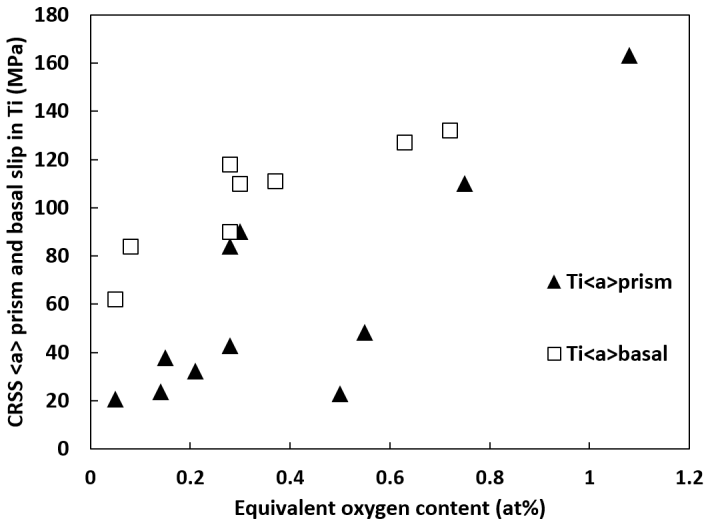


Figure 2.7: Effect of interstitial content on CRSS values of Ti at room temperature [13, 36, 20, 37, 38].

become preferred over prism slip when oxygen content is above 1.2 at% according to the trend reported by Britton *et al.* [36]. Yu *et al.* [12] studied the oxygen strengthening effect in titanium using advanced scanning transmission electron microscopy (STEM) and first-principles density functional theory (DFT) calculation. They found a direct interaction between oxygen interstitials and screw dislocation cores, the cores of screw dislocation were profoundly altered as the oxygen content increased from 0.1 to 0.3 wt% (about 0.3 to 0.9 at%). DFT also revealed that there is a strong interaction between interstitial oxygen atoms and screw dislocations, oxygen atoms are forced to change their position from octahedral sites to the nearby basal planes and meanwhile part of the dislocation is forced to cross-slip to the nearest neighbouring prismatic plane.

At increased oxygen content, the slip mode also changes from wavy to planar slip at lower temperatures due to the fact that the difficulty of cross-slip also increased [39, 40]. However, changing to planar slip leads to the loss of ductility, which is problematic. When exposing Ti to a high temperature in an oxygen environment, there is not only an oxidation layered formed at the surface but also a deeper penetration of oxygen into the material and give rise to an oxygen concentration gradient ('α-case'). Rugg *et al.* [41] illustrated the significant variation of hardness

and difference of CRSS through the oxygen penetration layer (approximately 100 μm) of Ti64 alloy. Nanoindentation results showed that the hardness decreased from the edge into the sample and at 100 μm the hardness was almost half of the hardness measured from the edge. Micro-cantilever results showed similar trend of how CRSS of $\overrightarrow{a}$ prism slip changes as the distance from the edge increased. Oxygen content was also measured using atom probe tomography, it was found that within this 100 μm layer the variation of oxygen content was from 0.4 (datum) to more than 1wt% (edge). In service, the α-case layer which results in a huge variation in performance can lead to easy crack initiation in both tensile and cyclic loading cases [42, 43].

In case of substitutional alloying additions to Ti, Al is no doubt the most common and crucial. Figure 2.8 summarises the CRSS value for both prismatic and basal slip tested by Sakai & Fine [44, 45] and William *et al.* [46] using Ti-Al single crystals. For prismatic slip, there is great agreement of their results but Sakai & Fine show a significant hardening between 0.5 and 3wt% in basal slip, whereas William *et al.* showed relatively little change in CRSS of basal slip. However, in general both sets of data indicate the hardening effect brought in by increasing Al content. For prismatic slip, the hardening is due to a narrowing of the slip bands and deformation becomes more localised and planar as the difficulty of cross-slip increases. More obviously, basal slip is relatively wavy in pure Ti and as Al is added it becomes planar. For the highest Al content sample (6.6wt%), William *et al.* found that ageing could produce a fine dispersion of Ti_3Al α_2 precipitates which is coherent to the matrix and they were destroyed when a dislocations within a slip band passed through. At lower Al content and also less extreme heat treatment, clustering and short range order (SRO) in Al distribution result in the hardening and increasing slip planarity [36].

In addition, aluminium is also known as the α-stabiliser. The difference between α-stabiliser and β-stabiliser is illustrated in Figure 2.9. As the content of α-stabiliser increases, the $\alpha \rightarrow \beta$ transition temperature increases so that at lower temperature α-phase is more favoured. In Figure 2.9(b), the addition of β-stabiliser results in a lower $\alpha \rightarrow \beta$ transition temperature. As long as the content of β-stabiliser is high enough, it is possible to make an alloy consist of entirely β-phase [21].

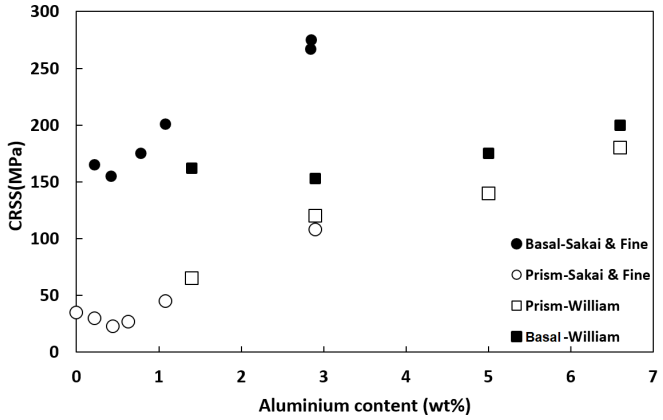


Figure 2.8: Effect of Aluminium content on CRSS values of Ti at room temperature [44, 45, 46].

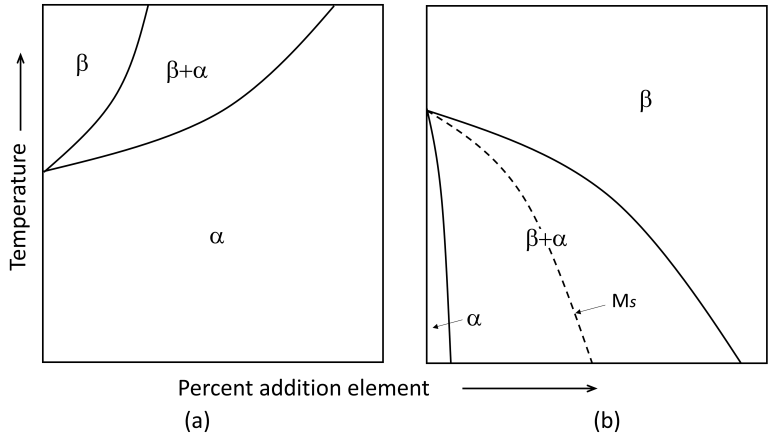


Figure 2.9: Phase diagrams of (a) α-stabiliser and (b) β-stabiliser alloying system [19].Aluminium is the most commonly used α-stabiliser, others include boron and tin [47].

In case of β-stabilisers, copper, chromium, vanadium, molybdenum, manganese and iron [48] are quite common. Combining the use of these alloying element, three classes of alloys are created: the α alloys, α/β alloys and pure β alloys.

2.2 Cold dwell fatigue

2.2.1 Overview

The specific phenomenon of cold dwell sensitivity was first discovered by Rolls-Royce in late 1972/early 1973 when two titanium compressor disks in their RB 211 engines failed far in advance of their predicted fatigue life [49]. These disks

were manufactured from near-α alloy IMI 685, which had satisfied all the fatigue criteria at that era (full scale, test rig and spinning assessments) before being put into service [2]. However, the failures pointed out that new factors were affecting the fatigue life and it was soon agreed that simple load on-load off cycles were not representative to describe fatigue in titanium at low temperatures.

A typical flight operation cycle is shown in Figure 2.10, the appearance of a long term "dwell" at high stress state (i.e. the cruise) had strong influence on the fatigue response. Eylon and Hall [4] studied the low cycle fatigue of IMI685 alloy under load control and at peak load of each cycle they introduced a "dwell" time. This dwell at peak load resulted in a huge reduction in fatigue life (98%). Evans and Gostelow [50] confirmed the significant drop in fatigue life of IMI 685 across the low cycle fatigue regime (10^3-10^5 cycles) due to 5 minute dwell at peak stress. In addition, both of these papers pointed out that specimens tested in dwell fatigue showed sub-surface failures.

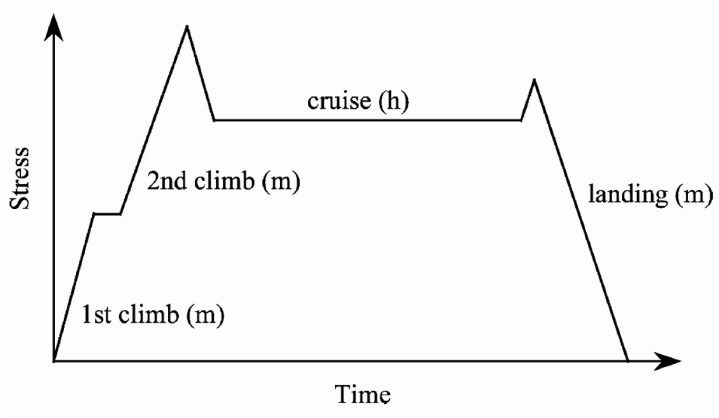


Figure 2.10: Schematic diagram of a single duty cycle of aeroengine. Operational time scales represents as minutes (m) or hours (h) [2].

It is undoubted that the failures are initiated by the presence of "quasi-cleavage" facets (as shown in Figure 2.11). These kind of intrinsic features which can be produced during the early stages of fatigue fracture in all α and α/β titanium alloys, are found to form on the basal plane of the HCP unit cell [51]. Despite the presence of "quasi-cleavage", it is still not considered to be the result of a brittle

fracture mechanism. Instead, it is believed to be due to the gradual separation of slip damage concentrated within a persistent planar slip band [11].

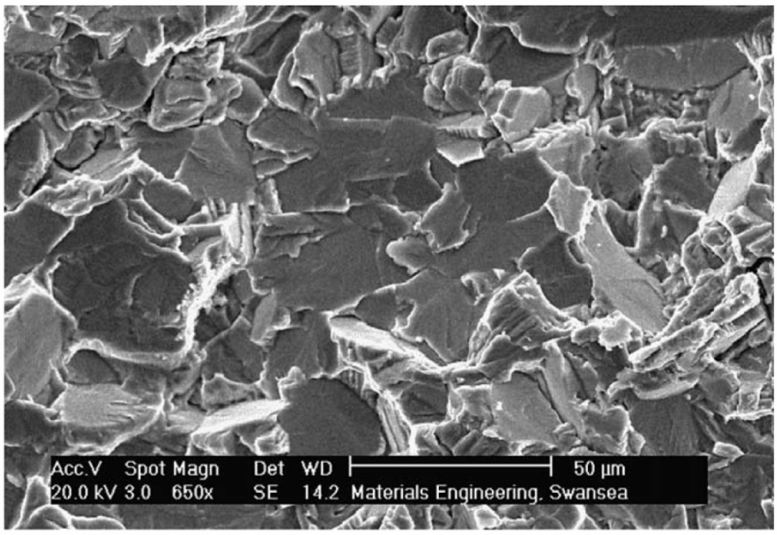


Figure 2.11: Quasi-cleavage facets formed at a subsurface initiation site in Ti64 [2, 51].

Cold dwell fatigue is mainly manifested in the α phase (HCP) Ti [13, 52, 8, 46], and is highly sensitive to the crystallographic orientation of grains. Post-mortem fatigue crack analysis indicates that dwell fatigue is enhanced by loading along the {0002} crystal plane normal direction, where the crack surface was found to be associated with the formation of facet near the {0002} and lies nearly perpendicular to the loading direction [53, 54, 55]. A more recent mechanistic study by Dunne *et al.* [56, 57] proposed that cold dwell fatigue results from a stress redistribution between 'soft' and 'hard' grain pairs, where a 'soft' grain is well orientated for the major prismatic and basal slip systems while a 'hard' grain is poorly orientated for slip (with its c-axis approximately parallel to the loading direction). During a stress dwell, localised time dependent plasticity of easily activated slip systems (basal and prismatic slip) in 'soft' grains leads to load shedding which in turn causes a large increase in stress within the neighbouring 'hard' grains, where the facets are observed to initiate. In the next section, stress redistribution behaviour will be further discussed.

Creep is mainly considered at high temperatures (when $T > 0.3T_m$ where T_m refers to the melting temperature of the metal) [58]. However, many papers have

been published confirming that the ability of titanium alloys to accumulate plastic strain under sustained load at ambient temperature. Mills and co-workers [59, 60] showed that the room temperature strain accumulation is mainly due to planar slip damage. It has been suggested that 'Cold dwell fatigue' is strongly affected by temperature and dwell fatigue is suppressed by increasing temperature and disappears when temperature is above 200 °C [16]. Zhang *et al.* [17] investigated the temperature sensitivity of load shedding and cold dwell fatigue using the crystal plasticity simulations on a model Ti-6Al alloy. It was shown that at a temperature above 230 °C thermally activated creep results in a rapid stress redistribution and elimination of local load shedding between hard-soft grain pairs. An intermediate temperature of about 120 °C exists at which the cold dwell debit is at its worst. However, the mechanism has also not yet been verified by experimental observations.

As discussed before, interstitial elements provide an improvement in strength of Ti alloys but also accompanied by a reduction in ductility and embrittlement [13, 33, 34, 35, 61]. The formation of brittle hybrids, through the time dependent diffusion of hydrogen under the influence of a hydrostatic stress field, has been proposed to lead to dwell fatigue phenomenon [62].

Gerland *et al.* [63] studied the effect of hydrogen on dwell load in an α/β Ti6242 alloy. Results indicated that microcracks nucleated at α/β interfaces along localized slip bands in aligned colonies or α laths nearly parallel to the loading axis. This damage was highly dependent on pyramidal slip, which was strongly localised. An increase in hydrogen content up to 300 ppm was found to reduce the proportional limit and the serrations on the tensile curves but to increase the conventional yield stress at high strain rate, so that it either slowed down or enhanced room-temperature creep, depending on the applied stress. Also a tendency for H to partition to β phase was also observed. Therefore, hydrogen plays an important role in controlling the plastic deformation and creep behaviour of Ti alloys. However, the role of other important interstitial element oxygen in dwell fatigue and creep remains unclear.

2.2.2 Stress redistribution

Evan and Bache [11] compared facet formation with planar slip band model of Stroh [6]. Based on this model, the process of stress redistribution between "weak" and "strong" grains was described, which is believed to represent early crack formation in all titanium alloys under fatigue loading and up to now it is still a widely accepted model in titanium research. Research using the electron back scattered diffraction (EBSD) technique, has shown that the strength of neighbouring grains are highly depends on their orientations (i.e. the angle between basal plane and loading axis) [51, 64, 65]. This technique has then been widely extended to other titanium research including GE Engine Company [51]. The technique allows researchers to obtain the orientation of each individual grain, texture information of the materials and grain size statistics.

The origin of the formation of "strong" and "weak" grains is an anisotropic property of HCP metals. As discussed in Section 2.1.3, there is a huge difference in both elastic modulus and CRSS between c-axis and a-axis (see Figure 2.2 and Figure 2.6). It is highly likely that neighbouring grains aligned in different orientations and therefore the elastic behaviour of them is clearly different. Microscopically, this anisotropic property agreed with the redistribution model and it is believed to control the early stage of deformation and facet deformation [2].

In the Stroh model shown in Figure 2.12, slip within the "weak" grain, whose basal plane (source slip band) is favourably aligned to the loading axis, induced a pile up at the boundary with the adjacent "strong" grain. This then results in a shear stress in the neighbouring "strong" grain, which induces a slip band within the "strong" grain as well. Assisted by an applied tensile load σ_1, the tensile stress σ becomes high enough to generate a crack at the failure slip band. One problem with the Stroh model is that the model was 'static' and did not explicitly consider either repeated load cycles or the time dependent processes during load hold.

Later Dunne *et al.* [3, 57] reported the worst case combination of grain orientations for HCP crystals. As shown in Figure 2.13(a), three grains with different orientations named primary, secondary and tertiary grains (path A-A was drawn

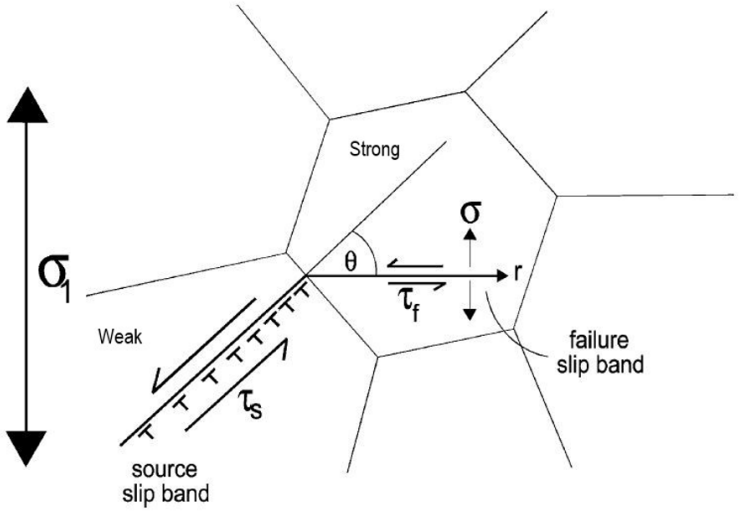


Figure 2.12: The planar slip band model [2, 6].

through them). In this case Dunne called this combination "rogue" grains, in which the primary 'hard' grain, with *c*-axis nearly parallel to the loading axis, adjacent to two (secondary and tertiary) 'soft' grains, with *c*-axis nearly perpendicular to the loading axis. During stress dwell, plastic slip systems in the 'soft' grain will be activated but within the 'hard' grain no easy slip systems exist and the elastic stiffness is at its highest. Plastic strain increases as dislocations accumulate and glide within the 'soft' grain. Due to grain compatibility, the 'hard' grain has to accommodate the strain increment by elastic strain, which results in an increase in stress within the 'hard' grain [9]. As shown in Figure 2.13(c), a 2% strain was applied to this polycrystal at a time of 0.01 s followed by a 0.01 s of strain hold. There is controversy about the hold time, 0.01 s of hold has been confirmed to be too short to reveal the influence of time dependent behaviour [1, 66, 67, 68], despite this work has successfully explained the influence between hard-soft grains.

Figure 2.14 illustrates the yy stresses developed at a time of 0.01 s for a range of relative angles of the secondary 'soft' grain (where orientation of the primary 'hard' grain is fixed). It is shown that there is a large stress difference (about 120 MPa) at the boundary of primary and secondary grains. Maximum stress variation is developed when a worst case combination of orientations is achieved,

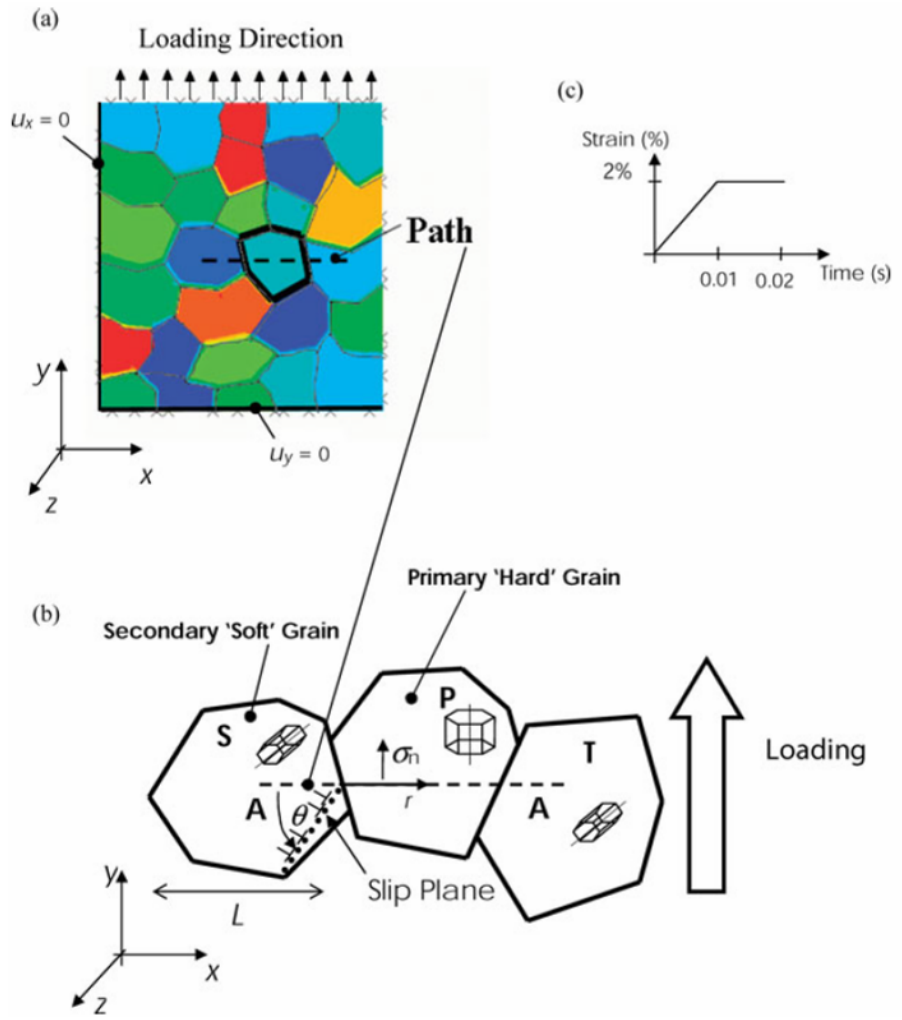


Figure 2.13: (a) Schematic polycrystal showing the path through three grains along which stresses are determined and the boundary conditions; (b) The respective crystallographic orientations of primary, secondary and tertiary grains; (c) the strain-controlled loading applied at the top boundary of the polycrystal shown in (a) [3].

which *c*-axis of the primary grain is near-parallel to loading axis and the prismatic slip system of secondary grain orientated 70° to the normal to the loading axis. In addition, effect of the orientation of secondary grains vanishes very quickly as there is no clear influence on stress in tertiary grain, indeed, this effect diminishes at half way across the primary grain. This slip inhibition in the primary grain is due to the fact that its 'hard' orientation must be a considerable contributor to this feature [3]. In this model, during the strain-controlled dwell period there is a stress redistribution which leads to an increase in stress within the primary grain. As a result, a cleavage facet is developed in the primary 'hard' grain. When

the polyscrystal was in stress-controlled loading, the local stress was found to increase dramatically after dwell, the softer grains (secondary and tertiary) grains creep leading to a local stress relaxation. However, to maintain the macro applied stress level, stress in the 'hard' grain must increase. This phenomenon was first defined as "load-shedding" by Hasija *et al.* [9].

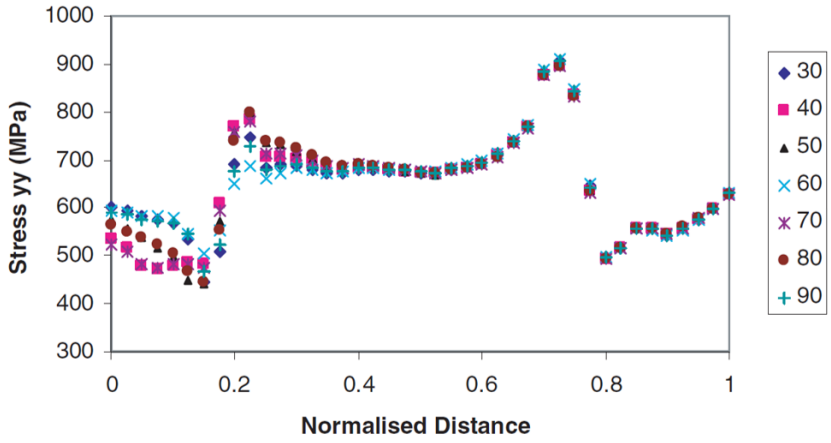


Figure 2.14: Stress yy along the path shown in Figure 2.13(b) through the primary, secondary and tertiary grains for the in-plane orientations of grain S (denoted by θ in Figure 2.13(b)) [3].

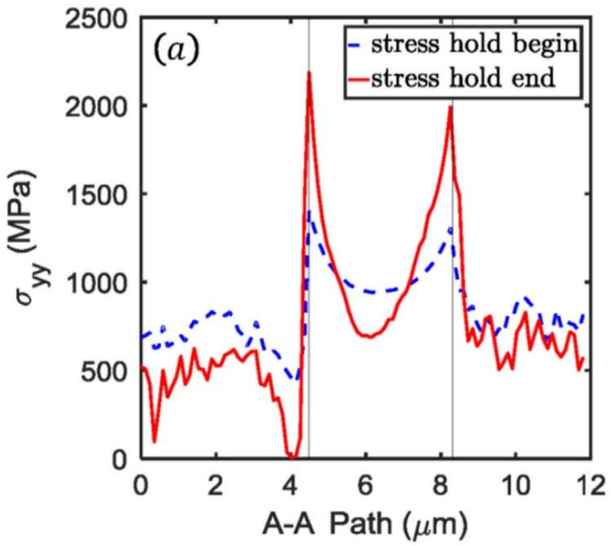


Figure 2.15: The yy-stress along the A-A path for Ti6242 measured by the CPFE model [1].

A stress-controlled loading leads to notably higher stresses within the primary

grain compared to strain-controlled loading. Experimental results also showed that facet formation under cyclic loading with a dwell period is much more likely under stress-controlled loading. Therefore, stress-controlled dwell is more damaging than strain-controlled dwell [3]. As shown in Figure 2.15, 4 s of peak stress hold time can result in such a huge stress concentration and this stress redistribution is strongly time dependent, with even longer dwell time facet can be found in the 'hard' grain [3].

2.2.3 Strain rate sensitivity

Strain rate sensitivity (SRS) is a crucial factor that governs the load shedding phenomenon [69]. Results in the literature are often expressed in terms of a strain rate sensitivity parameter, m, which corresponds to the gradient of a plot of log (σ) against log ($\dot{\varepsilon}$) and would imply the strain rate exponent in a simple power law expression for stress:

$$m = \mathrm{d}(\log(\sigma))/\mathrm{d}(\log(\dot{\varepsilon})) \tag{2.2}$$

Titanium alloys are highly anisotropic at the grain scale, both elastically and plastically [70]. SRS was also found to be grain orientation dependent, where grains in the 'soft' orientations have higher m values over that of 'hard' grains according to abundant of research on commercially pure titanium [69, 71, 72, 73, 74]. This was also confirmed by Jun *et al.* [69] using nanoindentation, showing grain orientation dependent rate sensitivity in Ti6242. They used EBSD maps to select favoured grain orientations and performed nanoindentation tests on hard and soft grains. Jun *et al.* [67] continued this study using *in situ* compression testing of micro-pillars manufactured from the α phase of Ti6242, which successfully isolated the behaviour of each slip system. Significant slip system dependent rate sensitivity was observed where prism slip has a significantly higher strain rate sensitivity exponent, m, over basal slip ($m_{prism} = 0.07$ and $m_{basal} = 0.03$). Subsequent, finite element simulation of these tests by Zhang *et al.* [68] attempted to account for contributions to measured indenter displacement from contributions such punching in of the pillar into the substrate and deformation of a glue line in the sample mounting. This

led to a different conclusion that the basal slip system had the higher strain rate sensitivity. Such an approach has the benefit of isolating the response of different slip systems, but is time and labour intensive and analysis has led to somewhat ambiguous conclusions. Although abundant research on strain rate sensitivity has been performed and the hypothesis has been verified, interpreting the m value and correlating it to physical phenomena is still an open question [67].

2.3 Techniques and Instruments

2.3.1 Electron Back Scatter Diffraction

Titanium alloys are often composed of two phases: the α phase with HCP crystal structure and the β phase with BCC crystal structure. Commonly used alloys contain large proportion of α phase, which is highly anisotropic. Therefore, crystal orientation and texture are very significant factors in mechanical and especially in fatigue properties. On studying cold dwell fatigue behaviour of Ti alloys, Electron Back Scatter Diffraction (EBSD) is certainly a very useful technique. EBSD possess several benefits [75]:

- High spatial resolution
- Accurate measurement of grain orientation
- Global crystallographic texture determination
- Local strain determinations
- Accurate identification of minor phases
- Visualisation of microstructure for grain size and local texture
- Relatively easy sample preparation

Electron Backscatter Diffraction (EBSD) is a scanning electron microscope (SEM) based technique that gives crystallographic information about the microstructure of a sample. A tilted sample (normally 70°) is placed in SEM chamber while

a stationary electron beam interacts with its surface. Diffraction patterns are recorded by a fluorescent screen, as shown in Figure 2.16.

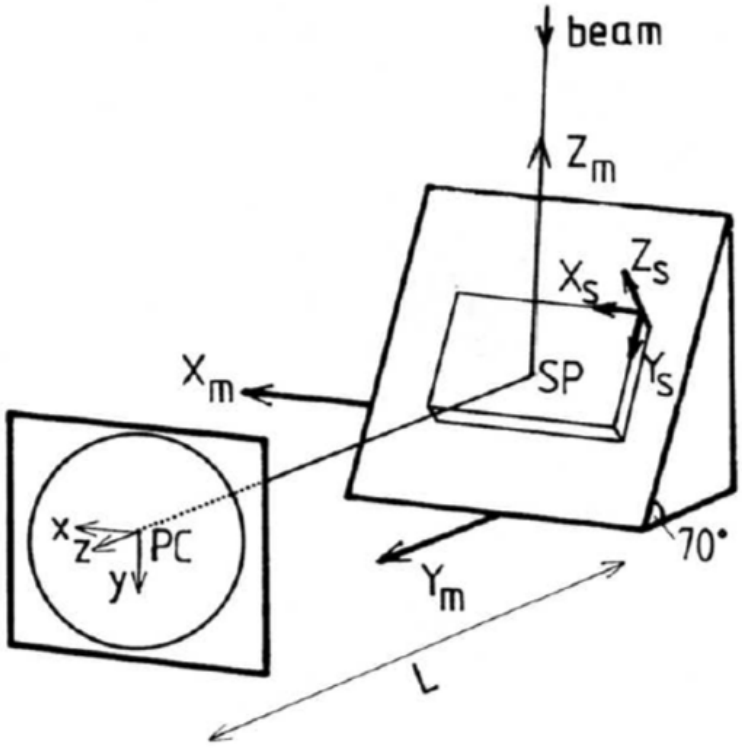


Figure 2.16: Configuration for EBSD measurement [76].

The characteristic pattern is also known as Kikuchi diffraction pattern, which was first explained by Kikuchi [77]. As the electron beam interacts with surface of the sample, electrons are diffracted by crystal planes. According to Bragg's law: $n\lambda = 2d\sin\theta$, where n is an integer, λ is the wavelength of the electrons, d is the spacing of the diffracting plane, and θ is the angle of incidence of the electrons on the diffracting plane, for crystal plane satisfying Bragg's law, the diffraction waves are constructive and form a cone with strong back-scattered signal. When cones interact with the detector screen, it gives Kikuchi lines (almost straight due to θ_B being very small). Since there will be lattice planes on either side of the original electron source, there will be two cones, one from either side. Therefore, each plane family appears on the screen as a pair of parallel lines, known as Kikuchi Band [21], as shown in Figure 2.17.

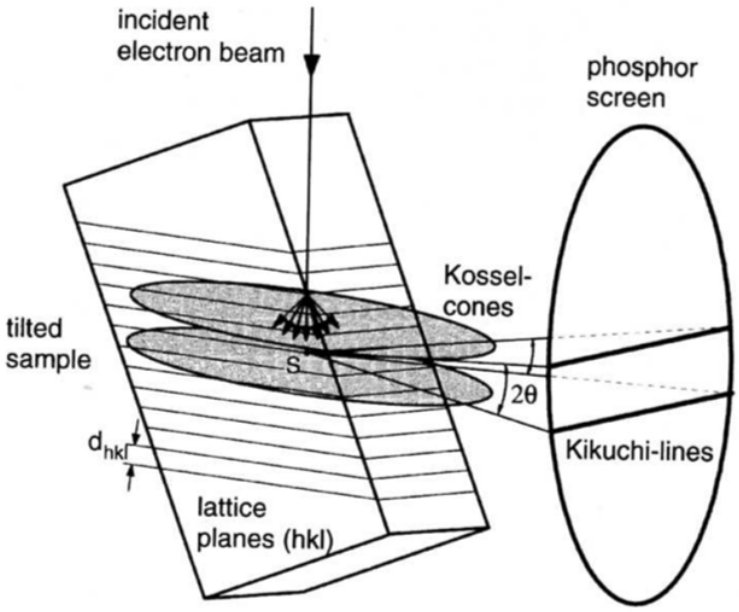


Figure 2.17: Formation of Kikuchi band [76].

Modern software is used to index the bands and determine the orientation. As the electron beam is scanned in a grid across a polycrystalline sample and the crystal orientation is measured at each point, the resulting map contains information about the grain morphology, orientations and boundaries. This data can also be used to show the preferred crystal orientation (i.e. texture) within the sample. Thus, a complete and quantitative representation of the microstructure can be established with EBSD.

Wilkinson, Meaden and Dingley [78, 79] first introduced a cross-correlation-based analysis of EBSD patterns which is able to map the elastic strain variation in polycrystals. Elastic strain variation and small lattice rotations within the sample crystal results in small shifts in the positions of zone axes in EBSD patterns. The magnitudes as well as directions of shifts vary systematically with position across the EBSD pattern, hence, equations can be established which link the shifts and the magnitude and nature of the strain. Within each grain, a reference pattern is selected and all measurements are made relative to this reference pattern. Absolute strains can be measured only when the strain of the point that was selected as reference pattern is known. However, other significant information such as lattice

curvatures and elastic strain gradients can still be obtained and the calculated lattice curvatures are used to recover the geometrically necessary dislocation (GND) density distribution. In polycrystals, multiple reference patterns must be selected in order to measure the strain gradients and lattice curvatures within each individual grain [80].

Littlewood and Wilkinson [81] applied EBSD and correlation-based strain mapping technique to study inhomogeneous deformation of Ti-6Al-4V in tension, fatigue and cold-dwell fatigue. Results showed that the inhomogeneous deformation is related to orientation of the grains (c-axis with respect to loading axis). Crack nucleation was observed in high strain concentration regions in both fatigue and dwell fatigue loading. In dwell fatigue, room-temperature creep was found to make an important contribution to deformation.

2.3.2 Crystal plasticity finite element modelling

Much work has been done in order to develop crystal plasticity models [82, 83, 84] especially for FCC metals and several studies have been carried out to investigate fatigue behaviour using such models [85, 86, 87, 88, 89]. The approach is also used to predict the formation of fatigue crack initiation in well-characterised HCP polycrystals and comparison with experimental observations has been made [90]. Nowadays, the crystal plasticity model is well-established, where the derivation of the key constitutive law is based on physics rather than empirical laws. Many researchers have successfully applied the crystal plasticity finite element (CPFE) model to analyse the complex cold dwell fatigue problem in Ti. Goh *et al.* [91] applied crystal plasticity modelling to study fretting in the titanium alloy Ti-6Al-4V. Hasiji *et al.* [9] developed rate-dependent crystal plasticity for alpha Ti-6Al alloy so that load shedding effect was studied at grain level. Results showed that stress relaxation has the effect of stress redistribution (stress reduction in 'soft' grains and increase in stress in neighbouring 'hard' grains), which results in crack initiation.

It is well known that cold dwell effect is due to time-dependent behaviour [9, 92, 11]. Consider a particular slip system α with normal $\boldsymbol{n_\alpha}$, and slip direction $\boldsymbol{s_\alpha}$, containing a dislocation pinned by obstacles (as shown in Figure 2.18).

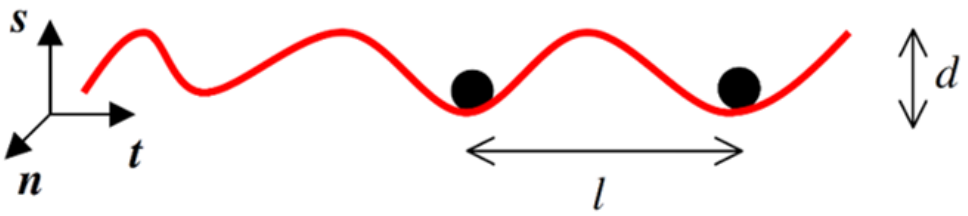


Figure 2.18: Schematic diagram of a pinned dislocation on slip plane with normal n, where l is the pinning distance and d is the length of thermal activation [56].

Gibbs pointed out that for a pinned dislocation free to glide a local thermal activation is required. The average glide velocity was given by $d \times$ rate of escape (s^{-1}) of dislocations. The latter was derived by Granato *et al.* [93] giving the expression of average velocity of:

$$v_g = \frac{d\nu b_\alpha}{2l} \exp\left(-\frac{\Delta G_\alpha}{k_B T}\right) \tag{2.3}$$

where ν is the jumping frequency (i.e. attempts of dislocations to jump over the energy barrier), k_B is the Boltzmann constant, T is the absolute temperature and ΔG_α is the Gibbs free energy of the α^{th} slip system.

Gibbs [94] developed a strain rate equation based on density of gliding dislocations, ρ_m ,which is controlled by pinning (e.g. at precipitates or solute atoms), and the average dislocation glide velocity, v_g. Therefore shear strain rate of the α^{th} slip system is obtained as [95]:

$$\dot{\gamma}_\alpha = \rho_m v_g b_\alpha \tag{2.4}$$

where b_α is the Burgers' vector.

When there is the presence of a stress field, ΔG_α then becomes:

$$\Delta G_\alpha = \Delta F_\alpha - \tau_\alpha \Delta V_\alpha \tag{2.5}$$

where ΔF_α is the Helmholtz free energy which also known as the thermal energy barrier, τ_α is the resolved shear stress (RSS) and ΔV_α is the activation volume of the α^{th} slip system. $\tau_\alpha \Delta V_\alpha$ represents the work done by the stress field. Combining

the above three expressions and a further approximation of $d \approx l$ gives the slip rate on the α^{th} slip system as:

$$\dot{\gamma}_\alpha = \rho_m b_\alpha^2 \nu \exp\left(-\frac{\Delta F_\alpha}{k_B T}\right) \sinh\left(\frac{(|\tau_\alpha| - \tau_\alpha^c)\Delta V_\alpha}{k_B T}\right) \text{sign}(\tau_\alpha) \tag{2.6}$$

τ_α^c is the critical resolved shear stress (CRSS) of the slip system α. Therefore, plastic deformation on one slip system is induced only when the RSS becomes higher than the CRSS. The hyperbolic sine represents the forward and backward motion of dislocations.

2.3.3 Synchrotron X-ray diffraction

X-ray diffraction (XRD) is a powerful tool for characterising crystalline materials. The fingerprints for materials are provided by XRD peaks, which are generated by constructive interference of a white or a monochromatic beam of X-rays diffracted at specific angles from each set of lattice planes in a sample [96]. According to Bragg's law, $n\lambda = 2d\sin\theta$, the link between lattice spacing, d and diffraction angle, θ (defines the peak positions) can be built. Matching the characteristic peaks with a standard database can help to identify an unknown material with very high accuracy. For known materials, XRD can be utilised to determine the lattice strain by comparing the peaks position before and after an applied deformation or heat treatment.

The lab based X-ray sources usually have relatively low beam intensity. As a result, the exposure time becomes relatively high. This is not ideal for studying the deformation of rate sensitive materials (such as cold dwell fatigue problem in Ti alloys). Novel synchrotron light sources were developed to enhance the performance of X-ray diffraction technique. Compared to lab based X-ray source, synchrotron X-ray source has the following advantages:

- High intensity: This can ensure measurements to be conducted at very high speed, making *in situ* experiments possible.
- Parallel beams: Excellent signal to noise ratio.
- Tuneable energy: This can make scattering atom specific.

- Plane polarised.
- Precise time structure.

There have been several studies on the deformation of α-titanium using synchrotron X-ray diffraction [97, 98, 99, 100, 101, 102, 103, 104]. Such experiments enable direct assessment of lattice strains from grain families with common grain orientations from polycrystal sample. Behaviours of different slip systems can be separated by assessing the lattice strain of grains orientated favourably for certain slip systems.

Abdolvand *et al.* [105] looked at strong grain neighbour effects in polycrystals using crystal plasticity modelling and 3D synchrotron X-ray diffraction method, which allows to study the evolution of grain-resolved stresses over many contiguous grains in HCP polycrystals deformed *in situ*. They found that grain-resolved stresses in loading direction can drop while applied stress increases in absence of deformation twinning. 'Hard' grains surrounded by 'hard' neighbours experience maximum stress drop. Crystal plasticity modelling results confirmed that elastic and plastic anisotropy of single crystals and strong grain-grain interaction are the main factors which contribute to the stress drop.

2.4 Summary

Lots of work have been done to understand cold dwell fatigue behaviour and it is evident that this phenomenon is due to the presence of stress redistribution (load shedding) during the dwell period. The load shedding effect is associated with the so-called hard-soft (rogue) grain pairs. The time dependent plasticity in the 'soft' grain (c-axis nearly perpendicular to the loading direction, favourably for slip) is thought to be critical for the load shedding. During stress dwell, the deformation behaviour in grains with different crystallographic orientations ('hard' and 'soft' grains) should be understood. To make progress beyond current understandings, it is important to quantify the plasticity processes in the hard and soft grains as a function of time. Specifically, this must describe the dislocation processes on major (prismatic and

basal) slip systems with respect to their critical resolved shear stresses. In Chapter 5, the time dependent plastic behaviour of CP-Ti (grade 4) at room temperature was studied, and the effect of crystal orientation on cold dwell fatigue was revealed.

The role of some common alloying elements (such as Oxygen) on time dependent plasticity and cold dwell fatigue is still not clear; a better understanding is highly attractive as it may guide future alloy design strategies and impurity control to suppress the cold dwell effect. In Chapter 6, The effect of Oxygen on cold dwell fatigue was revealed by comparing the different time dependent plasticity behaviours in two CP-Ti alloys (grade 1 and grade 4 with different oxygen content).

The majority of studies that have investigated cold dwell fatigue have been performed at ambient temperature. However, there is clear evidence showing that the cold dwell effect is also sensitive to temperature, noting that the effect is not observed at high temperature. The worst-case scenario temperature in Ti6Al alloy is around 120 °C and is diminished when the temperature exceeds 230 °C. To understand this effect in greater detail, the effect of temperature on dislocation activity of different slip systems needs to be understood and quantified in the context of cold dwell fatigue. In Chapter 6 and 7, the effect of temperature on the two major slip systems (prism and basal) was studied in the two CP-Ti alloys and a Ti6Al alloy. The mechanism of worst-case scenario temperature was explained and the effect of temperature on cold dwell fatigue was revealed.

The mechanism of load shedding in rogue grain pairs is well established by some modelling work but there is a lack of experimental data. To make progress beyond this, a combination of the mechanisms in modelling and experimental results is highly important. Load shedding and thus cold dwell effect should be assessed by evaluating the behaviours of rogue and non-rogue grain pairs in real samples. In Chapter 7, Load shedding behaviours were studied by comparing the plastic deformation in different grain pairs (rogue and non-rogue) during cold creep, the evidence of load shedding was found in real experiments.

Modern techniques such as EBSD and crystal plasticity modelling are found to be well suited to study such problem, also synchrotron X-ray diffraction is a

very powerful method for investigating the evolution of elastic lattice strain during *in situ* deformation. This project will combine these techniques to explore the effects of crystallographic orientation, common alloying elements, temperatures and local microstructures on cold dwell fatigue.

3
Techniques and methods

Contents

3.1 Electron back scattered diffraction 35
3.2 Synchrotron X-ray diffraction 36
3.3 Crystal plasticity finite element model 40
3.4 Digital image correlation 43

3.1 Electron back scattered diffraction

Microstructural analysis was conducted using electron back scattered diffraction (EBSD). Samples were ground step by step using silicon carbide paper down to 4000 grit followed by chemical–mechanical polishing using a 50 nm colloidal silica suspension. This method applied to all the Ti samples in this work. Electron backscatter diffraction (EBSD) maps were obtained from these polished samples using a Zeiss Merlin scanning electron microscope (SEM) equipped with a Bruker e-flash detector, operating at an accelerating voltage of 20 kV and a probe current of 20 nA. EBSD map plotting, texture analysis and denoising were achieved using software AZtecHKL by Oxford Instruments [106] and MTEX Toolbox [107, 108] in MATLAB.

3.2 Synchrotron X-ray diffraction

A set of stress relaxation experiments were carried out on beamline I12 [109] at the Diamond Light Source (experiment EE17222) to characterise the time dependent plasticity behaviour of Ti. Figure 3.1 shows a sketch of the experiment setup and Figure 3.2 shows the real picture of the experimental hutch and experiment setup.

The beamline was operated with a monochromatic X-ray beam with a constant energy of 79.79 keV and an incident beam size of 1 x 1 mm^2. The 1 x 1 mm^2 beam size was selected to ensure a sample volume containing over 10000 grains to be analysed, allowing statistical analysis of large polycrystals possible. On the other hand, the large beam size results in a large instrument broadening (details can be found in Appendix A.10). The X-ray beam was calibrated using a CeO_2 standard. Ti tensile samples were probed with the high energy X-ray beam, resulting in Debye Scherrer diffraction cones which were collected on a 2D Pixium area detector placed 1097 mm away from the samples. The detector-to-sample distance was selected to ensure a considerable number of diffraction rings (more than 25 diffraction rings) can be collected by the detector (this is to ensure various grain orientations can be studied) without sacrifice the lattice strain resolution. The results in Chapter 5 and Chapter 6 shows that this detector-to-sample distance meets the expectation. The exposure time for each frame was 1 second, giving an acquisition rate of 1 frame per second.

The samples were deformed and heated on an Instron Electro-Thermal-Mechanical Tester (ETMT). Here, sample deformation was applied through an in-line drive, displacement controlled 0.5 kN mechanical loading assembly [110, 111, 112]. Samples were heated through a DC current that was fixed between water cooling grips, that gives a parabolic temperature distribution [111, 113, 112]. Temperature measurement and control was achieved from an R-type thermocouple spot welded mid-way along each sample gauge. To ensure the temperature of the sample volume probed by the X-rays was known, the samples were centred on the incident beam path and positioned using radiographic imaging (as shown in Figure 3.3) such that the sample volume was in close proximity to the thermocouples. The copper wires were welded onto the sample and designed to measure the sample macroscopic strain

by measuring the resistance change during experiment. However, the resistance data was found to be extremely noisy and not reliable for strain measurements and thus not used in data analysis. At each designated temperature, samples were heated and held idle for 30 seconds to allow for temperature stabilisation, followed by deformation whilst Debye Scherrer diffraction rings were collecting in-situ. Diffraction patterns were recorded as 16-bit images which were synchronised with the ETMT mechanical test data for further analyses.

Examples of the diffraction patterns are shown in Figure 3.4. It is found that the quality of the diffraction patterns are highly depends on the sample grain size, when the sample grain size is large (e.g. the CP-Ti grade 1 sample) the number of grains within the X-ray probed volume is relatively small and thus results in spotty diffraction rings. As a result, the lack of diffraction spots along certain direction (i.e. the loading direction) could be problematic. To better address this problem and make full use of the diffraction ring, we applied ellipse fitting method instead of the more widely used cake integration method for diffraction data reduction. More details of this diffraction pattern analysis routine is discussed in Chapter 5.

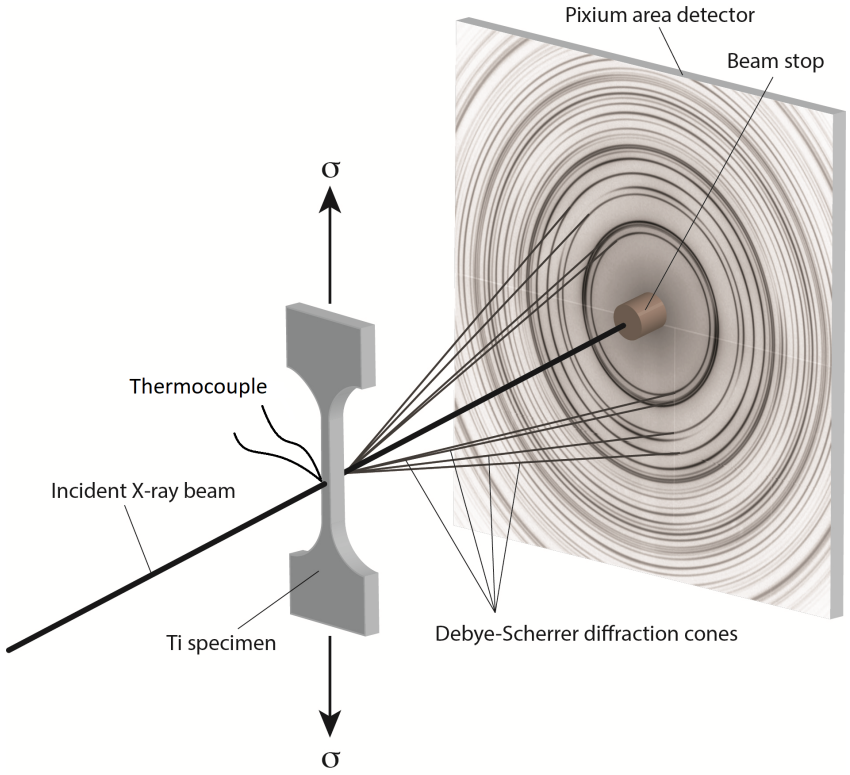


Figure 3.1: Schematic of the synchrotron diffraction experiment setup.

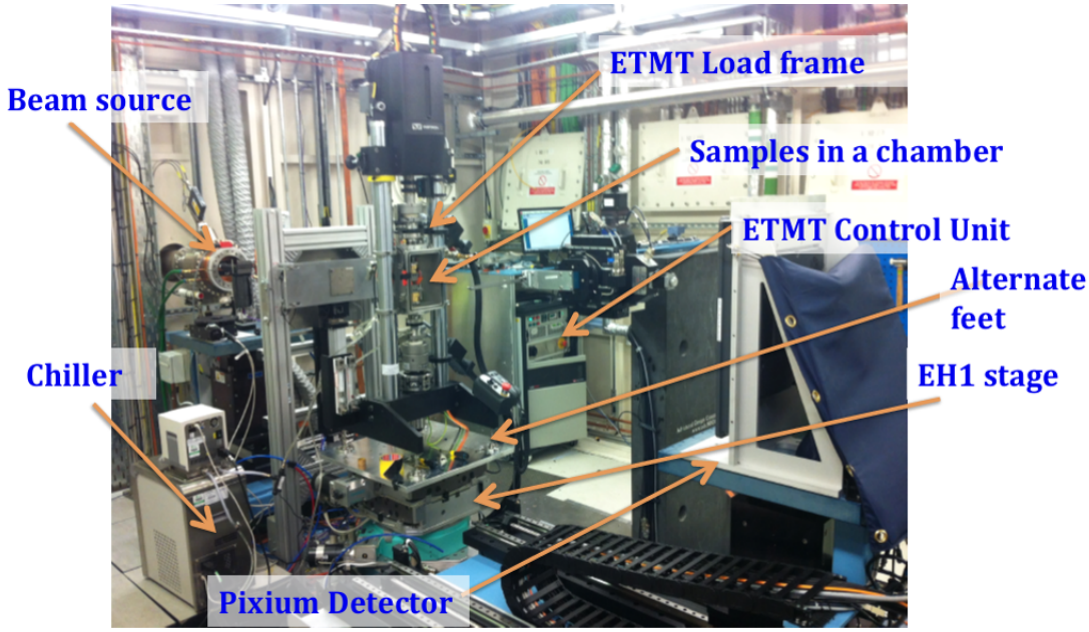


Figure 3.2: Real picture of the synchrotron diffraction experiment setup.

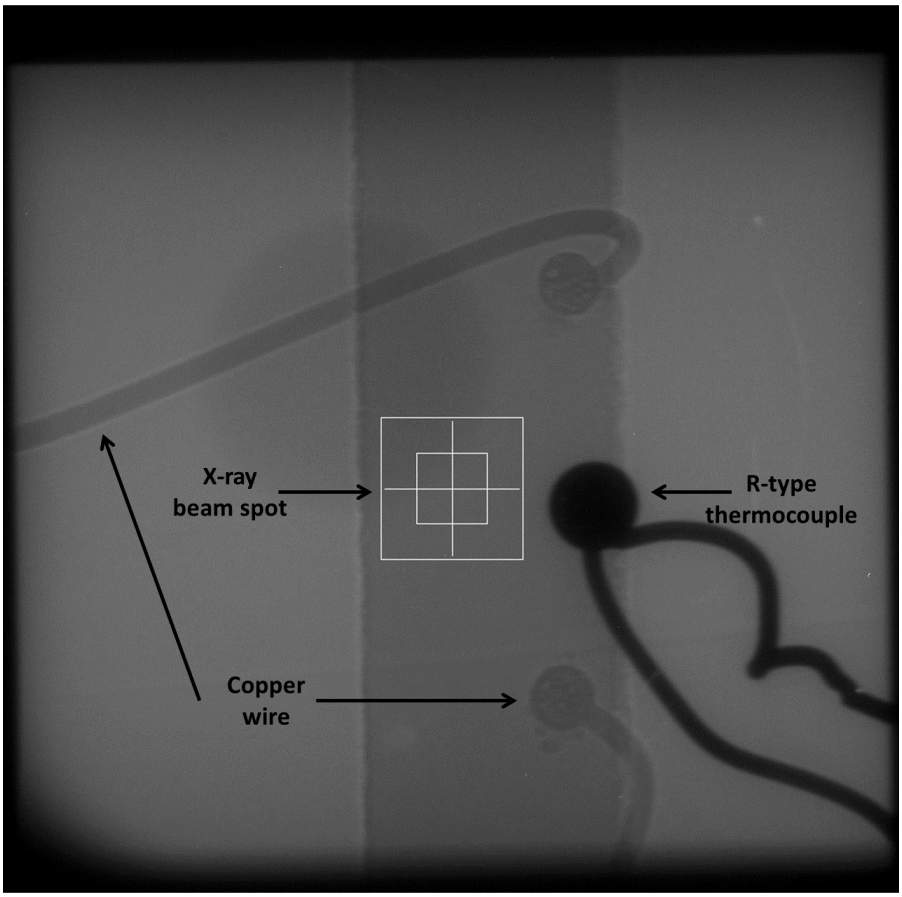


Figure 3.3: An example of the radiograph (CP-Ti grade 4 sample).

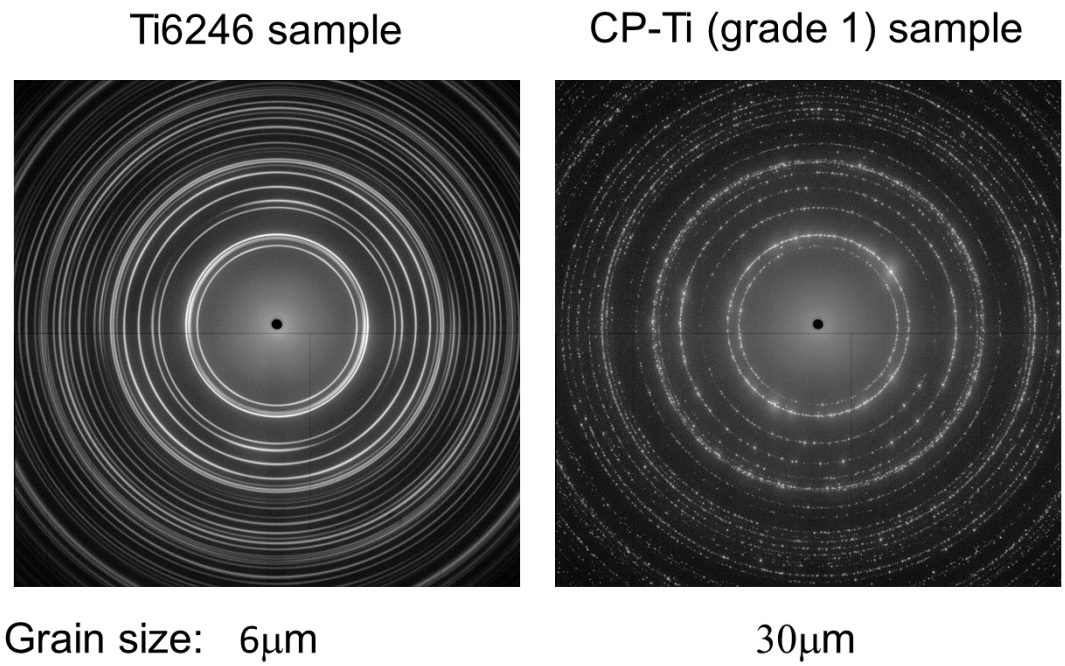


Figure 3.4: Examples of the diffraction patterns of the Ti6246 and CP-Ti grade 1.

3.3 Crystal plasticity finite element model

A crystal plasticity model was implemented using the commercial finite element (FE) software Abaqus 2016 through a user material (UMAT) subroutine developed by Tarleton *et al.* [114] based on a formulation initially proposed by Dunne *et al.* [56]. The crystal plasticity code is available in the following repository [115]. Briefly, the kinematics are governed by the deformation gradient ($\boldsymbol{F}$) which is decomposed multiplicatively into an elastic ($\boldsymbol{F}^e$) and plastic ($\boldsymbol{F}^p$) part. The rate of change of the plastic deformation gradient ($\dot{\boldsymbol{F}}^p$) required to calculate the increment in plastic strain over a small time increment can be written in terms of the plastic velocity gradient ($\boldsymbol{L}^p$) which comes from the linear sum of shear strain rates over the possible crystallographic slip systems.

The material properties were next introduced through the constitutive law relating the shear strain rate on each slip system to the local stress state. We use the constitutive law that was physically derived by Dunne *et al.* [56], in which the slip rate, $\dot{\gamma}^\alpha$ when $|\tau^\alpha| > \tau_c^\alpha$ on a slip system α is given by:

$$\dot{\gamma}^\alpha = \rho b^2 \nu \exp\left(-\frac{\Delta F^\alpha}{k_B T}\right) \sinh\left(\frac{(|\tau^\alpha| - \tau_c^\alpha)\Delta V^\alpha}{k_B T}\right) \text{sign}(\tau^\alpha) \tag{3.1}$$

where ρ is the density of gliding dislocations (here taken to be a constant 5 μm^{-2} following [1, 56, 116]), b is the magnitude of the Burgers vector (from the measured a and c values), ν is the jump frequency (i.e. attempts of the dislocations to exceed their energy barriers which was taken to be 10^{11} Hz, following [1, 56, 116]), k_B is the Boltzmann constant and T is the absolute temperature. The remaining three terms are material specific parameters that govern dislocation motion and are the variables to be obtained for the materials under investigation: ΔF^α is the slip system dependent activation energy, which corresponds to the energy barrier that a dislocation on a slip system α needs to overcome to continue gliding beyond the pinning obstacle, ΔV^α is the activation volume, which refers to the volume that a dislocation is swept when it passes obstacles [56] (ΔV^α is typically in the range 1-100b^3), and τ_c^α is the critical resolved shear stress (CRSS) for slip system α. If the resolved stress falls below CRSS, slip does not occur. In this condition

$\dot{\gamma}^{\alpha}$=0. The slip system dependent parameters ΔF, ΔV and τ_c are fitted for various alloys and temperatures in this study.

Summing up these shear strain rates over the possible crystallographic slip systems allows the plastic velocity gradient to be determined [56]:

$$\boldsymbol{L_p} = \sum_{\alpha=1}^{N_{\text{slip}}} \dot{\gamma}_{\alpha} \boldsymbol{s_\alpha} \otimes \boldsymbol{n_\alpha} \tag{3.2}$$

where $\boldsymbol{s_\alpha}$ is the unit slip direction and $\boldsymbol{n_\alpha}$ is the unit normal to the slip plane of the α^{th} slip system.

The constitutive model calculates the Cauchy stress $\boldsymbol{\sigma}$ based on the total strain increment $\Delta\boldsymbol{\varepsilon}$ at each time step, which is calculated from the deformation gradient $\mathbf{F}$ provided by the finite element solver. The plastic strain $\boldsymbol{\varepsilon}_p$ is the internal variable that quantifies the irreversible plastic deformation induced by the slip movement of dislocations. The time evolution of the plastic strain takes into account of N_{slip} =30 slip systems in the HCP crystal [117, 118]:

$$\dot{\boldsymbol{\varepsilon}}_{\text{p}}(\boldsymbol{\sigma}) = \frac{1}{2} \sum_{\alpha=1}^{N_{\text{slip}}} \dot{\gamma}_{\alpha} \left(\boldsymbol{s}_{\alpha} \otimes \boldsymbol{n}_{\alpha} + \boldsymbol{n}_{\alpha} \otimes \boldsymbol{s}_{\alpha} \right)$$

The slip systems of HCP Ti used are reported in Table 3.1. $\boldsymbol{s}_{\alpha}^{0}$ and $\boldsymbol{n}_{\alpha}^{0}$ are the slip directions and normals in the crystal reference frame. $< c + a >$ Pyramidal slip is much more difficult to activate due to its higher τ_{α}^{c}, which is about three times the value of basal slip at temperature between 20 °C and 300 °C [9, 17, 46]. The values of τ_{α}^{c} for pyramidal slip was set to be three time the value of basal slip.

At each time step Δt, the increment of the Cauchy stress in the sample reference frame is calculated as [119, 120]:

$$\begin{aligned} \Delta\boldsymbol{\sigma} &= \mathbb{C}\Delta\boldsymbol{\varepsilon}_e + \left(\boldsymbol{W}_e\boldsymbol{\sigma}_0 - \boldsymbol{\sigma}_0\boldsymbol{W}_e\right)\Delta t \\ &= \mathbb{C}\left(\Delta\boldsymbol{\varepsilon} - \dot{\boldsymbol{\varepsilon}}_{\text{p}}(\boldsymbol{\sigma})\,\Delta t\right) + \left(\boldsymbol{W}_e\boldsymbol{\sigma}_0 - \boldsymbol{\sigma}_0\boldsymbol{W}_e\right)\Delta t\ , \end{aligned} \tag{3.3}$$

where $\boldsymbol{W}_e$ is the elastic continuum spin and $\boldsymbol{\sigma}_0$ is the stress at the start of the time increment.

The elastic parameters for polycrystalline Ti crystal plasticity model under uniaxial loading at all 6 different temperatures examined in this thesis are summarised in Table 3.2. The conversion from elastic constants to the stiffness matrix is as follow [121]:

$$\mathbb{C} = \begin{bmatrix} \frac{1}{E_{11}} & -\frac{\nu_{12}}{E_{11}} & -\frac{\nu_{31}}{E_{33}} & 0 & 0 & 0 \\ -\frac{\nu_{12}}{E_{11}} & \frac{1}{E_{11}} & \frac{\nu_{31}}{E_{33}} & 0 & 0 & 0 \\ -\frac{\nu_{13}}{E_{11}} & -\frac{\nu_{13}}{E_{11}} & \frac{1}{E_{33}} & 0 & 0 & 0 \\ 0 & 0 & 0 & \frac{1}{2G_{12}} & 0 & 0 \\ 0 & 0 & 0 & 0 & \frac{1}{2G_{13}} & 0 \\ 0 & 0 & 0 & 0 & 0 & \frac{1}{2G_{13}} \end{bmatrix}$$

where $E_{11} = E_{22}$, $\nu_{12} = \nu_{21}$, $\nu_{13} = \nu_{23}$, $\nu_{31} = \nu_{32}$, $G_{13} = G_{23}$.

Table 3.1: Slip systems used in the model. Slip directions and normals are expressed in the crystal reference frame. The vectors are normalised.

Slip system	$\boldsymbol{s}_\alpha^0$	$\boldsymbol{n}_\alpha^0$
<a> basal slip	$[-0.5, \pm 0.866, 0]$	$[0, 0, 1]$
	$[1, 0, 0]$	$[0, 0, 1]$
<a> prismatic slip	$[-0.5, \pm 0.866, 0]$	$[\mp 0.866, -0.5, 0]$
	$[1, 0, 0]$	$[0, -1, 0]$
<a> 1st order pyramidal slip	$[-1, 0, 0]$	$[0, \mp 0.7559, 0.6547]$
	$[-0.5, -0.866, 0]$	$[\pm 0.6547, \mp 0.3780, 0.6547]$
	$[-0.5, 0.866, 0]$	$[\mp 0.6547, \mp 0.3780, 0.6547]$
<c+a> 1st order pyramidal slip	$[-0.3536, 0.6124, \pm 0.7071]$	$[\pm 0.6547, \mp 0.3780, 0.6547]$
	$[-0.3536, -0.6124, \mp 0.7071]$	$[-0.6547, -0.3780, \pm 0.6547]$
	$[0.7071, 0, \pm 0.7071]$	$[\mp 0.6547, \pm 0.3780, 0.6547]$
	$[\mp 0.7071, 0, 0.7071]$	$[\pm 0.6547, \pm 0.3780, 0.6547]$
	$[-0.3536, -0.6124, \pm 0.7071]$	$[0, \pm 0.7559, 0.6547]$
	$[\pm 0.3536, \mp 0.6124, 0.7071]$	$[0, \pm 0.7559, 0.6547]$
<c+a> 2nd order pyramidal slip	$[-0.3536, 0.6124, \pm 0.7071]$	$[\pm 0.3536, \mp 0.6124, 0.7071]$
	$[-0.3536, -0.6124, \pm 0.7071]$	$[\pm 0.3536, \pm 0.6124, 0.7071]$
	$[0.7071, 0, \pm 0.7071]$	$[\mp 0.7071, 0.0000, 0.7071]$

Table 3.2: Elastic parameters for polycrystalline Ti crystal plasticity model under uniaxial loading at 6 different temperatures [56, 17].

	E_{11}(GPa)	E_{33}(GPa)	G_{12}(GPa)	G_{13}(GPa)	ν_{12}	ν_{13}
RT	84.7	118.4	28.6	39.5	0.46	0.22
75 °C	80.5	113.8	27.5	37.9	0.47	0.22
120 °C	77.0	108.8	26.2	36.2	0.47	0.22
145 °C	75.1	106.1	25.5	35.2	0.47	0.23
230 °C	68.5	96.8	23.2	31.9	0.48	0.23
250 °C	66.9	94.6	22.6	31.2	0.48	0.23

The geometrically necessary dislocation (GND) density is calculated using a least square minimisation of the dislocation energy [122]. This energy is assumed proportional to the sum of the squares of the GND densities on the different slip systems: $\sum_{\alpha=1}^{N_{\text{slip}}} \rho_\alpha^2$. A constrained minimisation algorithm is applied. Given the simulated plastic deformation gradient $\mathbf{F}_p$, the GND densities ρ_α must satisfy the condition:

$$(\nabla \times \mathbf{F}_p)^T = \sum_{\alpha=1}^{N_{\text{slip}}} \rho_\alpha \boldsymbol{b}_\alpha \otimes \boldsymbol{l}_\alpha \ , \tag{3.4}$$

where $\boldsymbol{b}_\alpha$ is the Burgers vector and $\boldsymbol{l}_\alpha$ is the dislocation line unit vector for the α^{th} slip system. The right-hand side of Equation 3.4 is known as Kröner-Nye tensor [123]. The dislocation energy is minimised while respecting the condition in Equation 3.4, therefore the different ρ_α can be calculated at each time step of the simulation. More details of the algorithm are given by Das *et al.* [114].

The crystal plasticity simulations were performed on a PC with an Intel Xeon(R) CPU E5-2687W v2 @ 3.40GHz with 8 cores.

3.4 Digital image correlation

In order to measure strain on the sample surface, an optical DIC technique was used. This requires a speckle pattern to be applied to monitor pattern motion and subsequent strain estimation. This was achieved by spraying a polyurethane paint onto the polished surfaces of the cubic samples. Black paint was used first to generate a uniform background, then a white paint diluted with isopropyl alcohol was applied to the surfaces using an airbrush kit to generate speckle patterns. An example of the speckle pattern is shown in Figure 3.5, the size of the white spots vary from 1-10 μm. The images were recorded at 16-bit depth using a high speed camera (Hamamatsu Photonics Ltd - ORCA-Flash 4.0) with an image resolution of 2048×2048 pixels. A Questar QM100 lens attachment was employed to increase the working distance and to enable focus on the sample through a furnace window for high temperature experiments. With the working distances used in this experiment, the pixel size corresponds to 1.5 μm.

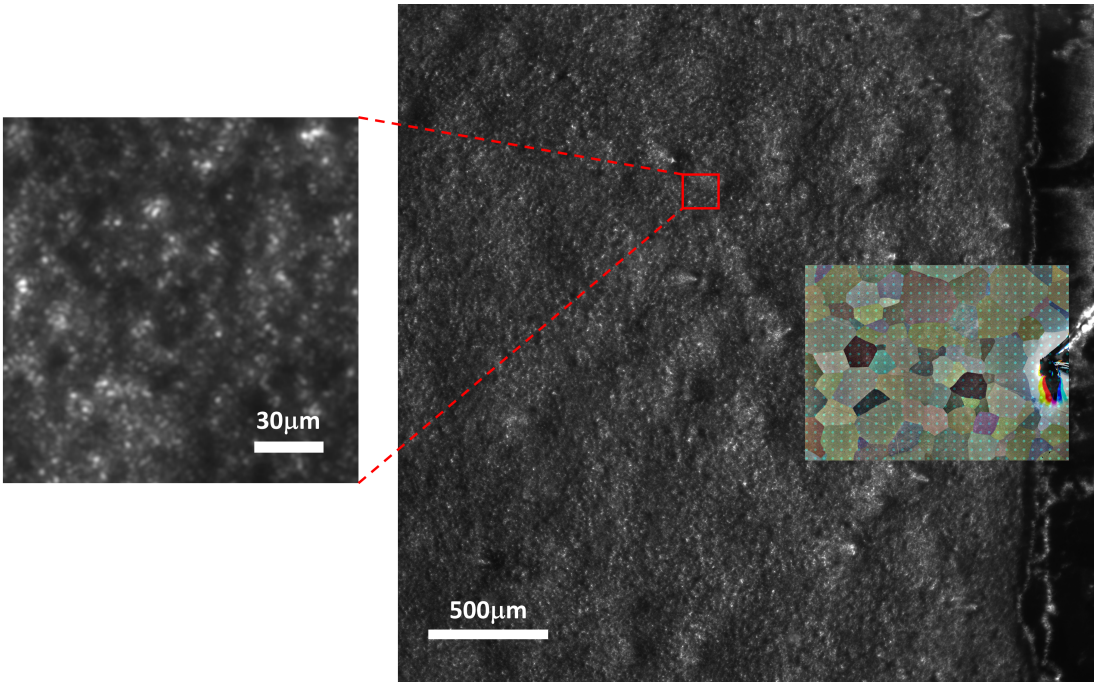


Figure 3.5: Example image for DIC measurement, EBSD scanned area was located by matching a mark pre-scratched on the sample. Grid of nodes were generated within the EBSD scanned area. Loading along the vertical direction of this image.

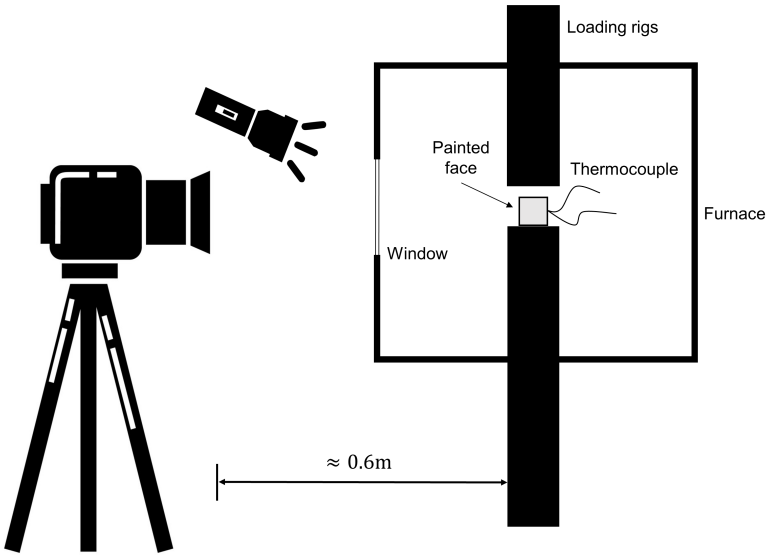


Figure 3.6: Sketch of the DIC experiment setup.

Figure 3.6 shows the experiment setup and the real picture of this setup is shown in Figure 3.7. Samples with thermocouples spot welded on one face, were placed in an environmental chamber (manufactured by Severn Thermal Solutions). DIC images were recorded by the high speed camera through the furnace window. An

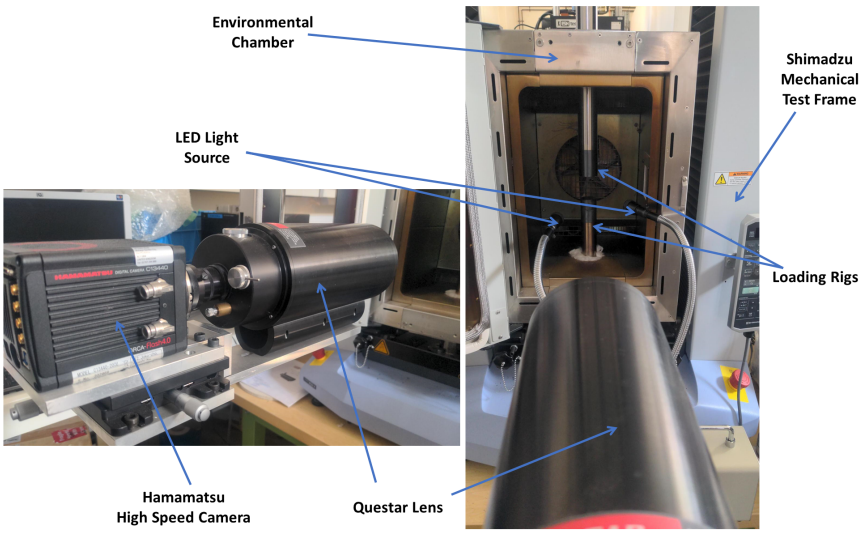


Figure 3.7: Real photo of the DIC experiment setup.

LED light source was placed outside the furnace chamber, illuminating the sample surfaces with speckle patterns, so that the exposure time of the camera could be reduced down to 20 ms without sacrifice the quality of the images. The acquisition rate was set to be constant at 1 frame per second for all the tests.

As shown in Figure 3.5, identification marks were scratched on the painted surfaces so that the area of the EBSD scan can be correlated to the DIC strain measurements. A grid of nodes were generated within the EBSD scanned area, with intervals of 25 pixels. DIC strain measurements were performed on the images captured by the camera via a modified version of the Python based DIC code [124] so that the in-plane strain components at the nodes can be calculated.

The error analysis of this DIC measurements can be found in Appendix A.9.

4

Macroscopic analysis of time dependent plasticity in some selected Ti alloys

Contents

4.1 Introduction 47
4.2 Materials 49
4.3 Stress relaxation tests 52
4.4 Relaxation curves analysis 53
4.5 Key parameters 56
4.6 Strain rate sensitivity 58
4.7 Summary 60

4.1 Introduction

Commonly used alloys in aeroengine compressor disks, such as Ti-6Al-2Sn-4Zr-xMo alloys show accelerated failure via the accumulation of plastic strains when subjected to a dwell stress [125]. The role of bulk composition is known to influence dwell damage; the propensity for dwell debit is minor in high Mo containing Ti6246 alloys, whereas it is significant in low Mo containing Ti6242 alloys which have a lower β phase fraction. The role of chemistry and microstructure, both known to affect the severity of dwell fatigue, is not well established. Although this problem has drawn attention for many decades and great efforts have been

made to understand this problem, the majority of the work has been performed at room temperature. In practice, it is found that cold dwell fatigue is suppressed at elevated temperature, and is no longer present for operating temperatures exceeding 200 °C [16, 17]. To establish a better understanding of the cold dwell fatigue problem, a broader study that explicitly explores the sensitivity of temperature to time dependent plasticity is necessary.

This proposed experiment seeks to gain mechanistic understanding and quantification of key parameters across a range of industrially relevant Ti alloys and microstructures by using simple stress relaxation loading at different temperatures up to 250 °C. The effect of chemistry, microstructure and temperature on time dependent plasticity has been explored here, which aims to benefit the future design of alloys and provide better lifetime prediction under conditions observed in service. Although not capturing the local extreme conditions at the grain level, the macroscopic stress-strain-time response gives an readily accessible route to assessing the propensity for different alloy compositions, microstructures and textures to influence the extent of time dependent plasticity in the temperature regime of interest for cold dwell behaviour. Macroscopic assessment of time dependent plasticity is the aim of this chapter.

Table 4.1: Materials composition (in wt%) and microstructure information.

	Al	V	Sn	Zr	Mo	Fe	O	N	Others total	Microstructure	β phase content	Grain size (μm)
CP-Ti grade 1	<0.05	0.11	<0.05	<0.05	<0.05	<0.05	0.077	0.02	0.2	Pure α	0%	30
CP-Ti grade 4	<0.05	0.15	<0.05	<0.05	<0.05	0.055	0.32	0.006	0.4	Pure α	0%	17
Ti64 α	6.74	3.98	<0.05	<0.05	<0.05	<0.05	0.218	0.001	0.2	Primary α	6%	15
Ti64 Bimodal	6.63	3.87	<0.05	<0.05	<0.05	<0.05	0.191	0.002	0.3	$\alpha+\beta$	18%	8
Ti6242	6.21	0.28	1.27	4.21	1.86	<0.05	0.079	<0.001	0.4	Primary α	10%	12
Ti6246	5.98	0.15	0.87	4.24	5.35	<0.05	0.157	<0.001	0.3	$\alpha+\beta$	60%	6

4.2 Materials

In this Chapter, the stress relaxation behaviour of 6 different Ti alloys was studied. An overview of the chemistry and microstructures of the alloys is summarised in Table 4.1. The materials compositions were measured using XRF and LECO analysis provided by AMG Superalloys UK Ltd. Samples were cut from the raw materials then analysed using a Zeiss Merlin scanning electron microscope (SEM) equipped with a Bruker e-flash detector. Exemplar microstructures of these alloys are shown in Figure 4.1(a)-(f). Due to the lack of processing information on the raw materials, the percentage of β phases was estimated using ImageJ on these SEM images, where the dark phases are α and the bright phases are β phase. Grain size measurements were performed based on lower magnification map containing over 3000 grains. The two grades of commercially pure Ti (CP-Ti) were used to study the effect of the common interstitial, oxygen, on cold dwell fatigue. Two Ti64 alloys with different microstructures were studied to establish the effect of the β phase content. In the two Ti64 alloys, β phase was found to appear at the α grains boundaries and mainly at the triple junctions. The Ti6242 and Ti6246 alloys were used to study the effect of both the β phase and the alloying element Mo on time dependent plasticity. In the Ti-6Al-2Sn-4Zr-xMo alloys, β phase appear in form of lamellar structure. Texture is an important factor that affects the deformation behaviour of α-Ti due to the anisotropic properties of the HCP crystal structure. The CP-Ti grade 4, CP-Ti grade 1, Ti64 α and Ti6242 have over 90% of the α phase and the raw materials were supplied as rolled sheets. This gives a strong texture in these four materials (as shown in Figure 4.2(a)-(d)). The pole figures, calculated from EBSD measurements, were obtained from larger areas that contains over 3000 grains. Although the

processing history of these raw materials was not available, it can be speculated that the CP-Ti grade 1, CP-Ti grade 4 and the Ti6242 alloys were hot-rolled. There was preference for the c-axes to be perpendicular to the macroscopic rolling axis, which is quite common in hot-rolled titanium alloys [126]. To ensure the major slip systems are activated, there should be a considerable number of 'soft' grains with respect to the loading direction. The test samples were cut from the raw materials with the loading direction along the X0 direction in these pole figures.

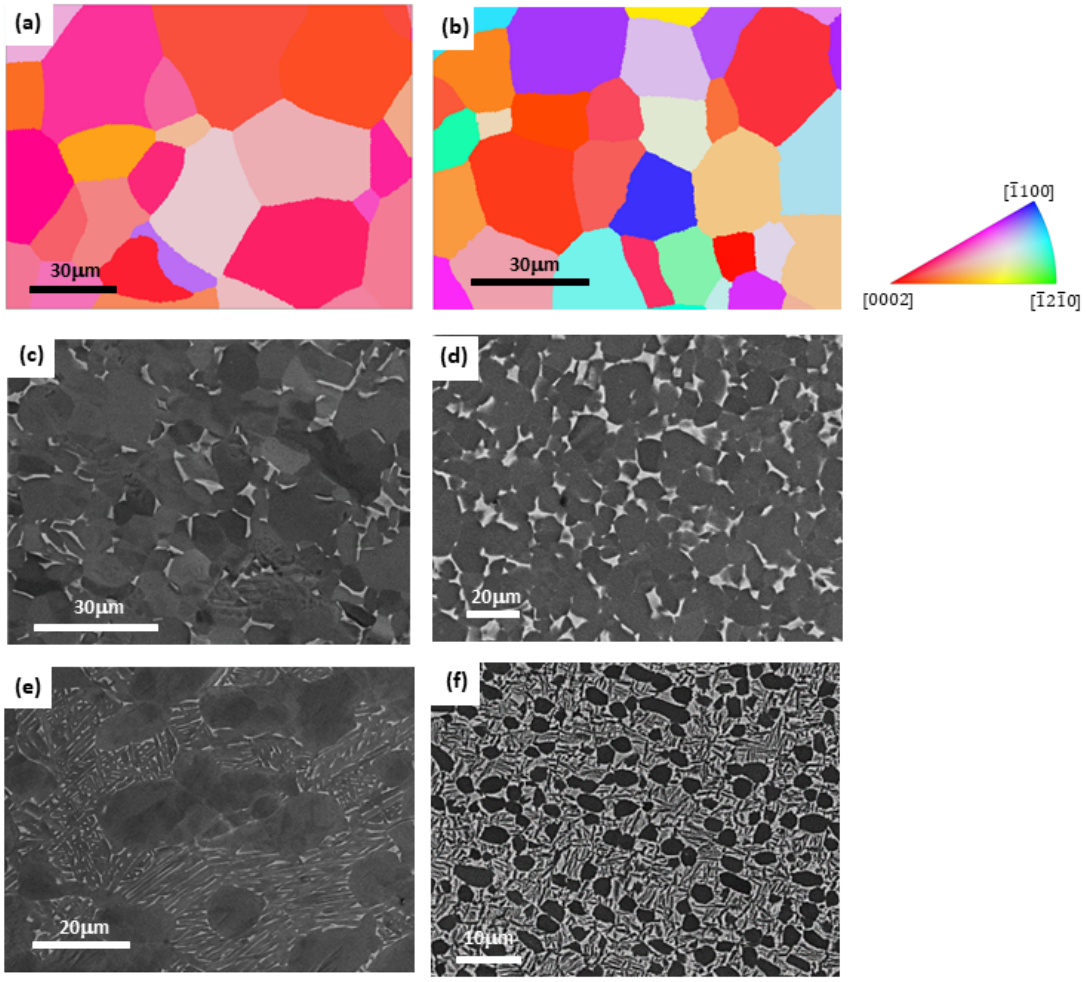


Figure 4.1: Microstructures of the raw materials: (a) EBSD map of the CP-Ti grade 1 alloy (IPF map in normal direction of the raw material); EBSD map of the CP-Ti grade 4 alloy (IPF map in normal direction of the raw material); SE images of the (c) Ti64 α alloy; (d) Ti64 Bimodal alloy; (e) Ti6242 alloy and (f) Ti6246 alloy.

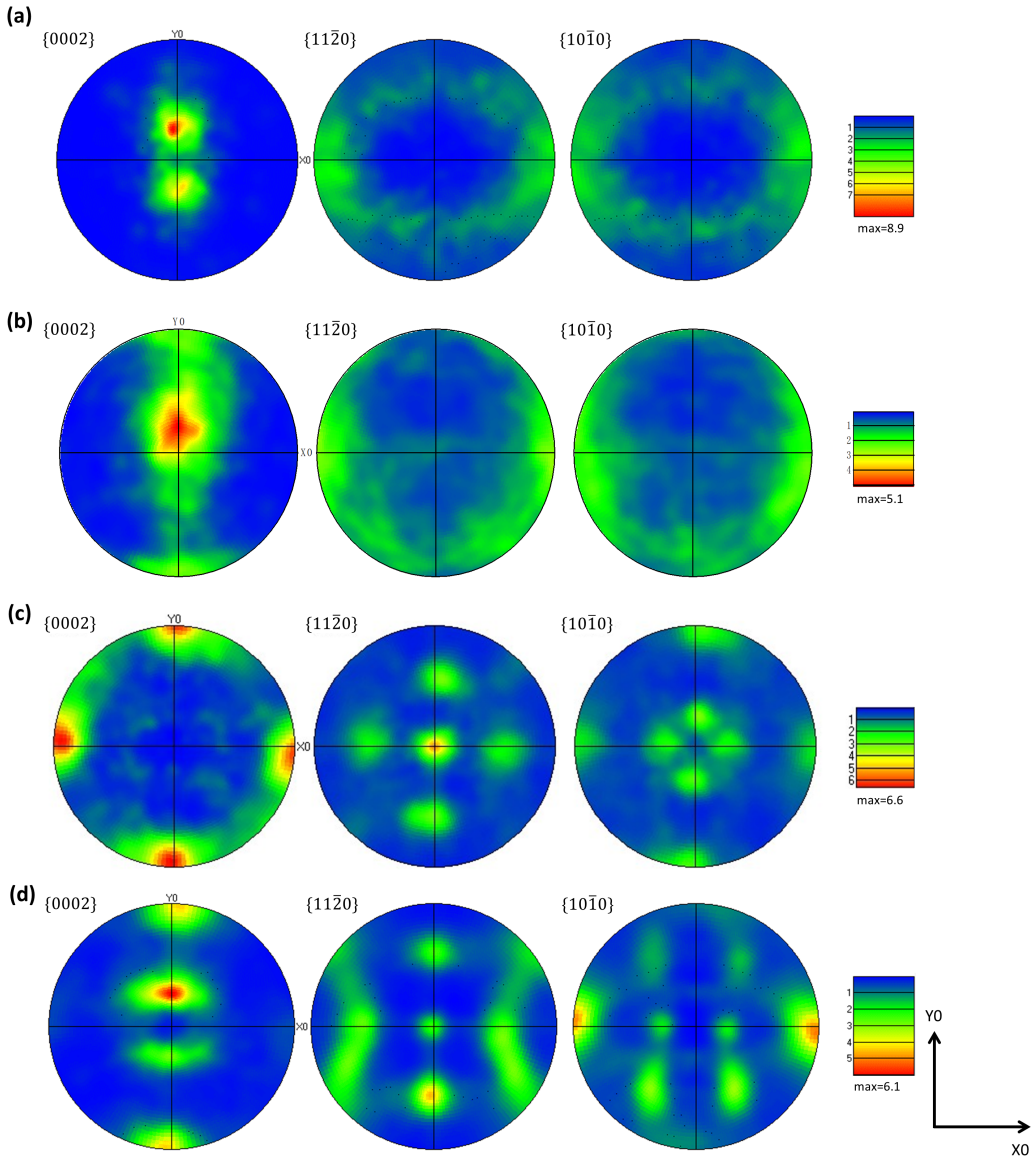


Figure 4.2: Pole figures of the raw material with a 10° width used for contours plotting calculation: (a) CP-Ti grade 1 alloy; (b) CP-Ti grade 4 alloy; (c) Ti64 α alloy and (d) Ti6242 alloy.

4.3 Stress relaxation tests

A series of samples in each alloy derivative was subjected to stress relaxation loading (load-up and strain hold) using an Instron ETMT (Electro-Thermal-Mechanical Tester), where test samples can be subjected to user defined mechanical and thermal profiles. Figure 4.3(a) shows the geometry of the ETMT dogbone sample, having a 52 mm length and the gauge length of 16 mm with a 2 mm width and a 1 mm thickness. Each alloy was tested at four different temperatures: room temperature, 75°C, 145°C and 250°C (CP-Ti grade 1 at 250°C test was abandoned due to its extremely low strength at this temperature). The microstructure changes during the experiments were ignored as these test temperatures were far lower than the common heat treatment temperatures of Ti [16]. Prior to in-situ testing, target loads were obtained from trial tests. The target loads corresponded to a stroke displacement at which the yield stress had just been exceeded. The ramp up of loading was completed at a constant stress rate (different for different samples) in around 100 s. Once the target load had been reached, the sample displacement (and thus the total strain) was then held constant for a period of 5 minutes, during which the macroscopic stress was found to relax. A typical stress relaxation loading curve is shown in Figure 4.3(b).

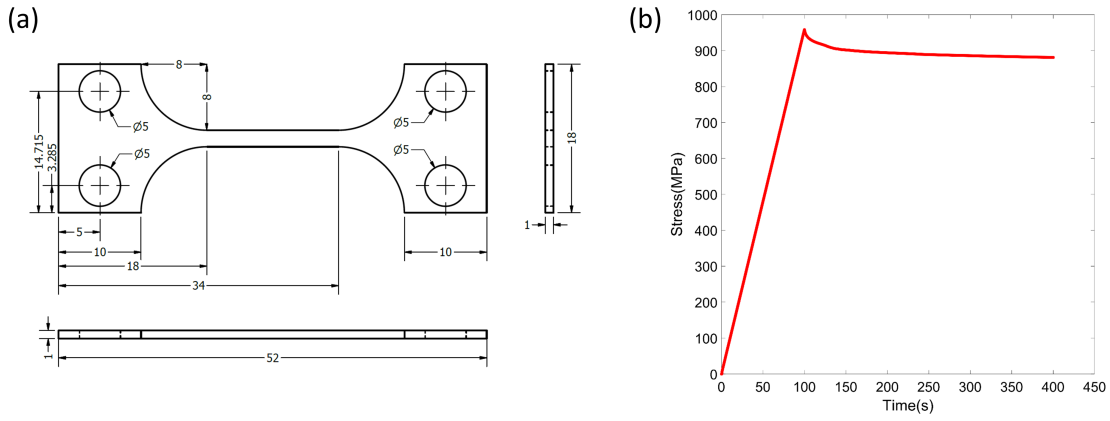


Figure 4.3: (a) Geometry of the ETMT tensile test sample; (b) An example of the stress relaxation loading (Ti64 α at room temperature).

4.4 Relaxation curves analysis

The stress relaxation curves were numerically analysed using a same form of constitutive law [56], which instead links the macroscopic plastic strain rate, $\dot{\varepsilon}_p$, to the macroscopic applied stress, σ:

$$\dot{\varepsilon}_p = \rho b^2 \nu \exp\left(-\frac{\Delta F}{k_B T}\right) \sinh\left(\frac{(\sigma - \sigma_c)\Delta V}{k_B T}\right) \tag{4.1}$$

$$\begin{aligned} \Delta\varepsilon_e = -\Delta\varepsilon_p = -\dot{\varepsilon}_p \Delta t \\ \rightarrow \Delta\sigma = E\Delta\varepsilon_e \\ \rightarrow \sigma_{i+1} = \sigma_i + \Delta\sigma \end{aligned} \tag{4.2}$$

where ρ is the density of gliding dislocations (the validation of constant ρ in the constitutive law can be found in Appendix A.5), b is the magnitude of the Burgers vector (the value of b at room temperature was taken from other studies on Ti64, Ti6242 and Ti6246 alloys [5, 68, 127, 128], at higher temperatures the values of b used were calculated based on lattice parameters meassured in Chapter 6), ν is the jump frequency, k_B is the Boltzmann constant. These parameters are constant and are summarised in Table 4.2. T is the absolute temperature. The remaining three terms are material dependent and are the key parameters controlling plasticity: ΔF is the thermal activation energy, σ_c is the critical stress and ΔV is the activation volume [56]. The three key parameters were determined via this constitutive law and the experimental stress relaxation curves.

Table 4.2: Values of the fixed parameters in the slip law [5, 68, 127, 128].

ρ	5 μm^{-2}
b (RT)	0.295 nm
ν	10^{11} Hz
k_B	1.38×10^{-23} JK^{-1}

To obtain the slip law parameters, the following steps were used, as shown in Equation 4.2, the initial applied stress, σ_i, was substituted into the Equation 4.1 to generate the plastic strain rate, $\dot{\varepsilon}_p$. The change in plastic strain, $\Delta\varepsilon_p$, over a

time step, Δt (here taken to be 0.2 s) can then be calculated by the product of $\dot{\varepsilon}_p$ and Δt. The change in elastic strain, $\Delta\varepsilon_e$, can be matched by the negative change in plastic strain, $\Delta\varepsilon_p$ during the stress relaxation (as the total strain was held constant). The change in stress, $\Delta\sigma$, is obtained by multiplying the Young's modulus, E for Ti at each temperatures [17, 14] to the $\Delta\varepsilon_e$. The stress at next time step, σ_{i+1},was then calculated by adding the $\Delta\sigma$ to the σ_i. This process was repeated so that a modelled stress relaxation curve could be generated. Three key parameters were optimised using a fitting tool in MATLAB so that the modelled relaxation curves and the experimental relaxation curves show good agreement with errors of less than 1%, as shown in Figure 4.4(a). The confidence intervals for the three parameters are $\pm 0.2 \times 10^{-20}$J for ΔF, $\pm 1b^3$ for ΔV and $\pm$5MPa for σ_c.

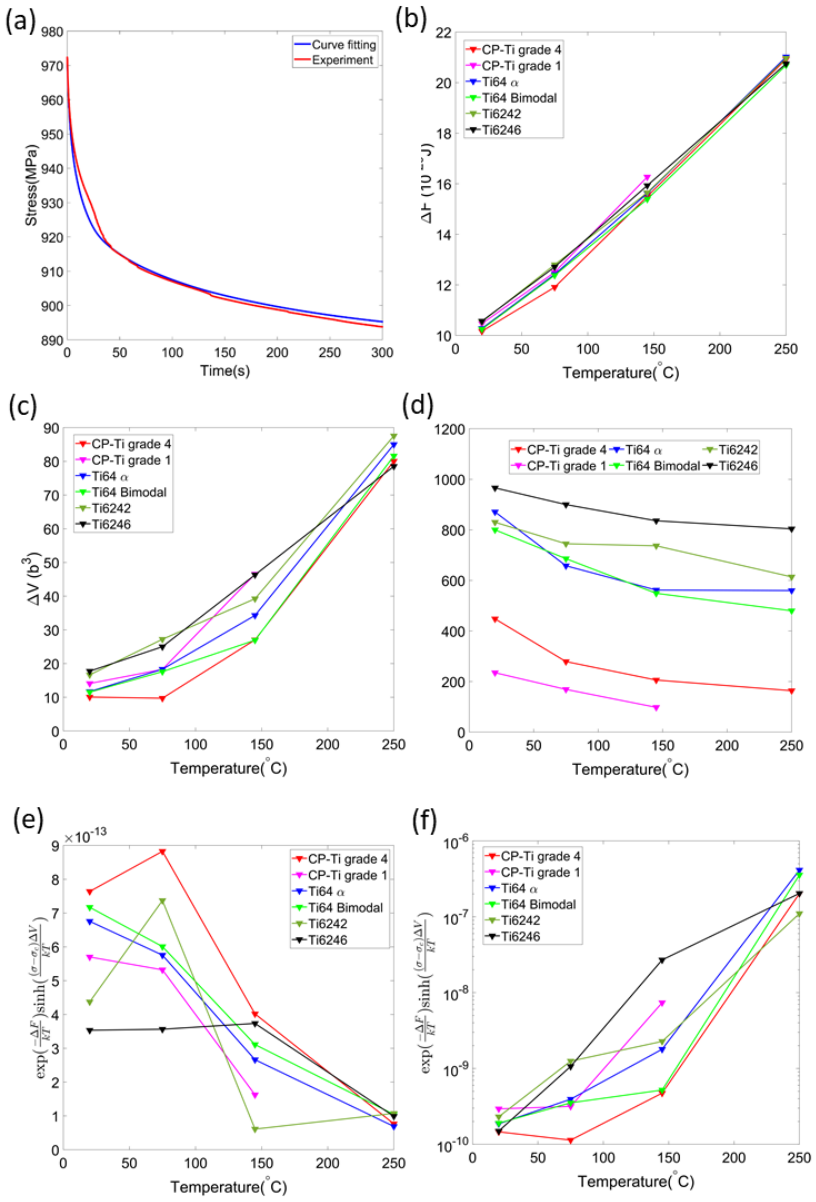


Figure 4.4: (a) A fitted stress relaxation curve (Ti64 α at room temperature, as an example). (b) Thermal activation energy, ΔF and (c) Activation volume, ΔV (d) Critical stress, σ_c, as a function of temperature for the 6 alloys; (e) Contribution of the three key parameters to the form of the plastic strain rate when the critical stress is exceeded by 1 MPa (low stress condition) and (f) 50 MPa (high stress condition). (The confidence intervals for the three parameters are $\pm 0.2 \times 10^{-20}$J for ΔF, $\pm 1b^3$ for ΔV and $\pm$5MPa for σ_c)

4.5 Key parameters

Figure 4.4(b)-(d) show the three key parameters vs. temperature for the six different alloys. Both ΔF and ΔV increased with temperature, where the relationship between ΔF and temperature was almost linear, which is consistent with the observations in BCC steel [129]. The effect of temperature on ΔF was seen to be markedly stronger than the alloy to alloy variation. CP-Ti had the lowest critical stress and relatively lower ΔV among the three different alloy systems. Comparing the two CP-Ti alloys, the grade 4 with a higher oxygen content had a higher critical stress over the low oxygen content grade 1, corroborating the known potent strengthening effect of oxygen in Ti [12, 36]. A higher activation volume was found in the low oxygen content grade 1 samples over the grade 4. The Ti-6Al-4V alloys system had both moderate critical stress and activation volume among the three alloy systems. With the addition of Al and V into the pure Ti, the strength was largely increased (i.e. the σ_c of Ti64 α had approximately double the value for the CP-Ti grade 4 and triple the value for the grade 1). With further alloying additions, the most complex alloys system Ti-6Al-2Sn-4Zr-xMo system had a relatively higher ΔV and the highest σ_c. There is no significant difference in σ_c between the Ti6242 and the two Ti64 alloys, but σ_c for the Ti6246 is evidently higher than them. This shows the excellent strengthening effect of Mo [130]. The higher Mo content Ti6246 had higher σ_c over the Ti6242, but there was no obvious trend between the ΔV of Ti6242 and Ti6246.

The activation volume, ΔV, expresses the volume which is physically swept by a dislocation from a ground equilibrium state to an activated state after the deformation, and it is proportional to the dislocation pinning distance (or the mean free path of dislocation) [56, 131]. In CP-Ti, interstitial oxygen atoms provide a strengthening effect by acting as obstacles for dislocations. The pinning distance reduces when there are more oxygen atoms, resulting in a smaller activation volume in the higher oxygen content CP-Ti grade 4 compared to the CP-Ti grade 1. However, it is not possible to explain the variation of activation volume in different alloys simply by pinning distance, as different alloys have different microstructures and

critical stresses. Direct comparison of the activation volume between different alloy seems unfair. Values of activation volume reported here were based on the alloys examined in this experiment. The temperature dependence of activation volume in each alloy is related to the corresonding critical stress levels and is consistent with a kink-pair mechanism [132, 133]. The attractive stress generated by kinks of opposite sign making up a pair are markedly stronger at small separations, so that the the equilibrium kink-pair separation (activation volume) decreases significantly as the externally imposed stress is increased. As temperature increases, critical stresses in all six alloys decrease and thus resulting in increases in the activation volumes. The value of ΔV is an effective reflection of rate-dependent deformation mechanisms [131]. The intersection of forest dislocations usually gives rise to an extremely large activation volume (several thousand b^3). A dislocation climb process, however, yields a lower activation volume of $1b^3$ [131]. Overcoming the Peierls barrier, point defect drag and point defect interactions typically give an activation volume of $10b^3$ to $100b^3$ according to Evans and Rowlings [134]. In this work, the values of ΔV of all six alloys at all four temperatures were found to lie within this range, indicating the rate-dependent deformation mechanism remains unchanged and the mechanism is not affected by alloying or temperatures.

Figure 4.4(e) and (f) show the contribution of the three key parameters into the plastic strain rate and thus time dependent plasticity. The prefactor $\rho b^2 \nu = 4.35 \times 10^4 s^{-1}$ is constant in Equation 4.1 and was ignored in this calculation. The contribution of the three key parameters to the plastic strain rate was calculated when $(\sigma - \sigma_c)$=1 MPa (low stress condition, see Figure 4.4(e)) and when $(\sigma - \sigma_c)$=50 MPa (high stress condition, see Figure 4.4(f)). When the critical stress was just exceeded, similar to the dwell fatigue condition, the contribution decreased as the temperature increased from room temperature to 250°C and the values were still of the same order of magnitude. Generally, CP-Ti grade 4 had the highest strain rate, Ti-6Al-4V systems had a moderate strain rate and Ti6246 had the lowest strain rate. All six alloys had very low strain rate at 250°C, and in most of the alloys, there is a sharp drop in strain rate when the temperature reached

145°C. For the high stress condition, the trend is reversed, where the contribution of key parameters to the plastic strain rate increased with temperature and the difference could be up to 4 orders of magnitude. The CP-Ti grade 4 had the lowest strain rate and Ti6246 had the highest. In both stress conditions, the two Ti64 alloys show relatively similar strain rates. The deformation behaviour was not strongly affected by the β phase fraction.

4.6 Strain rate sensitivity

The strain rate sensitivity (SRS) exponent, m, can be calculated follow the equation [67, 69]:

$$m = \mathrm{d}(\log(\sigma))/\mathrm{d}(\log(\dot{\varepsilon})) \tag{4.3}$$

In this stress relaxation experiment, the m values are determined by fitting a straight line to the stress-strain rate plots on a log scale (see Figure 4.5(a)). The gradient of the straight line is the strain rate sensitivity exponent. As shown in Figure 4.5(b), the commercially pure Ti had the highest m values, Ti-6Al-4V had a medium SRS and the values for the Ti-6Al-2Sn-4Zr-xMo system is the lowest. The SRS for CP-Ti grade 4 is the highest and Ti6246 is the lowest among the six alloys. The percentage of stress relaxed were calculated to represent the accumulation of plastic strain during a stress relaxation cycle, as the total strain was held constant. The relaxed stress (elastic strain) can be matched by the increased plastic strain. A higher strain rate sensitivity will lead to more plastic deformation and thus higher plastic strain during stress relaxation [104, 135], as a result, the trend found in Figure 4.5(c) is very similar to the trend in Figure 4.5(b). It is also noted that, there were sharp increases in SRS and relaxed stress as temperature increases from room temperature to 75°C in the two CP-Ti alloys. This indicates the strong dislocation activity at this intermediate temperature. This temperature agrees well with the predicted worst-case scenario temperature (90 to 120 °C) for dwell debit according to Zhang *et al.* [17].

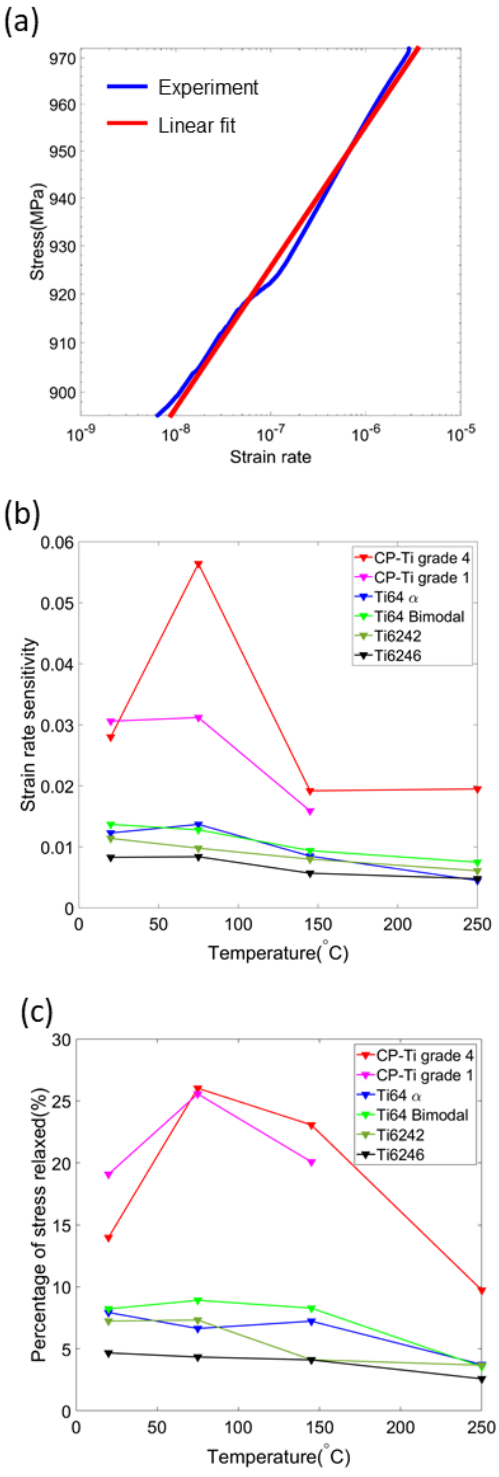


Figure 4.5: (a) Fitting a straight line to the stress vs. strain rate on a log scale, the gradient represents the strain rate sensitivity exponent m (Ti64 α at room temperature as an example); (b) Strain rate sensitivity vs. Temperatures for the six different alloys; (c) Percentage of stress relaxed vs. Temperatures for the six different alloys.

4.7 Summary

In this Chapter, an overview of cold dwell fatigue was given by results of stress relaxation tests on six different alloys at 4 different temperatures up to 250°C. The cold dwell fatigue effects were compared in different alloys at different temperatures at macroscopic level. Some key conclusions are summarised below:

Key parameters (thermal activation energy ΔF, activation volume ΔV and critical stress σ_c) governing the time dependent plasticity were obtained by fitting the macroscopic stress relaxation cycles to the slip law. Commercially pure Ti has the lowest strength but the highest strain rate sensitivity, as a result, the dwell fatigue effect is the strongest among the three alloy systems. Ti-6Al-4V has both moderate strength and strain rate sensitivity, the dwell fatigue effect was not significantly influenced by the fraction of β phase in Ti64. The Ti-6Al-2Sn-4Zr-xMo system had the highest strength but the lowest strain rate sensitivity, dwell fatigue effect was highly suppressed in these alloys. Oxygen has an excellent strengthening effect but does enhance the dwell fatigue effect. Mo evidently offers both a strengthening effect and significant resistant to dwell fatigue. At dwell fatigue stress conditions (when critical stress is just exceeded), both the contribution of the key parameters to strain rate and strain rate sensitivity sharply decreased in all six alloys when temperature is above 145°C. As a result, plastic strain accumulation at 250°C is at a very low level, dwell fatigue is suppressed at high temperature.

5

Effect of crystallographic orientation on cold dwell fatigue

Contents

5.1 Introduction 61
5.2 Material and experiment procedures 62
5.2.1 Material 62
5.2.2 Stress relaxation tests 63
5.2.3 Diffraction pattern analysis 65
5.2.4 Crystal plasticity finite element model 67
5.3 Results and discussion 69
5.3.1 Macroscopic stress relaxation 69
5.3.2 Development of lattice strain during loading phase . . . 70
5.3.3 Modelling results 74
5.3.4 Strain rate sensitivity 78
5.3.5 GND densities 83
5.4 Summary 84

5.1 Introduction

The cold dwell effect is controlled by load shedding between 'soft' and 'hard' grain pairs [3, 6], where the 'soft' grain has its crystallographic c-axis approximately perpendicular to the loading direction while a 'hard' grain has its c-axis approximately parallel to the loading direction. Characteristic of the HCP α-

titanium crystal structure, plastic slip systems in the 'soft' grain will be activated but within the 'hard' grain no easy slip systems exist and the elastic stiffness is at its highest [7, 8]. During a dwell period, localised time dependent plasticity in the 'soft' grain leads to load shedding as dislocations accumulate and glide. Due to grain compatibility, the 'soft' grain may impose an increased stress in a neighbouring 'hard' grain [9, 10]. With multiple loading cycles, the stress in the 'hard' grain incrementally increases until it fractures. Fractography has revealed facet formation associated with these 'hard' grains, where the facets themselves were typically parallel to the basal plane [2, 11]. Such mechanism, however, has not been satisfactorily confirmed with experimental observations.

To make progress beyond present understanding of dwell fatigue behaviour, it is necessary to understand the different deformation behaviour in grains with different crystal orientations (i.e. 'hard' and 'soft' grain orientations) and especially the plastic deformation during the stress dwell period. To achieve this, it is important to quantify the plasticity processes as a function of time. Specifically, this must describe the dislocation processes on prismatic and basal slip systems with respect to their critical resolved shear stresses.

In this chapter, time dependent plasticity (stress relaxation) behaviour of commercially pure titanium (CP-Ti) was observed by synchrotron X-ray diffraction. Measured lattice strains from multiple lattice families were compared with and used to calibrate simulations lattice strains from crystal plasticity finite element (CPFE) model using methods established in prior work [136]. The objective of this chapter was to quantify the key parameters controlling the time dependent plasticity of CP-Ti and understand the effect of crystal orientation on cold dwell fatigue.

5.2 Material and experiment procedures

5.2.1 Material

The raw material used in this work was CP-Ti grade 4 rod provided by Timet with a composition indicated in Table 4.1 Microstructural analysis was firstly conducted. Samples were cut from the rod then ground and polished down to a colloidal silica

finish. Electron backscatter diffraction (EBSD) maps were obtained from the as received material. Figure 5.1(a) shows an example map of the microstructure, which has a mean average grain size of 17 μm. The material texture was obtained from a larger area containing over 3500 grains, shown by the pole figures in Figure 5.1(b), where there is a preference for the *c*-axes to be perpendicular to the macroscopic rod axis, which is quite common in hot-rolled titanium alloys [126]. In order to ensure the easy slip system (prismatic) was activated during the stress relaxation experiment, the Electro-Thermal-Mechanical Tester (ETMT) samples were cut with the load axis along the axial direction of the rod, X0 direction in these pole figures. Due to the fact that the majority of the grains have their basal plane {0002} aligned approximately perpendicular to the tensile axis (X0 in the pole figures), the basal Schmid factor of these grains became very small, therefore prismatic slip will be the dominant slip system in this experiment.

5.2.2 Stress relaxation tests

The ETMT was used to subject the Ti samples to pre-determined load-hold cycles. Prior to in-situ testing, target loads were obtained from trial tests. The target loads corresponded to a stroke displacement at which the yield stress had just been exceeded. For in-situ testing, the sample was loaded at a constant load rate of 7.2 Ns^{-1} until the macroscopic yield point had been exceeded by a small plastic strain. This corresponded to a strain rate of 3.38×10^{-5} s^{-1} during the initial elastic part of the loading phase. Once the target load had been reached, the sample displacement (and thus the total strain) was then held constant for a period of 5 minutes. After the 5 minutes hold, the load was incremented to a level a little below the peak load used at the start of the previous stress relaxation cycle. This load increment procedure follows that of Wang *et al.* [137] and corresponds to an elastic deformation of the sample, allowing the stress relaxation at two stress levels to be compared with a negligible change in dislocation substructure. The sample was again held at a constant displacement for a further period of stress relaxation. This load-then-hold cycle was repeated for a total of 5 stress relaxation periods with diffraction patterns

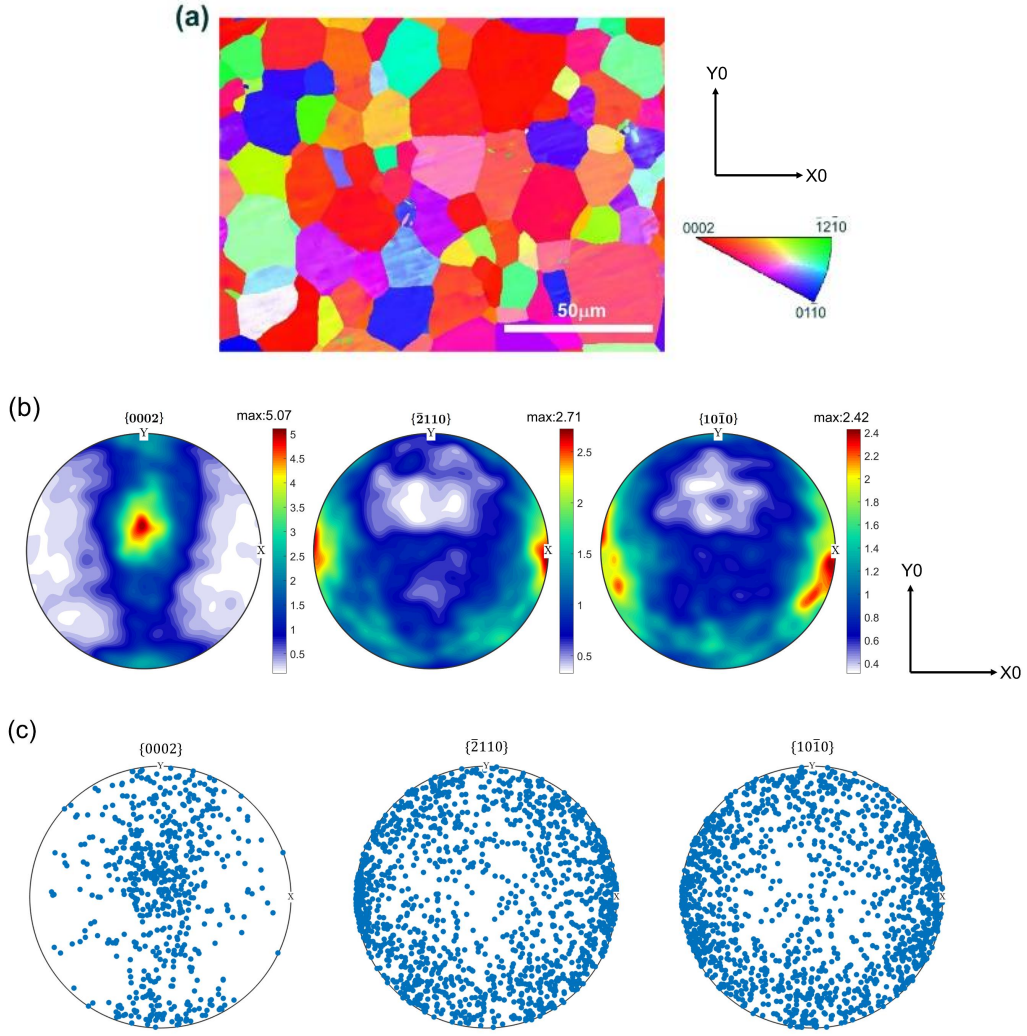


Figure 5.1: (a) Inverse pole figure (IPF map in radial direction of the rod) showing the grain morphology and grain size; (b) Pole figures of the raw material (X0 along the axial direction, which was the loading direction and Y0 along the tangential direction of the rod) with a 10° width used for contours plotting calculation; (c) Scatter pole figure plots of the simulated orientation used in the polycrystal finite element model.

collected throughout (shown in Figure 5.2). During these relaxation periods, the stress level swept through a range of values from 450 MPa to 535 MPa, and as the plastic strains remain relatively small, changes in the mobile dislocation density ρ should also be small. The elastic reloads were introduced to verify this.

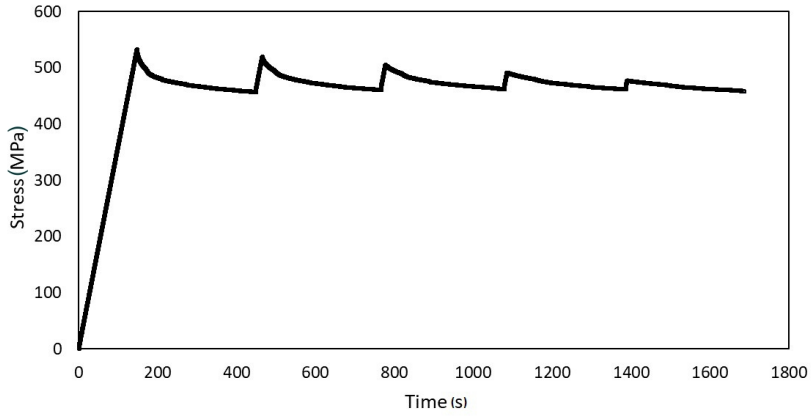


Figure 5.2: Loading cycles of a stress relaxation test for the CP-Ti grade 4 at room temperature.

5.2.3 Diffraction pattern analysis

The Data Analysis WorkbeNch (DAWN) [138] was used for diffraction pattern data reduction. The 2D diffraction rings were fitted with ellipses; value of the major and minor radii were determined, where the former was near parallel to the horizontal and the latter was near parallel to the vertical axis. The radius and thus the scattering vector, q, at any azimuth angle around a diffraction ring could then be found from the size and alignment of the major and minor axes. Ellipse fitting was applied to the first 21 rings with ascending ring radius, as shown in Figure 5.3 (with loading along the vertical axis). For further details of the data reduction process, the reader is referred Filik *et al.* [139]. The scattering vectors were used to obtain the temporal lattice spacings by $d^{hkil} = 2\pi/q$. As the sample was deformed, lattice strain, ε^{hkil}, was subsequently calculated using $\varepsilon^{hkil} = (d^{hkil} - d_0^{hkil})/d_0^{hkil}$, where d_0^{hkil} is the initial lattice spacing for plane $hkil$.

To find a consistent set of stress-free lattice parameters, a and c, the following procedure was used. For each diffraction ring, an initial d_i^{hkil} value was obtained by performing a linear fit to the d spacing vs. time plot (as shown in Figure 5.4(a)) during the initial elastic loading, then extrapolating the fitted linear function to time zero. These temporal d_i^{hkil} values from different diffraction planes were then

fitted to the crystal geometry equation for HCP:

$$\frac{1}{d^{hkil}} = \frac{3(h^2 + hk + k^2)}{4a^2} + \frac{l^2}{c^2} \tag{5.1}$$

where a and c are the lattice parameters of HCP crystal, h, k and l are the Miller Indices of a crystal plane. Therefore, the stress-free lattice parameters of this CP-Ti sample were taken to be the best fit values over the 21 diffraction rings, which were $a = 2.9512 \pm 0.002$ Å and $c = 4.6861 \pm 0.004$ Å (see Figure 5.4(b)). The stress-free lattice spacing, d_0^{hkil}, for each plane family was then obtained using these values of a and c and the formula above.

The large intrinsic line broadening width from the geometry we employed on the I12 instrument is too large to separate the sample contribution to broadening [136]. This makes determination of the peak broadening due to sample deformation prohibitive.

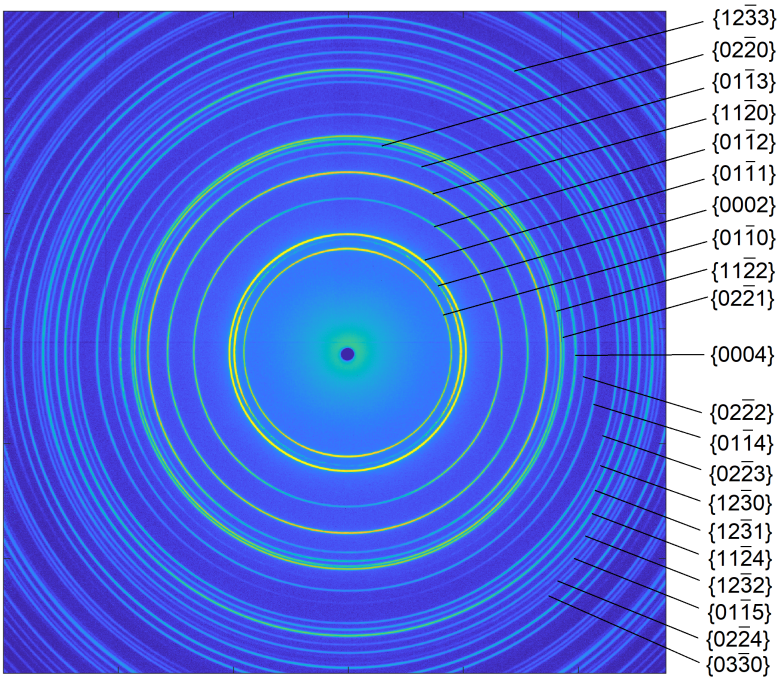


Figure 5.3: Debye Scherrer diffraction patterns of CP-Ti at room temperature (the vertical direction of the diffraction patterns was the axial direction and the horizontal direction is the transverse direction of the CP-Ti rod).

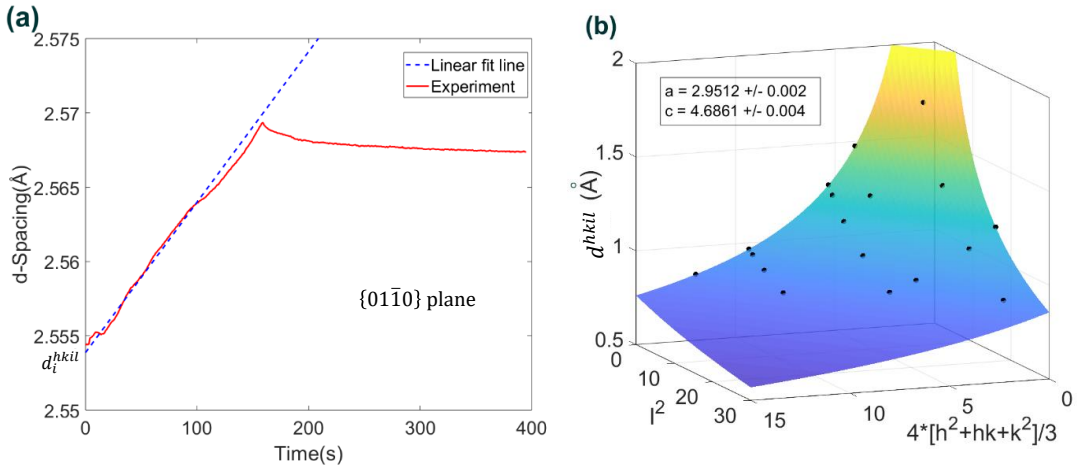


Figure 5.4: (a) Linear fit of d spacings during elastic loading to determine initial d_i^{hkil} for each plane family (the $\{01\bar{1}0\}$ plane is shown here as example); (b) Non-linear regression fit of the crystal geometry equation (Equation 5.1) for a HCP crystal.

5.2.4 Crystal plasticity finite element model

The CP-Ti material was modelled as a single phase, α, with a HCP crystal structure. The elastic parameters used are indicated in Table 3.2. Dislocation slip occurs predominantly with $\overrightarrow{a}$ type Burgers vector on the basal and prismatic slip planes in Ti alloys [46, 59, 140], while the CRSS required to activate $\overrightarrow{c} + \overrightarrow{a}$ 1^{st} & 2^{nd} order pyramidal slip can be about three time the value of basal slip [3, 8]. Since in this experiment, the sample was loaded just beyond the yield point, the $\overrightarrow{c} + \overrightarrow{a}$ slip was relatively difficult to activate, hence, little activity of pyramidal slip was expected.

A polycrystal finite mesh containing 512 grains with 64 quadratic elements (C3D20R) per grain with 8 integration points per element was generated in Abaqus as shown in Figure 5.5. For simplicity the model adopted a simplified morphology approximating the grains as a regular cubic array [136, 141]. The discrete orientations, as measured by EBSD, were selected at random to assign orientations grain by grain, therefore the overall texture in the model was approximately the same as the real sample (as shown in Figure 5.1(c)). The boundary conditions

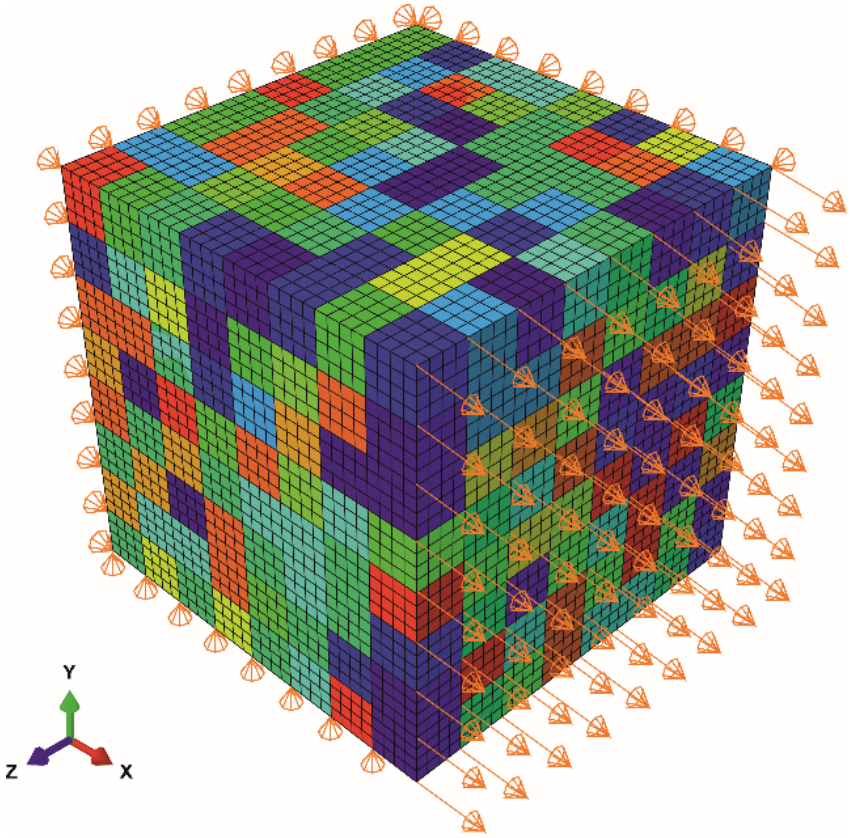


Figure 5.5: Finite element mesh of the RVE used with the CPFE model. The colours represent the grain orientation shown in Figure 5.1, and arrows indicate the uniaxial boundary conditions.

are illustrated in Figure 5.5, a uniaxial displacement of 1.4 μm was applied to the right surface over 150 s (the total length of one edge of the model was 240 μm, therefore the displacement corresponded to a strain rate of 3.8×10^{-5} s^{-1}), and then the displacement was held fixed along the load axis for 300 s while the left, bottom and back surfaces were constrained in the X, Y and Z directions respectively.

The simulated elastic strains, were compared with elastic lattice strains obtained from diffraction measurements. The Green-Lagrange elastic strain tensor in the sample frame, given by $\boldsymbol{E_e}$, is rotated into the lattice orientation frame through the rotation matrix $\boldsymbol{R}$ to give the lattice strain $\boldsymbol{E^0}$ as follows [141]:

$$\boldsymbol{E^0} = \boldsymbol{R^T E_e R} = \frac{1}{2}\boldsymbol{R^T}(\boldsymbol{F_e^T F_e} - \boldsymbol{I})\boldsymbol{R} \tag{5.2}$$

As illustrated in Figure 5.6, diffraction from the $\{01\bar{1}0\}$ planes, for example, with diffraction observed along the vertical axis and transverse axis have diffrac-

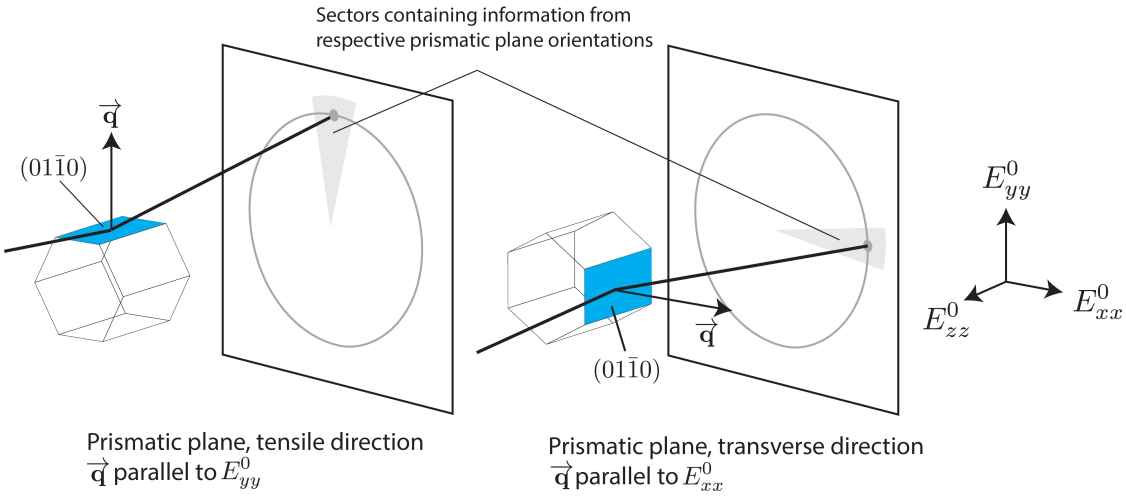


Figure 5.6: Assessed prismatic plane diffraction orientations.

tion vectors, q, approximately parallel (with 10° tolerance) to the E^0_{yy} and E^0_{xx} components respectively. For grains that satisfy this condition, the E^0_{yy} and E^0_{xx} components of the $\boldsymbol{E^0}$ matrix were averaged from all the elements within these grains and directly compared with the experimental lattice strains.

5.3 Results and discussion

5.3.1 Macroscopic stress relaxation

The macroscopic stress relaxation response, calculated from the measured force from the ETMT load cell is shown in Figure 5.7. It was firstly fitted using the same form of constitutive law as Equation 3.1, but instead linking the macroscopic plastic normal strain rate to the macroscopic normal stress. The detail of this fitting method was discussed in Section 4.4.

Table 5.1: Fitted parameters obtained from the best-modelled relaxation curves.

	Parameters
σ_c^{macro}	449.8 MPa
ΔF^{macro}	10.17×10^{-20} J
ΔF^{macro}	0.63 eV
ΔV^{macro}	9.93 b^3
Fitting error	0.61%

This numerically fitted parameters are broadly similar to those used by other

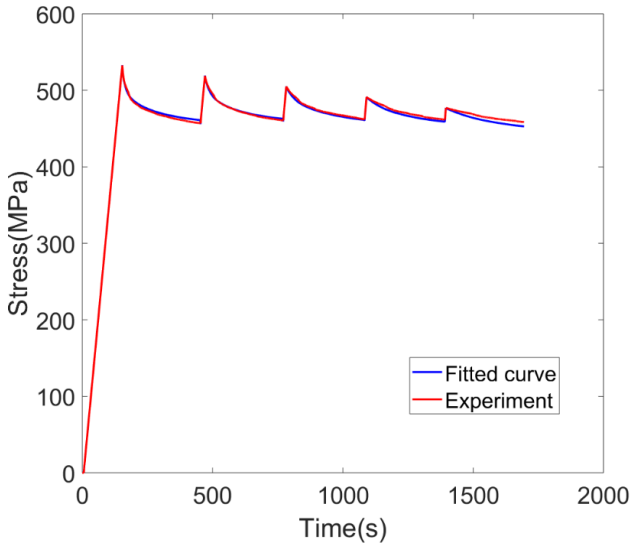


Figure 5.7: Macroscopic stress relaxation curve fitting.

workers in CPFE modelling, where Dunne *et al.* [56] stated that ΔF=0.73 eV for a Ti-6Al alloy, Zheng *et al.* [1] used ΔF=0.6 eV and ΔF=0.66 eV for Ti-6242 and Ti-6246 alloys respectively while ΔV=0.5 b^3 for both alloys and Zhang *et al.* [116] demonstrated that ΔV is different for α and β phases: ΔV_α=11.97 b^3 and ΔV_β=0.0021 b^3 (the ΔV_β was too small and just a fitted value which does not have physical meanings), in a Ti-6242 alloy, while all of these studies used the same prefactors for Ti alloys as this work (ρ=5 μm^{-2}, b=0.295 nm and ν=10^{11} Hz). This indicates that this numerically fitting macroscopic stress relaxation curve method is able to give a corroborating prediction of these key parameters of the alloy tested. Therefore, these values stated in Table 5.1 were then used as the initial values in the crystal plasticity simulations. The ability to find a good fit that is consistent across the five repeated periods of stress relaxation indicates that strains are sufficiently low that the evolution of dislocation microstructure through the test can be neglected.

5.3.2 Development of lattice strain during loading phase

Deformation of α-Ti is highly anisotropic both elastically and plastically, resulting in deformation properties that vary significantly depending on the crystallographic orientation of a grain. In order to quantify the crystallographic orientation, the

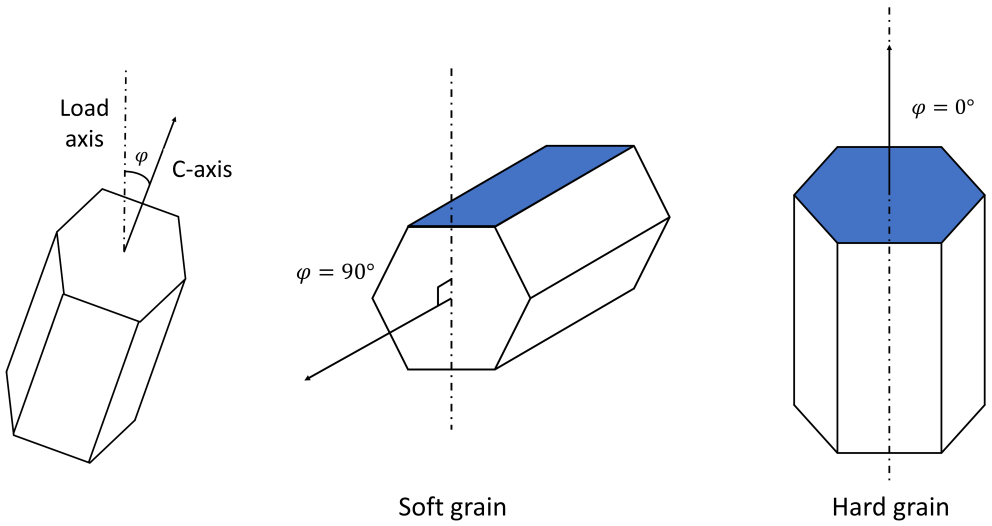


Figure 5.8: Schematic of HCP crystals that illustrates the c-axis declination angle, ϕ. Example grains in 'soft' and 'hard' orientations are shown.

concept of a c-axis declination angle is introduced (as shown in Figure 5.8), which is the angle, ϕ, between the load axis and the c-axis of the α-Ti HCP crystal. When a grain with prismatic $\{01\bar{1}0\}$ planes satisfy the diffraction condition with its diffraction vector, q, approximately parallel to the load axis, the c-axis declination angle is 90°. Grains in this orientation are referred to as 'soft'. When a grain with its basal $\{0002\}$ planes satisfy the diffraction condition, again with the diffraction vector, q, approximately parallel to the load axis. Its c-axis declination angle is 0° and the grain is considered to be 'hard' [3]. Other than these two special crystal orientations, the c-axis declination angle can be calculated from the angle between the c-axis and the normal of the plane satisfying the diffraction condition along the loading direction. As the c-axis declination angle varies between 0° to 90°, the grain orientation changes gradually from 'hard' to 'soft'.

The development of axial lattice strains is shown in Figure 5.9(a) and 5.9(b) for $\{01\bar{1}0\}$ and $\{12\bar{3}0\}$ planes as examples, measured from the vertical axis (loading direction) of the diffraction patterns. Linear fitting was applied to the initial stage (elastic part) of the macroscopic stress vs. lattice strain plots. The gradient of the fitted function was used to measure the stiffness of each corresponding orientation.

The different plane family stiffnesses against their c-axis declination angle are shown in Figure 5.9(c). It is shown that as the declination angle increases, the stiffness decreases (from 135 GPa to 96 GPa). This neglected the two data points at ϕ=0°, which were deemed unreliable as they were obtained from data with high noise. This trend agrees with the elastic modulus variation with declination angle for titanium, where the elastic modulus along the c-axis of the α-titanium unit cell is about 1.4 times higher the value of that along the a-axis (see Table 3.2) [56, 142, 16]. Applying the same method to the transverse lattice strain, the transverse stiffness was calculated (Figure 5.9(d)). Showing a reversed behaviour to the axial stiffness, the transverse stiffness increases with the increasing declination angle. By combining the axial and transverse stiffness, the Poisson's ratio was determined (Figure 5.9(e)), which increases from 0.2 to 0.46 as the declination angle increases from 0° to 90°, this agrees well with the literature values [142, 143].

By extending the linear fitted lines backward in Figure 5.9(a) and 5.9(b), the intersections of these lines with x and y axes were calculated to estimate the residual lattice strain and stress. As shown in Figure 5.9(f) and 5.9(g), the residual strain and stress are also anisotropic, due to the combined action of thermal and mechanical treatments during processing [7, 8, 144].

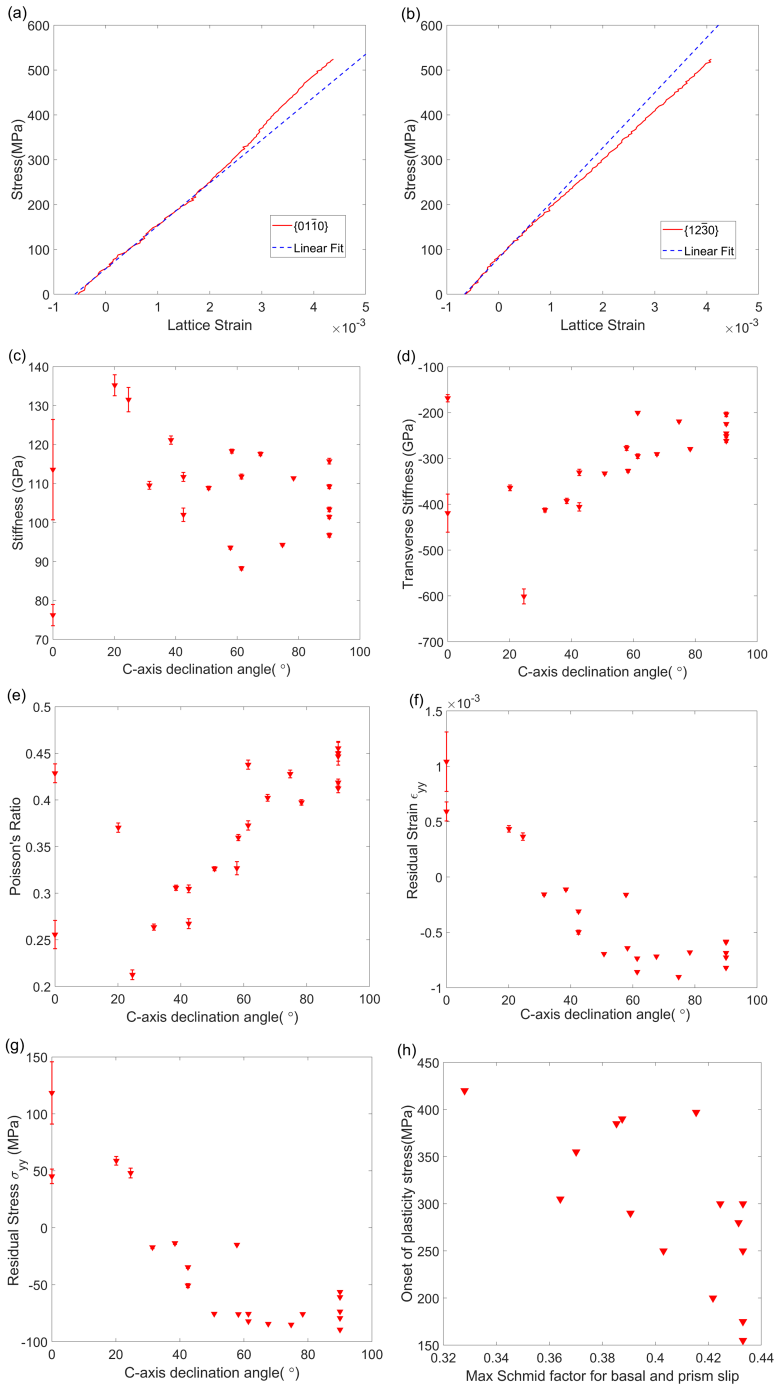


Figure 5.9: (a) Development of the elastic lattice strain in the loading direction for the $\{01\bar{1}0\}$ plane; (b) Development of the elastic lattice strain in loading direction of the $\{12\bar{3}0\}$ plane; (c) Axial stiffness vs. *c*-axis declination angle; (d) Transverse stiffness vs. *c*-axis declination angle; (e) Poisson's ratio vs. *c*-axis declination angle; (f) Axial residual strain vs. *c*-axis declination angle; (g) Axial residual stress vs. *c*-axis declination angle; (h) Onset of plasticity stress vs. maximum Schmid factor for basal and prism slip.

Gradient changes were observed during the loading process (Figure 5.9(a) and 5.9(b)), which appear at ≈200 MPa for the $\{01\bar{1}0\}$ lattice planes and ≈155 MPa for the $\{12\bar{3}0\}$ lattice planes. Different lattice planes start to deviate from a linear macroscopic stress-lattice strain variation, indicating plastic deformation. For most of the plane families, grains have a lower increment in lattice strain (elastic strain) with respect to macroscopic stress (loading curves deviate upwards, see Figure 5.9(a)), due to the activation of plastic deformation. As a result some plane families, where plastic deformation was not activated, have the opposite response (Figure 5.9(b)) so that the whole system is in static equilibrium. The initiation of plastic deformation is related to the activation of slip systems. At the stress level for this experiment, the prismatic and basal slip systems are more important than the hard pyramidal slip system (see Section 5.2.4 and Appendix A.3), therefore the maximum Schmid factor among prism and basal slip systems were calculated for the 21 plane families and correlated to this onset of plasticity stress. Figure 5.9(h) shows the onset of plasticity stresses of 16 plane families whose gradient change can clearly be observed against their maximum Schmid factor for prism and basal slip. It is found that grains with a higher maximum Schmid factor tends to activate plastic deformation at a lower macroscopic stress.

5.3.3 Modelling results

The lattice strains developed during the first 5-minute whilst the sample displacement was held were used to calibrate the model. Simulated lattice strains were extracted to fit with three important reflections; these comprised the prismatic plane $\{01\bar{1}0\}$, the first order pyramidal plane $\{01\bar{1}1\}$ and the second order pyramidal plane $\{11\bar{2}2\}$. The parameters related to dislocation motion in the slip law (Equation 3.1) were adjusted until the simulated axial lattice strains fitted well with the experimental axial lattice strain of these three reflections. The basal plane $\{0002\}$ was not available in the simulations due to the texture of the sample, giving too few grains diffracting along the loading axis or the axial direction of the CP-Ti rod (recall Figure 5.1(b) and 5.1(c)). Residual strain was not included in the simulations;

details of justification of this assumption can be found in Appendix A.1. It was assumed that little $\overrightarrow{c}+\overrightarrow{a}$ pyramidal slip will be activated in this small strain deformation, therefore parameters ΔV and ΔF for pyramidal slip were fixed to the parameters calculated from the macroscopic stress relaxation curve in Section 5.3.1. The CRSS of pyramidal slip was fixed to be 3 times the value of CRSS of basal slip [3, 8] (justification of these assumption can be found in Appendix A.3). Hence, there are six parameters (ΔV, ΔF and τ_c for prismatic and basal slip systems) to calibrate in order to obtain an optimal fit.

Parametric studies of the effects of fitting parameters on the lattice strain relaxation curves generated by the simulation showed that the outputs are not so sensitive to ΔV changes compared to the other fitting parameters (details can be found in Appendix A.3). This applies for the relatively low strain rates seen in the tests performed, but of course may not hold at higher strain rates where ΔV might be expected to have a more significant impact on behaviour. Therefore, the value of ΔV was fixed to the value obtained from macroscopic stress relaxation for both basal and prismatic slip systems. The lattice strain of the $\{01\bar{1}0\}$ planes is thought to be dominated by prismatic slip as the basal plane for the grain family is nearly parallel to the loading direction, and so the basal slip Schmid factor is approximately zero. Fitting the model output to the $\{01\bar{1}0\}$ lattice strain variation first allows an initial focus on only two unknown parameters i.e. ΔF and τ_c for prism slip. Changing ΔF will result in a clear shape change of the strain relaxation curve (i.e. the amount of relaxation within the hold period) while τ_c mainly affects the lattice strain level (an increase in τ_c shifts the whole relaxation curve upwards and vice versa). The $\{01\bar{1}0\}$ lattice strain result was fitted first to confirm the parameters for prismatic slip. This was followed by consideration of the $\{01\bar{1}1\}$ and $\{11\bar{2}2\}$ lattice strains, which were affected by parameters describing both basal and prismatic slip. Finally, the simulated macroscopic stress relaxation curve was also compared with the experiment curve.

Figure 5.10(a) shows the best-fit lattice strain relaxation curves along the loading direction for the $\{01\bar{1}0\}$, $\{01\bar{1}1\}$ and $\{11\bar{2}2\}$ planes. The transverse lattice strains

(not used in the fitting) are compared between the experiment and simulation in Figure 5.10(b). The macroscopic stress relaxation also shows a good fit with the experimental results (Figure 5.10(c)). It is noted that whilst the prefactor ρ (mobile dislocation density) was fixed through all five relaxation cycles, the simulation results show good agreement with the experimental results. This verified that the change in mobile dislocation density remains relatively small (recall Section 5.2.2).

The corresponding slip law parameters for these best fits are summarised in Table 5.2. The CRSS ratio between basal and prismatic slip is a particularly important factor for the deformation of HCP metals. For both basal and prismatic slip to be activated during deformation, a ratio should be close to 1.0 [145], which is also beneficial for ductility and to reduce the effect of texture. The ratios have been well studied and values from the literature are listed in Table 5.3 in comparison to our result.

The values of both τ_c^{basal} and τ_c^{prism} determined in this work are higher than the values in Table 5.3 (except the one tested on a single crystal). This is because materials used in the present work is CP-Ti grade 4, which has a much higher oxygen content compared to others. Oxygen, as an interstitial atom, and has very pronounced strengthening effect in Ti alloys even at low concentration [146, 34, 35]. Besides this, researchers have also reported that the strengthening effect of oxygen is more pronounced on the softer prism slip systems than basal slip systems [147, 148]. This explains why $\tau_c^{basal}/\tau_c^{prism}$ in this work is lower than examples reported in the literature for lower oxygen concentrations. Unlike prior modelling studies, the values obtained for the activation energy ΔF was found to be different for prismatic and basal slip systems, where ΔF^{basal} is about 17% larger than ΔF^{prism}. This indicates that basal slip activation is more difficult than prismatic slip due to two factors: basal slip has a higher room temperature critical resolved shear stress and a higher energy barrier to overcome.

Table 5.2: Key parameters associated with dislocation motion for prismatic and basal slip.

	τ_c(MPa)	$\Delta F(\times 10^{20}$ J)	ΔF(eV)	$\Delta V(b^3)$
Prismatic slip	154	9.0	0.56	9.93
Basal slip	252	10.5	0.65	9.93
Pyramidal slip	756	10.17	0.63	9.93

Table 5.3: CRSS for basal and prismatic slips values for commercially pure Ti. The nominal oxygen content and average grain sizes from each study is listed.

τ_c^{prism}(MPa)	τ_c^{basal}(MPa)	$\tau_c^{basal}/\tau_c^{prism}$	O(wt%)	Grain size(μm)	Ref.
120	182	1.5	0.16	40	[149]
30	150	5.0	<0.01	30	[150]
60	120	2.0	0.17	80	[151, 152]
68	175	2.6	0.12	50	[153]
90	180	2.0	0.11	9	[154]
181	209	1.2	0.07	Single crystal	[155]
96±18	127±33	1.7-2.1	0.17	100	[145]
154	252	1.63	0.32	17	This work

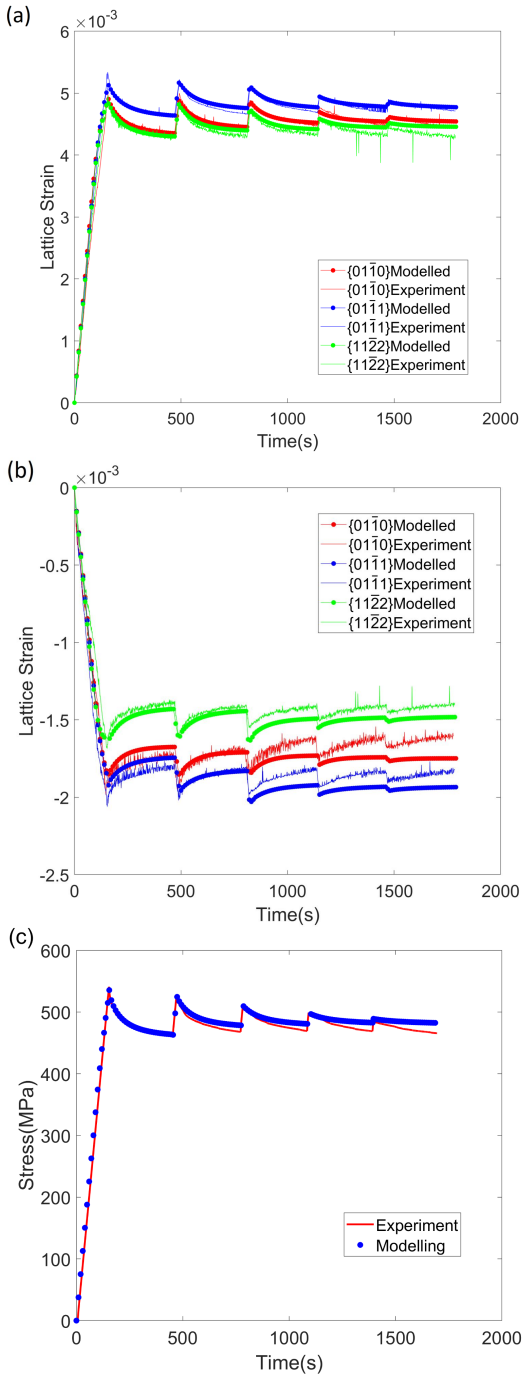


Figure 5.10: (a) Lattice strain evolution along the loading direction; (b) lattice strain evolution along the transverse direction and (c) macroscopic stress relaxation curves.

5.3.4 Strain rate sensitivity

This study was motivated by a need to understand the technologically important cold dwell fatigue, which effects some but not all Ti alloys and is thought to be

caused by time dependent plastic deformation on the softer slip systems. Significant stress relaxation at room temperature (≈0.15 of the melting point) was clearly demonstrated in the commercially pure Ti studied here and captured in lattice strain drops measured via synchrotron XRD during macroscopic strain hold periods. The extent of relaxation varies between different grain families as indicated by the increment of plastic strain inferred from lattice strain variations over the first 5 min hold period shown in Figure 5.11(d). Deconvolving this grain orientation effect on the relaxation behaviour requires CPFE simulations which shows that the activation energy is higher for basal compared to prism slip. This is in addition to the expected higher CRSS for basal compared to prism slip. These combine to give a greater strain rate sensitivity for the softer prism slip system.

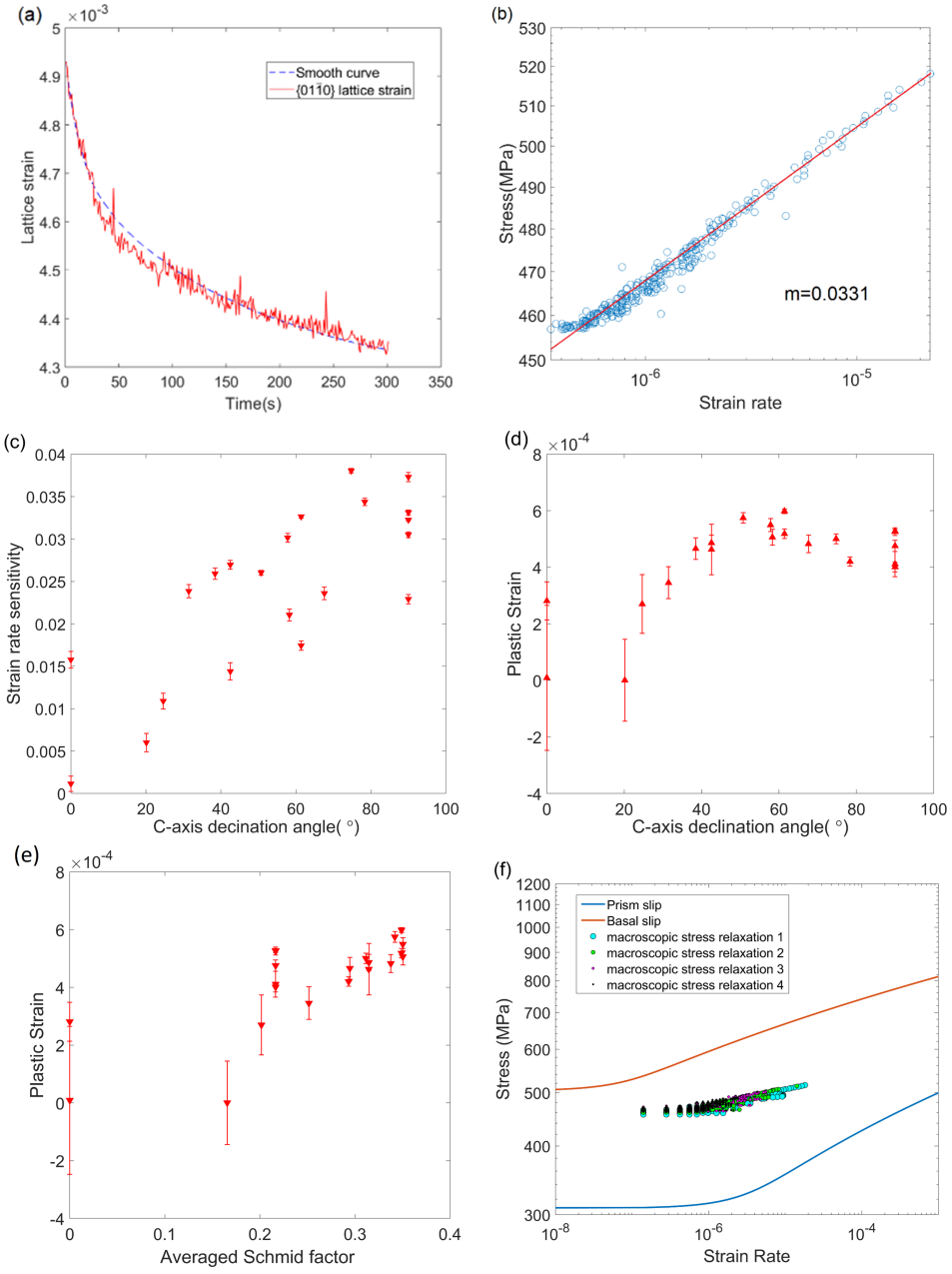


Figure 5.11: (a) Smoothing fit the first strain relaxation curve of the $\{01\bar{1}0\}$ plane; (b) Determination of strain rate sensitivity of $\{01\bar{1}0\}$ plane; (c) Strain rate sensitivity vs c-axis declination angle; (d) Plastic strain increment during the first macroscopic strain hold period for different grain families (diffraction rings) plotted as a function of c-axis declination angle; (e) Plastic strain increment during first macroscopic strain hold period for different grain families (diffraction rings) plotted as a function of averaged Schmid factor of prism and basal slip. (f) Strain rate-stress variation given by the slip laws for prism and basal slip as well as macroscopic response measured by the ETMT during the first 4 periods of stress relaxation.

Results in the literature are often expressed in terms of a strain rate sensitivity parameter, m, which corresponds to the gradient of a plot of log (σ) against log ($\dot{\varepsilon}$) and would imply the strain rate exponent in a simple power law expression for stress. Here, the strain rate sensitivity of different grain families was assessed by analysing the lattice strain relaxation data for individual reflections (e.g. Figure 5.11(a)). The noise in the experimental lattice strain results increases the difficulty in calculating strain rate. The lattice strain relaxation curves were smoothed using the same method as fitting the macroscopic stress data relaxation (discussed in Section 4.4). The gradient of the smoothed and fitted lattice strain relaxation curve at each second (out of total 300 s) were calculated to represent the lattice strain rate at each second. Lattice strain rates, which are negative, are assumed to be matched by positive plastic creep strain rates so that the overall strain in that grain family is held constant. The stresses for that grain family are obtained from the product of the lattice strain value and the corresponding stiffness (Figure 5.9(c)). This allows creep rates and corresponding stresses to be assembled in a log-log plot (Figure 5.11(b)), the gradient of which gives the effective SRS parameter, m, for that grain family. The variation of grain family effective SRS values with c-axis declination angle is shown in Figure 5.11(c), and implies that softer grains have higher effective SRS than those of harder grains. However, assuming that the external boundary condition of a fixed total strain can be imposed on individual grain families is questionable, as for the softer grains, larger plastic strains may be achieved if accommodated by smaller plastic strains in a harder neighbouring grain environment. The plastic strain rate for the softer grain families is thus likely to be underestimated in this analysis, and conversely overestimated for the harder grains. This coupling to other grains in the neighbourhood prevents sound knowledge of the boundary conditions and is what drives the need to use a CPFE simulation approach in which spatial variation in stress and strain evolution is accounted for.

An increment of plastic creep strain during the first macroscopic strain hold period was obtained by subtracting the lattice strain at the end of the relaxation period from the lattice strain at the beginning of the relaxation period. As shown

in Figure 5.11(d), the increment of plastic creep strain was found to be larger in softer grains than that of harder grains. The same trend was found in the plot of plastic strain increments for 21 reflections against their averaged Schmid factor for prism and basal slips, as shown in Figure 5.11(e). Combining with the variation of SRS vs. *c*-axis declination angle, the relationship of the SRS and the accumulation of plastic strain during creep can be correlated. A higher SRS can be seen to result in greater plastic strain increments during cold creep of Ti.

Figure 5.11(f) shows plots of stress vs. strain rate variation given by the slip laws for prism and basal slip. Shear stress was adjusted to normal stress by dividing by a Schmid factor of 0.5, and from shear strain rate to normal strain rate by multiplying by the Schmid factor (again taken to be 0.5). Also shown on this plot is the sample averaged response measured by the ETMT during the first 4 periods of stress relaxation, which fall between those for the basal and prism slip laws. This plot is important in showing that strain rate sensitivity can be expected to vary significantly with the strain rate range over which it is determined. In the relatively low strain rate range directly covered by the experimental data (10^{-7} to 10^{-5}) the slip laws can be approximated by SRS values of 0.052 for prism, and 0.040 for basal slip. For comparison with the work by Jun *et al.* [67] who reported SRS values of 0.07 for prism and 0.03 for basal slip for micro-pillars cut from single α phase crystals in Ti6242 measured over the strain rate domain 10^{-4} to 10^{-2}. Extrapolating to this higher range of strain rates for the slip laws determined here for grade 4 CP-Ti gives SRS values of 0.064 for prism and 0.039 for basal slip. These values for CP-Ti and Ti6242 are in remarkable agreement. It is intriguing that such similar results are found across the relatively simple and soft commercially pure Ti, and the much harder alloy with significant substitutional alloying but lower interstitial content.

The analysis process suggested very similar activation volumes for the two slip systems so that in the very high stress, very high strain rate regime the SRS of prism and basal slip should tend to the same value. The activation volume is too small ($\approx 10b^3$) to suggest pinning by dislocation-dislocation interactions (at the assumed dislocation density of 5×10^{12} m^{-2} the spacing would suggest an activation volume

$\approx 1500b^3$), but significantly larger than the $\approx 1b^3$ expected for an atomistic diffusion process. However, in the BCC metals activation volumes of the size seen here have been ascribed to kink pair nucleation mechanisms which limit the motion of the slower screw dislocations [132]. A similar physical basis seems reasonable here.

These differences in strain rate sensitivity will obviously impact on the details of how load is transferred from 'soft' grains onto 'hard' grains as whether slip is on a prismatic or basal slip system effects the rate and extent of the stress accumulation in the 'hard' grain. The specifics of the so-called rogue grain pairs leading to the most extreme stress enhancement should perhaps be revisited in reassessing how texture and nearest neighbour micro-texture affect the probabilities of nucleating a crack in dwell fatigue loading.

5.3.5 GND densities

As shown in Figure 5.12, the change in the GND density during the first relaxation cycle were calculated from the model. For grains that accumulate a greater GND density during relaxation are generally in a 'soft' orientation (high c-axis declination angle) and have a higher averaged prism/basal Schmid factor. However, the scatter in the data is large and a clear trend is difficult to identify, implying that at grain-grain level, the plastic deformation not only depends on the orientation of a grain, but more importantly, the contribution of a neighbouring effect cannot be ignored. This observation corroborates well with other studies that show deformation in α-titanium is strongly affected by neighbouring grain orientations [105, 156]. In the context of cold creep, load shedding was studied by assessing different combinations of the neighbouring grain orientations using the crystal plasticity model, a worst case scenario does exist in which a grain that is well oriented for slip has an active slip system oriented at about 30° to the direction of the adjacent 'hard' grain c-axis [3]. This effect could be further understood with a suitable experiment dedicated to directly measuring GND densities during cold creep. Such data will direct modelling and aid calibration of crystal plasticity models. It should also be noted that these GND density changes are at most less than 20% of the initial mobile dislocation

density value (which ρ=5 μm^{-2}=5×10^{12} m^{-2}), and more typically less than 10%. This is in accord with the finding that a good fit could be established with the dislocation density held constant in the model, and the lack of any appreciable changes in the diffraction peak widths.

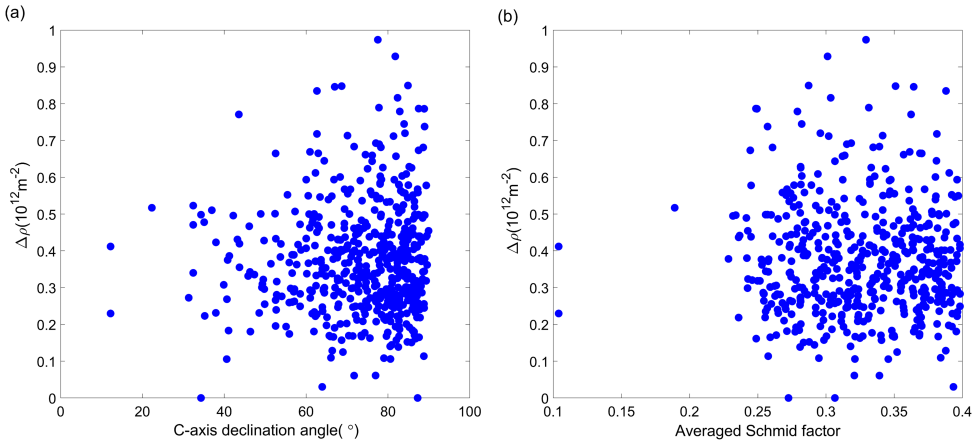


Figure 5.12: Simulated GND density increment during the first relaxation cycle for all the grains in the model vs. (a) *c*-axis declination angle of each grain and (b) averaged prism/basal Schmid factor of each grain.

5.4 Summary

In this Chapter, time dependent plasticity process were studied and quantified in grains with different orientations, results revealed the plastic deformation process during stress relaxation and the effect of crystal orientation on cold dwell fatigue was understood. An in-situ X-ray diffraction method was used to measure the lattice strain evolution in a commercially pure Ti grade 4 sample. The sample was deformed in tension to a small plastic strain, followed by a five-minute strain hold to allow stress relaxation to occur. The results were interpreted using a crystal plasticity finite element model. The study has the following key conclusions:

1. During loading, observation of individual lattice strains was used to identify the behaviour of different basal and prismatic slip systems. Combining with the crystal plasticity finite element analysis, key parameters in the slip rule for each slip system were isolated and determined.

2. Crystal plasticity modelling of lattice strain results were adjusted to match the experiment axial lattice strain results of $\{01\bar{1}0\}$, $\{01\bar{1}1\}$ and $\{11\bar{2}2\}$ plane families. The following parameters for basal and prismatic slip were found: τ_c^{basal}=252 MPa, τ_c^{prism}=154 MPa, ΔF^{basal}=10.5×10^{-20} J (0.67 eV) andΔF^{basal}=9.0×10^{-20} J (0.56 eV).

3. The slip activation energy, ΔF, and critical resolved shear stress, τ_c, were found to be higher for basal slip over prismatic slip, indicating basal slip is more difficult to activate than prismatic slip. Coupled to this is a higher strain rate sensitivity for prism slip at the relatively low strain rates studies here.

4. The strain rate sensitivity was found to be higher in grains with a 'soft' orientation over those classified as 'hard'. The change in plastic strain during a stress relaxation period was also found to be higher in 'soft' grains.

6

Effect of oxygen content and temperature on cold dwell fatigue

Contents

6.1 Introduction 87
6.2 Materials and experiment procedures 88
6.2.1 Materials 88
6.2.2 Stress relaxation tests 91
6.2.3 Crystal plasticity model 93
6.3 Results and discussion 94
6.3.1 Thermal expansion and elastic deformation 94
6.3.2 Macroscopic stress relaxation 97
6.3.3 Lattice strain simulation results 99
6.3.4 Strain rate sensitivity 106
6.4 Summary 111

6.1 Introduction

The majority of studies that have investigated cold dwell fatigue have been performed at ambient temperature. However, there is clear evidence showing that the cold dwell effect is also sensitive to temperature, noting that the effect is not observed at high temperature [16]. Zhang *et al.* [17] utilised a crystal plasticity model to show that the worst-case scenario temperature in Ti6Al alloy is around 120 °C

and is diminished when the temperature exceeds 230 °C. To understand this effect in greater detail, the effect of temperature on dislocation activity of different slip systems needs to be understood and quantified in the context of cold dwell fatigue. In addition, oxygen is a common interstitial in titanium alloys. Typically, in high strength grade Ti alloys, oxygen is intentionally added in order to improve the strength, corrosion and wear resistance of the alloy [14, 15]. However, in most of Ti alloys, oxygen is unintentionally introduced during its raw metal processing or due to service conditions [12]. Although oxygen is present in almost all Ti alloys, the role of oxygen on time dependent plasticity and cold dwell fatigue is not clear; a better understanding is highly attractive as it may guide future alloy design strategies and impurity control to suppress the cold dwell effect.

In this chapter, stress relaxation behaviour at different temperatures up to 250 °C of two commercially pure titanium (CP-Ti) alloys with different oxygen content was characterised using synchrotron X-ray diffraction. A crystal plasticity finite element (CPFE) model was calibrated from the measured lattice strains from multiple lattice plane families [136]. The purpose of this work was to determine the key parameters (activation volume, activation energy and critical resolved shear stress) governing the time dependent plasticity of two grades of CP-Ti alloys to reveal the effect of temperature and oxygen on the cold dwell fatigue phenomenon. The strain rate sensitivity exponent, m, is often used to describe rate effects, though m itself can vary significantly with strain rate. Here, values of m were determined over a defined strain rate range, for individual lattice plane families and for an individual slip system, which aims to correlate the m value with physical phenomena, in context to the cold dwell fatigue.

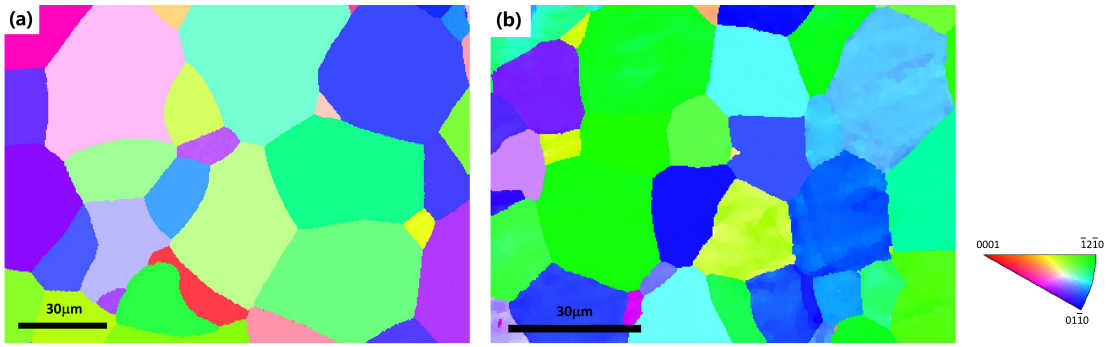
6.2 Materials and experiment procedures

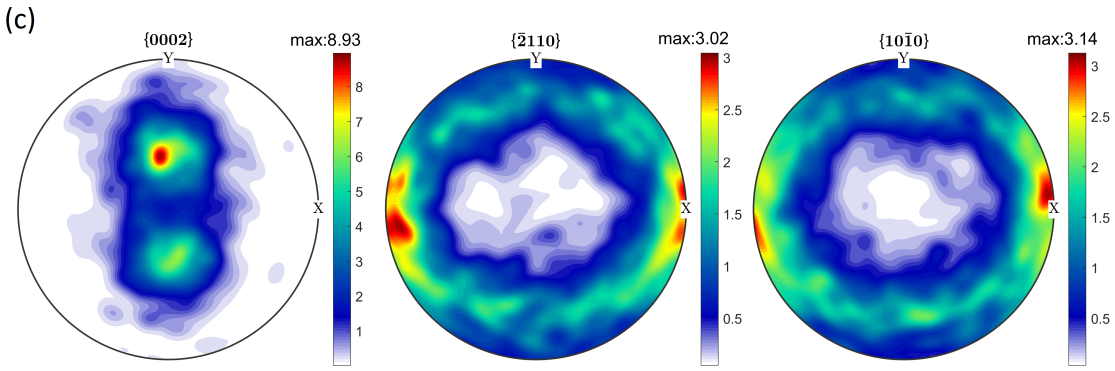
6.2.1 Materials

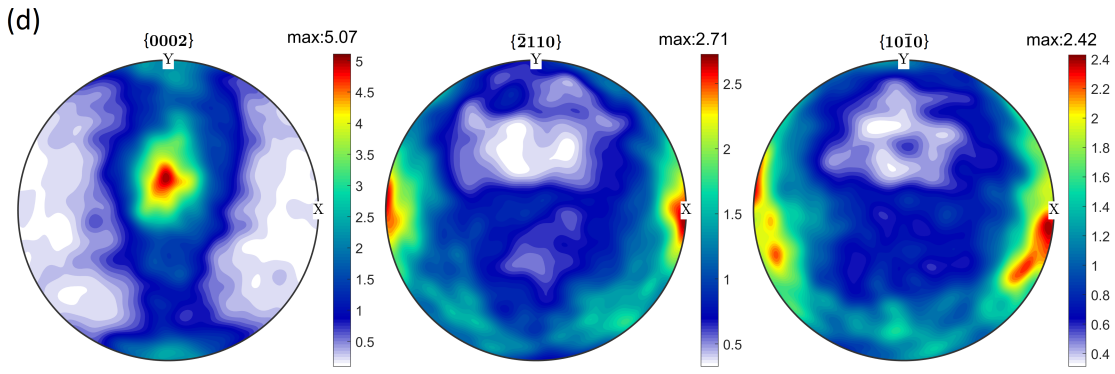
Two types of commercially pure titanium (grade 1 and grade 4) with different oxygen content were selected in this experiment, where the grade 1 material was

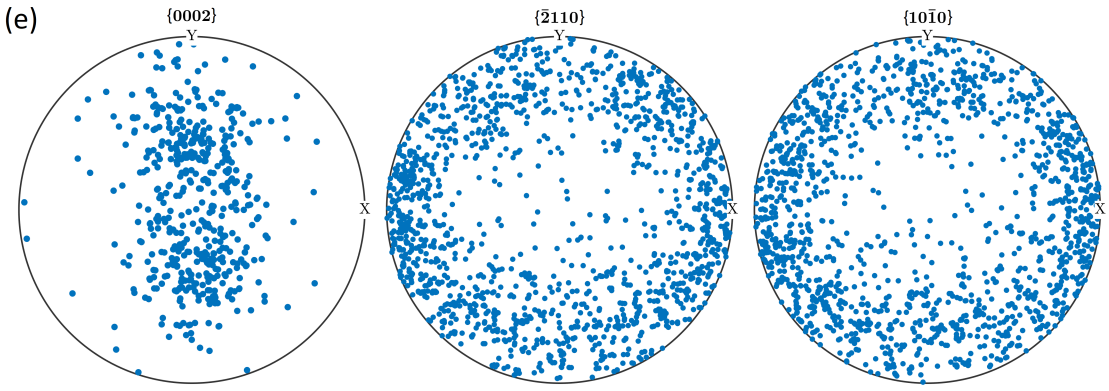
supplied in the form of a rolled sheet while the grade 4 material was supplied in the form of a rolled bar. The composition of these two materials are shown in Table 4.1.

The microstructures of the materials are shown in Figure 6.1(a) and Figure 6.1(b), with both grade 1 and grade 4 having equiaxed grains with an average grain size of 30 μm and 17 μm respectively.


(a)
30μm
(b)
30μm
0001
$\bar{1}2\bar{1}0$
$01\bar{1}0$


(c)
{0002}
max:8.93
$\{\bar{2}110\}$
max:3.02
$\{10\bar{1}0\}$
max:3.14
Y
X


(d)
{0002}
max:5.07
$\{\bar{2}110\}$
max:2.71
$\{10\bar{1}0\}$
max:2.42
Y
X


(e)
{0002}
$\{\bar{2}110\}$
$\{10\bar{1}0\}$
Y
X

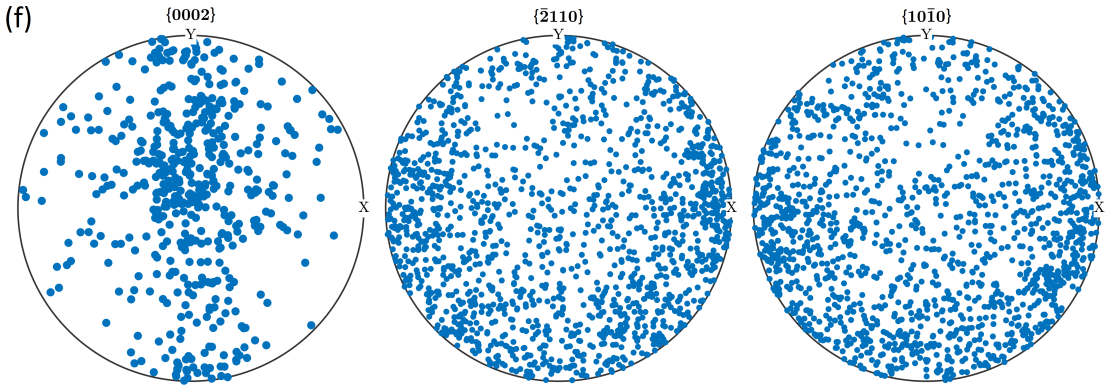


Figure 6.1: (a) EBSD map of CP-Ti grade 1 (IPF colour map along the rolling direction of the raw material); (b) EBSD map of CP-Ti grade 4 (IPF colour map along the rolling direction of the raw material) showing the grain size and morphology; (c) Pole figures of the CP-Ti grade 1 (X along the rolling direction, which was the loading direction); (d) Pole figures of the CP-Ti grade 4 (X along the rolling direction, which is the loading direction) with 10 degree of width used for contours calculation; (e) Scatter pole figure plots of the polycrystal finite element model for CP-Ti grade 1; (f) Scatter pole figure plots of the polycrystal finite element model for CP-Ti grade 4.

The texture of the materials are shown in the pole figures in Figure 6.1(c) and Figure 6.1(d), which were calculated from larger maps than in Figure 6.1(a) and (b) that measured more than 3000 grains. There is a preference for the *c*-axis to be nearly perpendicular to the rolling direction, which is commonly found in hot-rolled titanium alloys [126]. In order to ensure the activation of the easy slip system (prismatic) during stress relaxation experiments, dog-bone shaped tensile samples were cut with the loading axis along the rolling direction of the rod and the sheet, the X direction in these pole figures. With the predominant basal {0002} plane aligned approximately perpendicular to the loading direction (X in the pole figures) in these specimens, the calculated Schmid factor for basal slip was low, encouraging prismatic slip as the dominant slip system in the experiment.

6.2.2 Stress relaxation tests

The stress relaxation cycles are identical to the repeated load-then-hold cycles introduced in Section 5.2.2. To within slight differences between samples, the loading processes were completed in the range of 120 s and 150 s, which corresponded to

macroscopic strain rates of approximately 3×10^{-5} s^{-1} (as measured from the ETMT stroke rate) within the elastic region.

Diffraction patterns were again collected at 1 frame per second and processed using Data Analysis WorkbeNch (DAWN) [138]. Figure 6.2 shows the lattice strain evolution during heating, loading and first relaxation cycle of CP-Ti grade 4 at 145 °C (as an example). It is found that the lattice d-spacing only increases by less

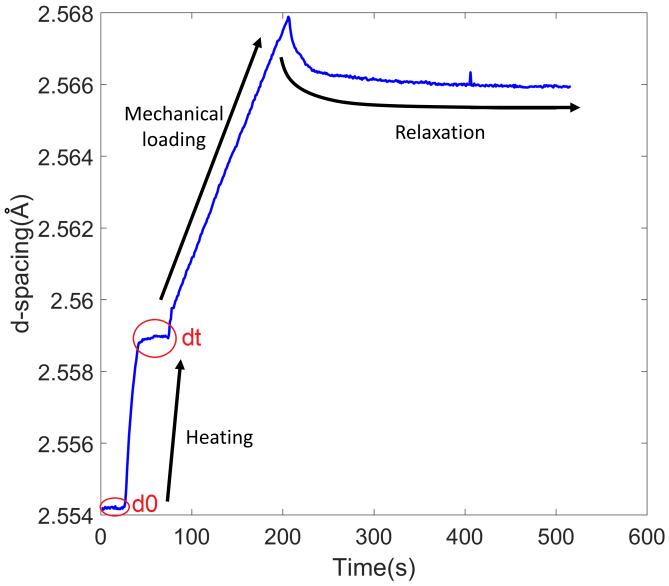


Figure 6.2: Determination of d_0 and d_t using the two periods of idle for each plane family ($\{01\bar{1}0\}$ plane in CP-Ti grade 4 at 145 °C as example).

than 0.01 Å relative to zero load during the whole test, highlighting the importance in determining the initial lattice spacing d_0^{hkil} in order to calculate lattice strain. To do this, a consistent set of stress free lattice parameters a and c needs to be determined, and for each diffraction ring, a d_0 value was obtained by averaging the d-spacing values during the first idle period at zero load and room temperature (as shown in Figure 6.2). These d_0 values from each diffraction ring (hence each diffraction plane) were then averaged for both vertical and horizontal directions (assuming at zero load the diffraction ring is perfect circle), which yield d^{hkil} at zero load. These d^{hkil} values for 21 different plane families were substituted into the crystal geometry equation for HCP (Equation 5.1), more detail of this method has been discussed in Section 5.2.3.

6.2.3 Crystal plasticity model

The CP-Ti alloys were modelled assuming the microstructure comprised HCP α phase alone. The elastic parameters at four different temperatures are indicated in Table 3.2. The thermal expansion coefficients used in the crystal plasticity model are stated in Table 6.1. All of these parameters were taken from literature values.

Table 6.1: Thermal expansion coefficients for single crystal Ti [52, 8].

Coefficient	11	22	33
$\alpha(K^{-1})$	1.8×10^{-5}	1.8×10^{-5}	1.1×10^{-5}

Polycrystal simulations with 512 ($8 \times 8 \times 8$) cubic grains [5, 136, 141, 157] were carried out using Abaqus 2016. Validation of the cubic grain morphology used in this work can be found in Appendix A.6. Each grain consists of 64 ($4 \times 4 \times 4$) quadratic elements (C3D20R). The setup of the model is identical to the model setup discussed in Section 5.2.4. The sample grain orientations (Euler angles), as measured by EBSD (Figure 6.1(c) and Figure 6.1(d)), were converted into rotation matrices, $\boldsymbol{R}$, then selected randomly and assigned to each orientation grain by grain in the model. Therefore, the overall texture of the model was approximately equal to that of the real sample (Figure 6.1(e) and Figure 6.1(f)), so that the effect of texture on lattice strains was minimised. The boundary conditions are shown in Figure 5.5. As some samples were tested at higher temperatures, three stages were implemented. In all three stages, the X=0, Y=0 and Z=0 surfaces were constrained in the X, Y and Z directions respectively. During the heating stage, temperatures were raised to each target temperature in 30 s whilst the other three surfaces were free to expand. During the loading stage, a uniaxial displacement was applied to the top surface over the same period of time as the experiments (with a corresponding strain rate of *ca.* 3×10^{-5} s^{-1}). During the relaxation stage, the displacement of the top surface was held constant along the loading direction (X axis) for a period of 5 minutes.

In order to compare the simulation result with the lattice strain measured by diffraction, the Green-Lagrange elastic strain tensor, $\boldsymbol{E_e}$, is rotated to the lattice

orientation frame (X_L, Y_L and Z_L) through the rotation matrix $\boldsymbol{R}$ to give the lattice strain $\boldsymbol{E_e^0}$ as follows [141]:

$$\boldsymbol{E_e^0} = \boldsymbol{R^T E_e R} = \frac{1}{2}\boldsymbol{R^T}(\boldsymbol{F_e^T F_e} - \boldsymbol{I})\boldsymbol{R} \tag{6.1}$$

As illustrated in Figure 5.6, the $\{01\bar{1}0\}$ planes diffract along the vertical axis with diffraction vectors, q, approximately parallel (with 10° tolerance) to the load axis. For grains that satisfy this condition, strain along the scattering vector, q, was extracted from the elastic strain $\boldsymbol{E_e^0}$ matrix and then averaged from all the elements within these grains. This averaged strain was then calibrated from the experimental lattice strains measured from the same plane family. The five crystal plane families with the highest diffraction intensities along the loading direction were selected for calibration, their high intensity implying that a large number of grains satisfied the diffraction condition, ensuring more reliable results. These five crystal plane families were the prismatic plane $\{01\bar{1}0\}$, first ordered pyramidal plane $\{01\bar{1}1\}$, second ordered pyramidal planes; $\{11\bar{2}2\}$, $\{02\bar{2}1\}$ and $\{12\bar{3}1\}$ for grade 1. For grade 4, these were the prismatic plane $\{01\bar{1}0\}$, first ordered pyramidal plane $\{01\bar{1}1\}$, second ordered pyramidal planes, $\{11\bar{2}2\}$, $\{02\bar{2}1\}$ and $\{01\bar{1}2\}$. Another important crystal plane $\{0002\}$, the basal plane, was not deemed to be available in either grade 1 or grade 4 due to the sample texture and the experimental setup with the incident beam along normal direction (recall Figure 6.1(c) and 6.1(d)).

6.3 Results and discussion

6.3.1 Thermal expansion and elastic deformation

The lattice parameters at elevated temperatures, a_t and c_t, can be calculated using the method for calculating a_0 and c_0 values as discussed in Section 6.2.2, but instead using the d-spacing values in the second idle period. A series of a_t and c_t values are therefore determined at each target temperature. The increase in lattice spacing between a_0, c_0 and a_t, c_t are purely from thermal expansion as the ETMT load was set to zero in a feedback loop, therefore no force is applied to

the samples. Within each sample, the lattice strain caused by thermal expansion can then be calculated as follows:

$$\varepsilon_{11} = (a_t - a_0)/a_0 \tag{6.2}$$

$$\varepsilon_{33} = (c_t - c_0)/c_0 \tag{6.3}$$

Figure 6.3(a) shows the strain in lattice parameters against changing temperatures of CP-Ti grade 4 samples, the gradients of the linear fitted lines represent the thermal expansion coefficient in the a and c directions of the Ti HCP crystal structure. It was found that the thermal expansion coefficients in the a direction is higher than that of the c direction, which agrees with values reported on a single crystal of Ti (see Table 6.1). This is due to the anisotropic elasticity, where the c direction is stiffer than the a direction. Therefore, as temperature increases, strain caused by thermal expansion in the c direction is expected to be less than that of the a direction. Hence, a lower thermal expansion coefficient is expected. In comparison with literature values of single crystal Ti, thermal expansion coefficient along the c direction, α_{33} agrees well while along the a direction, α_{11} was found to be lower. This difference is likely from the elastic constraint of a single grain within a polycrystalline aggregate, compared to a single crystal which may expand without restriction. With the constraint in a polycrystal, α_{11} is found to be lower compared to the value of a single crystal.

As the grain-grain interactions can be successfully captured in the crystal plasticity model, the thermal properties implemented in the model are the values of a single crystal of Ti shown in Table 6.1. This can be verified by lattice strains that developed along the loading direction by increasing the temperature as shown in Figure 6.3(b) and 6.3(c), where the model was able to reproduce thermal strains for the five selected plane families. These are shown to be consistent with the experimental expansion strains at all temperatures and for both grade 1 and grade 4 samples.

Figure 6.3(d) shows the change in stiffness as temperature increases, the stiffness values were obtained from the gradients of stress-lattice strain curves during elastic

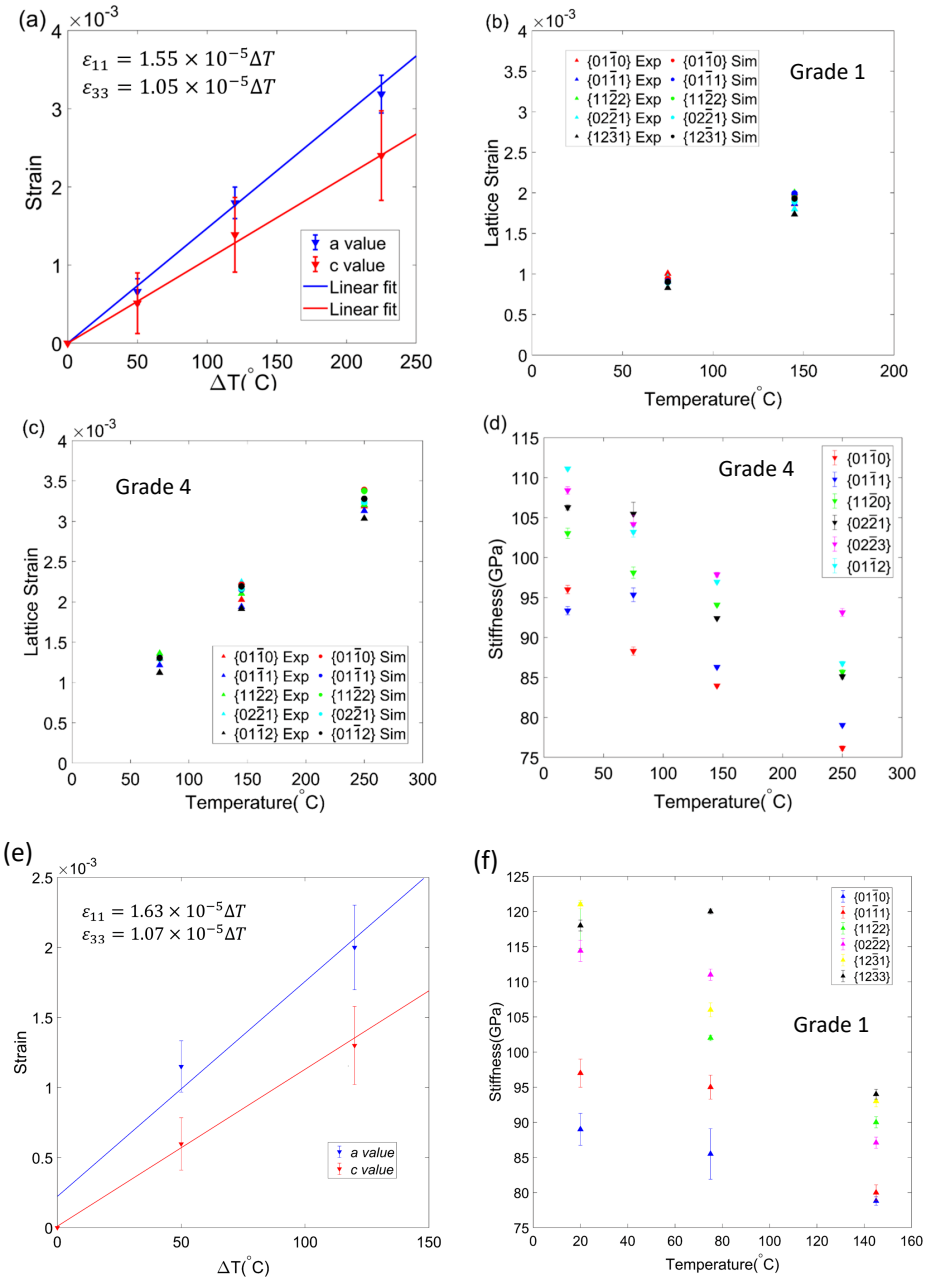


Figure 6.3: (a) Thermal expansion strain in the a and c directions, the gradient of the linear fitted lines enables a measurement of the thermal expansion coefficient (CP-Ti grade 4 samples); (b) Comparison of the thermal expansion strain of the experiment and simulation of CP-Ti grade 1 along the loading direction; (c) Comparison of thermal expansion strain of the experiment and the simulation of CP-Ti grade 4 along the loading direction; (d) Variation of the stiffness of 6 plane families vs. temperature in CP-Ti grade 4; (e) Thermal expansion strain in the a and c directions in CP-Ti grade 1 samples; (f) Variation of the stiffness of 6 plane families vs. temperature in CP-Ti grade 1.

loading. Six plane families with lower noise level in stiffness were plotted. A linear trend is seen; as temperature increases the stiffness decreases.

6.3.2 Macroscopic stress relaxation

Figure 6.4(a) and 6.4(b) shows the macroscopic stress relaxation cycles, which were obtained by dividing the forces measured from ETMT by the gauge cross-section areas. They were then processed using the same method as described in Section 4.4. The best-fit relaxation curves (dashed lines in Figure 6.4(a) and 6.4(b)) were found using fitting tools in MATLAB with fitting error less than 1% and the optimal fitting parameters ΔF^{macro},ΔV^{macro} and σ_c^{macro} obtained, are shown in Figure 6.4(c), 6.4(d) and 6.4(e).

Figure 6.4(a)-(b) show that through repeated relaxation periods the experimental stress values are sometimes above and sometimes below the fitted variation. This observation was seen across multiple temperatures and both oxygen contents. Specifically, among a total of 35 stress relaxation cycles, 7 of the fitted stress relaxation cycles are "slower" than the experimental measurements, while 9 of them are "faster" than the experimental ones. Therefore, no systematic error is present for this numerical fitting method and parameters used. Both activation energy and activation volume were found to increase with temperature; the activation energy has a linear response with temperature, which replicates observations in BCC steel [129]. The lower oxygen content grade 1 system had both higher activation energy and activation volume compared to grade 4. Oxygen is known to be an interstitial in α-Ti and has a profound strengthening effect [3, 13, 36]. Similarly, lowering the ambient temperature has a significant effect on increasing the strength in Ti, as indeed it has in most HCP metals. Both the temperature and oxygen content effects on activation volume are likely due to the corresponding variations in stress levels and are consistent with a kink-pair mechanism [133, 132]. The attractive stress generated by kinks of opposite sign making up a pair are markedly stronger at small separations, so that the equilibrium kink-pair separation decreases significantly as the externally imposed stress is increased. The lower stress levels needed for

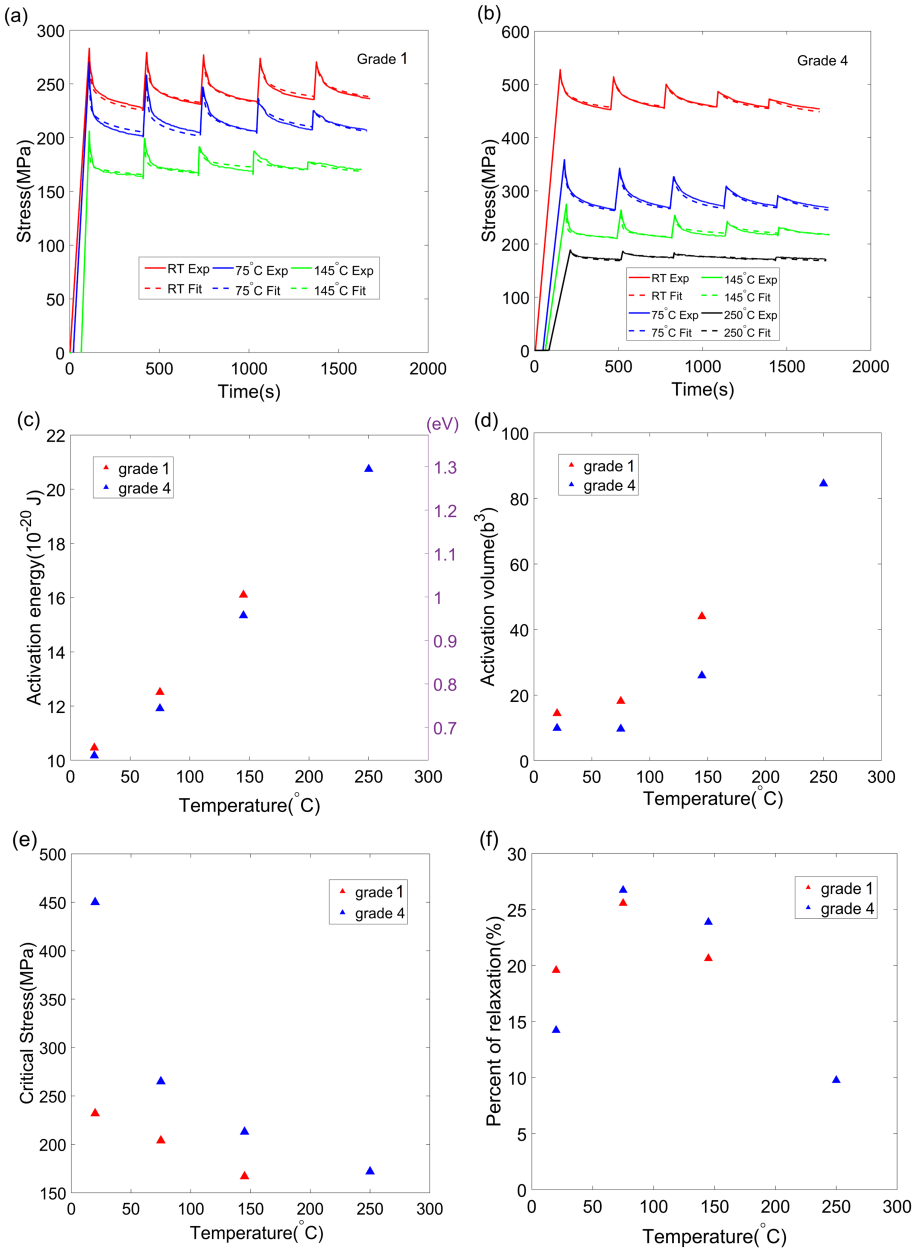


Figure 6.4: (a) Macroscopic stress relaxation curves of CP-Ti grade 1 at 3 different temperatures with dashed lines showing a fitted function based on the slip law; (b) Macroscopic stress relaxation curves of CP-Ti grade 4 at 4 different temperatures (the room temperature result is from the previous work [104], placed here for comparison with higher temperature results); (c) Macroscopic thermal activation energy, ΔF vs. temperature; (d) Macroscopic activation volume, ΔV vs. temperature; (e) Macroscopic critical stress, σ_c vs. temperature; (f) Percentage of stress relaxed vs. temperature.

deformation at lower oxygen content, and higher temperatures thus necessitate nucleation of kink-pairs with larger separation and thus larger activation volume.

During the five-minute stress relaxation period, the total strain was held constant and due to the time dependent plasticity, there was an increment of plastic strain and a relaxation of elastic strain and stress. Therefore, the amount of stress relaxed during the strain hold reveals the amount of plasticity and thus the activity of dislocations. As each sample was loaded to different macroscopic stresses, direct comparison of the absolute magnitude of the relaxed stress is not possible. However, ratios of relaxed stress to the initial stress at the beginning of the first stress relaxation cycles (percentage of relaxation) were calculated for comparison. Figure 6.4(f) shows the variation of percentage relaxation versus temperatures, where in both grade 1 and grade 4, the percentage relaxation first increases when the temperature increases to 75°C and then decreases as temperature further increases. At room temperature, dislocations in grade 1 are more active than in grade 4, but at higher temperatures (75°C and higher) the activity of dislocation in grade 4 exceeds grade 1 results from a sharper increase in percentage of relaxation in grade 4.

The mobile dislocation density, ρ, in Equation 3.1 could possibly be decreasing during relaxation, as reported in [158]. In the content of current work the dislocation density in Equation 3.1 should be considered as an average dislocation density during relaxation. The variation of the dislocation density can be estimated from the present experiment, but the evolution does not appear to be a simple monotonic decrease. Therefore, the simplest approach of assuming a constant mobile dislocation density is used in calculations. A parametric study showed that mobile dislocation density change of +/- 40% does not drastically change the quality of the agreement between the experimental and simulated lattice strains. Details of this verification can be found in Appendix A.5.

6.3.3 Lattice strain simulation results

As shown in Section 6.3.2, the macroscopic stress relaxation cycles were fitted using a function informed by a slip law, where one set of parameters can fit all

five relaxation cycles. Therefore, the lattice strains developed during the first 5-minute strain hold from the five selected planes families were used to calibrate the crystal plasticity model.

Because the loading strain rate is relatively slow (*ca.* 3×10^{-5} s^{-1}) in this work, at this strain rate the lattice strains are less sensitive to the change in the activation volume, ΔV. The activation volume used in the simulation are the same as those obtained from the macroscopic stress relaxation fit. Considering that the activity of the pyramidal slip is low, parameters for this slip type was not calibrated. The macroscopic ΔF were used for the pyramidal slip and CRSS for pyramidal slip was instead set to be three times the value of basal slip. Efforts were focused on the identification of the parameters: activation energy and CRSS for (1) basal and (2) prism slip to enable simulation of the lattice strains from relaxation cycles, which could then be fitted to the experimentally measured lattice strains.

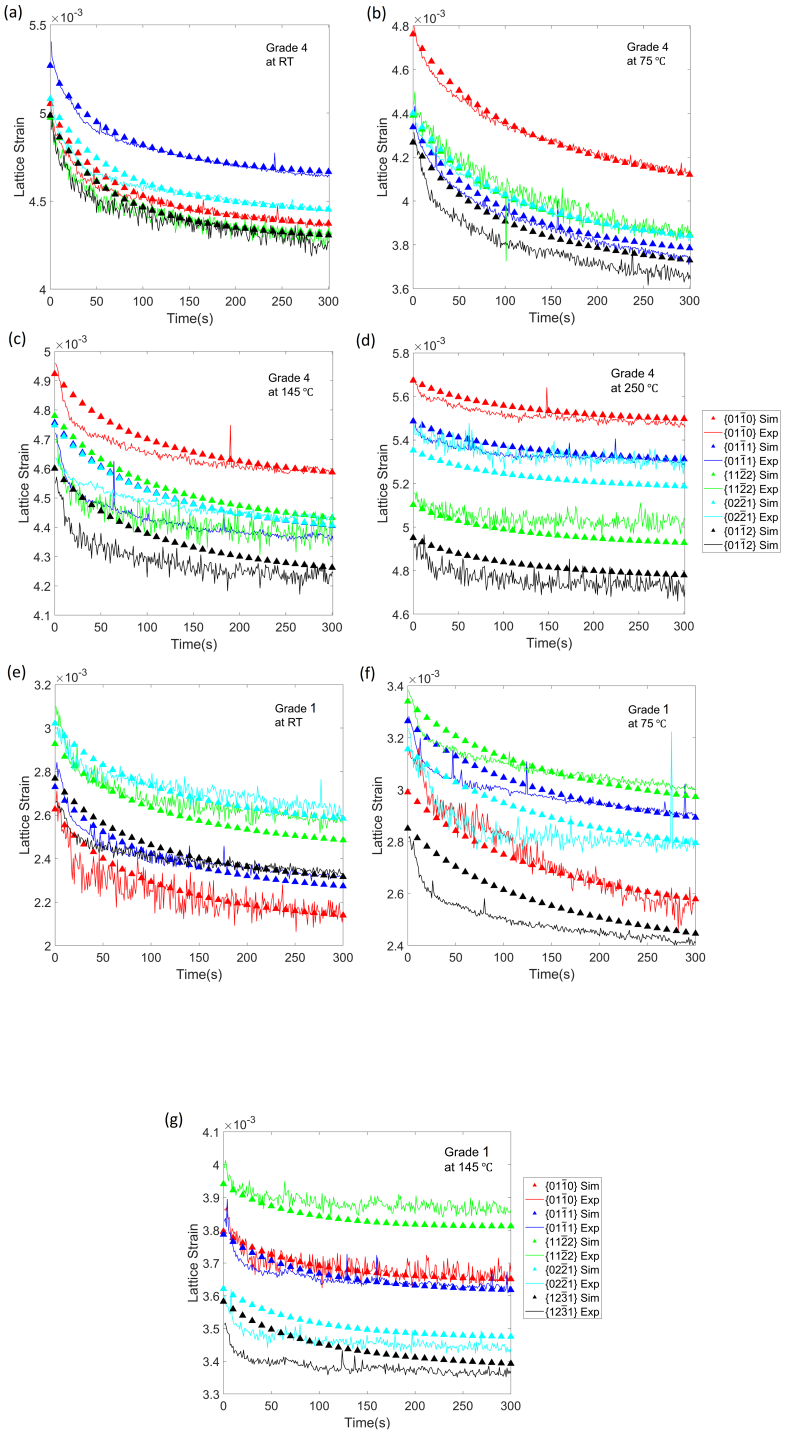


Figure 6.5: Comparison of lattice strain evolution along the loading direction between the experiment and the simulation of (a) CP-Ti grade 4 at room temperature; (b) CP-Ti grade 4 at 75 °C; (c) CP-Ti grade 4 at 145 °C; (d) CP-Ti grade 4 at 250 °C; (e) CP-Ti grade 1 at room temperature; (f) CP-Ti grade 1 at 75 °C; (g) CP-Ti grade 1 at 145 °C.(Note vertical axes are not the same in each plot)

Among the five selected plane families, three important planes in the HCP crystal structure (prismatic planes $\{01\bar{1}0\}$, first ordered pyramidal planes $\{01\bar{1}1\}$ and second ordered pyramidal planes $\{11\bar{2}2\}$) have a higher priority in the optimisation process. These planes were fitted with higher priority and then the fitting for other planes were achieved without damaging the fitting that already accomplished for the three important planes. Figure 6.5 shows a comparison of the simulated and experimental lattice strain relaxation curves, all of them show a good fit. The lattice strain variations through the initial relaxation period show the simulated results above the experimental measurements for some reflections (especially the grade 4 at 145°C and grade 1 at 75 °C samples) but below for others. This is due to the assumption of constant dislocation density as discussed in Section 6.3.2. Meanwhile, as the macroscopic stress relaxation curves also show good agreement with the simulated and experimental results (as shown in Figure 6.6), the confidence in the measurement of the parameters is high. Figure 6.6 shows generally similar averaged stress levels between simulations and experiments, though the rate of stress relaxation is initially mostly lower (slower) in the simulation than experiment. The simulated stress is higher than the experimental one at time smaller than 100 s, while it is lower at a later time due to some plastic strain has accumulated and the stress has reduced.

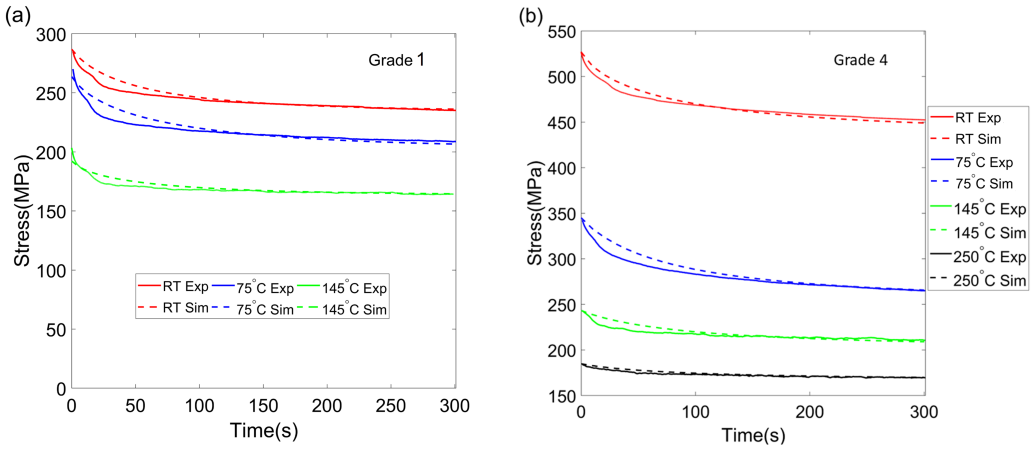


Figure 6.6: Comparison of macroscopic stress relaxation curves between experiment and simulation for (a) CP-Ti grade 1 at 3 different temperatures and (b) CP-Ti grade 4 at 4 different temperatures.

Figure 6.7(a) and 6.7(b) show the variation of CRSS and activation energy for the basal and prism slip as a function of temperature. Error bars were shown to give the range of these parameters i.e. changing parameters within these ranges results in a change in simulated lattice strain that is smaller than the experimental results error (fluctuation), and simulated lattice strain remains a good fit with experiment lattice strain.

CRSS values decrease as temperature increases. At room temperature, the CRSS for basal slip is significantly higher than that of prism slip in both grade 1 and grade 4. As the temperature increases, the CRSS for basal slip drops much faster than that of prism slip in grade 4. This results in CRSS value for basal slip to be lower than that of prism slip in CP-Ti grade 4 at 250 °C. However, this trend was not found in grade 1, where the difference between values of basal and prism slip remains almost the same for all three temperatures. Due to the strengthening effect of oxygen, grade 4, with higher oxygen content, has a higher CRSS for prism slip at all temperatures and basal slip at room temperature over grade 1. However, the CRSS for basal slip at 75 °C and 145 °C were found to be similar for these two CP-Ti grades. As a result, the ratio of τ_c^{basal} and τ_c^{prism} was found to be higher in grade 1 over grade 4 at room temperature, as temperature increases, the CRSS ratio was found to decrease in grade 4 while it increases in grade 1.

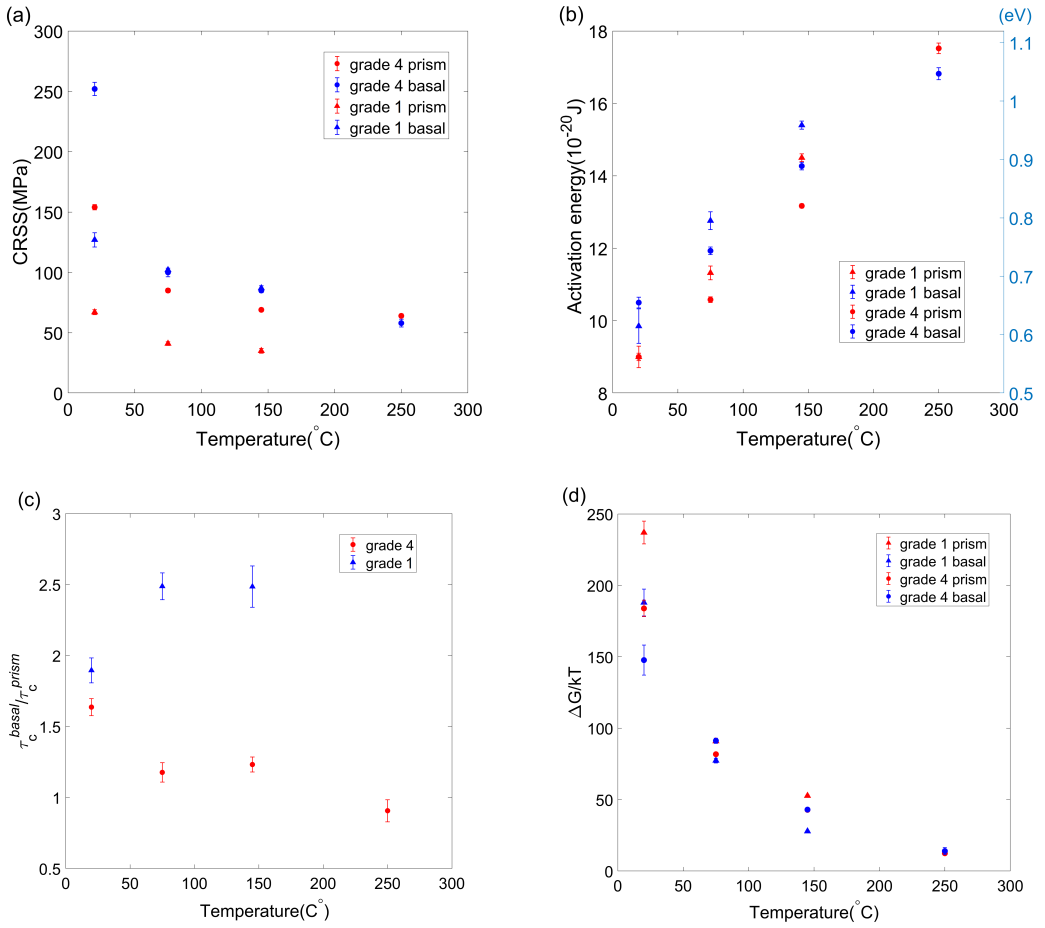


Figure 6.7: (a) CRSS vs. temperature; (b) Thermal activation energy, ΔF vs. temperature; (c) CRSS ratio vs. temperature; (d) Activation free energy as a multiple of available thermal energy, $\Delta G/k_BT$ vs. temperature.

This phenomenon can be explained by the difference in the strengthening effect of oxygen on these two slip systems. Yu *et al.* [12] suggested that there is a very strong repulsive interaction between a screw dislocation core and oxygen on octahedral site on the same prismatic plane. In comparison, the repulsion of a dislocation core and oxygen on an interstitial site on basal plane is an order of magnitude smaller. It was also found that once interacting with dislocation, the original oxygen octahedral site will gradually disappear. The oxygen would migrate to either a basal plane interstitial site (with lower energy) or a tetrahedral site and a new octahedral site on a prism plane (with higher energy). As the temperature increases, the thermal expansion in the a direction is larger than that of the c

direction (as discussed in Section 6.3.1), which results in a decrease in the c/a ratio. Therefore, the area of the basal plane becomes larger (a_1 and a_2 vectors increase, as c decreases) and the octahedral site becomes nearer to the basal plane, which results in a higher possibility for oxygen to move to a basal-plane interstitial sites. For a lower oxygen content Ti (grade 1); this results in a strengthening effect loss for the prism type slip. For a higher oxygen content Ti (grade 4), although some of the oxygen may migrate to a different interstitial site, the remaining oxygen still provides a much more significant strengthening effect for prism slip. To summarise the temperature effect and oxygen level effect, we can correlate the observation of the changing in CRSS ratio vs. temperatures have opposite trend in two grades of CP-Ti with different oxygen content.

The thermal activation energy shows an opposite trend to CRSS, and ΔF increases with temperature (as shown in Figure 6.7(b)), which is a trend commonly observed in coarse-grained materials [129]. It is found that the thermal activation energy for both basal and prism slip in the softer grade 1 is higher than that in grade 4, and similarly ΔF increases as the flow stress decreases with increasing temperature. Basal slip generally has a higher thermal energy barrier over prism slip except for grade 4 at 250 °C.

The total activation free energy barrier has two contributing factors: (1) the thermal activation energy barrier, ΔF and (2) the critical mechanical work done by an externally applied stress, $\tau_c \Delta V$. Therefore, the total free energy barrier for dislocation activation is given by [56]:

$$\Delta G = \Delta F - \tau_c \Delta V \tag{6.4}$$

where ΔG is the Gibbs free energy. This expression was then normalised by absolute temperature, T and Boltzmann constant, k_B giving: $\Delta G/k_B T$. Figure 6.7(d) shows the variation of the energy barrier for dislocation activation against temperature; it is found that as the temperature increases, $\Delta G/k_B T$ for both slips systems in grade 1 and grade 4 decreases, indicating that slip becomes easier to activate as temperature increases. Meanwhile, due to the reverse response of ΔF and τ_c as

the temperature is increased, the slip activation mechanism changes, where at low temperature slip activation is mainly driven by mechanical work while at high temperature slip activation is more driven by thermal energy.

6.3.4 Strain rate sensitivity

The method for obtaining strain rate sensitivity exponent, m, has been discussed in Section 4.6. Figure 6.8(a) shows an example of this fitting procedure. The strain rate (gradient of the lattice strain relaxation curve) at each second were calculated for this 300 s period of time, so that the stress vs. strain rate can be plotted at log scale (as shown in Figure 6.8(b)).

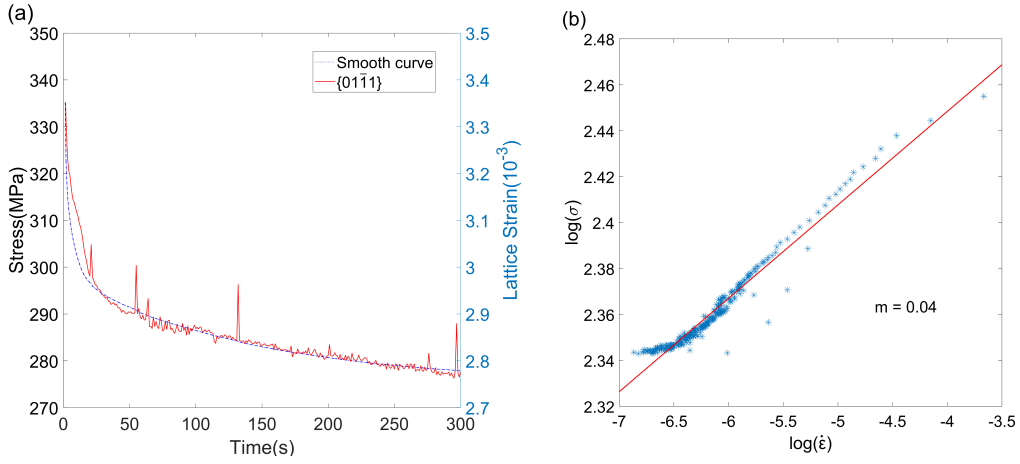


Figure 6.8: (a) Smooth fit the first stress/strain relaxation curve (stress was obtained from the product of lattice strain and plane stiffness); (b) Determination of strain rate sensitivity.(Using $\{01\bar{1}1\}$ plane of CP-Ti grade 1 at 75 °C as an example)

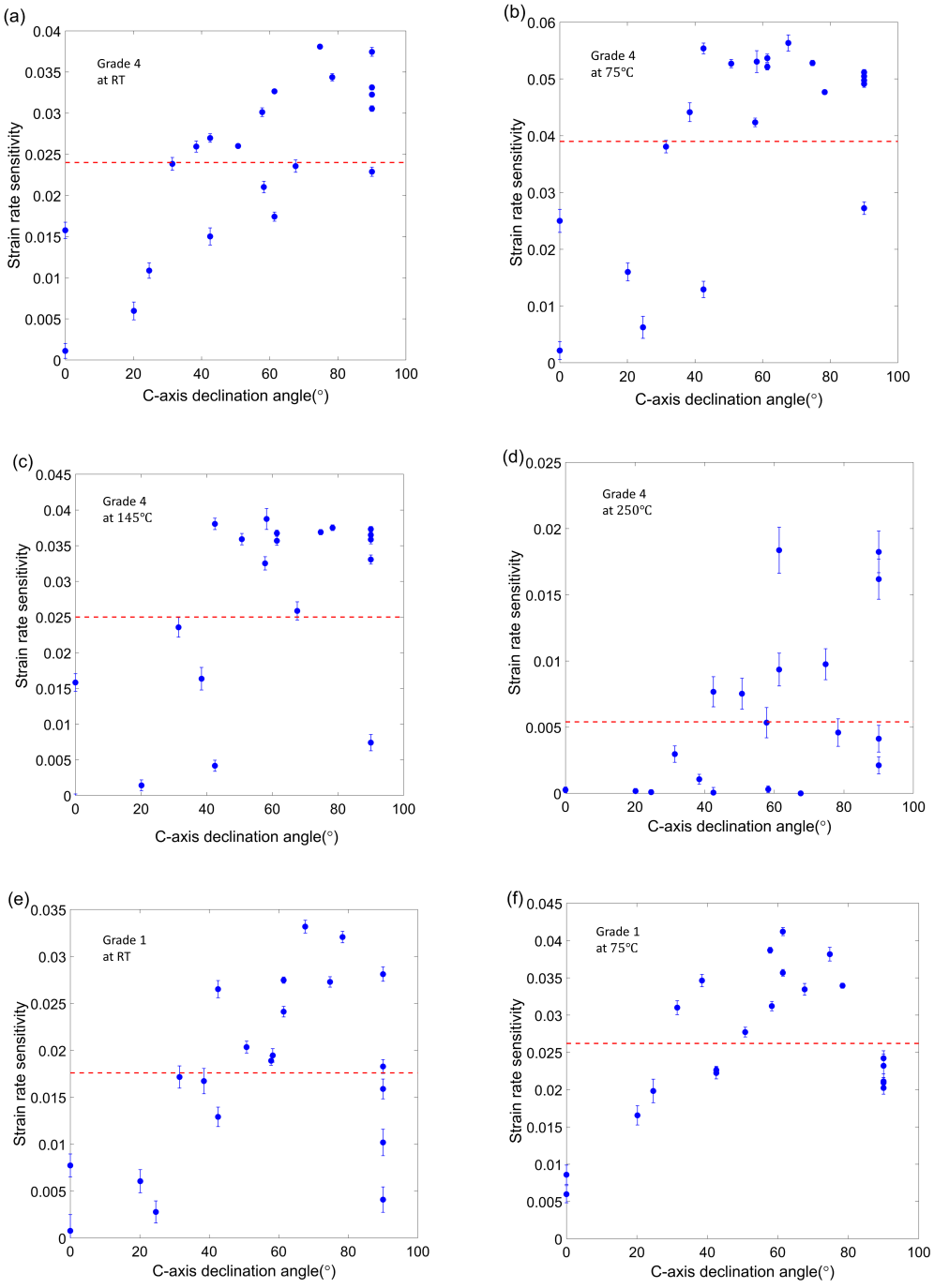
The strain rate sensitivity therefore can be calculated for the 21 plane families in the two CP-Ti alloys. As shown in Figure 6.9(a) and 6.9(e), the SRS values are highly anisotropic at room temperature, as the grain orientation changes from 'hard' (c-axis parallel to loading direction, declination angle is 0°) to 'soft' (c-axis perpendicular to loading direction, declination angle is 90°), SRS increases from 0 to 0.04 in CP-Ti grade 4 and to 0.035 in CP-Ti grade 1, which strongly agrees with other works on CP-Ti [69, 71, 72, 73, 74]. However, in the Ti6242 alloy, this trend was observed to be opposite by other researchers [67]. A higher SRS (m=0.039) was found for 'hard' grains over SRS (m=0.025) for 'soft' grains in α phase. For

higher temperature samples, as shown in Figure 6.9(b)-6.9(d), 6.9(f) and 6.9(g), the variation of SRS with orientations still exists but the SRS values are different at these temperatures. Figure 6.9(h) shows the averaged SRS values for the 21 plane families at different temperatures. It was found that for both grade 1 and grade 4, averaged SRS value increased as temperature increased to 75 °C and then decreased as the temperature further increased. These follow the same temperature dependence as the relaxed stress (recall Figure 6.4(f)), indicating that a higher SRS leads to more plastic strain accumulation during the same time period of creep, and thus more dislocations activities.

Similarly, the SRS can be calculated for each different slip system using the slip law (recall Equation 3.1). Inserting the slip parameters obtained from the simulation (Section 6.3.3), we can plot the stress vs shear strain rate over a strain rate range of 10^{-6} to 10^{0} s^{-1} (see Figure 6.10(a)). As the stress vs. shear strain rate curves are not linear and the gradient is not constant at different shear strain rate range, showing the SRS is different for a different strain rate range. Therefore, a narrower strain range (10^{-4} to 10^{-2} s^{-1}) was selected for reflecting the Ti aeroengine components in service and enables a better comparison to other values reported in the literature [69, 67, 68]. Grade 4 has a higher SRS over grade 1 for both prism and basal slips. Prism slip has a higher SRS than that of basal slip in both CP-Ti alloys, which agrees with the work done by Jun *et al.* [67], where micropillars were made from the α phase in Ti6242 alloy and the SRS values were determined using two different methods: a constant strain rate method (CRSM) and a conventional stress relaxation method (SRM). For both methods, SRS for prism slip is more than two times the values of basal slip. Correlating to the variation of SRS against c-axis declination angle, it is believed that the difference of SRS in different slip systems is the origin of this orientation-sensitive SRS.

The temperature dependence of SRS in basal and prism slips follow the similar trend as the averaged SRS and relaxed stress, where a peak value can be predicted between 75 °C and 145 °C. The peak temperature agrees with the worst-case temperature (90 °C to 120 °C) for dwell debit [17, 159]. Therefore, combining the

evidence collected in this work, the physical phenomenon correlating to strain rate sensitivity can be interpreted in the context of cold creep. During the same period of creep, higher strain rate sensitivity leads to greater accumulation of plastic strain. Strain rate sensitivity of each slip system is positively correlated to the activity of the slip system during stress dwell. For the lower oxygen content the CRSS of



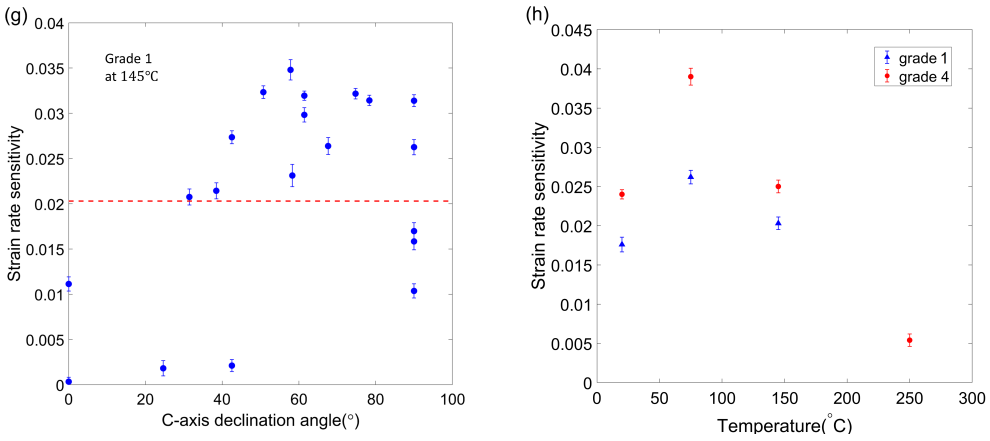


Figure 6.9: Strain rate sensitivity variation against c-axis declination angle of CP-Ti grade 4 at (a) room temperature (this is from the previous work [104], placed here for comparison with higher temperature results); (b) 75 °C; (c) 145 °C; (d) 250 °C; and CP-Ti grade 1 at (e) room temperature; (f) 75 °C; (g) 145 °C and (h) averaged SRS values of the 21 plane families at different temperatures. (The red dashed lines in (a)-(g) show the averaged SRS level for that sample)

prism slip always remains significantly smaller than that for basal slip, while at higher oxygen content the slip strengths become more comparable. Prism slip still remains the more likely contributor to load shedding and cold dwell fatigue issues due to its higher strain rate sensitivity compared to basal slip.

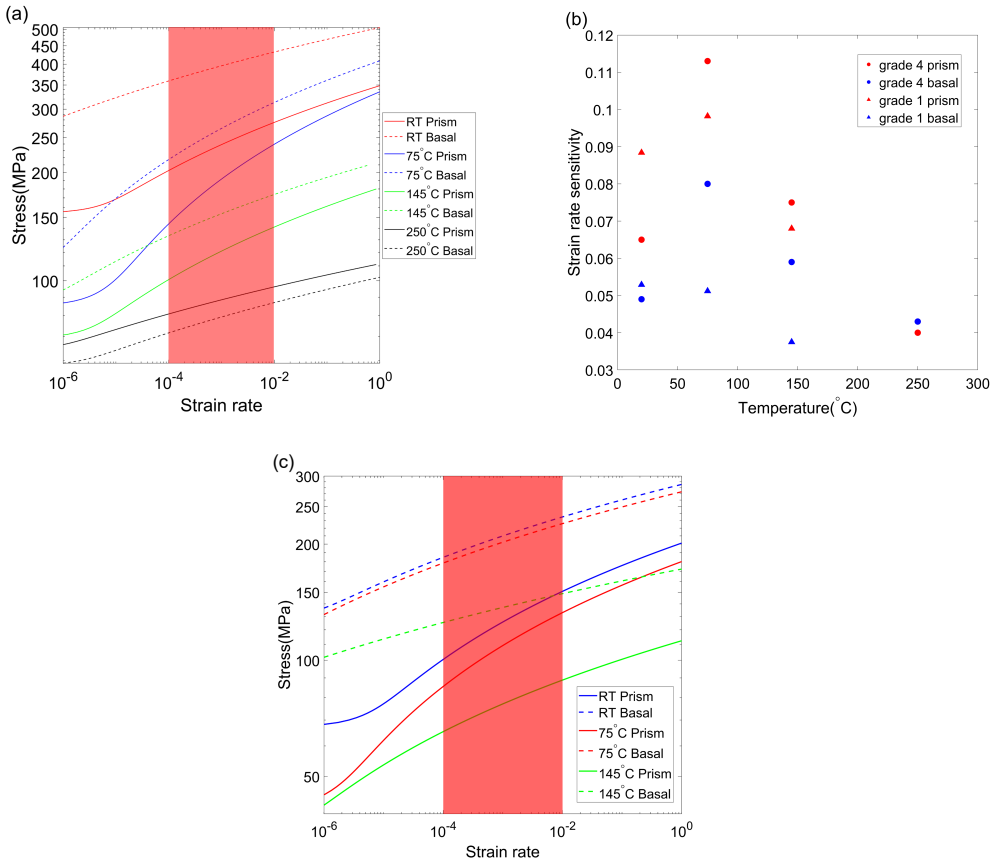


Figure 6.10: (a) Stress vs. strain rate plot over strain rate range between 10^{-6} to 10^{0} s^{-1} for prism and basal slips in CP-Ti grade 4 at 4 different temperatures (red shadow shows the typical strain rate range for Ti in service); (b) Variation of SRS values with temperatures for prism and basal slips; (c) Stress vs. strain rate plot over strain rate range between 10^{-6} to 10^{0} s^{-1} for prism and basal slips in CP-Ti grade 1 at 3 different temperatures.

6.4 Summary

In this Chapter, effects of oxygen and temperature on cold dwell fatigue were revealed. The time dependent plasticity processes in two commercially pure Ti alloys (grade 1 and grade 4) with different oxygen contents were studied using an *in situ* synchrotron X-ray diffraction approach and a crystal plasticity finite element model at four temperatures (room temperature, 75 °C, 145 °C and 250 °C). Dislocation related parameters in the constitutive slip law for basal and prismatic slip systems were isolated and determined. The study has the following conclusions:

1. At the macroscopic level, both the activation volume (ΔV) and the thermal activation energy (ΔF) were found to be higher in low oxygen content CP-Ti (grade 1) and were both observed to increases in response to the increasing temperature consistent with a controlling kink-pair nucleation mechanism. However, the strength decreased significantly with increasing temperature. The magnitude of stress relaxation was found to be largest at 75 °C for both grade 1 and grade 4.

2. The CRSS and thermal activation energy were both greater for basal slip over prism slip except at 250 °C in grade 4 where the trend is reversed. Due to the greater strengthening effect of oxygen on prism slip the ratio of CRSS values for grade 4 decreases significantly with temperature, while it does not for grade 1 (it may even increase slightly).

3. With increasing temperature, the activation energy barrier (ΔF) increases, but as the mechanical energy required for slip reduces as the CRSS values decrease so that thermal energy becomes a greater contributor to dislocation glide processes.

4. Strain rate sensitivity was determined from lattice strain relaxation in 21 plane families. It shows strong orientation dependence, where grains in 'soft' orientation have a higher SRS than that of grains in 'hard' orientation. The

highest average SRS among 21 plane families was found at 75 °C for both two CP-Ti alloys and grade 4 has higher SRS over grade 1.

5. The SRS for prism slip was found to be higher than that of basal slip. The temperature dependence of SRS for both slip systems follow similar trends as the average SRS and macroscopic relaxed stress, indicating that a higher SRS results in more plastic strain accumulation during creep.

7

A digital image correlation study of cold dwell fatigue:Load shedding in rogue and non-rogue grain pairs

Contents

7.1 Introduction 113
7.2 Materials and experiment procedures 114
7.2.1 Materials 114
7.2.2 Creep tests 115
7.2.3 Crystal plasticity model and simulations 116
7.3 Results 119
7.3.1 Critical resolved shear stress 119
7.3.2 Macroscopic stress 122
7.3.3 Slip activity and trace analysis 124
7.3.4 Load shedding 125
7.4 Discussion 129
7.5 Summary 134

7.1 Introduction

Cold dwell fatigue mainly occurs in α-Ti alloys [160]. The deformation of HCP crystal structure is highly anisotropic due to its low symmetric elasticity and different slip system strengths [9, 161]. Dunne *et al.* [56, 57] used a crystal plasticity finite

element (CPFE) model to investigate the worst case scenario, in a combination of a 'soft' and 'hard' grain, also known as 'rogue' grain pair. Upon deformation, large stresses accumulated at the grain boundary and also into the 'hard' grain. Sinha *et al.* [53, 162, 54] suggested that dwell fatigue crack nucleation is usually related to {0002} facets which lie almost perpendicular to the loading direction. This facet formation within the 'hard' grain is initiated by dislocation pile-up in the adjacent 'soft' grain [2, 11]. However, it has also been demonstrated that in some samples dwell sensitivity still occurs without the presence of a 'rogue' grain pair [163], but the mechanism remains not well explained. It is believed that understanding this behaviour of easy slip systems (basal and prism) during stress dwell will improve understanding of the complicated cold dwell fatigue problem.

In this work, a crystal plasticity finite element model is combined with experimental DIC measurements to investigate the temperature effect on cold dwell fatigue in a coarse grain Ti-6Al alloy. An optical digital image correlation (DIC) approach has been used to allow *in situ* measurement of strain in different grains while the samples were under load-up and load-hold (creep) type of deformation at 3 different temperatures up to 230 °C. True sample microstructures, captured by electron back scattered diffraction (EBSD), were reconstructed for crystal plasticity simulations. Critical resolved shear stresses (CRSS) of the two main slip systems (basal and prism) were determined as a function of temperature by matching the experimentally measured strain to the simulated strain in different grains. Load shedding was studied in both 'rogue' and 'non-rogue' grain pairs at different temperatures. The worst-case scenario temperature [17] is explained.

7.2 Materials and experiment procedures

7.2.1 Materials

The material used in this study is a Ti-6Al alloy bar, supplied by Timet UK Ltd. with composition shown in Table 7.1. Test samples were $5 \times 5 \times 5$ mm^3 cubes cut from the bar. In order to reduce the influence of pre-processing (e.g. residual stress and lattice defects) and homogenise the grain size, samples were annealed at

980 °C in a vacuum tube in furnace for 12 h, followed by slow cooling for a period of more than 24 h. The material composition was measured after the annealing heat treatment using XRF and LECO analysis provided by AMG Superalloys UK Ltd. Figure 7.1 shows the microstructure of these samples, the mean grain size after the heat treatment was found to be approximately 140±30 μm.

Table 7.1: Composition of the Ti6Al alloy.

Ti	Al (wt %)	Fe (wt %)	O (wt %)	N (wt %)	Others total (wt %)
Balance	5.79	<0.05	0.07	0.001	0.2

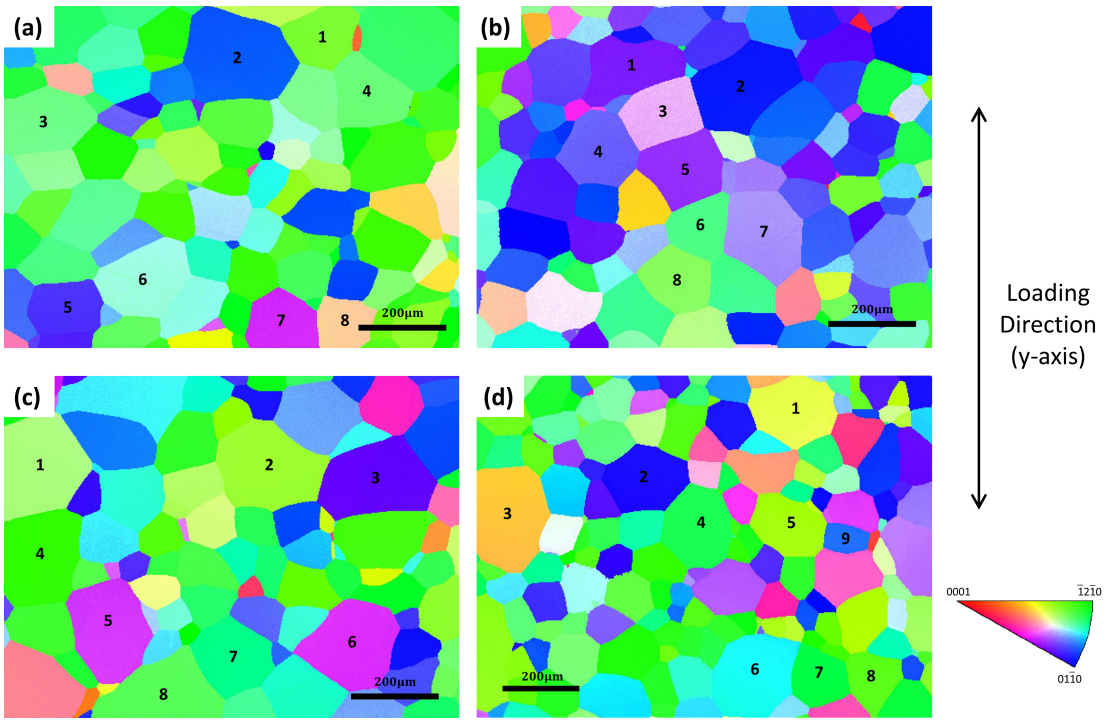


Figure 7.1: EBSD maps of the Ti6Al samples (IPF colour map along the loading direction of the samples): (a) Sample 1 tested at room temperature; (b) Sample 2 tested at 120 °C; (c) Sample 3 tested at 230 °C and (d) Sample 4 tested at room temperature. Numbered grains 1-8 were selected to calibrate the CPFE model.

7.2.2 Creep tests

Sample 1 to sample 3 were tested at room temperature, 120 °C and 230 °C (ambient temperature, intermediate temperature and temperature where cold dwell fatigue diminished). Compressive loads were applied to the samples using a Shimadzu

mechanical test frame (AGS-X series) after the temperature of each sample was stabilised at each target temperature for 5 minutes.

Samples were loaded in compression at constant stress rate of 5 MPa/s, so that the first gradient changes observed in the strain vs. time plots (see Figure 7.2(a)-(c)) represent the macroscopic yield. Sample 1-3 were designed to study the behaviour of the two major slip systems (basal and prism slip) during creep and thus were loaded beyond the macroscopic yield stresses to activate both the desired slip systems. After clear gradient changes were observed in strain vs. time data, the macroscopic stresses were held constant for a period of 10 minutes to mimic the dwell effect. The compression strain of these samples was found to increase during the stress dwell periods (cold creep). In the first half of this dwell period, strain appears to change faster than that of the subsequent half. This also implies that stress redistribution is more active in the first 5 minutes of the stress hold. Sample 4 was designed to focus on this first 5 minutes of creep under a stress below the macroscopic yield stress, which is a better representation of a real load condition of Ti alloys in-service. The loading curve of sample 4 is shown in Figure 7.2(d) and this sample starts to creep with strain still in elastic region, and the load hold period lasts for 5 minutes.

7.2.3 Crystal plasticity model and simulations

Values of ΔF and ΔV input into the model can be found in Figure 7.4, following the previous Chapters (recall Figure 4.4(b) and Figure 4.4(c), the temperature dependence of these two parameters follow simple empirical fit, which are straight line for the ΔF and parabola for the ΔV). The variation of ΔF from alloy to alloy is not significant and the effect of ΔV on simulation results were not significant as well (as discussed in Appendix A.3). Therefore, the input of ΔF and ΔV in this Chapter follows the empirical values. τ_α^c for prismatic and basal slip were the target values to be obtained in the optimisation procedure carried out in this work. $< c + a >$ Pyramidal slip is much more difficult to activate due to its higher τ_α^c, which is about three times the value of basal slip at temperature between 20 °C

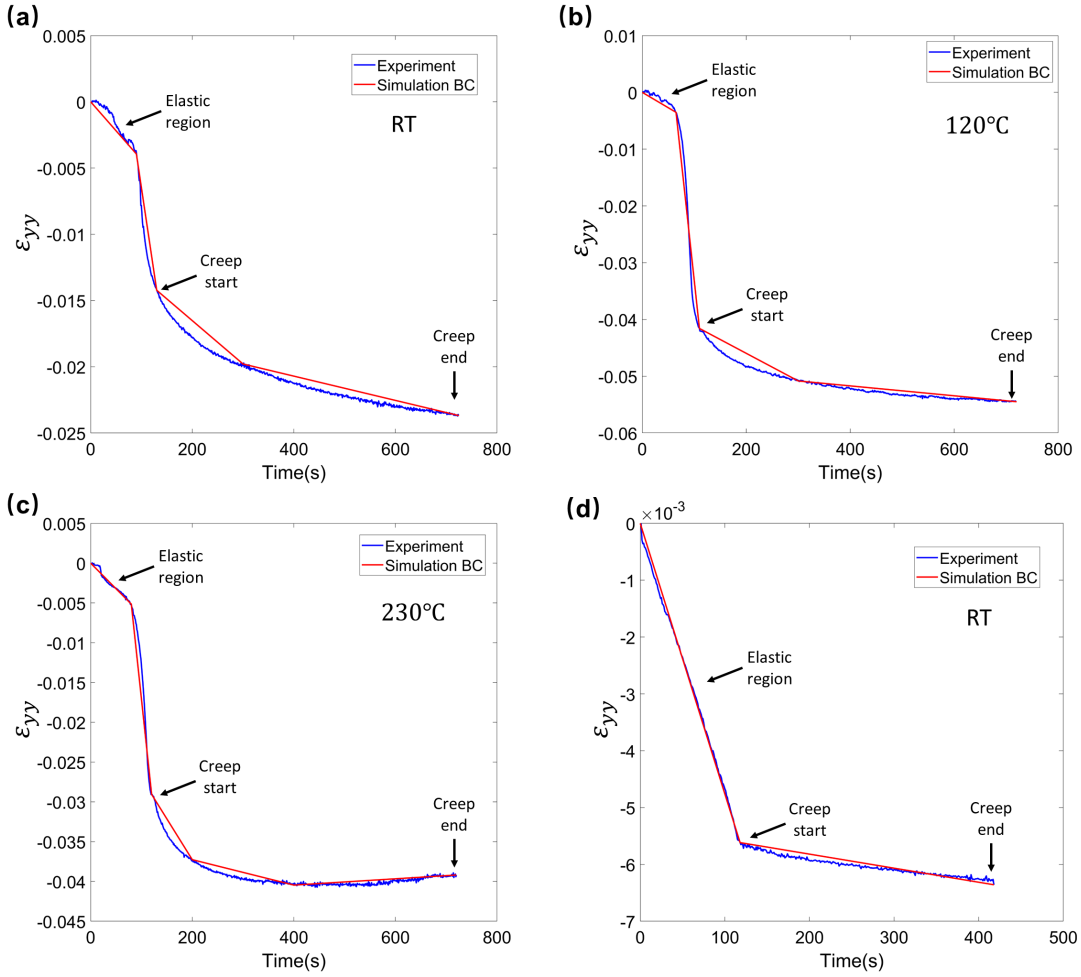


Figure 7.2: Strain vs. time curves of (a) Sample 1 loaded beyond macroscopic yield stress at room temperature; (b) Sample 2 loaded beyond macroscopic yield stress at 120 °C; (c) Sample 3 loaded beyond macroscopic yield stress at 230 °C and (d) Sample 4 loaded below macroscopic yield stress at room temperature.

and 300 °C [9, 17, 46]. The values of τ_α^c for pyramidal slip was set to be three time the value of basal slip in this work.

Figure 7.3 shows the representative volume of sample 4, which is generated using an EBSD map and a MATLAB function called ebsd2abaqus which is openly available [164]. Grain morphology and orientations were the same as the real samples. The element type was set to be quadratic with reduced integration (C3D20R) and meshed as a regular, equisized grid of size matched to 8 μm. The model was a 3D model with a depth of 2 elements, the 2 layers of elements were identical (validation can be found in the Appendix A.7). The movement of the left

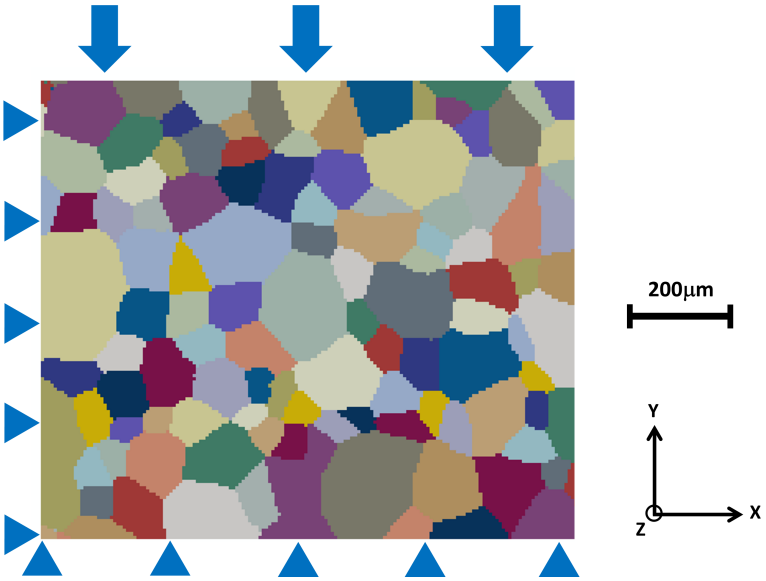


Figure 7.3: Example of the meshed model of sample 4, the depth of the model was 2 elements. Arrows show the boundary condition of the model, where the bottom and left surfaces were constrained in Y and X direction and uniaxial load was applied to the top surface. Grains were rendered with different colours so that the microstructure was found to consistent with the EBSD map.

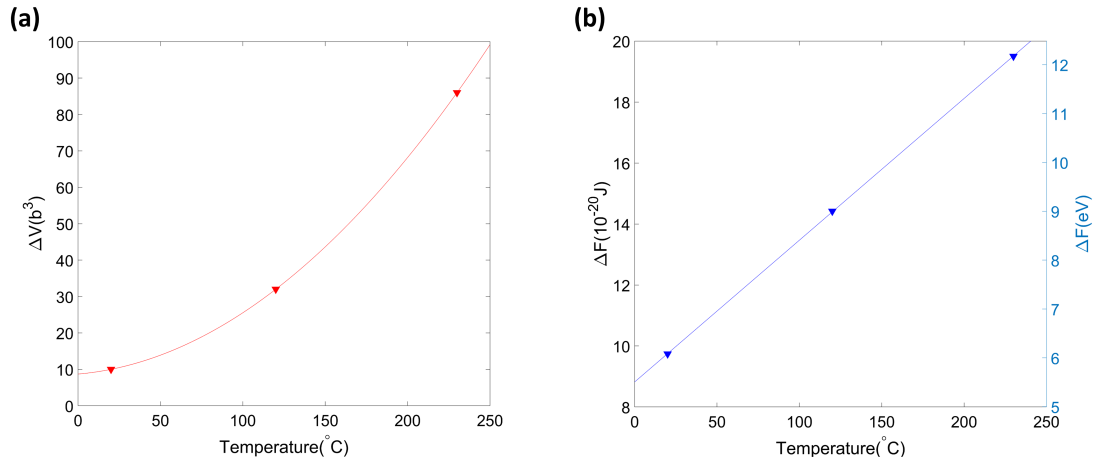


Figure 7.4: Input parameters of (a) activation volume (ΔV) and (b) activation energy (ΔF) as a function of temperature [135].

face, bottom face and back face were constrained along the X, Y and Z direction respectively. Displacement was applied to the top face so that the overall strain of the model matches with the averaged strain of the sample (as shown in Figure 7.2). Within each grain, nodes on the front surface in the central region of the grain (again the nodes near the grain boundaries were dismissed, to be a closer estimate

to DIC measurements) were grouped to represent the grain. Strain component ε_{yy} of these nodes was averaged and matched with the experimentally measured DIC strain, as described in the next section.

7.3 Results

7.3.1 Critical resolved shear stress

The CRSS for the two main slip systems (prism and basal) were obtained by calibrating the CPFE model. The optimisation was achieved using a Scipy package [165], by use of the Nelder-Mead method [166, 167]. In a typical loop, a set of initial guesses of the CRSS values were input into the model and the simulation job was submitted. Once the simulation was complete, strains from the 8 selected grains in each sample were compared with the experimental strain results of these grains. The differences between simulated strains and experimental strains were calculated and was aimed to be minimised. The Nelder-Mead algorithm then generated a new set of CRSS to re-run the simulation. This iterative process was carried out until the difference between simulated and experimental strain in the grains was reduced to an acceptable value (below 10%).

Figure 7.5 shows the comparison of the strains within the 8 chosen grains between experiments and simulations. The optimisation method was applied to samples 1-3, after which the difference between simulated and experimental strain in the grains becomes lower than 10%. All 3 samples show good agreement in experimental and simulated strains. The CRSS values of prismatic and basal slip systems were extracted at these three temperatures (as shown in Figure 7.6(a)). CRSS values at room temperature were then used for sample 4. As shown in Figure 7.5(g) and Figure 7.5(h), the simulated strains still fit well with the experimental strains.

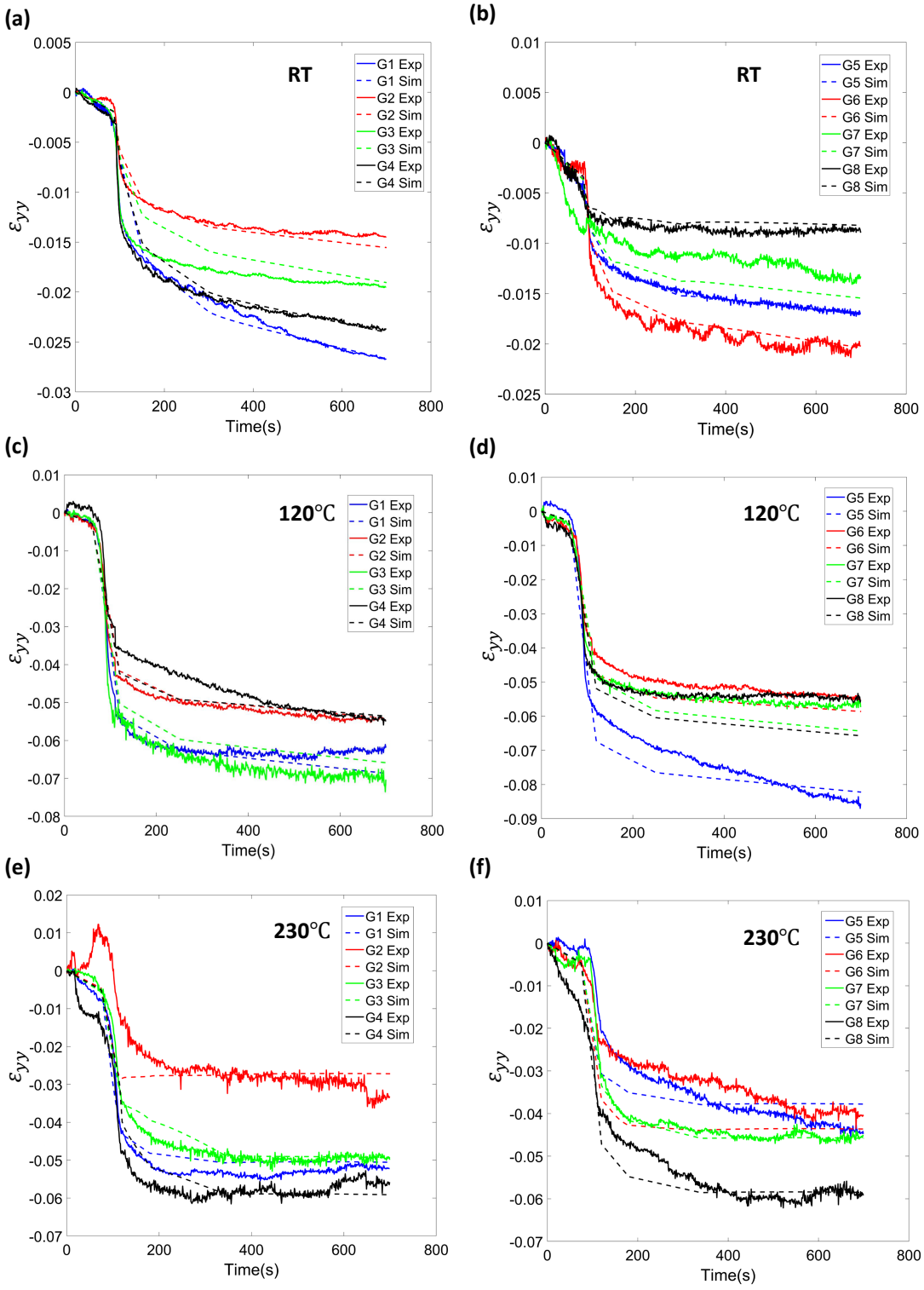
The relationship between τ_α^c and temperature can be fitted using an empirical power law function [168, 169]. The resulting temperature dependence of the CRSS of the prismatic and basal slip systems are given by:

$$\tau_{basal}^c = 1054.6T^{-0.472} \text{ (MPa)} \tag{7.1}$$

$$\tau^{c}_{prism} = 733.8T^{-0.4622} \text{ (MPa)} \tag{7.2}$$

where T is the temperature in °C.

Some results in literature show that the CRSS vs. temperature relationship can be fitted with quadratic functions [17, 170]. However, for this data-set, false minima were found at relatively low temperatures (150-200 °C as shown in Figure 7.6(b)). Although quadratic function can provide a better fitting, the trend of CRSS vs. temperature predicted by quadratic functions cannot reflect the true material behaviour as shown in Figure 7.6(b).


(a)
RT
G1 Exp
G1 Sim
G2 Exp
G2 Sim
G3 Exp
G3 Sim
G4 Exp
G4 Sim
ε_{yy}
Time(s)
(b)
RT
G5 Exp
G5 Sim
G6 Exp
G6 Sim
G7 Exp
G7 Sim
G8 Exp
G8 Sim
ε_{yy}
Time(s)
(c)
120℃
G1 Exp
G1 Sim
G2 Exp
G2 Sim
G3 Exp
G3 Sim
G4 Exp
G4 Sim
ε_{yy}
Time(s)
(d)
120℃
G5 Exp
G5 Sim
G6 Exp
G6 Sim
G7 Exp
G7 Sim
G8 Exp
G8 Sim
ε_{yy}
Time(s)
(e)
230℃
G1 Exp
G1 Sim
G2 Exp
G2 Sim
G3 Exp
G3 Sim
G4 Exp
G4 Sim
ε_{yy}
Time(s)
(f)
230℃
G5 Exp
G5 Sim
G6 Exp
G6 Sim
G7 Exp
G7 Sim
G8 Exp
G8 Sim
ε_{yy}
Time(s)

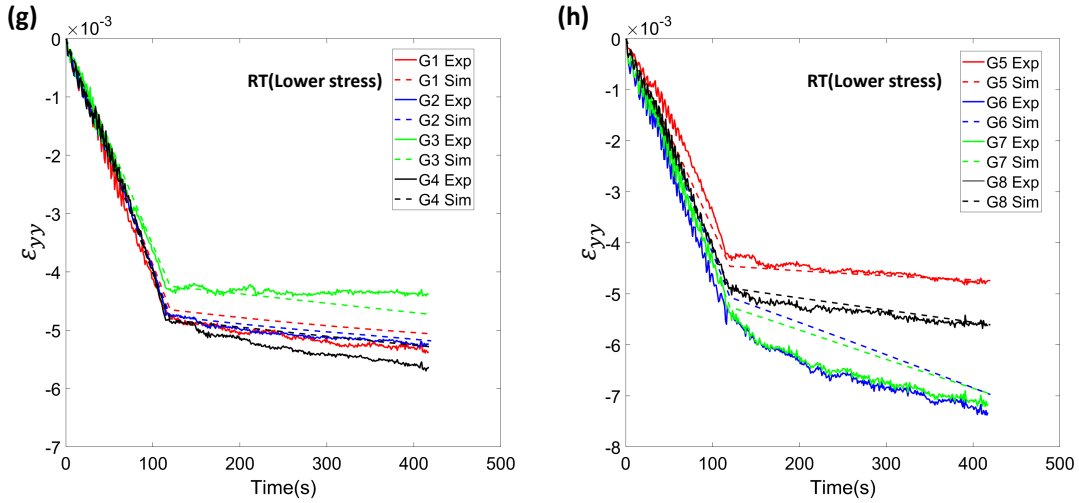


Figure 7.5: Strain vs. time plots of experiments and simulations of (a) sample 1 grain 1-4; (b) sample 1 grain 5-8; (c) sample 2 grain 1-4; (d) sample 2 grain 5-8; (e) sample 3 grain 1-4; (f) sample 3 grain 5-8; (g) sample 4 grain 1-4; (h) sample 4 grain 5-8 (Note that the scales of the vertical axes are different the plots).

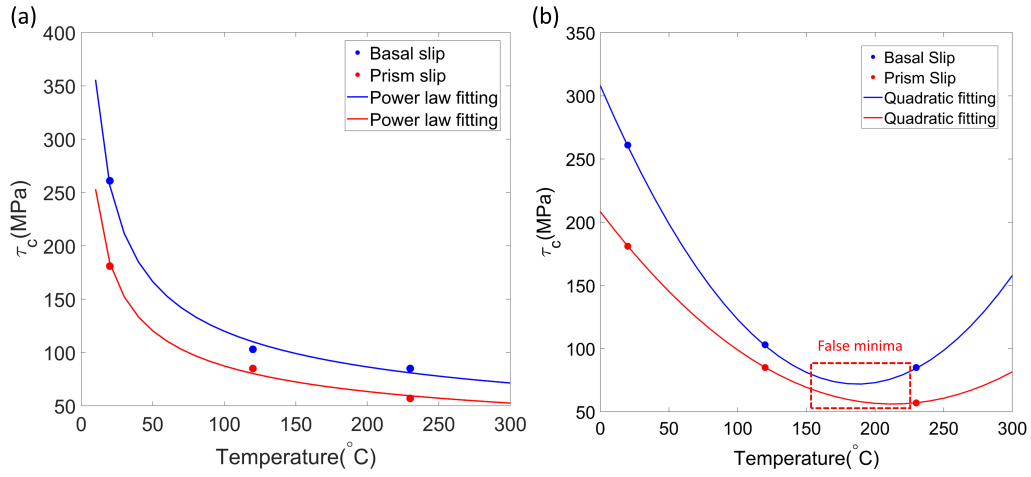


Figure 7.6: Calibrated CRSS values of prismatic and basal slip systems as a function of temperature: (a) fitted with power law functions; (b) fitted with quadratic functions.

7.3.2 Macroscopic stress

Figure 7.7 shows the comparison of macroscopic stresses between experiments and simulations for the four samples. The experimental stress was calculated by dividing the initial sample cross-section area from the force recorded by the mechanical test frame. In simulations, forces were applied by displacement and we simplified the curved strain vs. time curves with several straight line segments (recall Figure 7.2(a)-(c)). This results in the observation of stress relaxation periods in the simulation

stress, particularly for sample 1 and sample 2. Generally speaking, the macroscopic stress for experiments and simulations are in good agreement.

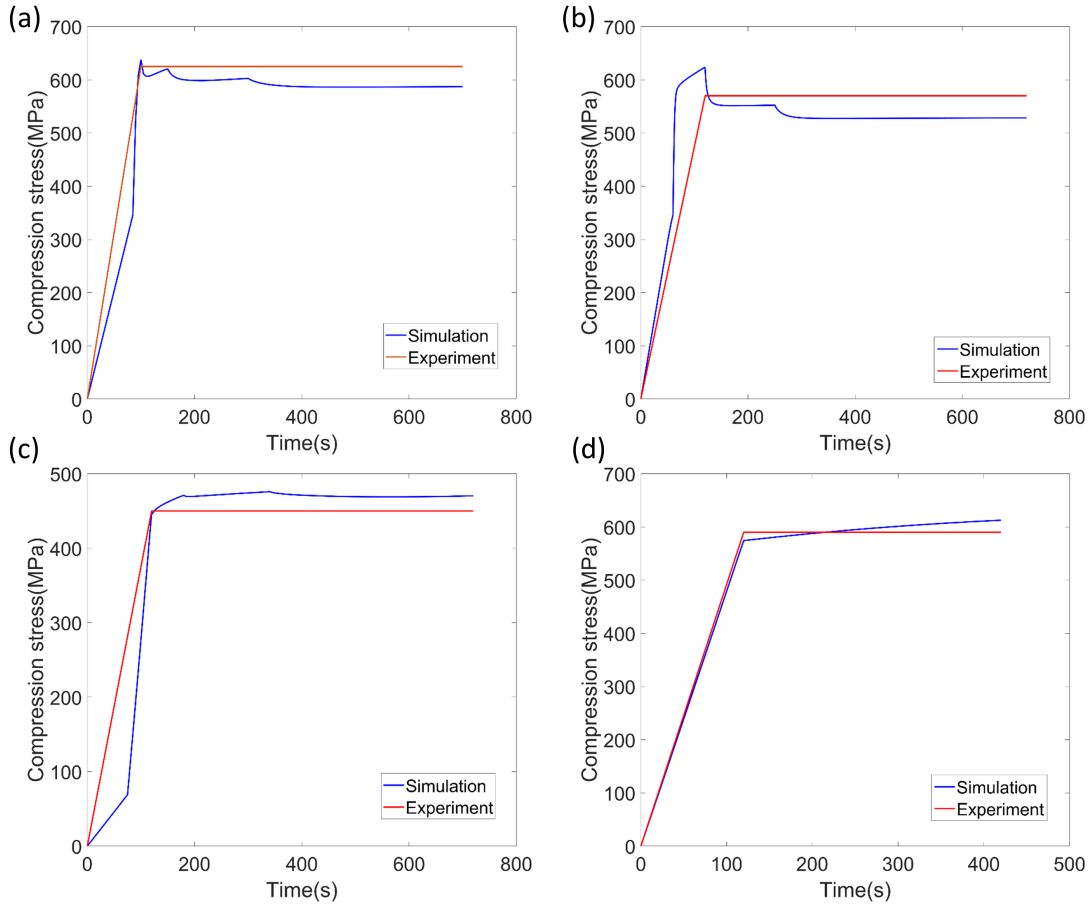


Figure 7.7: Comparison of the macroscopic stresses of experiments and simulations for (a) sample 1 at room temperature; (b) sample 2 at 120°C; (c) sample 3 at 230°C and (d) sample 4 at room temperature.

7.3.3 Slip activity and trace analysis

Figure 7.8 shows the geometrically necessary dislocations (GND) density calculated in the simulation for the three prism and the three basal slip systems in sample 4 at the end of creep. These maps were meant to identify the active slip systems within different grains. At the stress level of sample 4 (below the macroscopic yield), the basal slip was not activated. By contrast, prism slip was activated in some specific grains, as shown by the Prism #1 and Prism #3 GND density in Figure 7.8(d) and (f). There are two regions of interests: pair 1 (grain 5 & 9) represents the 'rogue grain pair' where only one grain (grain 9) activates plastic slip; pair 2 (grain 6 & 7) represents the 'non-rogue grain pair' where both grains activate plastic slip.

The simulated slip systems activities matches well with the experimental observations. Figure 7.9 shows the comparison of grain morphology of the two grain pairs before and after the experiment. Slip traces were observed in grain 6, grain 7 and grain 9 but not in grain 5. All the newly generated slip lines were found to be parallel within each grain, indicating only one slip system was activated for each grain. This agreed well with the simulated slip activity, where Prism 1 was activated in grain 7, Prism 3 was activated in grain 6 and grain 9. Slip lines simulated by the CPFE model were plotted for better comparison with the experimental observations. To do this, we used the method introduced by Guery *et al.* [171], where the slip plane normal, $\boldsymbol{n}_\alpha$ of the active slip system α was rotated into the sample coordinate system by the grain rotation matrix, $\boldsymbol{R}$. The slip line vector, $\boldsymbol{t}_\alpha$ was obtained by the cross product of the rotated slip plane normal $\boldsymbol{n}_\alpha^s$ and the sample surface normal $\boldsymbol{e}_z$ as:

$$\boldsymbol{t}_\alpha = \boldsymbol{n}_\alpha^s \times \boldsymbol{e}_z \tag{7.3}$$

These line segments from every element within grain 6, grain 7 and grain 9 were then plotted (as shown in Figure 7.9). There is good agreement between alignment of slip traces calculated in the model and experimental observation. The length of the segment was proportional to the magnitude of the averaged GND density of each element. The ratio of the averaged GND density in grain 6, grain 7 and grain 9 was

approximately 8:10:5 (i.e. the slip activity was the highest in grain 7 and the lowest in grain 9). This is also consistent with the slip line density observed in these grains.

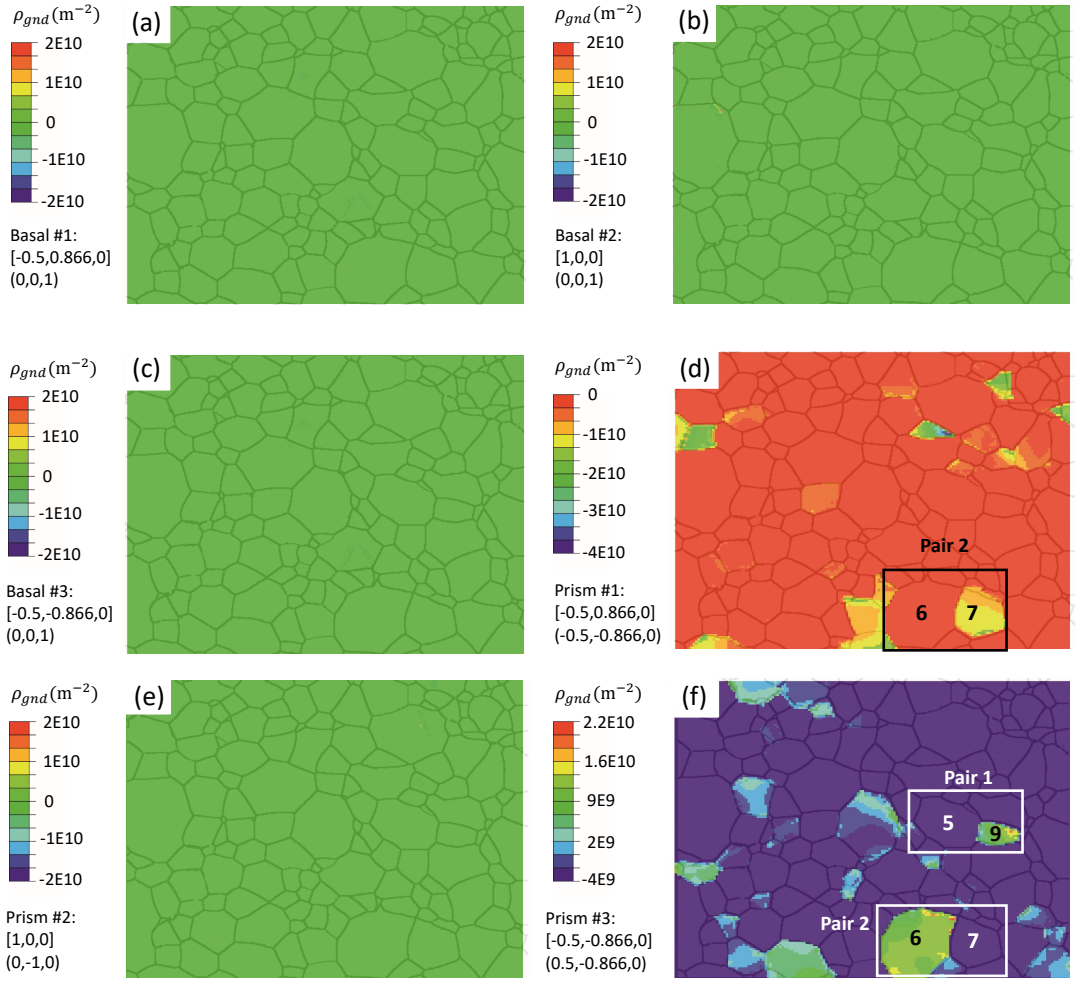


Figure 7.8: Slip activity of prism and basal slip in sample 4 at room temperature, clear contrast were observed in (d) and (f) showing the plasticity in certain grains, where Prism #1 was activated in grain 7 and Prism #3 slip was activated in grain 6 and grain 9.

7.3.4 Load shedding

As shown in Figure 7.10(a) and 7.10(b), along path A and path B in grain pair 1 and 2 respectively, the load shedding effect in 'rogue' and 'non-rogue' grain pairs has been studied. Figure 7.10(c)-(h) show the stress evolution along the paths at 3 different simulated temperatures. At room temperature, load shedding was obvious in the 'rogue' grain pair (pair 1). Compared to the start of the creep loading,

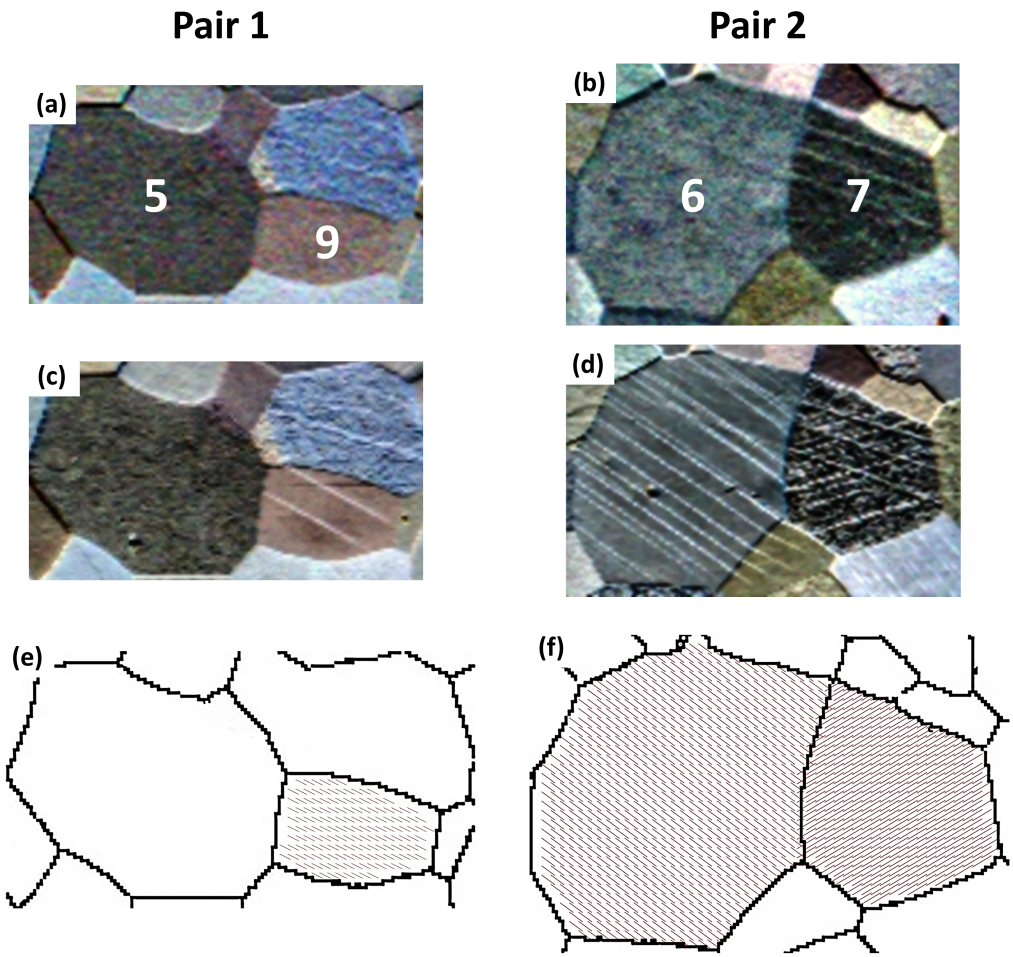
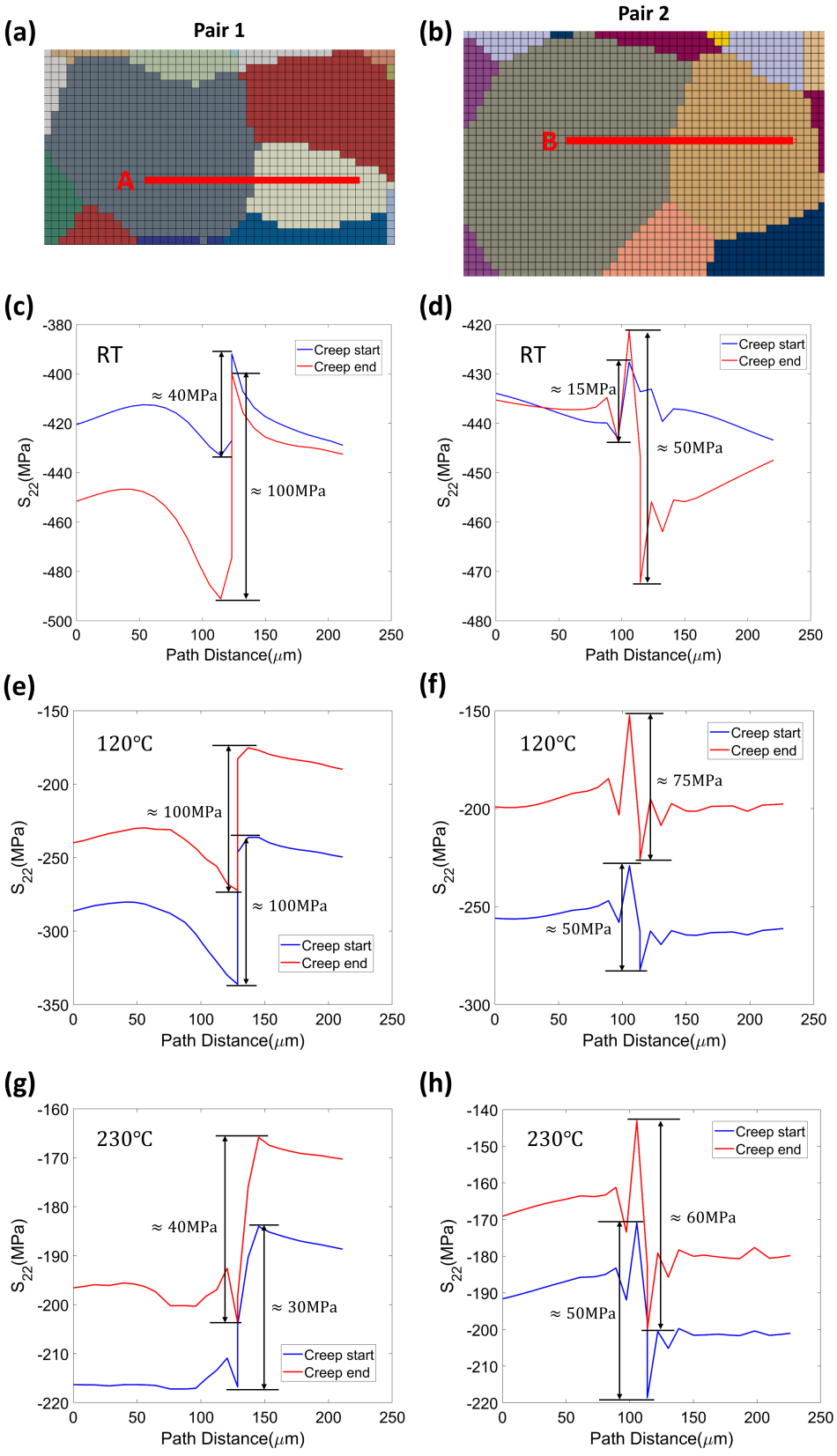


Figure 7.9: Images of the two grain pairs before and after the creep test and simulated slip traces from the CPFE model.

the stress at the end of creep within the 'hard' grain was found to increase while the stress within the 'soft' grain remained approximately at the same level. As a result, the stress difference near the grain boundary increased to a higher level of approximately 100 MPa. In comparison, load shedding was not as significant in the 'non-rogue' grain pair, where stress changes in both grains before and after the creep are smaller and the stress difference at the grain boundary after creep was only approximately 50 MPa.

Higher temperature simulations have been performed on the model of sample 4 for better comparison, the parameters (CRSS, ΔF, ΔV and elastic constants) were changed to parameters at 120 °C and 230 °C but the boundary condition remained the same. At higher temperatures, the stresses in all these four grains

were found to relax after creep, indicating plasticity. This is also confirmed by the increase of GND density in these grains as temperature rises and shown in Figure 7.10(i) and 7.10(j). GND densities at the grain boundaries were significantly higher than that within the grains, showing a dislocation pile-up [6, 172] at the grain boundaries. For the rogue grain pair, the initial stress difference across the grain boundary increases slightly for $T = 120°\text{C}$ compared to room temperature, then drops at higher temperature. But during the load hold, the stress difference does not increase as some plasticity is now also possible in the 'hard' grain (non-zero GND density in the 'hard' grain in Figure 7.10(i)).


(a)
Pair 1
A
(b)
Pair 2
B
(c)
RT
≈ 40MPa
≈ 100MPa
Creep start
Creep end
S22(MPa)
Path Distance(μm)
(d)
RT
≈ 15MPa
≈ 50MPa
Creep start
Creep end
S22(MPa)
Path Distance(μm)
(e)
120°C
≈ 100MPa
≈ 100MPa
Creep start
Creep end
S22(MPa)
Path Distance(μm)
(f)
120°C
≈ 75MPa
≈ 50MPa
Creep start
Creep end
S22(MPa)
Path Distance(μm)
(g)
230°C
≈ 40MPa
≈ 30MPa
Creep start
Creep end
S22(MPa)
Path Distance(μm)
(h)
230°C
≈ 60MPa
≈ 50MPa
Creep start
Creep end
S22(MPa)
Path Distance(μm)

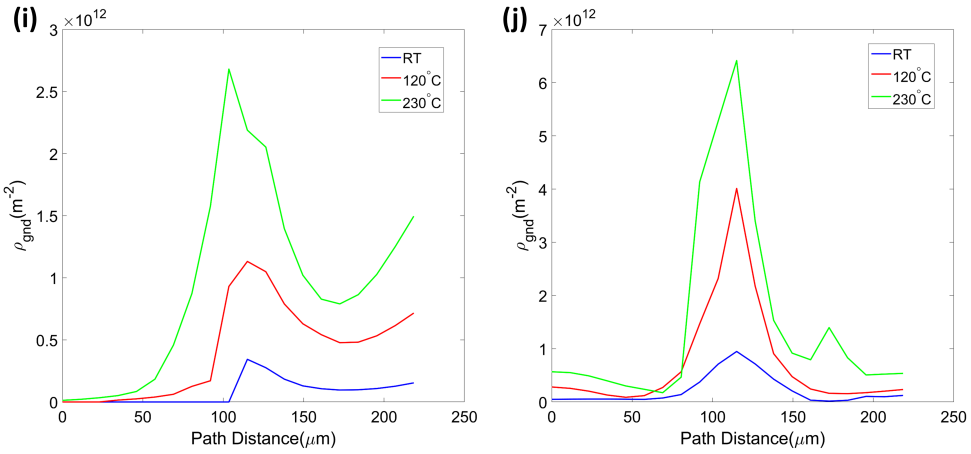


Figure 7.10: Path within the grain pairs of (a) pair 1 (path A); (b) pair 2 (path B); S_{22} component (along the loading direction) of (c) path A at room temperature; (d) path B at room temperature; (e) path A at 120 °C; (f) path B at 120 °C; (g) path A at 230 °C; (h) path B at 230 °C; GND density at the end of creep of (i) path A and (j) path B. (Note that the vertical axes are not the same in each plot).

7.4 Discussion

The CRSS values obtained in this work are in sound agreement with the values reported in literature [9, 17, 46, 36, 44, 173], but are perhaps slightly lower particularly at elevated temperatures. Two reasons for these differences could be: (1) the Ti6Al alloy tested in this work had lower Al content ($\approx$ 5.8 wt%) compared to that in the literature, (2) strain rates in our work extend to lower values. Aluminium, as a common substitutional alloying addition to Ti, has proved to have strengthening effect on both basal and prism slip [46, 44, 173, 174]. The strengthening is more marked for prism slip however so that the strengths of prism and basal slip systems are more similar in Ti6Al than in pure Ti.

The grain orientations of the two grain pairs are shown in Figure 7.11. The angles between the *c*-axis and the loading direction were 56° for grain 5, 83° for grain 9, 74° for grain 6 and 73° for grain 7. Although the grain pair 1 behaved as a 'rogue' grain pair in this experiment, it is not a typical hard-soft grain combination. In grain pair 1, grain 9 was in 'soft' orientation but grain 5 was not a typical 'hard' grain and in fact it yields in the simulations for 120°C and 230°C. This is consistent with the observation by Brandes *et al.* [163], where dwell fatigue facet was observed

in a material lacking 'hard' orientated grains (with their c-axis nearly parallel to the loading direction). These non-typical 'rogue' grain pair could also lead to dwell fatigue failure. Due to the stress level being quite low to activate basal slip in this experiment, grains oriented favourably for prism slip systems were classified as 'soft' grains. Xu *et al.* [172] suggested that the cold dwell fatigue and the dwell debit is sensitive to the dwell stress, which agrees well with the observations in this work. The origin of the dwell debit is the activation of slip systems, resulting in an accumulation of plastic strain during the stress dwell, which leads to load shedding from 'soft' grains to neighbouring 'hard' grains. High stress difference at the soft-hard grain boundary and stress increase in the 'hard' grain were observed and believed to lead to a nucleation of facets within the 'hard' grain [9, 162, 175]. As external stress changes, the activation of slip systems changes, thus the definition of 'soft' and 'hard' grains will vary dynamically. In reality the binary hard-soft nomenclature is in fact a continuum of varied relative grain strengths which are affected by external conditions such as temperature and macroscopic stress level.

Schmid factor analysis of these grains can be found in Table 7.2. The Schmid factor of the active slip systems are marked as red in the table. It is found that the actual slip systems activated were not always the ones with the highest Schmid factor. This implies that the local stress states is different from the macroscopic stress state arising from the loading direction on the sample itself. The activation of slip systems is thus not always dependent on only that particular grain orientation with respect to the macroscopic load direction, but the local stress states plays a more crucial role. As a result, predicting the 'hard' and 'soft' grains based on macroscopic load direction and grain orientations in polycrystal samples is not always viable.

In Figure 7.9, grain 6 and the grain at its bottom right have very similar crystallographic orientations (refer to Figure 7.1 along the loading direction). Slip transfers easily across the boundaries between these similar orientated grains, which behave as if the boundary between them was not present. Partially correlated group of grains are often present in Ti alloys and are known as macrozones and increase the effective grain or structural unit size [176, 177]. Creep can happen

in a 'soft' macrozone that is orientated favourably for slip, which leads to load shedding to a neighbouring 'hard' macrozone orientated poorly for slip and crack can initiate within the 'hard' macrozone [178, 179, 180].

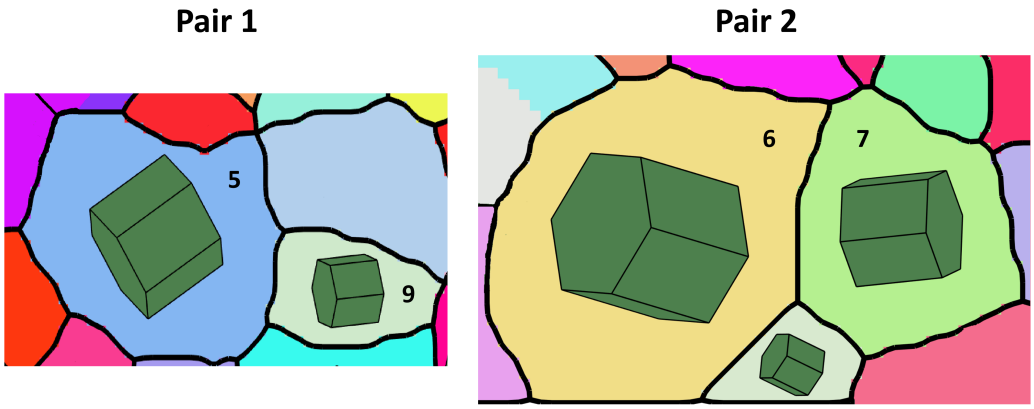


Figure 7.11: Grain orientations of the two grain pairs.

Table 7.2: Schmid factor of the three prism slip systems in the two grain pairs, the active slip systems were marked as red.

	Grain 5	Grain 9	Grain 6	Grain 7
Prism 1	0.026	0.356	0.374	0.299
Prism 2	0.095	0.170	0.110	0.024
Prism 3	0.121	0.185	0.264	0.061

Load shedding was found to be sensitive to temperature. As the energy required to activate basal and prismatic slip decreases when temperature increases [135], more plasticity was activated at higher temperatures. Stresses were found to relax in both 'rogue' and 'non-rogue' grain pairs. Although the stresses were relaxed, the differences in stress at the grain boundaries still exist. Since the stress level in each grain pair was different, direct comparison of the stress difference was not possible. Instead, the percentage of stress difference was calculated by dividing the averaged stress along the paths. Figure 7.12(a) shows the percentage of stress difference at the grain boundaries at the end of the creep against temperature. At room temperature and 120 °C, stress differences in grain pair 1 were significantly higher than that in grain pair 2. At 230 °C, the stress differences in the two pairs altered but both of them

reduce to relatively low levels. It was found that in both grain pairs, the percentage stress difference increased as temperature increased to 120 °C and decreased as the temperature further increased to 230 °C. Among the three temperature assessed, 120 °C was found to be the worst case scenario. To reveal the mechanism leading to this observation, the activity of slip systems need to be quantified.

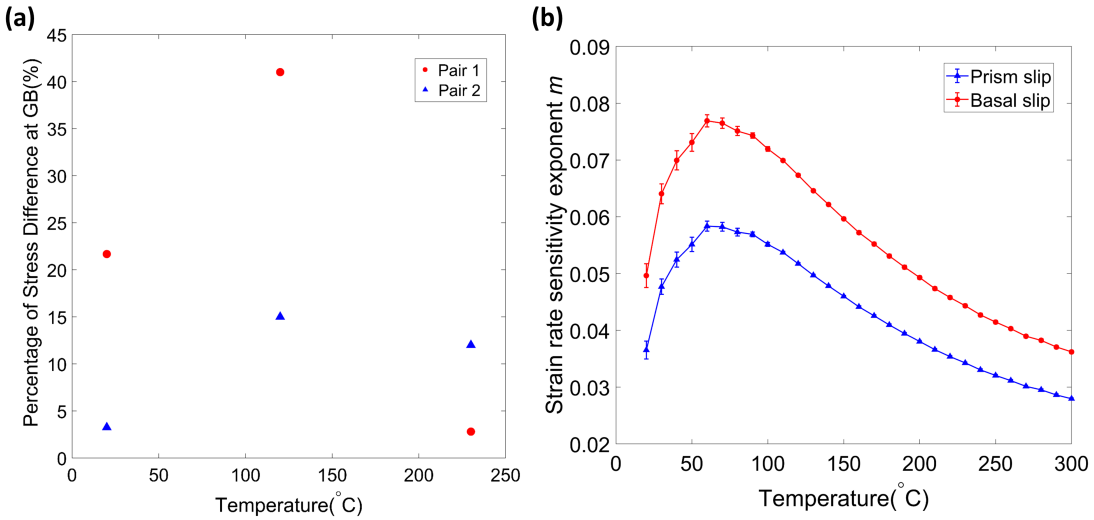


Figure 7.12: (a) Percentage of stress difference at the grain boundaries of the two grain pairs at the end of the creep vs. temperature; (b) Strain rate sensitivity of basal and prism slip vs. temperature.

Strain rate sensitivity (SRS) are often used to express the slip activity in literature and it is considered to be a significant factor that controls load shedding [69]. The strain rate sensitivity exponent, m, is calculated by:

$$m = \mathrm{d}(\log(\sigma))/\mathrm{d}(\log(\dot{\varepsilon})) \tag{7.4}$$

which corresponds to the gradient of a $\log(\sigma)$ vs. $\log(\dot{\varepsilon})$ plot. The m value is crystallographic orientation dependent [36], where m values of 'soft' grains are typically higher than that of 'hard' grains at room temperature [69, 104]. This phenomenon is deemed to be related to the different SRS in different slip systems, which is confirmed by Jun *et al.* [67], who reported that in α-Ti prism slip had higher SRS ($m = 0.07$) over basal slip ($m = 0.03$) at room temperature. Results in Chapter 6 shows that the SRS is also temperature dependent and higher SRS

of a slip system leads to more creep strain accumulation during a stress dwell (i.e. higher activity of the slip system). We attempted to evaluate the SRS for the two major slip systems (prism and basal) at different temperatures in order to interpret the worst case scenario temperature.

The three temperature dependent key parameters ΔV, ΔF and τ_c were fitted with quadratic, linear and power law functions [17, 135, 170, 129, 168, 169] so that the values can be predicted at different temperatures other than these experimentally tested (recall Figure 7.4 and Figure 7.6). The three parameters were calculated for every 10 °C between the range of 20 °C to 300 °C and were inserted into the slip law (recall Equation 3.1). This allowed applied shear stress, τ_α against shear strain rate, $\dot{\gamma}_\alpha$ to be plotted at log scale over a strain rate range of 10^{-7} to 10^{-5} s^{-1} (the creep strain rate range observed in this work). Linear fitting was performed on the $\dot{\gamma}_\alpha$ vs. τ_α curves and the gradients were obtained to represent the m values. The linear fitting errors are shown by the error bars. The strain rate sensitivity variation against temperature is shown in Figure 7.12(b). More details can be found in the previous work [135]. Prism slip has higher SRS over basal slip between room temperature and 300 °C. The SRS as a function of temperature for both prism and basal slip follow the same trend as the stress difference at grain boundaries (see Figure 7.12(a)). The peak values of m for both prism and basal slip can be expected at approximately 80 °C. The peak temperature is in remarkable agreement with the worst case scenario temperature for dwell debit from the experience of aero engine industry (between 90 °C and 120 °C) [17, 159]. The worst dwell debit was caused by the highest SRS of the two major slip systems (i.e. the highest slip activities). During stress dwell at the worst case scenario temperature, high slip activity results in a greater creep strain accumulation in the 'soft' grains which in turn cause dislocation pile-up at the soft-hard grain boundaries and load shedding which generates a high stress difference at the grain boundaries. At higher temperatures (e.g. above 200 °C), the SRS of both prism and basal slip systems reduced to lower levels compared to room temperature. The slip activity

of the two major slip systems were low at higher temperatures, which explained the phenomenon that cold dwell fatigue diminished at temperatures above 230 °C [17].

7.5 Summary

In this Chapter, load shedding was studied from experimental perspective, evidence of load shedding during cold dwell was successfully captured.

This work utilised DIC technique and CPFE modelling to study the temperature effect on cold dwell fatigue in Ti6Al alloy. CRSS of the two major slip systems (prism and basal) of α-Ti were quantified as a function of temperature by calibrating the CPFE model from experimentally measured strain evolution in individual grains during creep. Load shedding was clearly observed in the 'rogue' grain pair, resulting in an increase in stress within the 'hard' grain and high stress difference at the grain boundary. As temperature increased, the stress difference became larger at 120 °C. At higher temperatures (above 230 °C), the stress difference dropped to a reasonably low level.

Grain orientation analyses showed that the definition of 'soft' and 'hard' grain would dynamically vary depending on the applied stress and operating temperature, which results from the activation of different slip systems. Local stress state plays a more important role in the activation of slip systems compared to grain orientations with respect to macroscopic load direction in large polycrystals.

The strain rate sensitivity for prism slip is higher than that of basal at temperatures between room temperature and 300 °C. The SRS of both prism and basal slip show an increase-and-decrease trend as temperature increases. The peak SRS is expected to be at approximately 80 °C for both prism slip and basal slip. The worst case scenario temperature for dwell debit (between 90 °C and 120 °C) can be explained by the highest SRS and slip activity of the two major slip systems at these temperatures.

8

Conclusions and future works

Contents

8.1 Conclusions 135
8.2 Future works 138

The broad aim of this work was to investigate cold dwell effect in Ti alloys. The main conclusions from each chapter are now summarised and used to form a theory for understanding the mechanism of cold dwell fatigue and key factors that affect this critical technological problem. Finally, this chapter ends with suggestions for future work.

8.1 Conclusions

Stress relaxation tests were performed at four different temperatures (room temperature, 75 °C, 145 °C and 250 °C) on three major alloy systems: commercially pure titanium (two alloys with different oxygen content), Ti-6Al-4V (two alloys with different portion of β phase) and Ti-6Al-2Sn-4Zr-xMo (two alloys with different Mo content and portion of β phase). Key parameters controlling the time dependent plasticity were determined as a function of temperature from the macroscopic stress relaxation results. Commercially pure Ti has the lowest strength but the highest

strain rate sensitivity, as a result, the dwell fatigue effect is the strongest among the three alloy systems. Ti-6Al-4V has both moderate strength and strain rate sensitivity, dwell fatigue effect was not significantly affected by the fraction of β phase in Ti64. Ti-6Al-2Sn-4Zr-xMo system has the highest strength but the lowest strain rate sensitivity, dwell fatigue effect was highly suppressed in these alloys. Oxygen has excellent strengthening effect but enhance dwell fatigue effect. Mo has both strengthening effect and sound dwell fatigue resistance effect. At dwell fatigue stress condition (when critical stress is just exceeded), both the contribution of the key parameters to strain rate and strain rate sensitivity sharply decreased in all six alloys when temperature is above 145°C. As a result, plastic strain accumulation at 250°C is at very low level, dwell fatigue is suppressed at high temperature.

To understand the mechanism in greater details, an *in situ* X-ray diffraction method was used to measure the lattice strain (from 21 diffraction plane families) evolution in a commercially pure Ti grade 4 sample during stress relaxation at room temperature. During loading, observation of individual lattice strains was used to identify the behaviour of different basal and prismatic slip systems. Combining with the crystal plasticity finite element analysis, key parameters in the slip rule for each slip system were isolated and determined. The slip activation energy, ΔF, and critical resolved shear stress, τ_c, were found to be higher for basal slip over prismatic slip, indicating basal slip is more difficult to activate than prismatic slip. Coupled to this is a higher strain rate sensitivity for prism slip at the relatively low strain rates. The deformation of Ti is highly dependent on the crystallographic orientation, as the c-axis declination angle increased from 0° to 90°, the grain orientation changed from 'hard' to 'soft'. Both plastic strain accumulation and strain rate sensitivity were found to increase as the crystallographic orientation changes from 'hard' to 'soft'. This shows strong possibility for load shedding to happen.

The *in situ* X-ray diffraction combined with CPFE modelling was then extended to higher temperatures (75 °C, 145 °C and 250 °C) and different oxygen content (CP-Ti grade 1 with lower oxygen content and CP-Ti grade 4 with higher oxygen content) samples. The magnitude of stress relaxation (plastic strain accumulation)

vs. temperature was found to have similar trend for both grade 1 and grade 4, where plastic strain accumulation increased as temperature increased from room temperature to 75 °C and then decreased as temperature further increased to 250 °C. This indicated the worst-case scenario temperature is about 75 °C in the CP-Ti alloys. The CRSS and thermal activation energy were both greater for basal slip over prism slip except at 250 °C in grade 4 where the trend is reversed. Due to the greater strengthening effect of oxygen on prism slip the ratio of CRSS values for grade 4 decreases significantly with temperature, while it does not for grade 1 (it may even increase slightly). Combined the effects of oxygen on the main slip systems, the plastic strain accumulation during a stress relaxation period was enhanced by oxygen.

DIC technique and CPFE modelling were utilised to study the effect local grain combination and temperature on cold dwell fatigue in a coarse grain Ti6Al alloy. CRSS of the two major slip systems (prism and basal) of α-Ti were quantified as a function of temperature by calibrating the CPFE model from experimentally measured strain evolution in individual grains during creep. Load shedding was clearly observed in the 'rogue' grain pair, resulting in an increase in stress within the 'hard' grain and high stress difference at the grain boundary. As temperature increased, the stress difference became larger at 120 °C and at higher temperatures (above 230 °C), the stress difference dropped to a reasonably low level. This trend is similar to the plastic strain accumulation vs. temperature observed in CP-Ti samples. Both of them implies that the worst-case scenario temperature for cold dwell effect is between 75 °C and 120 °C. Grain orientation analyses showed that the 'soft' and the 'hard' grain would dynamically vary depending on the applied stress and operating temperature, which results from the activation of different slip systems. Local stress state plays a more important role in the activation of slip systems compared to grain orientations with respect to macroscopic load direction in large polycrystals.

Strain rate sensitivity is a crucial factor governing the time dependent plasticity and cold dwell effect. In the context of cold dwell fatigue, higher strain rate sensitivity leads to stronger activity of plastic slip and thus more plastic strain accumulation. The strain rate sensitivity for prism slip is higher than that of basal

at temperatures between room temperature and 300 °C, indication prism slip is more active than basal slip. With the knowledge of the key parameters (CRSS, ΔF and ΔV) in the slip law at different temperatures, prediction of the peak SRS is possible (as discussed in Chapter 7). It is found that the peak SRS is expected to be at approximately 80 °C for both prism slip and basal slip. The worst case scenario temperature for dwell debit can then be explained by the highest SRS and slip activity of the two major slip systems at these temperatures.

8.2 Future works

In order to fully understand the cold dwell fatigue problem in Ti alloys and provide suggestions for future alloy design and processing to address this complex issue, some suggestions for future work are listed.

Substitutional Al atoms are the most important alloying additions and give greater strengthening for the softer prism slip than for basal [36]. The addition of Al of sufficient concentration combined with ageing treatments can generate fine coherent α_2, while simple solutionising and slow cooling can introduce short range ordering (SRO) both of which increase slip planarity and reduce room temperature creep rates [136]. The effect of Al and presence of SRO should be investigated.

Commercial alloys also contain β stabilisers to provide microstructure control. In mill annealed conditions, the microstructure is predominately globular primary α with β at triple junctions and grain boundaries. The BCC β phase is also likely to contribute some rate dependency to the deformation; however, its significance is unknown. Commercial alloys may also exhibit finer colony microstructures; thin layers of β separating α lamellae. Slip transfer processes at the α/β interfaces is another interest to be studied.

This work mainly focused on samples with equiaxed grain morphology; however, various grain morphology could appear via different processing routes. Different grain morphology leads to different areas of grain boundaries, the effect on cold dwell fatigue remains unclear. In addition, macrozones are common in Ti alloys, which

could also affect the time dependent plasticity. The effect of grain morphology and macrozones need to be understood.

Deformation in Ti alloys is highly anisotropic, which is originates from the HCP crystal structure. It is found that cold dwell fatigue is strongly affected by the crystal orientations (i.e. behaviour of 'hard' and 'soft' grains are different during dwell loading). As a result, material texture play an important role in the deformation of Ti alloys. It is also possible that the cold dwell effect is affected by the material texture. It will be useful to compare the effect of material texture on cold dwell fatigue (e.g. changing the loading direction by 90° on a strong textured raw material).

Appendices

A
Appendices

Contents

A.1 Evaluation of the effect of residual strain 143
A.2 Justification of element size using lattice strain evolution 145
A.3 Sensitivity of lattice strain with changing parameters 147
A.4 Sensitivity of lattice strain to the initial orientation assignment 149
A.5 Variation of the dislocation density 151
A.6 Validation of the cubic grain morphology 154
A.7 Justification of the depth of the model 155
A.8 Fitting errors and optimisation efficiency 156
A.9 DIC error analysis 156
A.10 Peak width study 158

A.1 Evaluation of the effect of residual strain

The noise level of the lattice strain results were determined by fitting the experiment results with smooth curves (see Figure A.1). The Root-mean-squared deviation of the two curves was used to represent the noise level of the experimental result.

The residual strain was introduced into the model by adding a quenching step (from 400 °C to room temperature) prior to the mechanical loading step, as shown in Figure A.2(a), the initial residual strain levels were in approximately

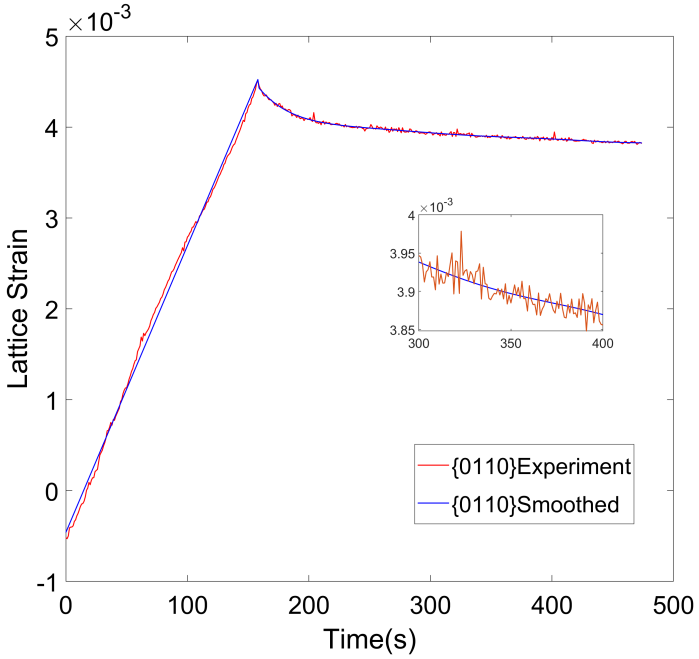


Figure A.1: Determination of noise level of experimental results of the $\{01\bar{1}0\}$ lattice strain.

the same range as the experiment (see Figure A.2(b)). There is little difference in the modelled residual strain in the $\{01\bar{1}0\}$, $\{01\bar{1}1\}$ and $\{11\bar{2}2\}$ planes, however, the experimental results show the difference among these three planes are much larger. It is possible that the residual strain in the sample was introduced not only by thermal but also by mechanical processes. The thermal expansion coefficient used in the model is stated in Table A.1.

Table A.1: Single crystal thermal expansion tensor coefficients for Ti [142, 148].

Coefficient	11	22	33
α	1.8×10^{-5}	1.8×10^{-5}	1.1×10^{-5}

As the reflection-to-reflection variation was not so well captured by the model and the effects are in any case relatively small, we sought to simplify the analysis. To do this, we compared the change in lattice strain (the lattice strain in response to the external load) results from the model with introduced residual strain and a strain-free model running with the same material parameters. As shown in Figure A.3, the difference in lattice strain and macroscopic stress is small and less

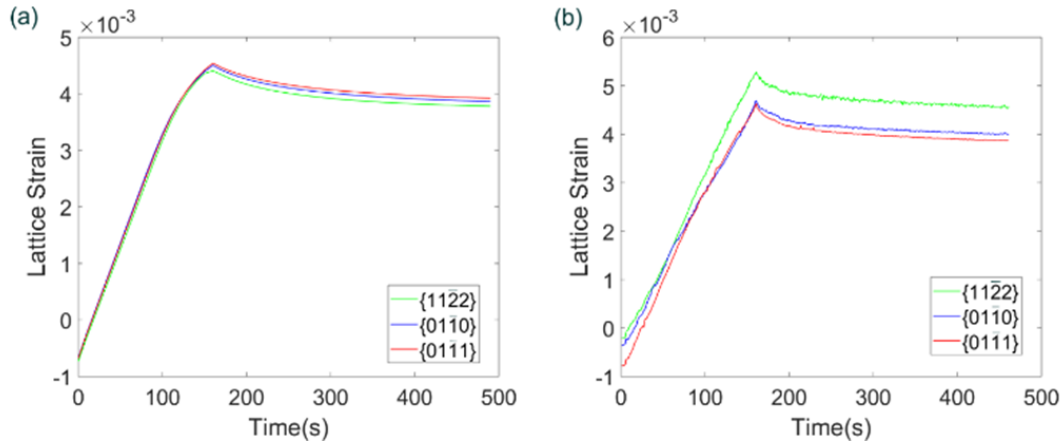


Figure A.2: (a) Modelled lattice strain with residual strain introduced by a quenching step; (b) Experimental lattice strain results.

than the noise of the experimental result (see Table A.2). Therefore, the residual strain is considered to be negligible in this work.

Table A.2: Comparison of the lattice strain difference caused by initial residual strain and noise of the experimental lattice strain results.

	$\{01\bar{1}0\}$	$\{01\bar{1}1\}$	$\{11\bar{2}2\}$
Difference caused by residual strain	8.1×10^{-6}	1.4×10^{-5}	4.9×10^{-5}
Noise of experimental result	4.9×10^{-5}	6.3×10^{-5}	7.4×10^{-5}

A.2 Justification of element size using lattice strain evolution

Five polycrystal models each with 512 grains shown in Figure A.4 were simulated with the same texture as the synchrotron stress relaxation test sample shown in Figure 5.1 and subjected to a uniaxial stress followed by a strain hold (same as the simulations shown in Figure 5.5(b)). Five models each had different mesh densities to justify the element size selected in the simulation. Lattice strain evolution of the $\{01\bar{1}0\}$ plane was compared with the finest mesh size model (6×6×6 elements per grain) as shown in Figure A.5 The results show that 2×2×2 and 3×3×3 elements per grain models show significant difference compared to the 6×6×6 model, and the lattice strain relaxation curves for both of them are above that of the 6×6×6 model. However, as the number of elements increased to 4×4×4 and 5×5×5 elements per

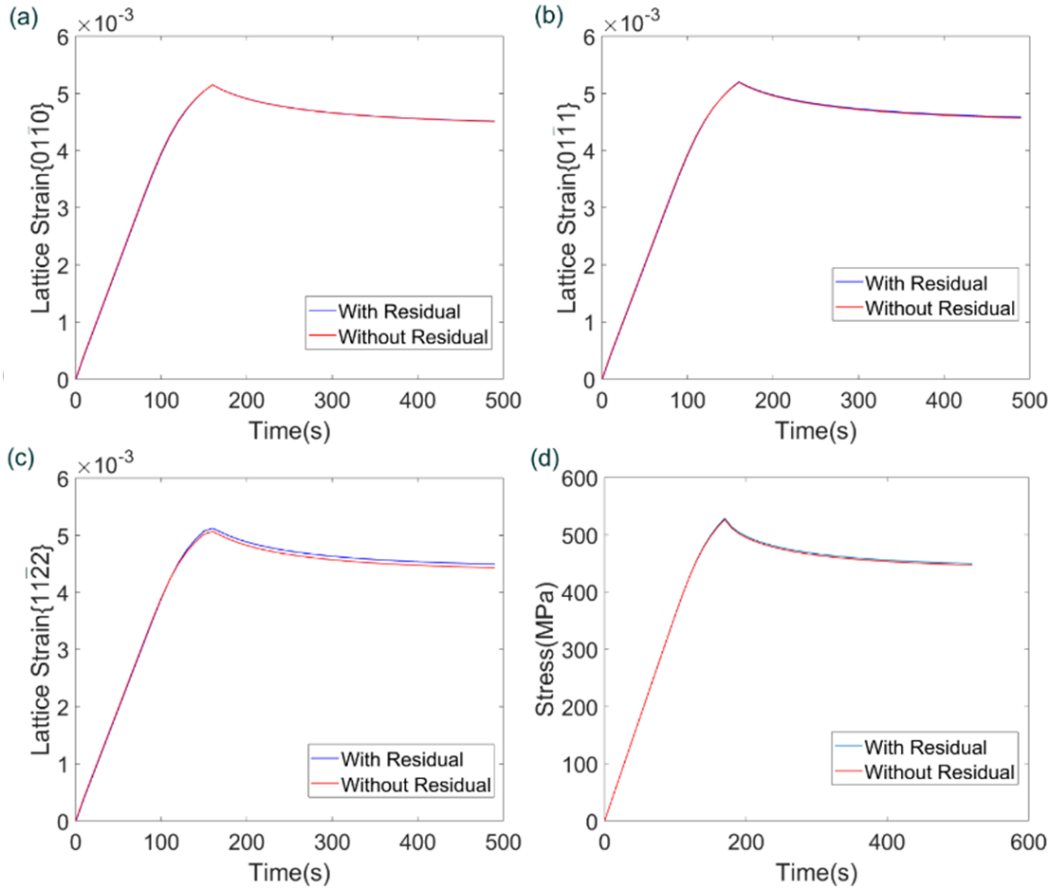


Figure A.3: Comparison of the model with and without residual strain of (a) $\{01\bar{1}0\}$ lattice strain; (b) $\{01\bar{1}1\}$ lattice strain; (c) $\{11\bar{2}2\}$ lattice strain; and (d) Macroscopic stress.

grain, little change in the relaxation curves were observed. Although the differences between the simulation outputs are systematic, the root-mean-squared deviation of the lattice strain output from the five models were calculated using the 6×6×6 model with the finest element size as the reference. Figure A.6 shows the deviation of the simulation results as a function of number of elements per grain. The red dashed line in Figure A.6 illustrates the mean error of the experiment results, and it is clear that for the 4×4×4 elements per grain model, the mesh convergence issues were smaller than the experimental noise, and so this was assumed sufficient for simulations presented in this paper.

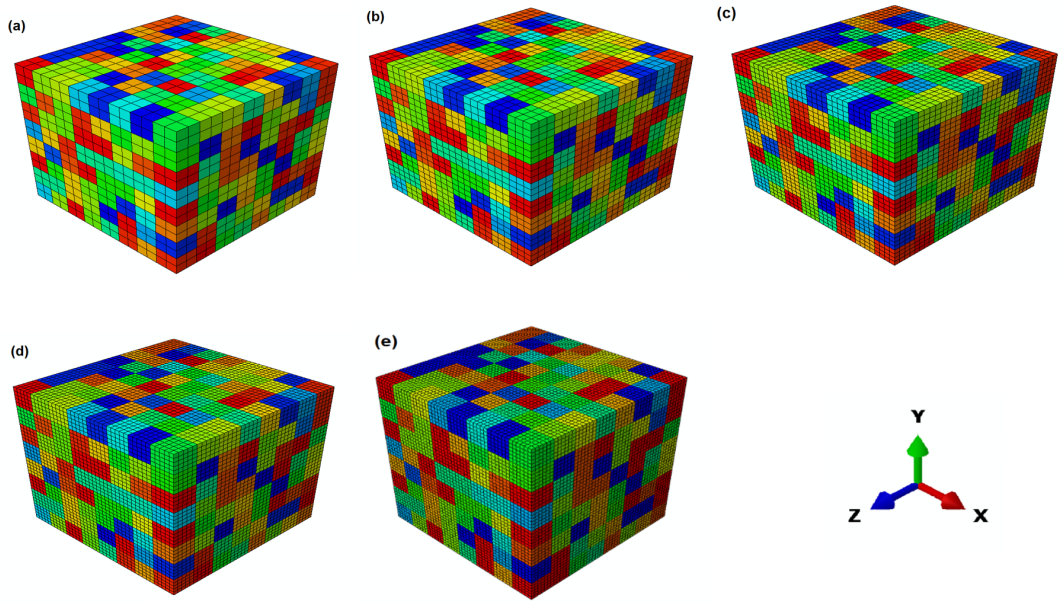


Figure A.4: The range of polycrystal models with differing number of elements within each grain (a) 2×2×2 elements; (b) 3×3×3 elements; (c) 4×4×4 elements; (d) 5×5×5 elements; (e) 6×6×6 elements, which are used to justify the mesh size.

A.3 Sensitivity of lattice strain with changing parameters

Efforts were made to study the effect of changing the CRSS of pyramidal slip on the lattice strain relaxation curves, the results are shown in Table A.3. The root-mean-square deviation (RMSD) was calculated for the $\{01\bar{1}0\}$ lattice strain with CRSS for pyramidal slip set to be 2 times, 3 times and 4 times the value of basal slip, compared to the $\{01\bar{1}0\}$ lattice strain with pyramidal slip completely switched off. The results indicate that there was negligible activity of pyramidal slip in this experiment.

Table A.3: RMSD of the $\{01\bar{1}0\}$ lattice strain with different CRSS of pyramidal slip.

$\tau_c^{pyramidal}$(MPa)	$2\times\tau_c^{basal}$	$3\times\tau_c^{basal}$	$4\times\tau_c^{basal}$
RMSD to no pyramidal slip	1.03×10^{-8}	0	0

Figure A.7 shows the root-mean-square deviation between modelled lattice strain with changing a certain parameter and original modelled lattice strain. Compared to ΔF and τ_c, ΔV results in a significantly less difference (about two order of

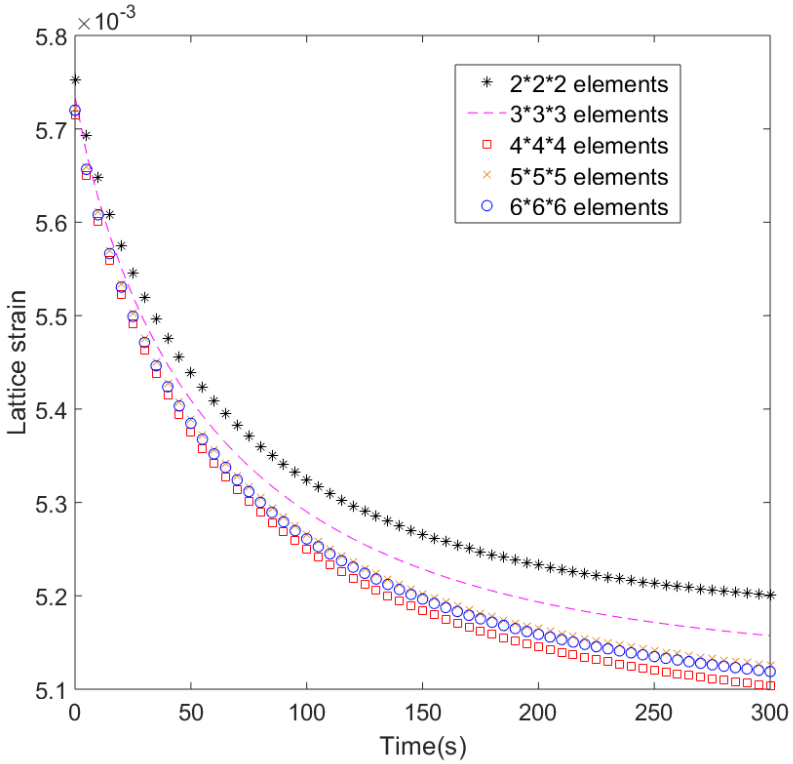


Figure A.5: The comparison of $\{01\bar{1}0\}$ plane lattice strain relaxation curves of the five models.

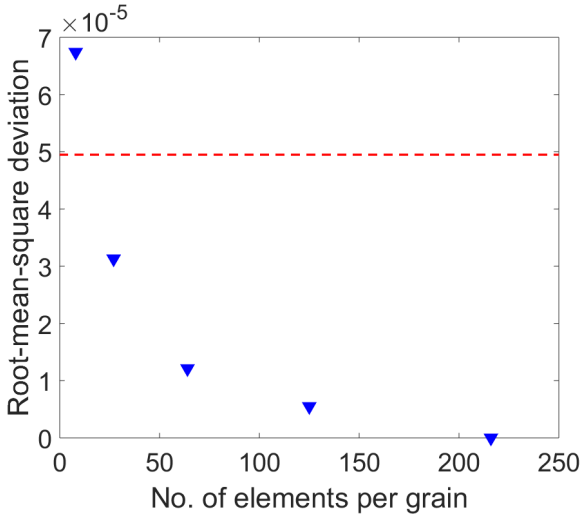


Figure A.6: Root-mean-squared deviation of the five models compared to the 6×6×6 elements per grain model. The dashed red line indicates level of experimental noise.

magnitudes) in lattice strain. Therefore, efforts were not been made to calibrate the ΔV. Instead, they were fixed to the value obtained from macroscopic stress relaxation for both basal and prismatic slip systems.

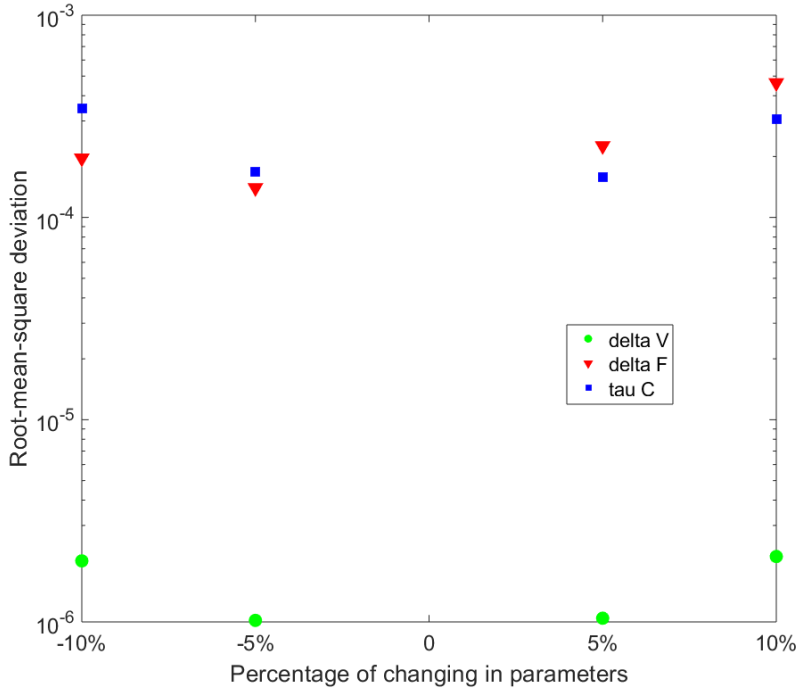


Figure A.7: Comparison of sensitivity of the lattice strain with respect to changing in parameters of (ΔV, ΔF and τ_c).

A.4 Sensitivity of lattice strain to the initial orientation assignment

A new model was created with discrete orientations that were randomly assigned from the EBSD measurement (same method as discussed in Section 5.2.4). The pole figures of this new model are shown in Figure A.8. Two models were subjected to the same boundary conditions and using the same set of materials parameters. Comparison of lattice strain evolution of the $\{01\bar{1}0\}$, $\{01\bar{1}1\}$ and $\{11\bar{2}2\}$ lattice planes during the first stress relaxation cycle in these two models is shown in Figure A.9. it can be seen that although the lattice strain results shifts by a small amount, the overall fitting remains reasonably good. The averaged root-mean-square deviation (RMSD) of the lattice strain of these three planes compared to the original model is 6.63×10^{-5} which is slightly higher than the average experimental error (see Figure A.6). However, a fitting error equivalent to the original model was obtained, the parameters require only a small refinement (as

shown in Figure A.7). Therefore, the simulated lattice strain is not strongly sensitive to the initial orientation assignment if the overall texture is generally the same.

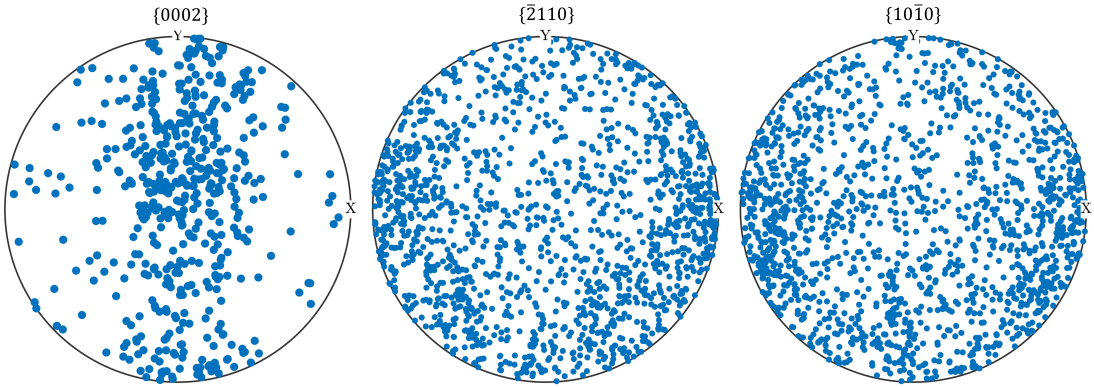


Figure A.8: Scatter pole figure plots of the new orientations assigned polycrystal finite element model.

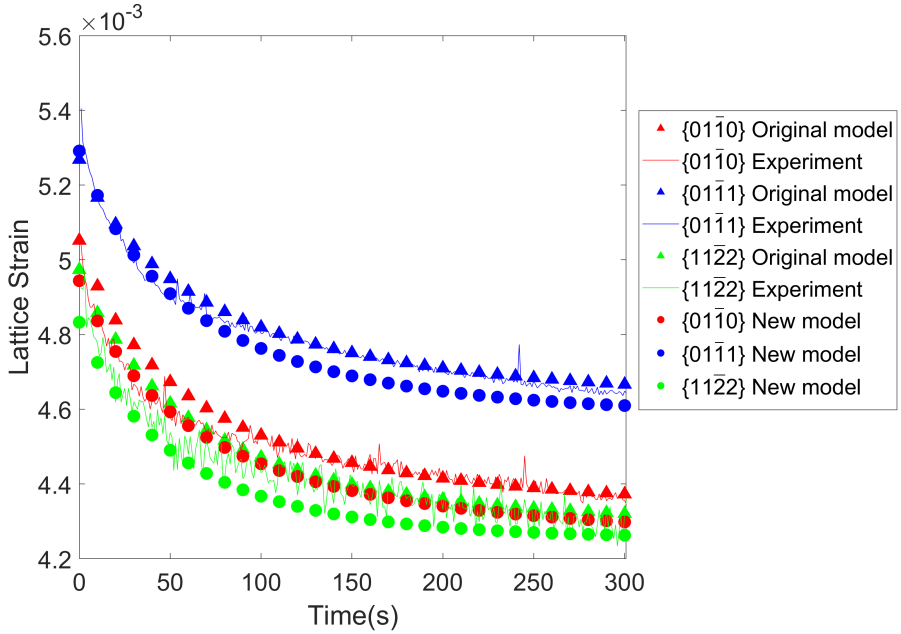


Figure A.9: Comparison of lattice strain evolution of {01$\bar{1}$0}, {01$\bar{1}\bar{1}$} and {11$\bar{2}\bar{2}$} planes during the first stress relaxation cycle between the original model and the new model.

A.5 Variation of the dislocation density

The variation of the mobile dislocation density ρ, which was assumed constant in Equation 3.1 and Equation 4.1, is estimated here. The macroscopic stress relaxation curve was fitted with Equation 4.1, detail of this method can be found in Section 4.4. The experimental and fitted stress relaxation curves were then divided by the Young's modulus E which gave rise to macroscopic strain relaxation curves, as shown in Figure A.10(a). Creep strain rates were calculated from the experimental and fitted strain relaxation curves. This is done by calculating the gradient of the relaxation curves over a time step of 3 seconds. A relatively large time step was selected here to reduce the noise that results from experimental data fluctuation and without sacrificing the number of data points (there are 100 data points using this method). The calculated experimental strain rates were then divided by the strain rate calculated from the fitted curve. The resulting scaling is due to change in the mobile dislocation density, ρ, because ρ is linearly related to the strain rate, $\dot{\varepsilon_p}$, in Equation 4.1. The experimental dislocation densities were then obtained by multiplying the scaling by the assumed constant mobile dislocation density ($\rho_0 = 5\ \mu m^{-2}$). Figure A.10(b) shows the calculated variation of mobile dislocation density during the relaxation. The red solid line shows the level of the assumed constant dislocation density and the red dashed lines provide the range of +/- 40% ρ. It is found that there is no real systematic variation of dislocation density during the relaxation and 95% of the data points lie within the +/- 40% ρ range. There is not a simple gradual decrease in ρ during the relaxation period as described by Caillard [158]. Given that this implies a complex evolution of mobile dislocation content and we have taken the simplest possible approach of keeping the mobile dislocation constant throughout.

The effect of the variation of the mobile dislocation density, ρ, on the fitting procedure used in Section 6.3.3 has been explored. Simulations have been repeated using values of ρ that are 40% lower or higher ($\rho = 3\ \mu\text{m}^{-2}$ and $\rho = 7\ \mu\text{m}^{-2}$) with respect to the reference value. The evolution of the lattice strain is shown in

Fig. A.11. The agreement is still within the experimental scatter. It would therefore be unfeasible with the existing data sets to include ρ as a fitting variable.

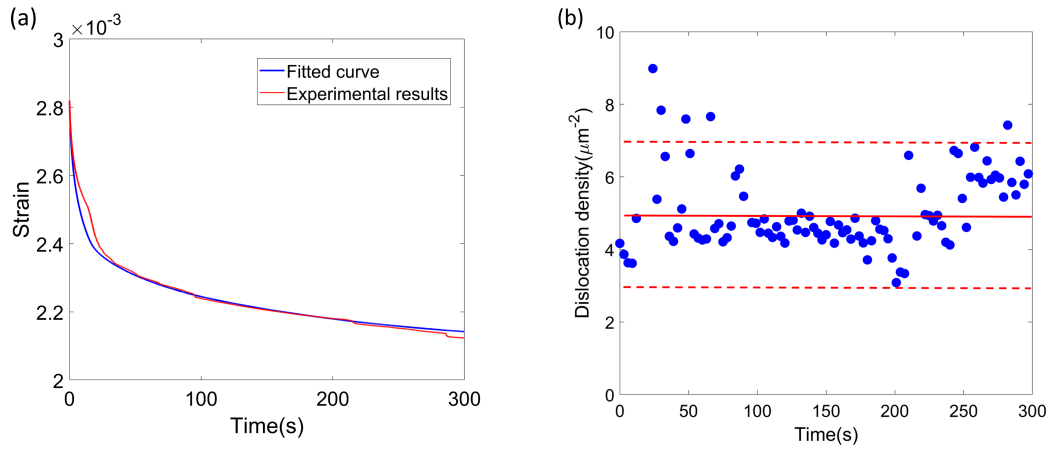
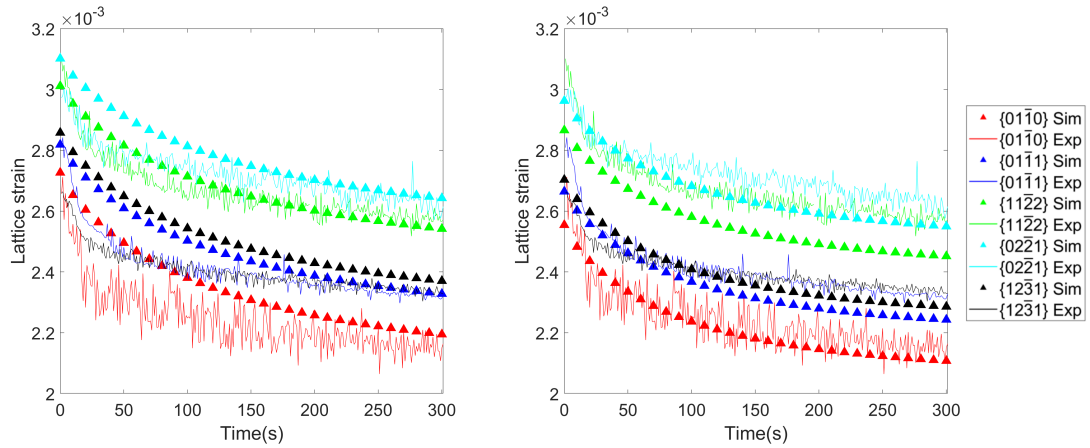


Figure A.10: (a) Experimental and fitted the first strain relaxation curves of CP-Ti grade 1 at room temperature; (b) Variation of the mobile dislocation density during the relaxation, red solid line implies the level of constant mobile dislocation density of $\rho = 5$ μm^{-2} and red dashed lines show the range of +/- 40% ρ.



(a) (b)

Figure A.11: Comparison of lattice strain evolution along the loading direction between the experiment and the simulation of CP-Ti grade 1 at room temperature for different values of the mobile dislocation density ρ in Equation 3.1: (a) $\rho = 3$ μm^{-2}, (b) $\rho = 7$ μm^{-2}.

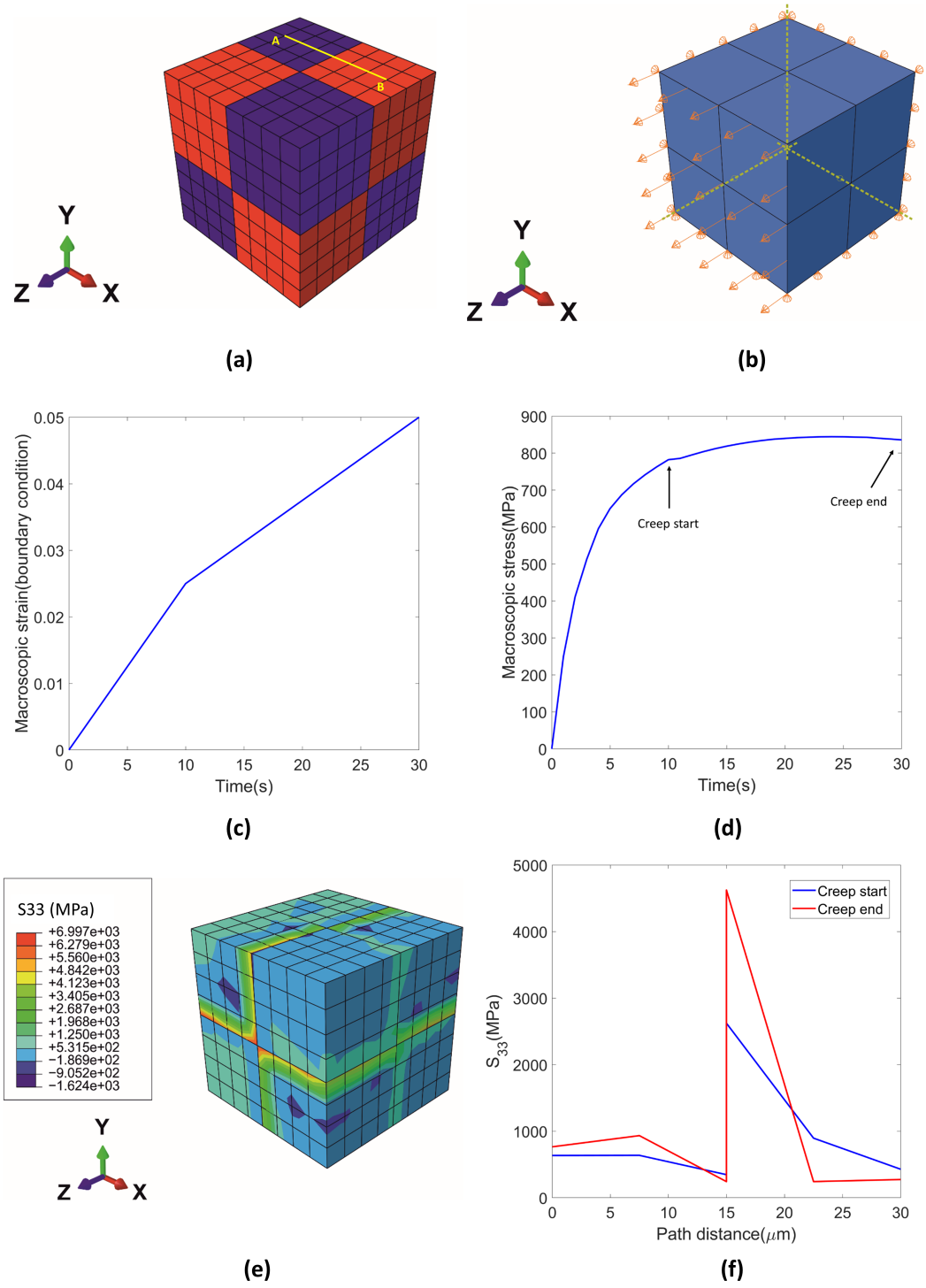


Figure A.12: (a) The 8 grain model with hard grains shown in red and soft grains shown in blue; (b) Tensile boundary conditions applied to the model; (c) Macroscopic strain applied to the model vs time; (d) Resulting macroscopic tensile stress vs time; (e) The stress along the loading direction at the end of the creep period; (f) The S_{33} along the path A-B.

A.6 Validation of the cubic grain morphology

The assumption of a simplified cubic grain morphology has been considered by the authors, and we can confirm that this assumption does indeed show load shedding. To support this statement, a simple validation simulation was performed. The results are shown in the Figure A.12.

The model consists of 8 grains with a cubic morphology, as shown in Figure A.12(a), red grains are hard grains (c-axis parallel to the loading direction) and blue grains are soft grains (c-axis perpendicular to the loading direction). Tensile displacement was applied to the front face while the back, left and bottom faces were constrained in Z, X and Y direction respectively (Figure A.12(b)). The boundary condition is shown in Figure A.12(c) and the resulting loading curve is shown in Figure A.12(d) in order to simulate a typical load-up and stress-hold loading cycle. The stress along the loading direction at the end of the creep period is shown in Figure A.12(e). Stress concentrations were found near the grain boundaries within the hard grains. The S_{33} along the path A-B in Figure A.12(a) is shown in Figure A.12(f), it is found that the stress within the soft grain remained largely unchanged after creep, however, a huge increase in stress at the grain boundary within the hard grain was observed. This is because there is no plasticity developed in the hard grain during the creep period. This observation of load shedding is consistent with the study on cold dwell fatigue by Zheng *et al.* [1].

Load shedding is typically localised within only part of the hard grain, while such grains taken as a whole tend to show the average stress decreasing. This is certainly true when average measurements via diffraction are obtained from grain families.

Homogenisation of any significant spatial or temporal fluctuations in behaviour when viewed at the individual dislocation level is at the heart of CPFEM methodology. This limitation in the detail is of course necessary to work at the level of grain aggregates making up a polycrystal.

A.7 Justification of the depth of the model

This section discuss the effect of the depth of the model on the output result for the experiment descreibed in Chapter 7. Three models with depth of 1 layer of elements, 2 layers of elements and 4 layers of elements were created for sample 1. Simulations were performed using same set of parameters (not the final optimised parameters). Figure A.13 shows the comparison of the strains of the grain 5 and the grain 7 from the three models and experimental results. It is found that as the depth of the models increased from 1 element to 4 element, the simulated strain decreased. However, the difference in strains of the three models is relatively small, which did not affect their fittings with the experimental strains. To ensure enough degree of freedom of the elements on the top layer (where simulation results output from) and efficiency of the simulations, the model depth was set to be 2 elements for simulations presented in Chapter 7.

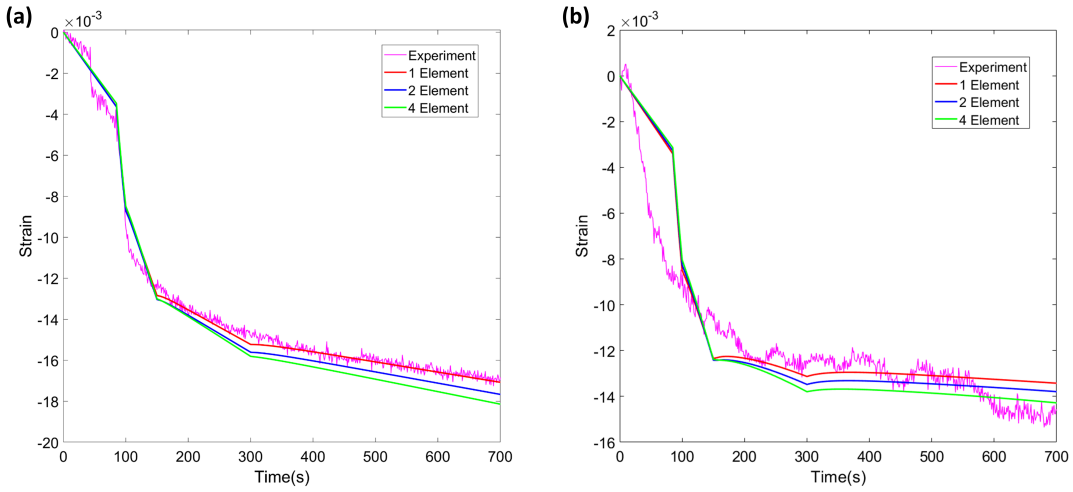


Figure A.13: Comparison of the strain in the models with 1 element, 2 elements and 4 elements in depth and the experimental strain of (a) grain 5 and (b) grain 7 in sample 1.

A.8 Fitting errors and optimisation efficiency

This section discuss the efficiency of the optimisation method descreibed in Chapter 7. The fitting errors and number of iterations are summarised in Table A.4. The optimisation procedures were performed on a high function PC with an Intel Xeon(R) CPU E5-2687W v2 @ 3.40GHz with 8 cores. It took approximately 80 minutes for one iteration of the Nelder-Mead method to complete. Therefore, the completion of the optimisation procedure for one sample could take 2-4 weeks. Using the automatic optimisation tool could save time for people but could also occupy the computer resources. The choice of the initial parameters that input into the Nelder-Mead method is extremely important. Sample 4, for example, using the calibrated CRSS values as input has the lowest averaged error among these four samples. The efficiency of optimisation could be improved by a more accurate estimation of the materials properties in our case. More advanced machine learning method [181] could also be applied to improve the efficiency.

Table A.4: Averaged difference in strain between the simulations and experiments of the 8 selected grains in four samples and approximate number of iterations of the Nelder-Mead method.

	Averaged errors	No. of iterations
Sample 1	4.3%	≈300
Sample 2	7.6%	≈500
Sample 3	6.8%	≈500
Sample 4	3.1%	NA

A.9 DIC error analysis

This section discuss the error of the DIC measurement. Here, we also examine the stability of the paint at high temperature. The painted sample was heated to 300°C and stabilised at this temperature for 5 minutes. DIC images were recorded every 10 seconds while there is no load applied to the sample. Figure A.14 shows the strain evolution of this zero load sample over a time period of 5 minutes. The paint was found to reliable as temperature not exceeds 300°C. The fluctuation of the

strain is the error from DIC measurements. The error is about 10^{-5} level, which corresponds to less than 1% error for experiment results in Chapter 7.

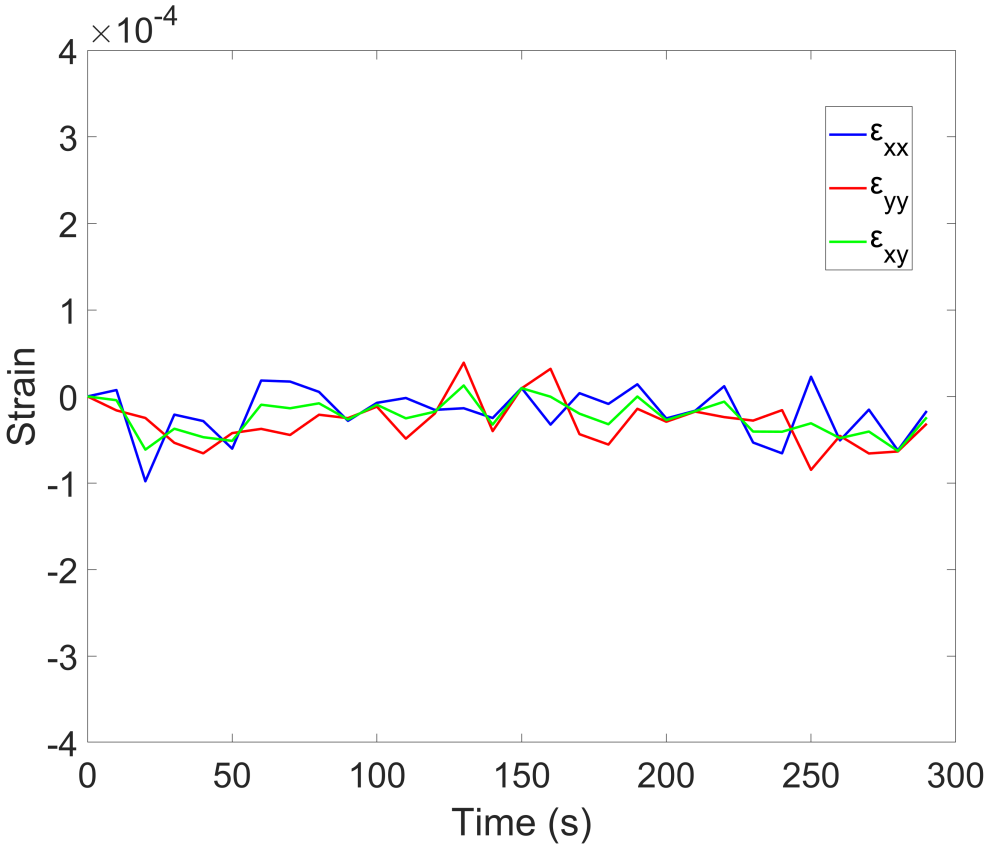


Figure A.14: Strain evolution of the sample with zero load over 5 minutes.

A.10 Peak width study

The synchrotron diffraction instrument broadening is studied in this Appendix. Figure A.15 show the peak profile integrated from the CeO_2 standard sample. Peak fit was performed on the first 21 peaks using DAWN, which enables the peak width to be measured. Figure A.16 shows the peak width vs. 2θ of the CeO_2 standard sample. It was found that the peak width increases (from 0.049° to 0.055°) as the 2θ value increases (from 2° to 14°). The trend was fitted by a quadratic function, so that the instrument peak width at any 2θ value can be predicted. Table A.5 summarises the change in peak width of the three important peaks ($\{01\bar{1}0\}$, $\{0002\}$ and $\{01\bar{1}1\}$) in the CP-Ti grade 4 sample at room temperature. The changes in peak width were calculated at the start of the first relaxation and the end of the first relaxation with respect to the first frame. It was found that the changes in peak width were two orders of magnitude smaller than the peak width (instrument broadening) from the CeO_2 standard sample. Therefore, it is not possible to separate the peak width changes caused by plastic deformation from the original peak width given by instrument broadening.

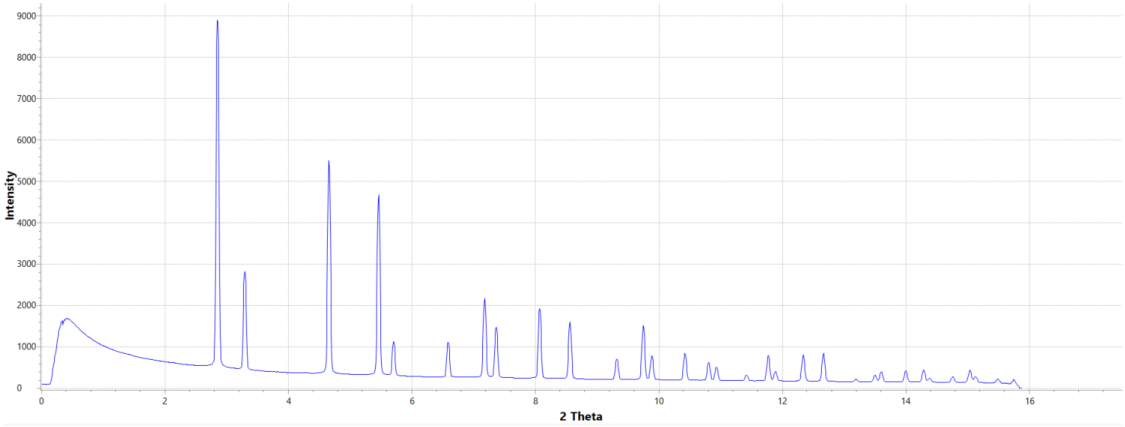


Figure A.15: Integrated peak profile of the CeO_2 standard.

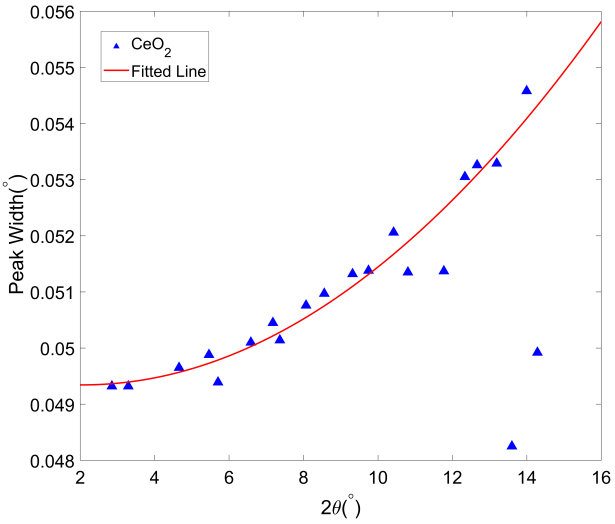


Figure A.16: Peak width vs. 2θ of the CeO_2 standard sample, the trend was fitted by a quadratic function.

Table A.5: Changes in peak width of the $\{01\bar{1}0\}$, $\{0002\}$ and $\{01\bar{1}1\}$ peaks of the CP-Ti grade 4 sample.

Changes in peak width	Start of the first relaxation	End of the first relaxation
$\{01\bar{1}0\}$	0.00030°	0.00063°
$\{0002\}$	0.00089°	0.000228°
$\{01\bar{1}1\}$	0.00118°	0.00226°

Bibliography

[1] Z. Zheng, D. S. Balint, and F. P. Dunne, "Dwell fatigue in two ti alloys: An integrated crystal plasticity and discrete dislocation study," *Journal of the Mechanics and Physics of Solids*, vol. 96, pp. 411 – 427, 2016. [Online]. Available: http://www.sciencedirect.com/science/article/pii/S002250961630223X

[2] M. Bache, "A review of dwell sensitive fatigue in titanium alloys: the role of microstructure, texture and operating conditions," *International Journal of Fatigue*, vol. 25, no. 9, pp. 1079 – 1087, 2003, international Conference on Fatigue Damage of Structural Materials IV. [Online]. Available: http://www.sciencedirect.com/science/article/pii/S0142112303001452

[3] F. P. E. DUNNE and D. RUGG, "On the mechanisms of fatigue facet nucleation in titanium alloys," *Fatigue & Fracture of Engineering Materials & Structures*, vol. 31, no. 11, pp. 949–958, 2008. [Online]. Available: https://onlinelibrary.wiley.com/doi/abs/10.1111/j.1460-2695.2008.01284.x

[4] D. Eylon and J. A. Hall, "Fatigue behavior of beta processed titanium alloy imi 685," *Metall Trans, A*, vol. 8, no. 6, pp. 981–990, 1977.

[5] M. Cuddihy, A. Stapleton, S. Williams, and F. Dunne, "On cold dwell facet fatigue in titanium alloy aero-engine components," *International Journal of Fatigue*, vol. 97, pp. 177 – 189, 2017. [Online]. Available: http://www.sciencedirect.com/science/article/pii/S0142112316304054

[6] A. N. Stroh and N. F. Mott, "The formation of cracks as a result of plastic flow," *Proceedings of the Royal Society of London. Series A. Mathematical and Physical Sciences*, vol. 223, no. 1154, pp. 404–414, 1954.

[7] A. ZARKADES and F. LARSON, "Elasticity of titanium sheet alloys," in *The Science, Technology and Application of Titanium*, R. JAFFEE and N. PROMISEL, Eds. Pergamon, 1970, pp. 933 – 941. [Online]. Available: http://www.sciencedirect.com/science/article/pii/B9780080065649501044

[8] N. Paton, R. Baggerly, J. Williams, and R. I. T. O. C. S. CENTER., *Deformation and Solid Solution Strengthening of Titanium-Aluminum Single Crystals*. Defense Technical Information Center, 1976. [Online]. Available: https://books.google.co.uk/books?id=Ku2ktgAACAAJ

[9] V. Hasija, S. Ghosh, M. J. Mills, and D. S. Joseph, "Deformation and creep modeling in polycrystalline ti–6al alloys," *Acta Materialia*, vol. 51, no. 15, pp. 4533 – 4549, 2003. [Online]. Available: http://www.sciencedirect.com/science/article/pii/S1359645403002891

[10] F. Dunne, A. Walker, and D. Rugg, "A systematic study of hcp crystal orientation and morphology effects in polycrystal deformation and fatigue," *Proceedings of the Royal Society A: Mathematical, Physical and Engineering Sciences*, vol. 463, no. 2082, pp. 1467–1489, 2007. [Online]. Available: https://royalsocietypublishing.org/doi/abs/10.1098/rspa.2007.1833

[11] W. Evans and M. Bache, "Dwell-sensitive fatigue under biaxial loads in the near-alpha titanium alloy imi685," *International Journal of Fatigue*, vol. 16, no. 7, pp. 443 – 452, 1994. [Online]. Available: http://www.sciencedirect.com/science/article/pii/0142112394901945

[12] Q. Yu, L. Qi, T. Tsuru, R. Traylor, D. Rugg, J. W. Morris, M. Asta, D. C. Chrzan, and A. M. Minor, "Origin of dramatic oxygen solute strengthening effect in titanium," *Science*, vol. 347, no. 6222, pp. 635–639, 2015. [Online]. Available: https://science.sciencemag.org/content/347/6222/635

[13] H. Conrad, "Effect of interstitial solutes on the strength and ductility of titanium," *Progress in Materials Science*, vol. 26, no. 2, pp. 123 – 403,

1981. [Online]. Available: http://www.sciencedirect.com/science/article/pii/0079642581900013

[14] J. Stringer, "The oxidation of titanium in oxygen at high temperatures," *Acta Metallurgica*, vol. 8, no. 11, pp. 758 – 766, 1960. [Online]. Available: http://www.sciencedirect.com/science/article/pii/000161606090170X

[15] C. Kale, P. Garg, B. G. Bazehhour, S. Srinivasan, M. Bhatia, P. Peralta, and K. Solanki, "Oxygen effects on crystal plasticity of titanium: A multiscale calibration and validation framework," *Acta Materialia*, vol. 176, pp. 19 – 32, 2019. [Online]. Available: http://www.sciencedirect.com/science/article/pii/S1359645419304148

[16] G. Lütjering and J. Williams, *Titanium*, ser. Engineering materials and processes. Springer, 2003. [Online]. Available: https://books.google.co.uk/books?id=GwI9ul_wAegC

[17] Z. Zhang, M. Cuddihy, and F. Dunne, "On rate-dependent polycrystal deformation: the temperature sensitivity of cold dwell fatigue," *Proceedings of the Royal Society A: Mathematical, Physical and Engineering Science*, vol. 471, p. 20150214, 09 2015.

[18] U. Zwicker, *Titan und Titanlegierungen*. Springer Berlin Heidelberg, 1974. [Online]. Available: https://doi.org/10.1007/978-3-642-80587-5

[19] P. L. Teed, "Titanium," *The Journal of the Royal Aeronautical Society*, vol. 60, no. 543, pp. 213–213, Mar. 1956. [Online]. Available: https://doi.org/10.1017/s036839310013439x

[20] E. D. Levine, "Deformation mechanisms in titanium at low temperatures," *Transactions of the Metallurgical Society of AIME*, vol. 236, p. 1558, 1966.

[21] P. D. Littlewood, "Microplasticity and fatigue crack initiation in titanium alloy ti-6al-4v," Ph.D. dissertation, University of Oxford, 2011.

[22] R. JAFFEE and N. PROMISEL, *The Science, Technology and Application of Titanium*. Elsevier, 1970. [Online]. Available: https://doi.org/10.1016/c2013-0-01574-5

[23] H. Burte, *Titanium Science and Technology*. Springer US, 1973.

[24] H. Ogi, S. Kai, H. Ledbetter, R. Tarumi, M. Hirao, and K. Takashima, "Titanium's high-temperature elastic constants through the hcp–bcc phase transformation," *Acta Materialia*, vol. 52, no. 7, pp. 2075–2080, 2004. [Online]. Available: https://www.sciencedirect.com/science/article/pii/S1359645404000138

[25] E. S. Fisher and C. J. Renken, "Single-crystal elastic moduli and the hcp → bcc transformation in ti, zr, and hf," *Phys. Rev.*, vol. 135, pp. A482–A494, Jul 1964. [Online]. Available: https://link.aps.org/doi/10.1103/PhysRev.135.A482

[26] I. Jones and W. Hutchinson, "Stress-state dependence of slip in titanium-6al-4v and other h.c.p. metals," *Acta Metallurgica*, vol. 29, no. 6, pp. 951–968, 1981. [Online]. Available: https://www.sciencedirect.com/science/article/pii/0001616081900493

[27] P. G. Partridge, "The crystallography and deformation modes of hexagonal close-packed metals," *Metallurgical Reviews*, vol. 12, no. 1, pp. 169–194, Jan. 1967. [Online]. Available: https://doi.org/10.1179/mtlr.1967.12.1.169

[28] M. H. Yoo, "Slip, twinning, and fracture in hexagonal close-packed metals," *Metallurgical Transactions A*, vol. 12, no. 3, pp. 409–418, Mar 1981. [Online]. Available: https://doi.org/10.1007/BF02648537

[29] N. Goossens, B. Tunca, T. Lapauw, K. Lambrinou, and J. Vleugels, "Max phases, structure, processing, and properties," in *Encyclopedia of Materials: Technical Ceramics and Glasses*, M. Pomeroy, Ed. Oxford: Elsevier, 2021, pp. 182–199. [Online]. Available: https://www.sciencedirect.com/science/article/pii/B9780128185421000151

[30] W.-K. Pang and I. Low, "18 - understanding and improving the thermal stability of layered ternary carbides and nitrides," in *Advances in Ceramic Matrix Composites (Second Edition)*, second edition ed., ser. Woodhead Publishing Series in Composites Science and Engineering, I. Low, Ed. Woodhead Publishing, 2018, pp. 429–460. [Online]. Available: https://www.sciencedirect.com/science/article/pii/B9780081021668000189

[31] N. E. Paton and J. C. Williams, *Deformation of body-centered-cubic titanium–vanadium single crystals.* United States: American Society for Metals, 1970. [Online]. Available: http://inis.iaea.org/search/search.aspx?orig_q=RN:03014724

[32] S. Laine, "The role of twinning in the plastic deformation of alpha phase titanium," Ph.D. dissertation, 09 2017.

[33] A. T. Churchman and T. E. Allibone, "The slip modes of titanium and the effect of purity on their occurrence during tensile deformation of single crystals," *Proceedings of the Royal Society of London. Series A. Mathematical and Physical Sciences*, vol. 226, no. 1165, pp. 216–226, 1954. [Online]. Available: https://royalsocietypublishing.org/doi/abs/10.1098/rspa.1954.0250

[34] W. Tyson, "Solution hardening of titanium by oxygen," *Scripta Metallurgica*, vol. 3, no. 12, pp. 917–921, Dec. 1969. [Online]. Available: https://doi.org/10.1016/0036-9748(69)90241-5

[35] M. L. Wasz, F. R. Brotzen, R. B. McLellan, and A. J. Griffin, "Effect of oxygen and hydrogen on mechanical properties of commercial purity titanium," *International Materials Reviews*, vol. 41, no. 1, pp. 1–12, Jan. 1996. [Online]. Available: https://doi.org/10.1179/imr.1996.41.1.1

[36] T. B. Britton, F. P. E. Dunne, and A. J. Wilkinson, "On the mechanistic basis of deformation at the microscale in hexagonal close-packed metals," *Proceedings of the Royal Society A: Mathematical, Physical and Engineering*

Sciences, vol. 471, no. 2178, p. 20140881, 2015. [Online]. Available: https://royalsocietypublishing.org/doi/abs/10.1098/rspa.2014.0881

[37] A. Akhtar, "Basal slip and twinning in α-titanium single crystals," *Metallurgical Transactions A*, vol. 6, no. 5, p. 1105, May 1975. [Online]. Available: https://doi.org/10.1007/BF02661366

[38] T. Tanaka and H. Conrad, "Deformation kinetics for $\{10\bar{1}0\} < 11\bar{2}0 >$ slip in titanium single crystals below 0.4tm," *Acta Metallurgica*, vol. 20, no. 8, pp. 1019–1029, 1972. [Online]. Available: https://www.sciencedirect.com/science/article/pii/0001616072901368

[39] J. C. Williams, A. W. Sommer, and P. P. Tung, "The influence of oxygen concentration on the internal stress and dislocation arrangements in α titanium," *Metallurgical and Materials Transactions B*, vol. 3, no. 11, pp. 2979–2984, Nov 1972. [Online]. Available: https://doi.org/10.1007/BF02652870

[40] G. Welsch and W. Bunk, "Deformation modes of the α-phase of ti-6al-4v as a function of oxygen concentration and aging temperature," *Metallurgical Transactions A*, vol. 13, no. 5, pp. 889–899, May 1982. [Online]. Available: https://doi.org/10.1007/BF02642403

[41] D. Rugg, T. Britton, J. Gong, A. Wilkinson, and P. Bagot, "In-service materials support for safety critical applications – a case study of a high strength ti-alloy using advanced experimental and modelling techniques," *Materials Science and Engineering: A*, vol. 599, pp. 166–173, 2014. [Online]. Available: https://www.sciencedirect.com/science/article/pii/S0921509314000616

[42] T. Parthasarathy, W. Porter, S. Boone, R. John, and P. Martin, "Life prediction under tension of titanium alloys that develop an oxygenated brittle case during use," *Scripta Materialia*, vol. 65, no. 5, pp. 420–423, 2011. [Online]. Available: https://www.sciencedirect.com/science/article/pii/S1359646211003083

[43] A. L. Pilchak, W. J. Porter, and R. John, "Room temperature fracture processes of a near-α titanium alloy following elevated temperature exposure," *Journal of Materials Science*, vol. 47, no. 20, pp. 7235–7253, Oct 2012. [Online]. Available: https://doi.org/10.1007/s10853-012-6673-y

[44] T. Sakai and M. Fine, "Plastic deformation of ti-al single crystals in prismatic slip," *Acta Metallurgica*, vol. 22, no. 11, pp. 1359–1372, 1974. [Online]. Available: https://www.sciencedirect.com/science/article/pii/0001616074900364

[45] ——, "Failure of schmid's law in tial alloys for prismatic slip," *Scripta Metallurgica*, vol. 8, no. 5, pp. 541–544, 1974. [Online]. Available: https://www.sciencedirect.com/science/article/pii/0036974874900659

[46] J. C. Williams, R. G. Baggerly, and N. E. Paton, "Deformation behavior of hcp ti-al alloy single crystals," *Metallurgical and Materials Transactions A*, vol. 33, pp. 837–850, 03 2002.

[47] R. M. Brick, R. B. Gordon, and A. Phillips, *Structure and properties of alloys: the application of phase diagrams to the interpretation and control of industrial alloy structures.* McGraw-Hill, 1965.

[48] S. Avner, *Introduction to physical metallurgy.* McGraw-Hill Education (India) Pvt Limited, 1997. [Online]. Available: https://books.google.co.uk/books?id=Vg75OsznivMC

[49] P. Pugh, *The magic of a name: the Rolls-Royce story, the first forty years.* London: Icon Books, 2002, oCLC: 908100083. [Online]. Available: http://public.ebookcentral.proquest.com/choice/publicfullrecord.aspx?p=2007136

[50] W. J. Evans and C. R. Gostelow, "The effect of hold time on the fatigue properties of a β-processed titanium alloy," *Metallurgical Transactions A*, vol. 10, no. 12, pp. 1837–1846, Dec 1979. [Online]. Available: https://doi.org/10.1007/BF02811727

[51] *Titanium ŷ5 - science and technology : proceedings of the Eighth World Conference on Titanium held at the International Convention Centre, Birmingham, UK, 22 - 26 October 1995 / ed. by P. A. Blenkinsop ... ; Vol. 1, World Conference on Titanium ; 8, Book / Institute of Materials*, vol. 620,1. London: Institute of Materials;, 1996, world Conference on Titanium ; 8. [Online]. Available: https://www.tib.eu/de/suchen/id/TIBKAT%3A216780209

[52] H. Conrad, "Thermally activated deformation of titanium below 0.4 tm," *Canadian Journal of Physics*, vol. 45, pp. 581–590, 02 2011.

[53] V. Sinha, M. Mills, and J. Williams, "Understanding the contributions of normal-fatigue and static loading to the dwell fatigue in a near-alpha titanium alloy," *Metallurgical and Materials Transactions A*, vol. 35, pp. 3141–3148, 10 2004.

[54] ——, "Crystallography of fracture facets in a near-alpha titanium alloy," *Metallurgical and Materials Transactions A: Physical Metallurgy and Materials Science*, vol. 37, pp. 2015–2026, 06 2006.

[55] V. Sinha, M. Mills, J. Williams, and J. Spowart, "Observations of the faceted initiation site in the dwell-fatigue tested ti-6242 alloy: Crystallographic orientation and size effects," *Metallurgical and Materials Transactions A: Physical Metallurgy and Materials Science*, vol. 37, pp. 1507–1518, 05 2006.

[56] F. Dunne, D. Rugg, and A. Walker, "Lengthscale-dependent, elastically anisotropic, physically-based hcp crystal plasticity: Application to cold-dwell fatigue in ti alloys," *International Journal of Plasticity*, vol. 23, no. 6, pp. 1061–1083, 2007. [Online]. Available: https://www.sciencedirect.com/science/article/pii/S0749641906001641

[57] F. Dunne, A. Walker, and D. Rugg, "A systematic study of hcp crystal orientation and morphology effects in polycrystal deformation and fatigue,"

Proceedings of The Royal Society A: Mathematical, Physical and Engineering Sciences, vol. 463, pp. 1467–1489, 06 2007.

[58] R. Evans, B. Wilshire, I. of Metals, and M. Society, *Creep of Metals and Alloys*, ser. Book (Institute of Metals). Institute of Metals, 1985. [Online]. Available: https://books.google.co.uk/books?id=ethiQgAACAAJ

[59] T. Neeraj, D.-H. Hou, G. Daehn, and M. Mills, "Phenomenological and microstructural analysis of room temperature creep in titanium alloys," *Acta Materialia*, vol. 48, no. 6, pp. 1225 – 1238, 2000. [Online]. Available: http://www.sciencedirect.com/science/article/pii/S1359645499004267

[60] S. Suri, T. Neeraj, G. Daehn, D.-H. Hou, J. Scott, R. Hayes, and M. Mills, "Mechanisms of primary creep in α/β titanium alloys at lower temperatures," *Materials Science and Engineering: A*, vol. 234-236, pp. 996–999, 1997. [Online]. Available: https://www.sciencedirect.com/science/article/pii/S0921509397003225

[61] D. H. Kohn and P. Ducheyne, "Tensile and fatigue strength of hydrogen-treated ti-6al-4v alloy," *Journal of Materials Science*, vol. 26, no. 2, pp. 328–334, Jan 1991. [Online]. Available: https://doi.org/10.1007/BF00576523

[62] J. E. Hack and G. R. Leverant, "The influence of microstructure on the susceptibility of titanium alloys to internal hydrogen embrittlement," *Metallurgical Transactions A*, vol. 13, no. 10, pp. 1729–1738, Oct 1982. [Online]. Available: https://doi.org/10.1007/BF02647828

[63] M. Gerland, P. Lefranc, V. Doquet, and C. Sarrazin-Baudoux, "Deformation and damage mechanisms in an α/β 6242 ti alloy in fatigue, dwell-fatigue and creep at room temperature. influence of internal hydrogen," *Materials Science and Engineering: A*, vol. 507, no. 1, pp. 132–143, 2009. [Online]. Available: https://www.sciencedirect.com/science/article/pii/S0921509308013488

[64] M. Bache, W. Evans, V. Randle, and R. Wilson, "Characterization of mechanical anisotropy in titanium alloys," *Materials Science and Engineering: A*, vol. 257, no. 1, pp. 139–144, 1998. [Online]. Available: https://www.sciencedirect.com/science/article/pii/S0921509398008326

[65] K. Ravichandran, R. O. Ritchie, and Y. Murakami, *Small fatigue cracks: mechanics, mechanisms and applications*. Elsevier, 1999.

[66] Z. Zhang, T.-S. Jun, T. B. Britton, and F. P. Dunne, "Determination of ti-6242 α and β slip properties using micro-pillar test and computational crystal plasticity," *Journal of the Mechanics and Physics of Solids*, vol. 95, pp. 393 – 410, 2016. [Online]. Available: http://www.sciencedirect.com/science/article/pii/S0022509616302307

[67] T.-S. Jun, Z. Zhang, G. Sernicola, F. P. Dunne, and T. B. Britton, "Local strain rate sensitivity of single α phase within a dual-phase ti alloy," *Acta Materialia*, vol. 107, pp. 298 – 309, 2016. [Online]. Available: http://www.sciencedirect.com/science/article/pii/S1359645416300544

[68] Z. Zhang, T.-S. Jun, T. B. Britton, and F. P. Dunne, "Intrinsic anisotropy of strain rate sensitivity in single crystal alpha titanium," *Acta Materialia*, vol. 118, pp. 317 – 330, 2016. [Online]. Available: http://www.sciencedirect.com/science/article/pii/S1359645416305523

[69] T.-S. Jun, D. E. Armstrong, and T. B. Britton, "A nanoindentation investigation of local strain rate sensitivity in dual-phase ti alloys," *Journal of Alloys and Compounds*, vol. 672, pp. 282 – 291, 2016. [Online]. Available: http://www.sciencedirect.com/science/article/pii/S0925838816304133

[70] T. Britton, H. Liang, F. Dunne, and A. Wilkinson, "The effect of crystal orientation on the indentation response of commercially pure titanium: Experiments and simulations," *Proceedings of the Royal Society a-Mathematical Physical and Engineering Sciences*, vol. 466, pp. 695–719, 03 2010.

[71] D. Peykov, E. Martin, R. Chromik, R. Gauvin, and M. Trudeau, "Evaluation of strain rate sensitivity by constant load nanoindentation," *Journal of Materials Science*, vol. 47, pp. 7189–7200, 10 2012.

[72] D. Chichili, K. Ramesh, and K. Hemker, "The high-strain-rate response of alpha-titanium: experiments, deformation mechanisms and modeling," *Acta Materialia*, vol. 46, no. 3, pp. 1025 – 1043, 1998. [Online]. Available: http://www.sciencedirect.com/science/article/pii/S1359645497002875

[73] M. Meyers, G. Subhash, B. Kad, and L. Prasad, "Evolution of microstructure and shear-band formation in α-hcp titanium," *Mechanics of Materials*, vol. 17, no. 2, pp. 175 – 193, 1994. [Online]. Available: http://www.sciencedirect.com/science/article/pii/0167663694900582

[74] R. Reed-Hill, C. Iswaran, and M. Kaufman, "A power law model for the flow stress and strain-rate sensitivity in cp titanium," *Scripta Metallurgica et Materialia*, vol. 33, no. 1, pp. 157 – 162, 1995. [Online]. Available: http://www.sciencedirect.com/science/article/pii/0956716X9500152L

[75] Ebsd, "Home." [Online]. Available: http://www.ebsd.com/introduction

[76] O. Engler and V. Randle, *Introduction to texture analysis: macrotexture, microtexture, and orientation mapping*. CRC Press, 2017.

[77] S. NISHIKAWA and S. KIKUCHI, "Diffraction of cathode rays by mica," *Nature*, vol. 121, no. 3061, pp. 1019–1020, Jun 1928. [Online]. Available: https://doi.org/10.1038/1211019a0

[78] A. J. Wilkinson, G. Meaden, and D. J. Dingley, "High-resolution elastic strain measurement from electron backscatter diffraction patterns: New levels of sensitivity," *Ultramicroscopy*, vol. 106, no. 4, pp. 307–313, 2006. [Online]. Available: https://www.sciencedirect.com/science/article/pii/S0304399105002251

[79] ——, "High resolution mapping of strains and rotations using electron backscatter diffraction," *Materials Science and Technology*, vol. 22, no. 11, pp. 1271–1278, 2006. [Online]. Available: https://doi.org/10.1179/174328406X130966

[80] A. J. Wilkinson, T. B. Britton, J. Jiang, and P. S. Karamched, "A review of advances and challenges in EBSD strain mapping," *IOP Conference Series: Materials Science and Engineering*, vol. 55, p. 012020, mar 2014. [Online]. Available: https://doi.org/10.1088/1757-899x/55/1/012020

[81] P. Littlewood and A. Wilkinson, "Local deformation patterns in ti–6al–4v under tensile, fatigue and dwell fatigue loading," *International Journal of Fatigue*, vol. 43, pp. 111–119, 2012. [Online]. Available: https://www.sciencedirect.com/science/article/pii/S0142112312000837

[82] R. J. Asaro, "Micromechanics of crystals and polycrystals," *Advances in Applied Mechanics*, vol. 23, pp. 1–115, 1983. [Online]. Available: https://www.sciencedirect.com/science/article/pii/S0065215608702424

[83] L. Anand and M. Kothari, "A computational procedure for rate-independent crystal plasticity," *Journal of the Mechanics and Physics of Solids*, vol. 44, no. 4, pp. 525–558, 1996. [Online]. Available: https://www.sciencedirect.com/science/article/pii/0022509696000014

[84] R. McGinty and D. McDowell, "A semi-implicit integration scheme for rate independent finite crystal plasticity," *International Journal of Plasticity*, vol. 22, no. 6, pp. 996–1025, 2006. [Online]. Available: https://www.sciencedirect.com/science/article/pii/S0749641905001269

[85] K. Saanouni and A. Abdul-Latif, "Micromechanical modeling of low cycle fatigue under complex loadings — part i. theoretical formulation," *International Journal of Plasticity*, vol. 12, no. 9, pp. 1111–1121, 1996. [Online]. Available: https://www.sciencedirect.com/science/article/pii/S0749641996000435

[86] L. Tóth, A. Molinari, and N. Zouhal, "Cyclic plasticity phenomena as predicted by polycrystal plasticity," *Mechanics of Materials*, vol. 32, no. 2, pp. 99–113, 2000. [Online]. Available: https://www.sciencedirect.com/science/article/pii/S016766369900040X

[87] R. Morrissey, D. McDowell, and T. Nicholas, "Microplasticity in hcf of ti–6al–4v," *International Journal of Fatigue*, vol. 23, pp. 55–64, 2001. [Online]. Available: https://www.sciencedirect.com/science/article/pii/S0142112301001190

[88] V. Bennett and D. McDowell, "Polycrystal orientation distribution effects on microslip in high cycle fatigue," *International Journal of Fatigue*, vol. 25, no. 1, pp. 27–39, 2003. [Online]. Available: https://www.sciencedirect.com/science/article/pii/S0142112302000579

[89] A. Manonukul, F. Dunne, and D. Knowles, "Physically-based model for creep in nickel-base superalloy c263 both above and below the gamma solvus," *Acta Materialia*, vol. 50, no. 11, pp. 2917–2931, 2002. [Online]. Available: https://www.sciencedirect.com/science/article/pii/S1359645402001192

[90] F. Dunne, A. Wilkinson, and R. Allen, "Experimental and computational studies of low cycle fatigue crack nucleation in a polycrystal," *International Journal of Plasticity*, vol. 23, no. 2, pp. 273–295, 2007. [Online]. Available: https://www.sciencedirect.com/science/article/pii/S0749641906000763

[91] C.-H. Goh, J. Wallace, R. Neu, and D. McDowell, "Polycrystal plasticity simulations of fretting fatigue," *International Journal of Fatigue*, vol. 23, pp. 423–435, 2001. [Online]. Available: https://www.sciencedirect.com/science/article/pii/S0142112301001505

[92] M. R. Bache and W. J. Evans, "Dwell sensitive fatigue response of titanium alloys for power plant applications," *Journal of Engineering for Gas Turbines and Power*, vol. 125, no. 1, pp. 241–245, Dec 2002. [Online]. Available: https://doi.org/10.1115/1.1494094

[93] A. V. Granato, K. Lücke, J. Schlipf, and L. J. Teutonico, "Entropy factors for thermally activated unpinning of dislocations," *Journal of Applied Physics*, vol. 35, no. 9, pp. 2732–2745, 1964. [Online]. Available: https://doi.org/10.1063/1.1713833

[94] G. Gibbs, "Thermodynamic analysis of dislocation glide controlled by dispersed local obstacles," *Materials Science and Engineering*, vol. 4, no. 6, pp. 313–328, 1969. [Online]. Available: https://www.sciencedirect.com/science/article/pii/0025541669900263

[95] A. H. Cottrell, *Dislocations and plastic flow in crystals*. Oxford, 1965.

[96] "Chapter 3 - methods for assessing surface cleanliness," in *Developments in Surface Contamination and Cleaning, Volume 12*, R. Kohli and K. Mittal, Eds. Elsevier, 2019, pp. 23 – 105. [Online]. Available: http://www.sciencedirect.com/science/article/pii/B9780128160817000036

[97] A. M. Stapleton, S. L. Raghunathan, I. Bantounas, H. J. Stone, T. C. Lindley, and D. Dye, "Evolution of lattice strain in ti–6al–4v during tensile loading at room temperature," *Acta Materialia*, vol. 56, no. 20, pp. 6186 – 6196, 2008. [Online]. Available: http://www.sciencedirect.com/science/article/pii/S135964540800596X

[98] J. Warwick, N. Jones, K. Rahman, and D. Dye, "Lattice strain evolution during tensile and compressive loading of cp ti," *Acta Materialia*, vol. 60, no. 19, pp. 6720 – 6731, 2012. [Online]. Available: http://www.sciencedirect.com/science/article/pii/S1359645412005812

[99] K. Chatterjee, J. Ko, J. Weiss, H. Philipp, J. Becker, P. Purohit, S. Gruner, and A. Beaudoin, "Study of residual stresses in ti-7al using theory and experiments," *Journal of the Mechanics and Physics of Solids*, vol. 109, pp. 95 – 116, 2017. [Online]. Available: http://www.sciencedirect.com/science/article/pii/S0022509617302600

[100] E. Wielewski, D. E. Boyce, J.-S. Park, M. P. Miller, and P. R. Dawson, "A methodology to determine the elastic moduli of crystals by matching experimental and simulated lattice strain pole figures using discrete harmonics," *Acta Materialia*, vol. 126, pp. 469 – 480, 2017. [Online]. Available: http://www.sciencedirect.com/science/article/pii/S1359645416309624

[101] P. R. Dawson, D. E. Boyce, J.-S. Park, E. Wielewski, and M. P. Miller, "Determining the strengths of hcp slip systems using harmonic analyses of lattice strain distributions," *Acta Materialia*, vol. 144, pp. 92 – 106, 2018. [Online]. Available: http://www.sciencedirect.com/science/article/pii/S135964541730890X

[102] K. Sofinowski, M. Šmíd, S. van Petegem, S. Rahimi, T. Connolley, and H. van Swygenhoven, "In situ characterization of work hardening and springback in grade 2 α-titanium under tensile load," *Acta Materialia*, vol. 181, pp. 87 – 98, 2019. [Online]. Available: http://www.sciencedirect.com/science/article/pii/S1359645419306299

[103] D. Zhang, L. Wang, H. Zhang, A. Maldar, G. Zhu, W. Chen, J.-S. Park, J. Wang, and X. Zeng, "Effect of heat treatment on the tensile behavior of selective laser melted ti-6al-4v by in situ x-ray characterization," *Acta Materialia*, vol. 189, pp. 93 – 104, 2020. [Online]. Available: http://www.sciencedirect.com/science/article/pii/S1359645420301804

[104] Y. Xiong, P. S. Karamched, C.-T. Nguyen, D. M. Collins, C. M. Magazzeni, E. Tarleton, and A. J. Wilkinson, "Cold creep of titanium: Analysis of stress relaxation using synchrotron diffraction and crystal plasticity simulations," *Acta Materialia*, vol. 199, pp. 561 – 577, 2020. [Online]. Available: http://www.sciencedirect.com/science/article/pii/S1359645420306078

[105] H. Abdolvand, J. Wright, and A. J. Wilkinson, "Strong grain neighbour effects in polycrystals," *Nature Communications*, vol. 9, no. 1, p. 171, Jan 2018. [Online]. Available: https://doi.org/10.1038/s41467-017-02213-9

[106] "Aztechkl-nanoanalysis." [Online]. Available: https://nano.oxinst.com/products/aztec/aztechkl#product-information-tabs

[107] R. Hielscher and H. Schaeben, "A novel pole figure inversion method: specification of the *MTEX* algorithm," *Journal of Applied Crystallography*, vol. 41, no. 6, pp. 1024–1037, Dec 2008. [Online]. Available: https://doi.org/10.1107/S0021889808030112

[108] R. Hielscher, C. B. Silbermann, E. Schmidl, and J. Ihlemann, "Denoising of crystal orientation maps," *Journal of Applied Crystallography*, vol. 52, no. 5, pp. 984–996, Oct 2019. [Online]. Available: https://doi.org/10.1107/S1600576719009075

[109] M. Drakopoulos, T. Connolley, C. Reinhard, R. Atwood, O. Magdysyuk, N. Vo, M. Hart, L. Connor, B. Humphreys, G. Howell, S. Davies, T. Hill, G. Wilkin, U. Pedersen, A. Foster, N. D. Maio, M. Basham, F. Yuan, and K. Wanelik, "I12: the joint engineering, environment and processing (JEEP) beamline at diamond light source," *Journal of Synchrotron Radiation*, vol. 22, no. 3, pp. 828–838, Apr. 2015. [Online]. Available: https://doi.org/10.1107/s1600577515003513

[110] Y. T. Tang, N. D'Souza, B. Roebuck, P. Karamched, C. Panwisawas, and D. M. Collins, "Ultra-high temperature deformation in a single crystal superalloy: Mesoscale process simulation and micromechanisms," *Acta Materialia*, vol. 203, p. 116468, 2021. [Online]. Available: https://www.sciencedirect.com/science/article/pii/S1359645420308855

[111] B. Roebuck, D. Cox, and R. Reed, "The temperature dependence of γ' volume fraction in a ni-based single crystal superalloy from resistivity measurements," *Scripta Materialia*, vol. 44, pp. 917–921, 2001.

[112] S. Sulzer, E. Alabort, A. Németh, B. Roebuck, and R. Reed, "On the rapid assessment of mechanical behavior of a prototype nickel-based superalloy

using small-scale testing," *Metallurgical and Materials Transactions A*, vol. 49, p. 4214–4235, 05 2018.

[113] B. Roebuck, D. Cox, and R. Reed, "An innovative device for the mechanical testing of miniature specimens of superalloys," *Superalloys*, pp. 523–528, 2004.

[114] S. Das, F. Hofmann, and E. Tarleton, "Consistent determination of geometrically necessary dislocation density from simulations and experiments," *International Journal of Plasticity*, vol. 109, pp. 18 – 42, 2018. [Online]. Available: http://www.sciencedirect.com/science/article/pii/S0749641918300068

[115] E. Tarleton, "Crystalplasticity," https://github.com/TarletonGroup/CrystalPlasticity, 2020.

[116] Z. Zhang, T.-S. Jun, T. B. Britton, and F. P. Dunne, "Determination of ti-6242 α and β slip properties using micro-pillar test and computational crystal plasticity," *Journal of the Mechanics and Physics of Solids*, vol. 95, pp. 393–410, Oct. 2016. [Online]. Available: https://doi.org/10.1016/j.jmps.2016.06.007

[117] S. R. Kalidindi, "Incorporation of deformation twinning in crystal plasticity models," *Journal of the Mechanics and Physics of Solids*, vol. 46, no. 2, pp. 267 – 290, 1998. [Online]. Available: http://www.sciencedirect.com/science/article/pii/S0022509697000513

[118] N. Grilli, E. Tarleton, P. D. Edmondson, M. N. Gussev, and A. C. F. Cocks, "In situ measurement and modelling of the growth and length scale of twins in α-uranium," *Phys. Rev. Materials*, vol. 4, p. 043605, Apr 2020. [Online]. Available: https://link.aps.org/doi/10.1103/PhysRevMaterials.4.043605

[119] R. Hill and J. Rice, "Constitutive analysis of elastic-plastic crystals at arbitrary strain," *Journal of the Mechanics and Physics of Solids*, vol. 20, no. 6, pp. 401 – 413, 1972. [Online]. Available: http://www.sciencedirect.com/science/article/pii/0022509672900178

[120] N. Grilli, A. C. Cocks, and E. Tarleton, "Crystal plasticity finite element modelling of coarse-grained α-uranium," *Computational Materials Science*, vol. 171, p. 109276, 2020. [Online]. Available: http://www.sciencedirect.com/science/article/pii/S0927025619305750

[121] W. M. Lai, D. Rubin, and E. Krempl, "Chapter 5 - the elastic solid," in *Introduction to Continuum Mechanics (Fourth Edition)*, fourth edition ed., W. M. Lai, D. Rubin, and E. Krempl, Eds. Boston: Butterworth-Heinemann, 2010, pp. 201–352. [Online]. Available: https://www.sciencedirect.com/science/article/pii/B9780750685603000050

[122] A. Arsenlis and D. Parks, "Crystallographic aspects of geometrically-necessary and statistically-stored dislocation density," *Acta Materialia*, vol. 47, no. 5, pp. 1597 – 1611, 1999. [Online]. Available: http://www.sciencedirect.com/science/article/pii/S1359645499000208

[123] J. Nye, "Some geometrical relations in dislocated crystals," *Acta Metallurgica*, vol. 1, no. 2, pp. 153 – 162, 1953. [Online]. Available: http://www.sciencedirect.com/science/article/pii/0001616053900546

[124] C. Bourigault, M. Senn, and C. Eberl, "Python DIC Software," Dec. 2016. [Online]. Available: https://github.com/phanikaramched/Python_DIC

[125] J. Qiu, Y. Ma, J. Lei, Y. Liu, A. Huang, D. Rugg, and R. Yang, "A comparative study on dwell fatigue of ti-6al-2sn-4zr-xmo (x=2 to 6) alloys on a microstructure-normalized basis," *Metallurgical and Materials Transactions A*, vol. 45, no. 13, pp. 6075–6087, Dec 2014. [Online]. Available: https://doi.org/10.1007/s11661-014-2541-5

[126] F. Larson and A. Zarkades, "Properties of textured titanium alloys," 1974.

[127] P. J. Ashton, T.-S. Jun, Z. Zhang, T. B. Britton, A. M. Harte, S. B. Leen, and F. P. Dunne, "The effect of the beta phase on the micromechanical response of dual-phase titanium alloys," *International*

Journal of Fatigue, vol. 100, pp. 377–387, 2017. [Online]. Available: https://www.sciencedirect.com/science/article/pii/S014211231730138X

[128] Z. Zhang and F. P. Dunne, "Microstructural heterogeneity in rate-dependent plasticity of multiphase titanium alloys," *Journal of the Mechanics and Physics of Solids*, vol. 103, pp. 199–220, 2017. [Online]. Available: https://www.sciencedirect.com/science/article/pii/S0022509616306858

[129] M. Tanaka and K. Higashida, "Temperature dependence of effective stress in severely deformed ultralow-carbon steel," *Philosophical Magazine*, vol. 96, no. 19, pp. 1979–1992, 2016. [Online]. Available: https://doi.org/10.1080/14786435.2016.1183828

[130] D. R. N. Correa, F. B. Vicente, R. O. Araújo, M. L. Lourenço, P. A. B. Kuroda, M. A. R. Buzalaf, and C. R. Grandini, "Effect of the substitutional elements on the microstructure of the ti-15mo-zr and ti-15zr-mo systems alloys," *Journal of Materials Research and Technology*, vol. 4, no. 2, pp. 180–185, 2015. [Online]. Available: https://www.sciencedirect.com/science/article/pii/S2238785415000320

[131] A. Sarkar and J. K. Chakravartty, "Activation volume and density of mobile dislocations in plastically deforming zr-1pctsn-1pctnb-0.1pctfe alloy," *Metallurgical and Materials Transactions A*, vol. 46, no. 12, pp. 5638–5643, Dec 2015. [Online]. Available: https://doi.org/10.1007/s11661-015-3153-4

[132] M. R. Gilbert, S. Queyreau, and J. Marian, "Stress and temperature dependence of screw dislocation mobility inα-fe by molecular dynamics," *Physical Review B*, vol. 84, no. 17, Nov. 2011. [Online]. Available: https://doi.org/10.1103/physrevb.84.174103

[133] M. Duesbery, "On kinked screw dislocations in the b.c.c. lattice—ii. kink energies and double kinks," *Acta Metallurgica*, vol. 31, no. 10, pp. 1759 – 1770, 1983. [Online]. Available: http://www.sciencedirect.com/science/article/pii/0001616083901748

[134] A. G. Evans and R. D. Rawlings, "The thermally activated deformation of crystalline materials," *physica status solidi (b)*, vol. 34, no. 1, pp. 9–31, 1969. [Online]. Available: https://onlinelibrary.wiley.com/doi/abs/10.1002/pssb.19690340102

[135] Y. Xiong, P. S. Karamched, C.-T. Nguyen, D. M. Collins, N. Grilli, C. M. Magazzeni, E. Tarleton, and A. J. Wilkinson, "An in-situ synchrotron diffraction study of stress relaxation in titanium: Effect of temperature and oxygen on cold dwell fatigue," *Acta Materialia*, p. 116937, 2021. [Online]. Available: https://www.sciencedirect.com/science/article/pii/S1359645421003177

[136] T. Erinosho, D. Collins, A. Wilkinson, R. Todd, and F. Dunne, "Assessment of x-ray diffraction and crystal plasticity lattice strain evolutions under biaxial loading," *International Journal of Plasticity*, vol. 83, pp. 1 – 18, 2016. [Online]. Available: http://www.sciencedirect.com/science/article/pii/S0749641916300432

[137] Y. WANG, A. HAMZA, and E. MA, "Temperature-dependent strain rate sensitivity and activation volume of nanocrystalline ni," *Acta Materialia*, vol. 54, no. 10, pp. 2715–2726, Jun. 2006. [Online]. Available: https://doi.org/10.1016/j.actamat.2006.02.013

[138] M. Basham, J. Filik, M. T. Wharmby, P. C. Y. Chang, B. E. Kassaby, M. Gerring, J. Aishima, K. Levik, B. C. A. Pulford, I. Sikharulidze, D. Sneddon, M. Webber, S. S. Dhesi, F. Maccherozzi, O. Svensson, S. Brockhauser, G. Náray, and A. W. Ashton, "Data analysis WorkbeNch(DAWN)," *Journal of Synchrotron Radiation*, vol. 22, no. 3, pp. 853–858, Apr. 2015. [Online]. Available: https://doi.org/10.1107/s1600577515002283

[139] J. Filik, A. W. Ashton, P. C. Y. Chang, P. A. Chater, S. J. Day, M. Drakopoulos, M. W. Gerring, M. L. Hart, O. V. Magdysyuk, S. Michalik,

A. Smith, C. C. Tang, N. J. Terrill, M. T. Wharmby, and H. Wilhelm, "Processing two-dimensional X-ray diffraction and small-angle scattering data in *DAWN 2*," *Journal of Applied Crystallography*, vol. 50, no. 3, pp. 959–966, Jun 2017. [Online]. Available: https://doi.org/10.1107/S1600576717004708

[140] S. Suri, T. Neeraj, G. Daehn, D.-H. Hou, J. Scott, R. Hayes, and M. Mills, "Mechanisms of primary creep in α/β titanium alloys at lower temperatures," *Materials Science and Engineering: A*, vol. 234-236, pp. 996–999, Aug. 1997. [Online]. Available: https://doi.org/10.1016/s0921-5093(97)00322-5

[141] N. Grilli, A. C. Cocks, and E. Tarleton, "Crystal plasticity finite element modelling of coarse-grained α-uranium," *Computational Materials Science*, vol. 171, p. 109276, Jan. 2020. [Online]. Available: https://doi.org/10.1016/j.commatsci.2019.109276

[142] Z. Zhang, M. A. Cuddihy, and F. P. E. Dunne, "On rate-dependent polycrystal deformation: the temperature sensitivity of cold dwell fatigue," *Proceedings of the Royal Society A: Mathematical, Physical and Engineering Sciences*, vol. 471, no. 2181, p. 20150214, Sep. 2015. [Online]. Available: https://doi.org/10.1098/rspa.2015.0214

[143] D. Tromans, "Elastic anisotropy of hcp metal crystals and polycrystals," *Int. J. Res. Rev. Appl. Sci.*, vol. 6, 01 2011.

[144] S. Kotha, D. Ozturk, and S. Ghosh, "Parametrically homogenized constitutive models (PHCMs) from micromechanical crystal plasticity FE simulations: Part II: Thermo-elasto-plastic model with experimental validation for titanium alloys," *International Journal of Plasticity*, vol. 120, pp. 320–339, Sep. 2019. [Online]. Available: https://doi.org/10.1016/j.ijplas.2019.05.007

[145] L. Wang, Z. Zheng, H. Phukan, P. Kenesei, J.-S. Park, J. Lind, R. Suter, and T. Bieler, "Direct measurement of critical resolved shear stress of prismatic and basal slip in polycrystalline ti using high energy x-ray diffraction

microscopy," *Acta Materialia*, vol. 132, pp. 598–610, Jun. 2017. [Online]. Available: https://doi.org/10.1016/j.actamat.2017.05.015

[146] A. T. Churchman and T. E. Allibone, "The slip modes of titanium and the effect of purity on their occurrence during tensile deformation of single crystals," *Proceedings of the Royal Society of London. Series A. Mathematical and Physical Sciences*, vol. 226, no. 1165, pp. 216–226, 1954. [Online]. Available: https://royalsocietypublishing.org/doi/abs/10.1098/rspa.1954.0250

[147] H. Conrad, "Effect of interstitial solutes on the strength and ductility of titanium," *Progress in Materials Science*, vol. 26, no. 2-4, pp. 123–403, Jan. 1981. [Online]. Available: https://doi.org/10.1016/0079-6425(81)90001-3

[148] Q. Yu, L. Qi, T. Tsuru, R. Traylor, D. Rugg, J. W. Morris, M. Asta, D. C. Chrzan, and A. M. Minor, "Origin of dramatic oxygen solute strengthening effect in titanium," *Science*, vol. 347, no. 6222, pp. 635–639, Feb. 2015. [Online]. Available: https://doi.org/10.1126/science.1260485

[149] B. Barkia, V. Doquet, J. Couzinié, I. Guillot, and E. Héripré, "In situ monitoring of the deformation mechanisms in titanium with different oxygen contents," *Materials Science and Engineering: A*, vol. 636, pp. 91–102, Jun. 2015. [Online]. Available: https://doi.org/10.1016/j.msea.2015.03.044

[150] X. WU, S. KALIDINDI, C. NECKER, and A. SALEM, "Prediction of crystallographic texture evolution and anisotropic stress–strain curves during large plastic strains in high purity α-titanium using a taylor-type crystal plasticity model," *Acta Materialia*, vol. 55, no. 2, pp. 423–432, Jan. 2007. [Online]. Available: https://doi.org/10.1016/j.actamat.2006.08.034

[151] Y. Yang, L. Wang, T. R. Bieler, P. Eisenlohr, and M. A. Crimp, "Quantitative atomic force microscopy characterization and crystal plasticity finite element modeling of heterogeneous deformation in commercial purity titanium," *Metallurgical and Materials Transactions A*, vol. 42, no. 3, pp. 636–644, Dec. 2010. [Online]. Available: https://doi.org/10.1007/s11661-010-0475-0

[152] L. Wang, R. Barabash, Y. Yang, T. Bieler, M. Crimp, P. Eisenlohr, W. Liu, and G. Ice, "Experimental characterization and crystal plasticity modeling of heterogeneous deformation in polycrystalline α-ti," *Metallurgical and Materials Transactions A*, vol. 42, no. 3, pp. 626–635, Jun. 2010. [Online]. Available: https://doi.org/10.1007/s11661-010-0249-8

[153] D. Gloaguen, G. Oum, V. Legrand, J. Fajoui, and S. Branchu, "Experimental and theoretical studies of intergranular strain in an alpha titanium alloy during plastic deformation," *Acta Materialia*, vol. 61, no. 15, pp. 5779–5790, Sep. 2013. [Online]. Available: https://doi.org/10.1016/j.actamat.2013.06.022

[154] K. Amouzou, T. Richeton, A. Roth, M. Lebyodkin, and T. Lebedkina, "Micromechanical modeling of hardening mechanisms in commercially pure α-titanium in tensile condition," *International Journal of Plasticity*, vol. 80, pp. 222–240, May 2016. [Online]. Available: https://doi.org/10.1016/j.ijplas.2015.09.008

[155] J. Gong and A. J. Wilkinson, "Anisotropy in the plastic flow properties of single-crystal α titanium determined from micro-cantilever beams," *Acta Materialia*, vol. 57, no. 19, pp. 5693 – 5705, 2009. [Online]. Available: http://www.sciencedirect.com/science/article/pii/S1359645409004996

[156] K. Chatterjee, A. Venkataraman, T. Garbaciak, J. Rotella, M. Sangid, A. Beaudoin, P. Kenesei, J.-S. Park, and A. Pilchak, "Study of grain-level deformation and residual stresses in ti-7al under combined bending and tension using high energy diffraction microscopy (HEDM)," *International Journal of Solids and Structures*, vol. 94-95, pp. 35–49, Sep. 2016. [Online]. Available: https://doi.org/10.1016/j.ijsolstr.2016.05.010

[157] F. Roters, M. Diehl, P. Shanthraj, P. Eisenlohr, C. Reuber, S. Wong, T. Maiti, A. Ebrahimi, T. Hochrainer, H.-O. Fabritius, S. Nikolov, M. Friák, N. Fujita, N. Grilli, K. Janssens, N. Jia, P. Kok, D. Ma, F. Meier, E. Werner, M. Stricker, D. Weygand, and D. Raabe,

"Damask – the düsseldorf advanced material simulation kit for modeling multi-physics crystal plasticity, thermal, and damage phenomena from the single crystal up to the component scale," *Computational Materials Science*, vol. 158, pp. 420–478, 2019. [Online]. Available: https://www.sciencedirect.com/science/article/pii/S0927025618302714

[158] "Chapter 2 - experimental characterization of dislocation mechanisms," in *Thermally Activated Mechanisms in Crystal Plasticity*, ser. Pergamon Materials Series, D. Caillard and J. Martin, Eds. Pergamon, 2003, vol. 8, pp. 13–53. [Online]. Available: https://www.sciencedirect.com/science/article/pii/S1470180403800329

[159] Z. Zheng, D. S. Balint, and F. P. Dunne, "Mechanistic basis of temperature-dependent dwell fatigue in titanium alloys," *Journal of the Mechanics and Physics of Solids*, vol. 107, pp. 185 – 203, 2017. [Online]. Available: http://www.sciencedirect.com/science/article/pii/S0022509616307918

[160] D. Ozturk, A. Pilchak, and S. Ghosh, "Experimentally validated dwell and cyclic fatigue crack nucleation model for α–titanium alloys," *Scripta Materialia*, vol. 127, pp. 15 – 18, 2017. [Online]. Available: http://www.sciencedirect.com/science/article/pii/S1359646216304079

[161] D. Deka, D. S. Joseph, S. Ghosh, and M. J. Mills, "Crystal plasticity modeling of deformation and creep in polycrystalline ti-6242," *Metallurgical and Materials Transactions A*, vol. 37, pp. 1371 – 1388, 2006. [Online]. Available: https://doi.org/10.1007/s11661-006-0082-2

[162] V. Sinha, M. J. Mills, and J. C. Williams, "Crystallography of fracture facets in a near-alpha titanium alloy," *Metallurgical and Materials Transactions A*, vol. 37, no. 6, pp. 2015–2026, Jun 2006. [Online]. Available: https://doi.org/10.1007/s11661-006-0144-5

[163] M. C. Brandes, M. J. Mills, and J. C. Williams, "The influence of slip character on the creep and fatigue fracture of an α ti-al alloy," *Metallurgical and Materials Transactions A*, vol. 41, no. 13, pp. 3463–3472, Dec 2010. [Online]. Available: https://doi.org/10.1007/s11661-010-0407-z

[164] N. Grilli, "ebsd2abaqusEuler," Oct. 2020. [Online]. Available: https://github.com/ngrilli/ebsd2abaqusEuler

[165] E. Jones, T. Oliphant, P. Peterson *et al.*, "SciPy: Open source scientific tools for Python," 2001.

[166] J. A. Nelder and R. Mead, "A Simplex Method for Function Minimization," *The Computer Journal*, vol. 7, no. 4, pp. 308–313, 01 1965.

[167] N. Grilli, P. Earp, A. C. Cocks, J. Marrow, and E. Tarleton, "Characterisation of slip and twin activity using digital image correlation and crystal plasticity finite element simulation: Application to orthorhombic α-uranium," *Journal of the Mechanics and Physics of Solids*, vol. 135, p. 103800, 2020. [Online]. Available: http://www.sciencedirect.com/science/article/pii/S0022509619306696

[168] K. Kishida, J. G. Kim, T. Nagae, and H. Inui, "Experimental evaluation of critical resolved shear stress for the first-order pyramidal $c + a$ slip in commercially pure ti by micropillar compression method," *Acta Materialia*, vol. 196, pp. 168–174, 2020. [Online]. Available: https://www.sciencedirect.com/science/article/pii/S135964542030478X

[169] T. Mitchell, "Yielding in crystals containing atomic-size obstacles," in *Encyclopedia of Materials: Science and Technology*, K. J. Buschow, R. W. Cahn, M. C. Flemings, B. Ilschner, E. J. Kramer, S. Mahajan, and P. Veyssière, Eds. Oxford: Elsevier, 2001, pp. 9827–9842. [Online]. Available: https://www.sciencedirect.com/science/article/pii/B0080431526017812

[170] Z. Zheng, A. Stapleton, K. Fox, and F. P. Dunne, "Understanding thermal alleviation in cold dwell fatigue in titanium alloys," *International Journal of Plasticity*, vol. 111, pp. 234 – 252, 2018. [Online]. Available: http://www.sciencedirect.com/science/article/pii/S0749641918302195

[171] A. Guery, F. Hild, F. Latourte, and S. Roux, "Slip activities in polycrystals determined by coupling dic measurements with crystal plasticity calculations," *International Journal of Plasticity*, vol. 81, pp. 249 – 266, 2016. [Online]. Available: http://www.sciencedirect.com/science/article/pii/S0749641916000188

[172] Y. Xu, S. Joseph, P. Karamched, K. Fox, D. Rugg, F. P. E. Dunne, and D. Dye, "Predicting dwell fatigue life in titanium alloys using modelling and experiment," *Nature Communications*, vol. 11, p. 5868, 2020. [Online]. Available: https://doi.org/10.1038/s41467-020-19470-w

[173] T. Sakai and M. Fine, "Basal slip of ti-al single crystals," *Scripta Metallurgica*, vol. 8, no. 5, pp. 545 – 547, 1974. [Online]. Available: http://www.sciencedirect.com/science/article/pii/0036974874900660

[174] ——, "Failure of schmid's law in tial alloys for prismatic slip," *Scripta Metallurgica*, vol. 8, pp. 541–544, 1974.

[175] M. R. Bache, F. P. E. Dunne, and C. Madrigal, "Experimental and crystal plasticity studies of deformation and crack nucleation in a titanium alloy," *The Journal of Strain Analysis for Engineering Design*, vol. 45, no. 5, pp. 391–399, 2010. [Online]. Available: https://doi.org/10.1243/03093247JSA594

[176] L. Germain, N. Gey, M. Humbert, P. Vo, M. Jahazi, and P. Bocher, "Texture heterogeneities induced by subtransus processing of near α titanium alloys," *Acta Materialia*, vol. 56, no. 16, pp. 4298–4308, 2008.

[177] K. Le Biavant, S. Pommier, and C. Prioul, "Local texture and fatigue crack initiation in a ti-6al-4v titanium alloy," *Fatigue & Fracture of Engineering*

Materials & Structures, vol. 25, no. 6, pp. 527–545, 2002. [Online]. Available: https://onlinelibrary.wiley.com/doi/abs/10.1046/j.1460-2695.2002.00480.x

[178] I. Bantounas, D. Dye, and T. C. Lindley, "The role of microtexture on the faceted fracture morphology in ti–6al–4v subjected to high-cycle fatigue," *Acta Materialia*, vol. 58, no. 11, pp. 3908 – 3918, 2010. [Online]. Available: http://www.sciencedirect.com/science/article/pii/S1359645410001916

[179] K. Zhang, K. Yang, A. Huang, X. Wu, and C. Davies, "Fatigue crack initiation in as forged ti–6al–4v bars with macrozones present," *International Journal of Fatigue*, vol. 80, pp. 288 – 297, 2015. [Online]. Available: http://www.sciencedirect.com/science/article/pii/S0142112315001772

[180] K. Zhang, K. Yang, S. Lim, X. Wu, and C. Davies, "Effect of the presence of macrozones on short crack propagation in forged two-phase titanium alloys," *International Journal of Fatigue*, vol. 104, pp. 1 – 11, 2017. [Online]. Available: http://www.sciencedirect.com/science/article/pii/S014211231730292X

[181] Y. Ozaki, M. Yano, and M. Onishi, "Effective hyperparameter optimization using nelder-mead method in deep learning," *IPSJ Transactions on Computer Vision and Applications*, vol. 9, no. 1, p. 20, Nov 2017. [Online]. Available: https://doi.org/10.1186/s41074-017-0030-7